Chromosome organization in *Corynebacterium glutamicum*

Dissertation

zur Erlangung des Doktorgrades der Naturwissenschaften

(Dr. rer. nat.)

an der Fakultät für Biologie der

Ludwig-Maximilians-Universität München

vorgelegt von

Kati Böhm

aus Neuhaus am Rennweg

München, Juni 2019

Die vorliegende Doktorarbeit wurde im Zeitraum von Januar 2015 bis Juni 2019 in der Arbeitsgruppe bakterielle Zellbiologie (Prof. Dr. Marc Bramkamp) an der Ludwig-Maximilians-Universität München durchgeführt.

1. Gutachter: Prof. Dr. Marc Bramkamp

2. Gutachter: Prof. Dr. Christof Osman

Tag der Abgabe: 18. Juni 2019

Tag der mündlichen Prüfung: 24. September 2019

Eidesstattliche Erklärung

Ich versichere hiermit an Eides statt, dass die vorgelegte Dissertation von mir selbständig und ohne unerlaubte Hilfsmittel angefertigt worden ist. Die vorliegende Dissertation wurde weder ganz, noch in wesentlichen Teilen einer anderen Prüfungskommission vorgelegt. Ich habe noch zu keinem früheren Zeitpunkt versucht, eine Dissertation einzureichen oder mich der Doktorprüfung zu unterziehen.

I hereby confirm that I have written the accompanying thesis by myself, without contribution from any sources other than those cited in the text. Moreover, I declare that I have not submitted or defended a dissertation previously without success. This thesis has not been presented to any other examining board.

München, den 18. Juni 2019

Kati Böhm

Index

Publications and contributions

Publications that were prepared and published in the scope of this study are listed in the following.

- **Böhm, K.**, Meyer, F., Rhomberg, A., Kalinowski, J., Donovan, C., and Bramkamp, M. (2017). Novel chromosome organization pattern in *Actinomycetales*—overlapping replication cycles combined with diploidy. mBio *8*, e00511-17.

  Kati Böhm, Dr. Catriona Donovan (AG Bramkamp, LMU Munich) and Prof. Dr. Marc Bramkamp designed the study. Kati Böhm performed the majority of the experiments and wrote the manuscript together with Prof. Dr. Marc Bramkamp. Automated image analysis was carried out in collaboration with Fabian Meyer and marker frequency studies were partly performed by Agata Rhomberg (AG Bramkamp, LMU Munich). Genome sequencing analysis was provided by Prof. Dr. Jörn Kalinowski from the Center for Biotechnology in Bielefeld.

- **Böhm, K.**, Giacomelli, G., Schmidt, A., Imhof, A., Koszul, R., Marbouty, M., and Bramkamp, M. (2019). Chromosome organization by a conserved condensin-ParB system in the actinobacterium *C. glutamicum*. Preprint available at BioRxiv; doi: 10.1101/649749. (submitted manuscript)

  Kati Böhm and Prof. Dr. Marc Bramkamp conceptionalized this study together with Prof. Dr. Romain Koszul and Dr. Martial Marbouty from the Institut Pasteur in Paris and wrote the manuscript. The majority of the experiments were performed by Kati Böhm. PALM microscopy was performed in collaboration with Giacomo Giacomelli (AG Bramkamp, LMU Munich). Chromosome conformation capture analysis was carried out in collaboration with Dr. Martial Marbouty and Prof. Dr. Romain Koszul. Dr. Andreas Schmidt and Prof. Dr. Axel Imhof from the Biomedical Center in Munich contributed with mass spectrometry data to this publication.

- Schubert, K., Sieger, B., Meyer, F., Giacomelli, G., **Böhm, K.**, Rieblinger, A., Lindenthal, L., Sachs, N., Wanner, G., and Bramkamp, M. (2017). The antituberculosis drug ethambutol selectively blocks apical growth in CMN group bacteria. mBio *8*, e02213-16.

  Kati Böhm contributed to this study with time lapse microscopy data and qPCR analysis of DivIVA mRNA levels in presence and absence of ethambutol.

- **Böhm, K.**, Giacomelli, G., Meyer, F., Bramkamp, M. (2019). Chromosome organization and cell growth of *Corynebacterium glutamicum*. In *Corynebacterium glutamicum*: Biology and Biotechnology, H. Yukawa, and M. Inui, eds. (Berlin, Heidelberg: Springer Berlin Heidelberg). (submitted manuscript)

  This review article was written by Kati Böhm, Giacomo Giacomelli, Fabian Meyer and Prof. Dr. Marc Bramkamp. Subchapters concerning chromosome structure and segregation, cell cycle and division site selection were written by Kati Böhm.

Abbreviations

ABC	ATP-binding cassette
ATP	Adenosine triphosphate
BHI	Brain heart infusion
bp	Base pairs
ChIP (-seq)	Chromatin immunoprecipitation (combined with deep-sequencing)
EDTA	Ethylendiamin-tetraacetat
FROS	Fluorescent repressor operator system
IPTG	Isopropyl β-D-1-thiogalactopyranoside
lacO/LacI	Lac Operator/Lac Repressor
LC-MS/MS	Liquid chromatography tandem mass spectrometry
Kb	Kilo base pairs
Mb	Mega base pairs
Mks	Muk-like SMC
oriC	Chromosomal origin of replication
PALM	Photoactivated localization microscopy
PldP	ParA-like division protein
PSF	Point spread function
rDNA	Ribosomal DNA
SDS	Sodium dodecyl sulfate
Sec-pathway	General secretory pathway
SMC	Structural maintenance of chromosomes
Tat	Twin-arginine translocase
terC	Chromosomal terminus of replication
Tris	Tris-(hydroxymethyl)-aminomethan
tRNA	Transfer RNA

Summary

Bacterial chromosome organization is spatiotemporally highly coordinated, where particularly the widely conserved DNA partitioning system ParABS and condensin complexes act as key players of genome homeostasis. Despite the discovery of diverging mechanisms of chromosome organization, current information is largely based on studies in a limited number of standard model species, like *Escherichia coli*, *Bacillus subtilis* and *Caulobacter crescentus*. Therefore, we aimed to elucidate ParABS- and condensin-mediated genome structuring, segregation dynamics and replication in the apically growing actinobacterium *Corynebacterium glutamicum*.

This study reveals a stable association of at least two chromosomal origins of replication (*oriC*) with the cell poles, while replication termini (*terC*) localize at midcell, pointing to a longitudinal chromosome arrangement in *C. glutamicum*. During the cell cycle newly replicated *oriC*s are segregated towards division septa after a highly flexible period of *oriC*-cohesion. In-depth cell cycle studies at different growth rates point to a strict diploidy and exceptionally high chromosome copy numbers per cell. Moreover, we evidenced replication overinitiation as an adaptation to fast growth, resulting in overlapping replication cycles. Further, our studies unveil the formation of large ParB-nucleoprotein complexes at ten *parS* sites that are each sub-structured into several ParB-dense clusters. Together the ten *parS* sites form a centromere-like region close to the *oriC*. Here, the presence of at least one *parS* site in an *oriC*-proximal region is necessary for reliable origin segregation along the nucleoid. We further identified two condensin complexes and their divergent functions in *C. glutamicum*. Structural maintenance of chromosomes (SMC) complexes are loaded ParB-dependently at *parS* sites and migrate from there on across the genome. By contrast, cell pole-associated MukBEF-like SMC (MksBEFG) complexes do not impact on genome structuring and instead, aid in plasmid maintenance.

Using chromosome conformation capture techniques, we elucidated the multi-scale chromosomal architecture of *C. glutamicum*. Here, both ParB and SMC are involved in folding of the *oriC* domain. Moreover, we demonstrate that migration of SMC along the chromosome mediates chromosomal inter-arm cohesion. Even ectopic *parS* sites distant to *oriC* recruit SMC, which results in the alignment of flanking chromosomal regions. Most strikingly, the nucleoid

serves as a spatial track for ParB-mediated *oriC*-segregation, providing spatiotemporal cues beyond its genetic information.

Finally, we characterized spatiotemporal dynamics of the homologous ATPases ParA and PldP and uncovered subcellular localization interdependencies of ParABS components including PldP. Our data provide evidence for an indirect role of PldP in division septum placement, while being spatially positioned by ParB.

In summary, we reveal in *C. glutamicum* a unique combination of chromosome organizing strategies, being representative for the huge diversity in genome maintenance amongst prokaryotes. This study further elucidates so far undescribed functional characteristics of the ubiquitous ParABS and condensin machineries that are of cross-cutting relevance for our understanding of bacterial chromosome organization.

Zusammenfassung

Bakterielle Chromosomenorganisation ist ein räumlich und zeitlich präzise koordinierter Vorgang. Insbesondere spielen der stark konservierte DNA Segregations-Apparat ParABS und Kondensin-Komplexe bei der Genom-Homöostase eine entscheidenede Rolle. Trotz der Entdeckung unterschiedlicher Strategien zur Organisation von Chromosomen, basiert der derzeitige Wissensstand hauptsächlich auf Studien in einer begrenzten Anzahl von Modellorganismen, wie *Escherichia coli*, *Bacillus subtilis* und *Caulobacter crescentus*. Daher war es unser Ziel ParABS- und Kondensin-vermittelte Genomstrukturierung, die Dynamik der Chromosomensegregation und Replikation in dem apikal wachsenden Actinobakterium *Corynebacterium glutamicum* zu entschlüsseln.

Diese Studie belegt eine dauerhafte Bindung chomosomaler Replikationsursprünge (*oriC*) an jeden Zellpol sowie eine zentrierte Lokalisation von Replikationstermini (*terC*), was auf eine longitudinale Chromosomenorganisation in *C. glutamicum* schließen lässt. Nach einer zeitlich sehr variablen Phase der *oriC*-Kohäsion werden im Laufe einer Generation replizierte *oriC*s in Richtung des Teilungs-Septums voneinander separiert. Detaillierte Untersuchungen zum Zellzyklus bei unterschiedlichen Wachstumsraten zeigten strikte Diploidie und unerwartet hohe Chromosomenzahlen pro Zelle auf. Zudem konnten wir eine Replikationsüberinitiierung als Anpassung an hohe Wachstumsraten nachweisen, die überlappende Replikationszyklen zur Folge haben. Des Weiteren belegen unsere Studien die Ausbildung großer ParB-Nukleoprotein-Komplexe an zehn *parS*-Sequenzen, die jeweils in mehrere Cluster mit erhöhter ParB-Dichte unterteilt sind. Insgesamt stellen die *parS*-Sequenzen eine Zentromer-ähnlichen Region nahe des *oriC*s dar. Für eine zuverlässige *oriC*-Segregation entlang des Nukleoids ist mindestens eine *parS*-Sequenz im Bereich der Zentromer-Region notwendig. Darüber hinaus identifizierten wir zwei Kondensin-Komplexe und deren unterschiedliche Funktionen in *C. glutamicum*. Structural Maintenance of Chromosomes (SMC)-Komplexe werden in Abhängigkeit von ParB an *parS*-Sequenzen geladen und verteilen sich von dort ausgehend entlang des Chromosoms. Im Gegensatz dazu wirken Zellpol-assoziierte MukBEF-ähnliche SMC (MksBEFG)-Komplexe nicht auf die Genomstruktur, sondern beeinflussen die Weitergabe von Plasmiden.

Mithilfe von „Chromosome conformation capture“-Techniken konnte die skalen-übergreifende Chromosomenarchitektur von *C. glutamicum* aufgeklärt werden. Hierbei wurde gezeigt, dass sowohl ParB als auch SMC an der Strukturierung der *oriC*-Domäne beteiligt sind. Die SMC-Migration entlang des Chromosoms vermittelt die Ausbildung von Kontakten zwischen Replichoren. Selbst ektopische *parS*-Sequenzenen in großer Distanz zu *oriC* binden SMC, was zu einer Zusammenlagerung angrenzender chromosomaler Regionen führt. Unsere Arbeiten zeigen deutlich, dass das bakterielle Nucleoid der ParB-vermittelten *oriC*-Segregation als Spur dient und enthält daher neben der gespeicherten genetischen Information Informationen zur räumlich-zeitlichen Organisation der Bakterienzelle.

Abschließend wurde die räumlich-zeitliche Dynamik der homologen ATPasen ParA und PldP charakterisiert und subzelluläre Lokalisationsabhängigkeiten der ParABS-Komponenten, eingeschlossen PldP, aufgedeckt. Unsere Daten weisen auf eine indirekte Positionierung der Zellteilungsebene durch PldP hin, dessen räumliche Ausrichtung durch ParB erfolgt.

Zusammenfassend beschreiben wir in *C. glutamicum* eine einzigartige Kombination an Strategien der Chromosomenorganisation, die repräsentativ für die große mechanistische Vielfalt innerhalb der Prokaryoten steht. Diese Studie klärt zudem bisher unbeschriebene funktionale Eigenschaften der konservierten ParABS- und Kondensin-Apparate auf, die weitreichende Schlussfolgerungen für die bakterielle Chromosomenorganisation zulassen.

1. Introduction

1.1. Preamble

Genomic information is stored in DNA that forms organizational units termed chromosomes. Chromosomes are highly organized structures, with DNA-compaction, replication and segregation being timed with all other cellular processes. Bacteria evolved various sophisticated strategies for spatiotemporal genome organization, where underlying protein machineries are diverse and may exist in variable combinations within cells, contributing corporately to chromosome homeostasis.

The next chapter provides an overview of this field of research and points to open questions. Primary objectives of this study are introduced at its end. This thesis resulted in one publication and one submitted manuscript regarding chromosome organization in the model organism *Corynebacterium glutamicum*. These data are presented together with associated unpublished results in the second chapter. Main findings of this study are analyzed and discussed in chapter three. Experimental procedures applied in this work are described at the end of the thesis.

1.2. Bacterial chromosome replication

Amongst all kingdoms of life, reliable DNA duplication is a prerequisite for stable genome inheritance throughout generations. While chromosome replication in eukaryotes is timely separated from segregation of sister nucleoids, bacteria merge both processes. However, bacterial genome duplications are highly ordered and regulated by a variety of control mechanisms ensuring a tight coordination with cell division (reviewed in Katayama et al., 2010; Reyes-Lamothe et al., 2012).

Bacterial chromosomes are usually circular structures in the range of several mega base pairs (Mb), where replication is initiated at one single chromosomal origin of replication (*oriC*) and proceeds bidirectionally towards the opposing terminus of replication (*terC*). Notably, few exceptions amongst bacteria exist that harbor linear chromosomes, including actinobacteria of

the genus *Streptomyces* (Volff and Altenbuchner, 2000). Fundamental features of a replicating bacterial chromosome are illustrated below (**Figure 1.1**). Here, regulatory systems, like CtrA in *Caulobacter crescentus* and SeqA in *Escherichia coli*, time replication initiation by scheduling the binding of the key replication initiator protein DnaA to recognition boxes at the *oriC* (Gorbatyuk and Marczynski, 2005; Lu et al., 1994; McGrath et al., 2006; Nievera et al., 2006; Quon et al., 1998). DnaA bound to DnaA-boxes at *oriC* mediates local DNA unwinding and successive recruitment of the replication machinery, termed replisome. In this multi-enzyme complex a DNA helicase mediates DNA duplex unwinding, which is stabilized by single strand-DNA binding proteins (reviewed in Beattie and Reyes-Lamothe, 2015). Further, processivity of the polymerase is facilitated by the β-sliding clamp DnaN, ensuring stable replication progression with velocities of up to 1000 base pairs (bp) per second (Pham et al., 2013; Tanner et al., 2009). Proceeding duplex unwinding induces positive DNA supercoiling ahead of the enzyme complex and catenation behind replication forks, which need to be relaxed by topoisomerases gyrase and topoisomerase IV, respectively (Hiasa and Marians, 1996; Zechiedrich and Cozzarelli, 1995). In general, the process of bacterial chromosome replication is confined to distinct cellular regions with species-dependent replisome dynamics, ranging from rather static to highly mobile replication forks (Jensen et al., 2001; Lemon and Grossman, 2000).

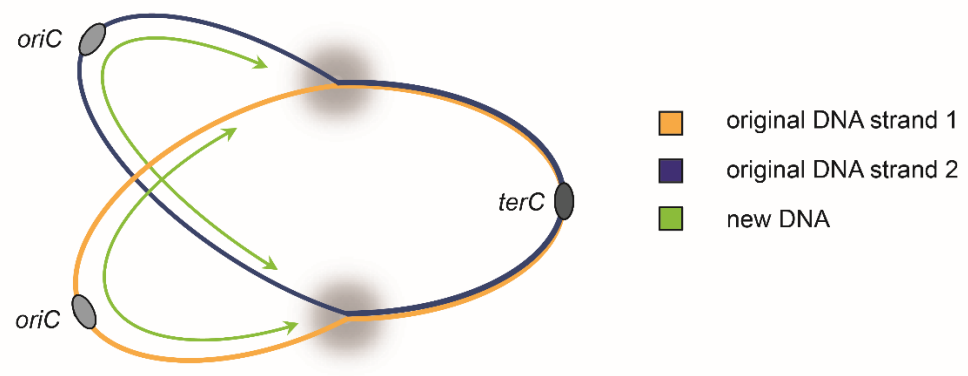

Figure 1.1: Bacterial chromosome during replication.

Replication is initiated at *oriC*, with two replication forks (grey blurred circles) emanating therefrom. Replisomes proceed bidirectionally along left and right replichores towards *terC*, giving rise to two sister chromosomes.

After replication termination recombinases XerCD mediate decatenation of sister chromosomes at *terC*-proximal *dif* sites (Blakely et al., 1993). This enzyme complex is usually associated with a DNA translocase, FtsK in *E. coli*, which aids in chromosome partitioning to daughter cells by directed pumping of chromosomal DNA across the closing septum shortly before completion of cell division (Aussel et al., 2002; Bigot et al., 2005; Massey et al., 2006).

1.3. The bacterial cell cycle

Chromosome replication and cell division are interdependent processes, which are prerequisites for cell growth (Arjes et al., 2014; Bates and Kleckner, 2005). Both define cell cycle parameters and, in turn, are timely regulated by the bacterial metabolism (reviewed in Willis and Huang, 2017). For instance, regulons involved in the central carbon metabolism negatively feedback on the replication initiator DnaA, cell division by Z-ring assembly and MreB-mediated cell wall synthesis (Jonas, 2014; Westfall and Levin, 2018).

In bacteria, cell cycles commonly consist of three phases, which are coupled with nutrient-availability. The time frame of chromosome replication is defined as C-period, while the subsequent D-period covers the interval between replication termination and completion of cell division (**Figure 1.2A**) (Cooper and Helmstetter, 1968). In general, the length of C- and D-periods remains relatively constant amongst different nutrient-rich growth conditions, however, can be prolonged in nutrient-poor media. Particularly at slow growth, replication is not synchronized with cell birth and is instead preceded by an additional B-period (Wang and Levin, 2009).

Moreover, different species-dependent cell cycle strategies exist. Slow-growing bacteria, like *C. crescentus* or *Mycobacterium tuberculosis*, perform one single round of replication per cell cycle (Marczynski, 1999; Nair et al., 2009). By contrast, many other species can adapt their cell cycles to fast growth conditions by overlapping C-periods, thereby reducing generation times (Cooper and Helmstetter, 1968; Stokke et al., 2011; Yoshikawa et al., 1964). To this end, new rounds of replication are initiated before termination of previous ones (**Figure 1.2B**), leading to multiply nested replication forks (Cooper and Helmstetter, 1968). Fast-growing *E. coli* cells can for instance double every 20 minutes, even though one C-period takes roughly twice as long (Cooper and Helmstetter, 1968). However, at any cell cycle mode, only one round of DNA replication is completed per life cycle (Bremer and Churchward, 1977).

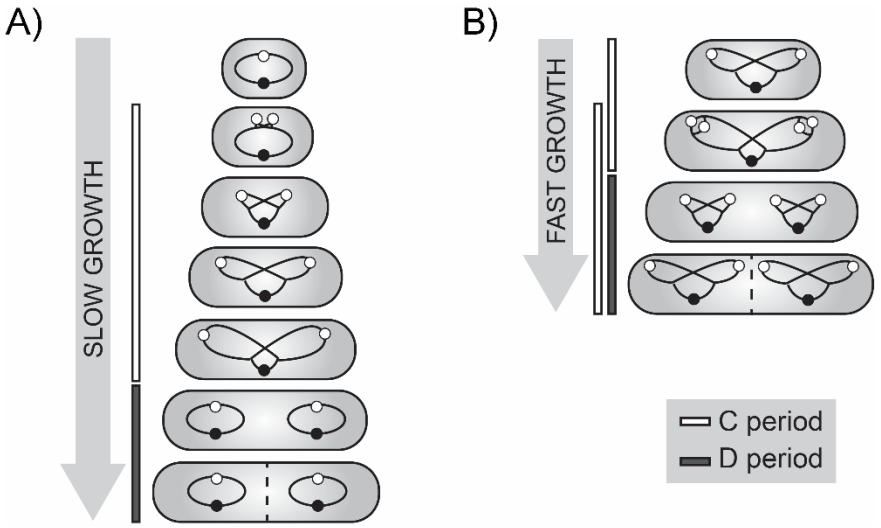

Figure 1.2: Scheme of cell cycles at slow and fast growth conditions.

Chromosomes are displayed as black lines with *oriC* and *terC* indicated by white and black circles. Different stages of the replication cycle are illustrated by bars next to schemes, where C-periods usually precede D-periods and terminate prior to cell division (**A**). Interleaved replication events that reduce generation intervals imply ongoing C-periods at cell division (**B**).

In addition to multifork replication, many prokaryotes naturally harbor high DNA contents due to various levels of ploidy, where two to ten thousand fully replicated genome copies per cell are maintained throughout generations (Griese et al., 2011; Hansen, 1978; Mendell et al., 2008; Nagpal et al., 1989; Pecoraro et al., 2011). Several evolutionary advantages, like reduced mutation rates, desiccation resistance or growth ability in phosphorous-depleted environments, have been attributed to this growth strategy (reviewed in Soppa, 2014).

1.4. Chromosome segregation system ParABS

Within every cell cycle, duplicated genomes must segregate to opposing cell halves, which will eventually turn into two separate daughter cells. In eukaryotes, a well-characterized cytoskeletal structure, the spindle apparatus, assembles in meiotic and mitotic cells to pull sister chromatids apart. Prokaryotes, on the other hand, evolved different strategies to segregate chromosomes. *E. coli* and related species separate duplicated chromosomes by a self-organizing process involving entropic forces of DNA polymers and only rely in a final segregation step on the FtsK/XerCD enzymatic machinery (Joshi et al., 2011; Jun and Mulder, 2006).

However, the vast majority of bacteria additionally possess a mitotic-like ParABS system type I, which actively segregates duplicated sister chromosomes (Livny et al., 2007). Notably, also plasmid-encoded *par* homologues exist, which drive segregation of low-copy-number plasmids accordingly (Kiekebusch and Thanbichler, 2014). In general, this partitioning mechanism involves two protein-coding genes ParAB and one centromere-like DNA sequence called *parS*. The sequence is a 16 bp palindromic motif close to the *oriC* region, which is in large parts identical in sequence amongst species (Lin and Grossman, 1998; Livny et al., 2007). The number of genomic *parS* sequences can differ between organisms, with the highest numbers being predicted for the genus *Streptomyces* with up to twenty-three sites per chromosome (Livny et al., 2007).

The dimeric partitioning protein ParB binds *parS* sequence-specifically with a helix-turn-helix-motif in its central domain (Leonard et al., 2004). In addition, ParB can interact with several kilo base pairs (Kb) of non-specific DNA surrounding *parS* by spreading along DNA after nucleation at *parS* sites (Breier and Grossman, 2007; Murray et al., 2006; Rodionov et al., 1999). In that respect, long-distance distribution of ParB can be impeded by strong DNA-binding proteins, which act as a road blocks. Spreading in combination with 3D-bridging events between ParB dimers, which induces DNA condensation, eventually leads to large nucleoprotein complex formation (Broedersz et al., 2014; Graham et al., 2014). According to a more recent model termed nucleation and caging (Sanchez et al., 2015), complex nucleation equally centers at stably bound ParB-*parS*. Here, locally high ParB concentration surrounding *parS* are stabilized by weak stochastic interactions between ParB dimers with itself and with surrounding non-specific DNA, forming a dynamic ParB-DNA lattice (**Figure 1.3**). Primarily conserved motives in the N-terminal ParB-domain have been implicated in oligomerization and DNA-bridging (Chen et al., 2015; Graham et al., 2014; Kusiak et al., 2011), however, network formation is likely mediated corporately with dimerization and non-specific DNA-binding interfaces in the central and the C-terminal protein domains (Fisher et al., 2017; Schumacher and Funnell, 2005). The contributions of several chromosomal *parS* sites, as existent in most bacteria, to the overall formation and structure of such ParB networks *in vivo* are yet poorly characterized.

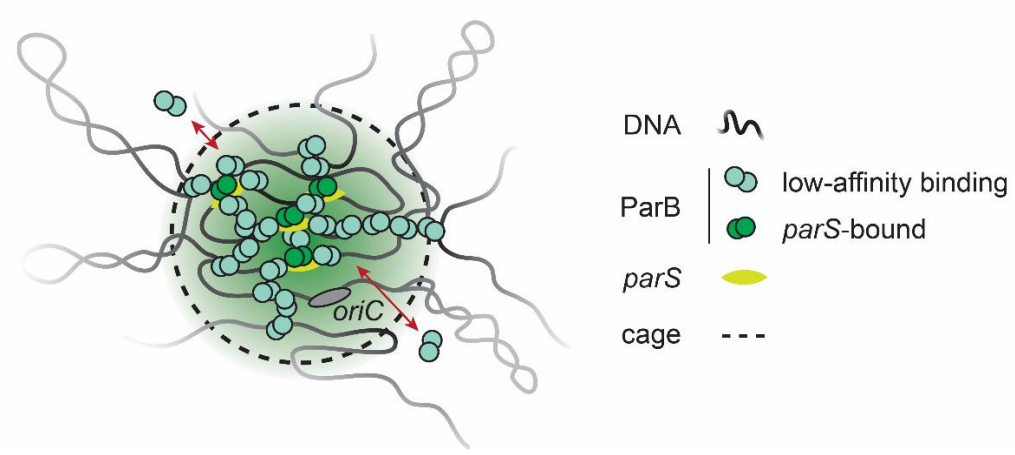

Figure 1.3: Dynamic structure of the ParB-*parS* partition complex.

ParB-nucleoprotein network forms by a combination of strong ParB-*parS* binding and weak interactions between ParB-ParB dimers and between ParB and non-specific DNA that lead to entrapment of ParB around *parS*. Such dynamic structures comprise large regions of *parS*-flanking DNA in cis and trans.

The partner protein of ParB is the P-loop ATPase ParA, which belongs to a diverse ParA/MinD family (Leipe et al., 2002). Proteins of this family have a deviant Walker A motif in common, which harbors two conserved lysines (Leipe et al., 2002). Both are involved in nucleotide binding; in particular the N-terminal 'signature' lysine is responsible for stabilizing phosphates of adenosine triphosphate (ATP) (Leonard et al., 2005). Upon dimer formation at ATP-interaction sites this family of ATPases usually bind to distinct cellular structures, and in turn, specific protein interactors can trigger ATP-hydrolysis and the release of ATPases from their binding matrix (reviewed in Lutkenhaus, 2012). **Figure 1.4A** displays the ATP cycle of ParA. Such capture- and release-cycles enable these proteins to position a broad spectrum of cargo within cells. Particularly, ParA-ATPases of ParABS systems bind via conserved arginine residues sequence-unspecifically to the bacterial nucleoid, which fills large parts of the cell volume (Hester and Lutkenhaus, 2007; Leonard et al., 2005).

In the course of ParABS-mediated chromosome or plasmid segregation, ParB and ParA act as a self-organizing Brownian ratchet (**Figure 1.4B**) (Hwang et al., 2013; Vecchiarelli et al., 2013; Zhang and Schumacher, 2017). Here, dynamic diffusion of ParB-*parS* complexes drives interactions with surrounding ParA, resulting in iterative ATP-hydrolysis and DNA-rebinding cycles of ParA. Slow conformational transitions upon ATP-binding delay DNA-rebinding of ParA and create a ParA depletion zone that trails behind the moving ParB-*parS* complexes (Vecchiarelli et al., 2010). At large, these processes mediate a directed movement of *ori*Cs away

from each other following a dynamic ParA gradient on the bacterial genome. A second model further extends the fundamental parameters for the persistence and directionality of the segregation process by elasticity of ParA-bound DNA (Lim et al., 2014).

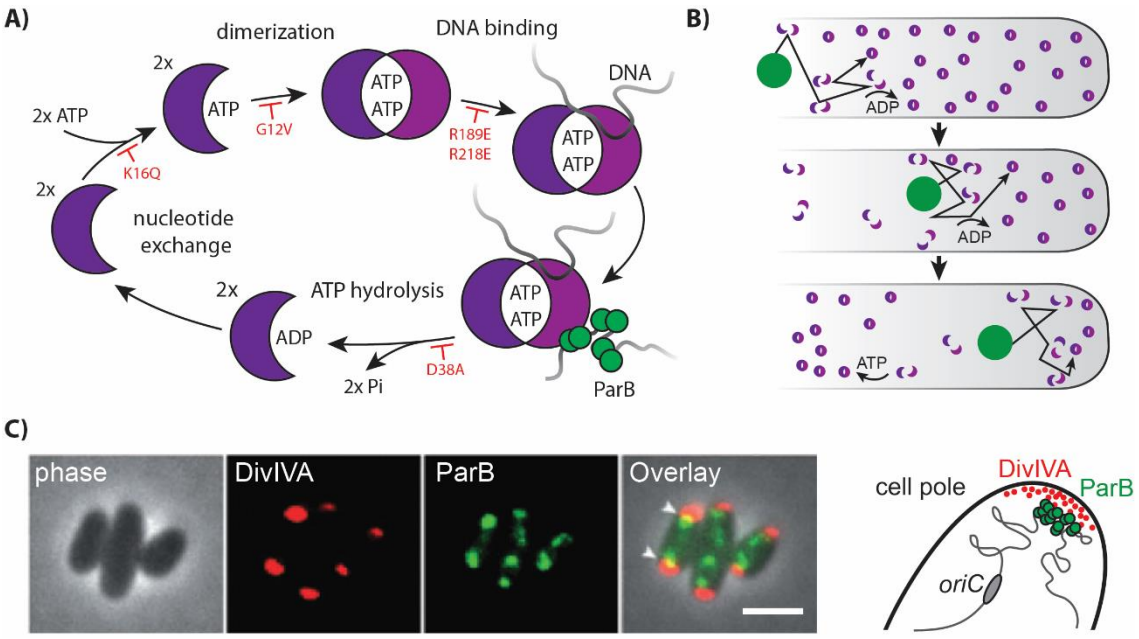

Figure 1.4: ParABS-mediated chromosome relocation and polar *oriC*-retention.

(**A**) Model of the ParA ATP cycle illustrating ATP-dependent binding of ParA to DNA and ParB-mediated nucleotide hydrolysis. Purple crescents indicate ParA monomers; mutations blocking specific steps of the ATP cycle are displayed in red for the *B. subtilis* ParA homologue Soj (Hester and Lutkenhaus, 2007; Leonard et al., 2005). (**B**) Illustration of the Brownian ratchet model for directed movement of a ParB-*parS* complex (green) along DNA-bound ParA (purple circles). A ParA gradient forms upon ParB-mediated release from DNA (ATP-hydrolysis, purple crescents) and subsequent rebinding events. (**C**) Direct interaction of *oriC*-proximal ParB with DivIVA in *C. glutamicum* cells. Left: Microscopy images are amended from Donovan et al. (2012), showing DivIVA-mCherry (red) and plasmid-encoded ParB-eCFP fluorescence (green), phase contrast and merge images; scale bar, 2 µm. White arrows display DivIVA-ParB interaction sites at cell poles. Right: Cartoon of cell pole illustrating aforementioned interaction.

In addition to the active ParABS segregation process, many bacteria stably tether *oriC*s to the cell poles. To this end, ParB-*parS* complexes are recruited to polar positions via ParB- or ParA-interactions with species-specific landmark proteins (Bowman et al., 2008; Ditkowski et al., 2013; Donovan et al., 2012; Ebersbach et al., 2008; Ginda et al., 2013; Lin et al., 2017; Schofield et al., 2010; Wu and Errington, 2003; Yamaichi et al., 2012). After replication initiation the newly segregated sister *oriC* is translocated via the ParABS system and eventually associates with distant

landmark structures. One of the well-studied polar tethering factors in Gram-positive bacteria is the coiled-coil protein DivIVA (Edwards et al., 2000), which targets negatively curved membranes at cell poles and division septa (Lenarcic et al., 2009; Ramamurthi and Losick, 2009). Polar tethering of *oriC* domains by DivIVA is shown exemplarily above in the actinobacterium *C. glutamicum* (**Figure 1.4C**). Besides maintaining chromosome segregation DivIVA further regulates other cellular processes species-dependently, like cell wall synthesis (Hempel et al., 2008; Letek et al., 2008; Nguyen et al., 2007) and division site selection (Bramkamp et al., 2008; Patrick and Kearns, 2008).

Disturbing the chromosome segregation system by ParAB deletions causes DNA mis-segregation defects that lead to the formation of DNA-free cells and cell length variabilities. However, the severity of this defect is species-dependent, reaching from mild effects up to major viability constraints with more than 15 % of anucleate cells (Charaka and Misra, 2012; Donovan et al., 2010; Ginda et al., 2013; Ireton et al., 1994; Jakimowicz et al., 2007a; Lewis et al., 2002) or even loss of viability (Iniesta, 2014; Mohl et al., 2001). Similar chromosome segregation effects occur upon mutation of *parS* sites. According to a recent study, the preservation of one out of four chromosomal *parS* sites is sufficient for ParAB-mediated DNA segregation in the Gram-negative bacterium *Pseudomonas aeruginosa*, yet, an *oriC*-proximal *parS* localization appears to be essential for the partitioning process (Lagage et al., 2016). Notably, this is the only study to date, which investigated the function of an essential ParABS system in the context of genomic *parS* deletions and delocalizations.

Deletions of *par* genes are, apart from chromosome segregation defects, further associated with cell division phenotypes, supporting the notion that both cellular processes are tightly linked (Donovan et al., 2013; van Raaphorst et al., 2017). Various spatial regulators of bacterial cell division have been described, which use the chromosome as topological factor for division site selection, including the ParA family member MipZ in *C. crescentus* (Thanbichler and Shapiro, 2006). Another ParA-like ATPase, termed ParA-like division protein (PldP, Cg1610), has as well been implicated in division site selection in *Corynebacterium glutamicum* (Donovan et al., 2010). PldP localizes to the site of future cell division, while its deletion causes altered placement of division septa. However, the underlying mechanism has not yet been investigated.

1.5. Genome structuring via condensins

Chromosomes need to be compacted to fit the dimensions of a cell. Nucleoid-structuring is particularly controlled by family members of structural maintenance of chromosomes (SMC) complexes that are found in eukaryotes and prokaryotes. Certain structural features and their internal motor activity facilitating enclosure of DNA loops and DNA compaction are considered to be conserved characteristics amongst all SMCs (Hassler et al., 2018; Terakawa et al., 2017).

Eukaryotes harbor three different SMC complexes, which differ in subunit composition and function. Firstly, condensin complexes play a key role in reshaping chromosomes during mitosis and meiosis, where they condense and individualize chromatids prior to segregation during anaphase (reviewed in Kalitsis et al., 2017). Roles of related cohesins are reviewed by Nasmyth and Haering (2009). In essence, these complexes act on metaphase chromosomes by sister chromatid cohesion and further function in DNA repair and transcriptional regulation during interphase. The third eukaryotic SMC5/6 class is involved in DNA repair, meiotic recombination and relaxation of supercoiled DNA upon replication stress (reviewed in Aragón, 2018), while being the closest homologue to prokaryotic counterparts (Palecek and Gruber, 2015). In bacteria, condensin SMC/ScpAB and the functionally related SMC-like condensin complexes MukBEF and MukBEF-like SMC (MksBEF) are equally implicated in genome segregation and folding.

Notably, further SMC-like proteins exist, including bacterial RecN and SbcC as well as the eukaryotic Rad50, which are implicated in repair of DNA double strand breaks or cleavage of DNA hairpins (reviewed in Nolivos and Sherratt, 2014). However, despite conserved motives and basic structural similarities to SMCs these proteins associate with atypical accessory proteins or lack known complex partners, presumably deviating in DNA interaction properties (Cobbe and Heck, 2004; Nolivos and Sherratt, 2014). The following section focusses on bacterial condensin complexes and provides an overview about their functional and regulatory characteristics.

1.5.1. SMC/ScpAB

The SMC/ScpAB complex is very ubiquitous amongst bacteria with only few exceptions, and yet is almost exclusively studied in *Bacillus subtilis* (Cobbe and Heck, 2004). SMC was identified as an essential factor for DNA segregation by compacting DNA into separate chromosomes (Britton et al., 1998). The complex is composed of two core SMC subunits, each consisting of an ATP-binding cassette (ABC)-type ATPase head domain that is connected by an antiparallel coiled-coil structure to a hinge domain (Melby et al., 1998). SMC dimers interact asymmetrically with the

kleisin subunit ScpA, which together assemble into a ring-like structure (Bürmann et al., 2013; Kamada et al., 2013). Dimeric ScpB further associates with ScpA (Bürmann et al., 2013; Kamada et al., 2013), thus completing the SMC/ScpAB complex (**Figure 1.5A**).

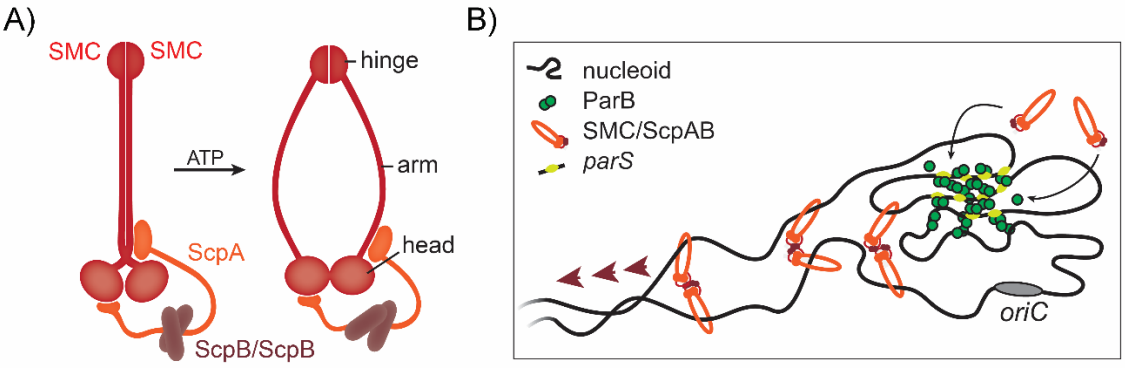

Figure 1.5: SMC/ScpAB complex composition and its genomic translocation starting at *parS*.

The *B. subtilis* condensin complex exhibits a 2:1:2 stoichiometry of SMC/ScpAB and undergoes ATP-dependent conformational changes of the SMC core subunits (**A**), which are essential for DNA entrapment at ParB/*parS* complexes and translocation along chromosomal arms (**B**).

Within the complex, hinge and arm domains of both SMC subunits can physically interact with each other, thereby juxtaposing the head regions (Lammens et al., 2004; Melby et al., 1998). Upon ATP binding at walker motifs head interfaces dimerize (Diebold-Durand et al., 2017), opening a cleft between both SMC arms (**Figure 1.5A**). In addition, a second compartment is formed between closed SMC heads and subunit ScpA. Current models suggest involvement of both compartments in capture and stabilization of DNA loops (Diebold-Durand et al., 2017; Vazquez Nunez et al., 2019). SMC arm-closure upon ATP hydrolysis leads to loop merging in the SMC head-kleisin compartment, while new loops are captured between reopened SMC arms. Recurrent ATPase cycles drive binding as well as translocation along DNA by extrusion of DNA loops (Minnen et al., 2016; Wilhelm et al., 2015) with velocities of 50 Kb/min in *B. subtilis* (Wang et al., 2017). Recent real-time imaging data of yeast condensin further demonstrate asymmetry in the conserved loop extrusion process, where complexes anchor onto DNA helices and pass them through the complex from only one side (Ganji et al., 2018).

Bacterial SMC/ScpAB are not loaded evenly along the chromosome, but rely on ParB protein bound to *parS* sequences as loading sites (Gruber and Errington, 2009; Minnen et al., 2011; Sullivan et al., 2009; Tran et al., 2017), pointing to a corporate function of both protein systems in

maintaining chromosome homeostasis (**Figure 1.5B**). However, evidence for direct ParB-condensin interactions is missing. Subsequent SMC/ScpAB redistribution to distant chromosomal regions results in co-alignment of right and left replichores (Le et al., 2013; Marbouty et al., 2015; Tran et al., 2017; Wang et al., 2017; Wang et al., 2015). Here, the *oriC*-proximal loading has been particularly implicated with robust SMC-translocation, circumventing convergent transcription and collisions with replication forks (Tran et al., 2017; Wang et al., 2017; Wang et al., 2015). Recent data on *B. subtilis* SMC/ScpAB suggest that this process is mediated by around 30 copies per *oriC*, where the low abundant complexes migrate in pairs, each acting on one arm (Wang et al., 2017; Wilhelm et al., 2015).

Chromosome structuring by SMC/ScpAB plays a fundamental role in segregation during fast growth in *B. subtilis*, where accelerated replication enhances DNA interconnections at the replication fork (Britton et al., 1998; Gruber et al., 2014). Here, SMC-mediated cohesion of chromosomal replichores along their length likely prevents the formation of intertwined sister chromosomes or promotes their resolution behind the fork (Gruber et al., 2014; Wang et al., 2014b). Remarkably, bacteria other than *B. subtilis* do not exhibit severe DNA segregation defects upon SMC deletion (Bouthier de la Tour et al., 2009; Güthlein et al., 2008; Le et al., 2013; Minnen et al., 2011; Petrushenko et al., 2011). Despite a conserved mode of action, details on the overall role of SMC/ScpABs in chromosome organization and segregation are lacking.

1.5.2. MukBEF

Many enterobacteria like *E. coli* harbor, instead of condensin SMC/ScpAB, the distantly related MukBEF complex. While SMCs are homologous to eukaryotic condensins, MukB shares only limited sequence similarity (Melby et al., 1998). Nonetheless, MukBEF is the structural and functional equivalent of SMC/ScpAB (Badrinarayanan et al., 2012; Palecek and Gruber, 2015). The core subunits MukB forms homodimers connected at their hinge regions, which are each linked by a coiled-coil structure with ABC-type ATP-binding sites in the head domain (Melby et al., 1998; Niki et al., 1992). Dimeric MukE contacts MukB and the kleisin subunit MukF (Woo et al., 2009). The ability to oligomerize via the N-terminal MukF domain is characteristic of these complexes (Fennell-Fezzie et al., 2005; Woo et al., 2009). Upon ATP-binding MukB head domains associate, forming ring-like structures or higher-order complexes (**Figure 1.6A**) that bind to DNA and alter DNA topology *in vitro* (Cui et al., 2008; Woo et al., 2009). Therefore, the basic mechanism underlying SMC/ScpAB- and MukBEF- translocation along chromosomes is assumed to be alike (Hassler et al., 2018).

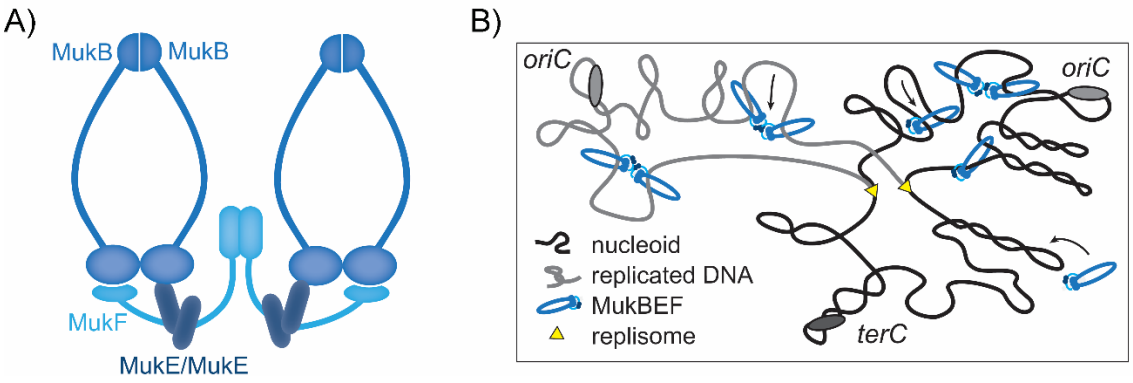

Figure 1.6: Condensin MukBEF extrudes DNA loops from random chromosomal regions.

E. coli MukBEF assemble into complexes that structurally resemble the SMC/ScpAB composition, yet Muk complexes interact via MukF subunits (**A**). MukBEF complexes establish chromosomal long-range interactions starting at arbitrary genomic positions that promote segregation of sister chromosomes (**B**).

Similar to SMC, deletion of *mukBEF* is synthetically lethal at fast growth conditions by impairing chromosome segregation in *E. coli* (Niki et al., 1991; Yamanaka et al., 1996). Further, *E. coli* condensin MukB stimulates Topoisomerase IV-activity in *E. coli* by a direct interaction (Hayama and Marians, 2010; Li et al., 2010) and topoisomerase I mutants alleviate *muk* phenotypes (Sawitzke and Austin, 2000). A recent study confirms a function in DNA-structuring, showing that the complexes establish long-range contacts in chromosomal arms (Lioy et al., 2018). Different to SMC/ScpAB, these condensins are likely loaded without topological recruiting factors at stochastic chromosomal loci (**Figure 1.6B**), yet being excluded from the *terC* domain by the DNA-binding protein MatP in *E. coli* (Lioy et al., 2018; Nolivos et al., 2016). Accordingly, MukBEF complexes do not align chromosomal arms (Wang et al., 2006) and typically localize in proximity to *oriC* domains within cells (Badrinarayanan et al., 2012).

1.5.3. MksBEFG

For a long time, prokaryotic genomes were considered to encode only one characteristic condensin complex. However, a third class of condensin complexes has been identified by sequence analysis that coexists with either SMC/ScpAB, MukBEF or both complexes (Petrushenko et al., 2011). These condensins were named MukBEF-like SMC, due to similarities in operon composition and predicted structure with the *E. coli* MukBEF (Petrushenko et al., 2011). In *P. aeruginosa* a *mksB* null mutant produces 1 % of anucleate cells, pointing to an

accessory role in DNA segregation (Petrushenko et al., 2011). A combination of *mksB* and *smc* deletions further yields in a minor viability decrease compared to single condensin mutations, suggesting a synthetic phenotype of SMC/ScpAB and MksBEF. The precise function of MksBEF in genome organization yet remains to be characterized. Different to *P. aeruginosa*, a large fraction of MksBEF complexes is encoded in an operon together with MksG, which is suggested to act as an additional subunit in the condensin complex (Petrushenko et al., 2011). A recent bioinformatics study predicted a role for MksBEFG complexes in plasmid-related defense, where heterologous condensin expression reduced the transformation efficiency of a high copy number plasmid (Doron et al., 2018). The authors further proposed that MksG subunits, harboring a putative topoisomerase domain, are essential for its specific function.

Chromosome structuring is, according to current view, a universal feature of condensins (Hassler et al., 2018). However, reasons for co-evolution of multiple condensins within prokaryotic cells, in particular the division of functions between such complexes and their putative interplay with other DNA-maintenance systems, have not yet been investigated.

1.6. Multilayer structuring of bacterial chromosomes

Bacterial chromosomes are dynamically folded into highly compacted nucleoids, which refold in the course of each cell cycle in order to allow for processes like gene expression, replication and segregation. Nucleoids are further shaped by DNA-supercoiling, condensin complexes and by an interactive system of nucleoid-associated proteins. A variety of chromosome folding strategies exist in model organisms that differ in composition of DNA-binding proteins and in spatial domain organizations. The following sections introduce bacterial chromosome conformation at different organizational scales and in the context of spatiotemporal domain localization in the course of the cell cycle.

1.6.1. High-resolution chromosome conformation

Bacterial nucleoids fold in a non-random, ordered way exhibiting conserved structural properties throughout cell populations. In particular recent chromosome conformation capture techniques (reviewed in Barutcu et al., 2016) have expanded the knowledge on bacterial genome-wide DNA-folding patterns and their underlying characteristics at low scales in Kb- up to Mb-ranges.

At smallest level, a negative net supercoiling condenses chromosomes, which is maintained by topoisomerase IV and gyrase (Sinden et al., 1980). Here, twisted DNA structures shape local self-interacting regions of around 10 Kb, termed topological domains (Postow et al., 2004). Entropic forces separate discontinuous DNA duplexes from each other by avoidance of frequent contacts with other genomic regions (Jun and Wright, 2010), thus forming higher-order chromosomal interaction domains (Le et al., 2013; Lioy et al., 2018; Marbouty et al., 2015; Val et al., 2016; Wang et al., 2015). Such DNA structures vary in size, where the average length amounts to 170 Kb in *B. subtilis* (Marbouty et al., 2015). In bacteria, chromosomal interaction domains are usually flanked by regions of high transcriptional activity (Le et al., 2013; Marbouty et al., 2015). Accordingly, chromosomal short-range contacts decline upon transcriptional inhibition, pointing to the importance of gene expression in genome conformation by altering DNA topology (Le et al., 2013; Marbouty et al., 2015). Further, genomic interactions at medium-range distances below one Mb frequently form between small domains, embedding them in a broader interaction context (Marbouty et al., 2015). Apart from transcription, nucleoid-associated proteins FIS and H-NS contribute to short- and medium-ranged contacts in *E. coli* (Lioy et al., 2018).

Higher-scale chromosome organization originate from long-range interactions establishing chromosomal macrodomains. These interactions are mainly maintained by nucleoid-associated proteins. In *E. coli* long-range contacts within chromosomal arms are promoted by HU and the condensin MukBEF, which is excluded from the *terC* region by MatP (Lioy et al., 2018; Nolivos et al., 2016). As a result, chromosomal arms are loosely structured with contacts in the Mb-range and contrast to the *terC* domain maintaining short-range contacts below 300 Kb (Lioy et al., 2018). Further long-range interactions have been described in *B. subtilis* and *C. crescentus* chromosomes, where condensin SMC/ScpAB mediates pairing of chromosomal arms by establishing inter-arm contacts (Le et al., 2013; Marbouty et al., 2015; Umbarger et al., 2011; Wang et al., 2015). Further, the *oriC* domain of *B. subtilis* is characterized by nested intra-domain interactions as well as long-range contacts along chromosomal arms, where distinct folding patterns depend on ParB, *parS* and SMC/ScpAB (Marbouty et al., 2015). Replication leads to a temporal decompaction of the *oriC* region. Finally, chromosomal arms appear to be twisted along the longitudinal cell axis in a variety of model organisms, forming helical patterns with high DNA-density regions distributed throughout the nucleoid (Berlatzky et al., 2008; Fisher et al., 2013; Hadizadeh Yazdi et al., 2012; Umbarger et al., 2011). Accordingly, chromosomal architectures display common basic structures amongst the few model bacteria studied to date, however, unique folding patterns indicate a high inter-species diversity that still remains to be discovered.

1.6.2. Spatiotemporal chromosome organization

Chromosomal macrodomains are further organized in the context of subcellular localization, where spatiotemporal positioning is defined by replication and segregation processes. Various characteristics of nucleoid orientation and positioning of the replication machinery have been described in model bacteria, which can roughly be divided into three main organizational strategies.

Firstly, slow-growing *E. coli* cells harbor a single chromosome at a transversal disposition prior to replication (**Figure 1.7**). Here, *oriC* and *terC* domains localize at midcell, while left and right replichores localize in distinct cell halves (Wang et al., 2006). In the course of replication, sister *oriC*s split and relocate to cell quarter positions, while replisomes remain positioned at midcell (Adachi et al., 2005; Bates and Kleckner, 2005). After completion of segregation macrodomains of both chromosomes orientate mostly asymmetrically towards each other, occupying a "right-*oriC*-left" orientation in separate cell halves.

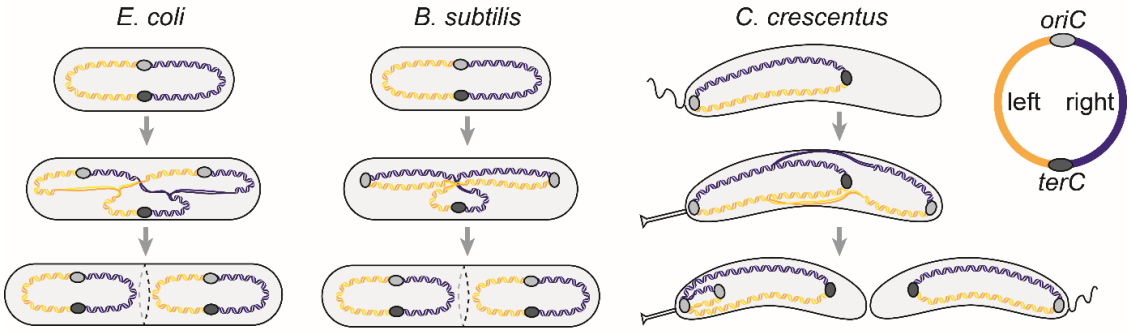

Figure 1.7: Spatial chromosome organization of model species.

Localization of chromosomal macrodomains in the course of the cell cycle in slow-growing *E. coli*, *B. subtilis* and *C. crescentus* cells. Compacted right (blue) and left (orange) replichores are pictured as curled lines with domains as indicated in the chromosome scheme on the right. Dashed lines mark septum positioning prior to cell division.

Similar to the *E coli* counterparts, chromosomal domains of *B. subtilis* cells arrange with *oriC* and *terC* localized at midcell, while replisomes form centrally and remain associated until replication termination (Lemon and Grossman, 2000). However, during replication sister chromosomes switch the right-*oriC*-left domain organization towards a longitudinal configuration (**Figure 1.7**), thereby positioning *oriC*s at maximal distance from each other at cell quarter positions (Wang et

al., 2014a). Further, each replichore pair is aligned along the long axis of the cell, mirroring one another at the transverse cell axis. Also *P. aeruginosa* alters chromosome arrangement in the process of replication alike, however, this organisms moves DNA loci successively towards central replisomes (Vallet-Gely and Boccard, 2013).

Finally, different from *B. subtilis* and *P. aeruginosa*, most other model species like *C. crescentus*, *Myxococcus xanthus* and *Vibrio cholerae* permanently maintain longitudinally-arranged chromosomes (David et al., 2014; Harms et al., 2013; Viollier et al., 2004). In the course of replication, one of the sister chromosomes translocates towards the opposite cell pole via a ParABS segregation system (**Figure 1.7**). In addition, *oriC* domains of these bacteria are stably tethered to aforementioned polar landmark proteins via ParA/ParB interactions, where replication machineries establish and move towards central positions as replication proceeds (Harms et al., 2013; Jensen et al., 2001; Stokke et al., 2011). Here, replisomes move simultaneously along the cell axis and have been shown to split and merge frequently. Also the actinobacterium *Mycobacterium smegmatis* likely organizes chromosomes longitudinally (Santi and McKinney, 2015), where *oriC*s are tethered to polar regions by a ParA interaction with a specific scaffold protein, similar to *Streptomyces coelicolor* (Ditkowski et al., 2013; Ginda et al., 2013). Here, *oriC*s do not localize as proximal to cell poles as in *C. crescentus* and *V. cholerae*, thus *oriC*s migrate a comparably short distance from their sister domains towards the opposite cell half in the course of chromosome replication (Ginda et al., 2013; Trojanowski et al., 2015). Accordingly, replisomes form at *oriC* domains and migrate towards midcell positions in close proximity to each other (Santi and McKinney, 2015; Trojanowski et al., 2015).

Despite the fact that pole-tethered *oriC* domains, which mediate longitudinal chromosome arrangements, are widespread amongst model organisms, this mode of genome arrangement has exclusively been studied in monoploid cells harboring only one replicating chromosome copy per life cycle. Spatiotemporal localization of more complex genome compositions is yet to be fully understood.

1.7. Aim of the study

Bacterial nucleoid folding and segregation processes are largely mediated by SMC/ScpAB and ParABS systems, two key players of chromosome organization. However, currently details on chromosome organization and their underlying mechanisms in other than the standard model species are poorly characterized. This study aims to give a comprehensive picture on chromosome organization in the apically growing actinobacterium *Corynebacterium glutamicum*. Its great industrial importance as amino acid and vitamin producer that comes with well-established genetic tools as well as its close relation to pathogens, like *M. tuberculosis* or *Corynebacterium diphteriae*, makes this organism an ideal cell biological model for the class of actinobacteria.

Based on initial studies on the ParABS system of *C. glutamicum* (Donovan et al., 2013; Donovan et al., 2010; Donovan et al., 2012) we aimed to elucidate spatiotemporal *oriC* domain localization by ParB-tracking *in vivo*. Following up this idea, localizing *terC* and the replisome itself should finally elucidate the overall chromosome and replisome positioning within cells. In order to put chromosome organization of *C. glutamicum* in the context of cell growth and replication, cell cycle parameters were needed to be specified for different growth rates.

A second project encompasses the question of how ParB-*parS* complexes and condensins contribute to chromosome folding in *C. glutamicum*. To this end, deleting and repositioning of *parS* sites to aberrant genomic regions had been chosen to analyze the impact of ParB-mediated *oriC* structuring and condensin loading on overall genome folding. Besides, unlike most other model species, *C. glutamicum* harbors two condensin complexes, SMC/ScpAB and MksBEFG, yet it is completely unknown whether both complexes are redundant in function and how they influence folding of genomic DNA. In order to address these open questions, we focused on confirming complex compositions as well as on analyzing corresponding chromosome-binding sites and phenotypes in depth.

Finally, we include ParA-ATPases ParA and the *C. glutamicum*-specific orphan ParA termed PldP in spatiotemporal localization studies, taking initial data on still images and phenotypic descriptions by Donovan et al. (2010) to the next level. ParAB were shown to be crucially important drivers of reliable nucleoid separation in *C. glutamicum*, while PldP had been suggested to function in division site selection (Donovan et al., 2010). Here, we further elucidate localization dependencies of ParAB and PldP on each other and on *parS* sites in order to differentiate the functions of *C. glutamicum* ParA-ATPases and screen for putative interaction partners of PldP.

Data presented here were obtained in collaborate effort by combining elaborate strategies of strain construction with the application of high-throughput techniques, like chromatin immunoprecipitations and chromosome conformation capture assays coupled with deep-sequencing, providing a global picture on protein functions in chromosome organization.

2. Results

2.1. Spatiotemporal chromosome organization in *C. glutamicum*

Here, we unveil global chromosome organization in *C. glutamicum*, which had been shown to be in large part mediated by a ParABS partitioning system (Donovan et al., 2010; Donovan et al., 2012). Apart from that, cellular *oriC*-localization had in previous work been successfully determined by a fluorescent repressor operator system (FROS) and further, fluorescently labeled versions of ParB have been shown to colocalize with *oriC* domains at cell poles, being consistent with the prediction of several *parS* sites close to *oriC* (Donovan et al., 2010). However, in-depth studies of spatiotemporal chromosome organization were still missing.

This chapter focusses on the organization of chromosomal macrodomains in *C. glutamicum* on a single cell-level. Therefore, we constructed strains harboring fluorescent ParB variants, a fluorescent replisome-component and FROS systems to spatiotemporally track *oriC* and *terC* domains and replication forks throughout a life cycle of *C. glutamicum* cells.

2.1.1. Localization pattern of ParB-origin complexes

Initially, we reanalyzed ParB-*oriC* complexes by time-resolved live cell imaging. To this end, allelic replacements of genomic *parB* by *parB-eYFP* were constructed, yielding in strains that harbor fluorescent ParB versions under the control of the native promoter. Notably, all strains constructed in this work likewise derive from clean allelic replacements of genomic loci.

First of all, we compared ParB-eYFP fluorescence in *C. glutamicum* RES167 wild type and Δ*parA* mutant backgrounds. ParB protein fusions appear to be stable without cleavage products being detected in Western Blots (**Figure 2.1A**), suggesting a reliable representation of cellular ParB localization by fluorescence signals. Further, fluorescent ParB fusions do not impact on cell growth or division (**Figure 2.1B**, **C**).

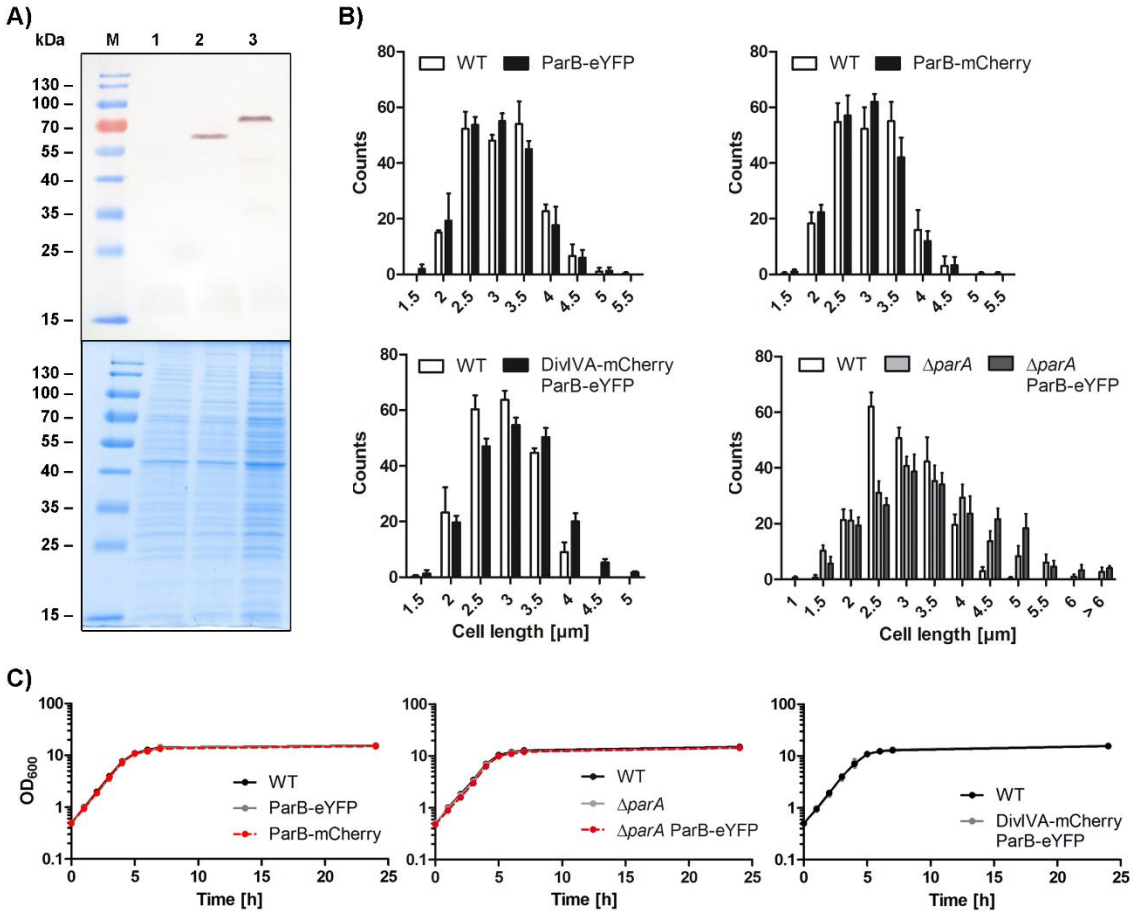

Figure 2.1: Phenotypes of strains used to determine cellular *oriC* localization.

(**A**) Validation of full-length fusion proteins ParB-mCherry (3) and DnaN-mCherry (2) via western blotting (top); Coomassie-stained gel (below). Whole cell lysates of wild type (1), CBK006 and CBK062 strains were probed; protein detection was performed using polyclonal α-mCherry antibody. (**B**) Cell length distributions and (**C**) growth curves of *C. glutamicum* wild type (WT, μ = 0.68 h^{-1}) and mutant strains CBK007 (ParB-eYFP, μ = 0.69 h^{-1}), CBK006 (ParB-mCherry, μ = 0.68 h^{-1}), CBK061 (DivIVA-mCherry ParB-eYFP, μ = 0.68 h^{-1}), CDC001 (Δ*parA*, μ = 0.61 h^{-1}), CBK072 (Δ*parA* ParB-eYFP, μ = 0.64 h^{-1}). Cells were grown in brain heart infusion (BHI) medium; values derive from triplicates with standard deviations indicated in all graphs (n = 200).

ParB-*oriC* complexes form large fluorescent foci within wild type and mutant cells (**Figure 2.2A**) Mainly two to five foci were detected per wild type cell, with cell poles being occupied by ParB-*oriC* complexes in any case. By contrast, Δ*parA* deletion causes varying complex numbers with up to 12 foci per cell (**Figure 2.2B**). However notably, cell lengths are equally variable, including approximately 20 % of anucleate minicells that are not taken into account for subsequent *oriC*-complex analyses (**Table S1**). Therefore, despite variations in foci counts per cell, ParB-*oriC* numbers correlate with cell length in both, wild type and Δ*parA* strains (**Figure 2.2B**).

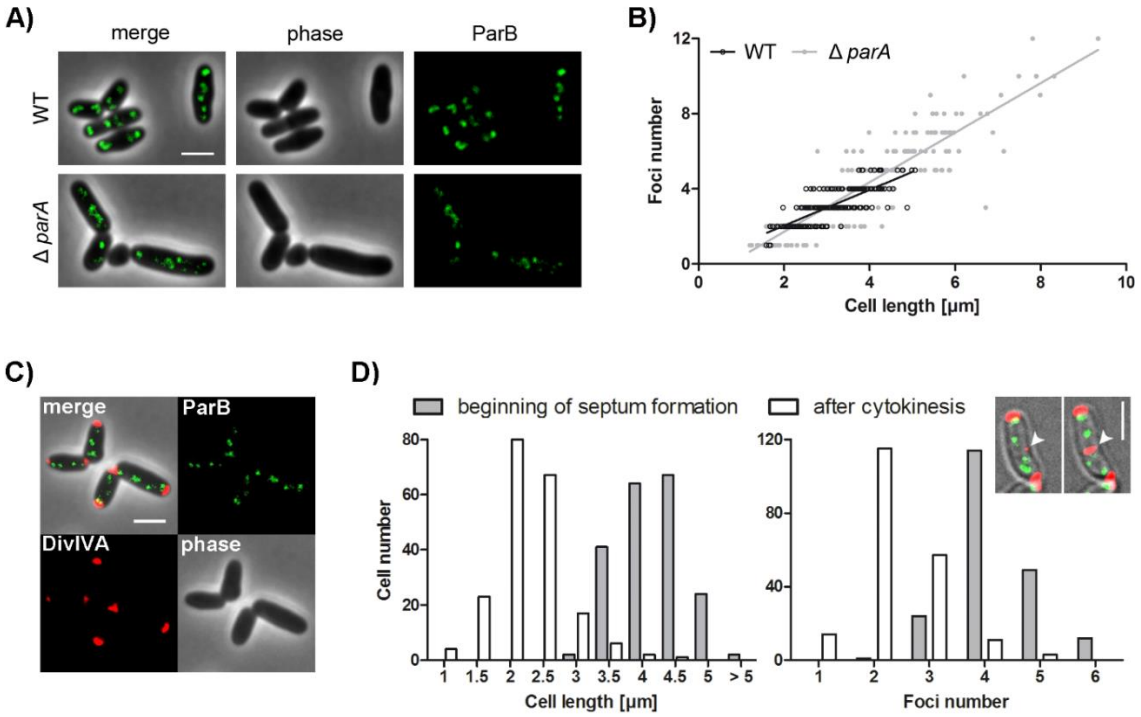

Figure 2.2: Correlation of ParB-*oriC* numbers to cell length in *C. glutamicum*.

(**A**) Localization of ParB-nucleoprotein complexes within representative wild type and Δ*parA* cells (CBK007, CBK072). Microscopy images illustrate ParB-eYFP fluorescence in green (ParB), including phase contrast and the overlay of both channels (merge). Scale bar, 2 µm. (**B**) ParB foci-numbers correlate to cell length independently of ParA. Foci counts per cell are depicted for above-named strains (n = 400), along with linear regression lines r (wild type) = 0.80, r (Δ*parA*) = 0.88. Slopes deviate from each other (ANCOVA, F (1, 396) = 16.10, p < .0001). (**C**) Visualization of DivIVA-mCherry (red) and ParB-eYFP (green) in exemplary CBK061 cells; depicted are separate channels, phase contrast and the merge microscopy image. Scale bar, 2 µm. (**D**) Time-lapse microscopy of CBK061 reveals maximal ParB-*oriC* cluster numbers prior to cell division. Exemplary microscopy images (white arrowheads) indicate time lapse of septum closure, tracked by DivIVA-mCherry reporter (red); scale bar, 2 µm. Cell lengths and foci numbers are shown for cells just before and after cytokinesis (n = 200).

Furthermore, ParB-*oriC* complexes commonly appear to have reduced fluorescence intensities in the *parA* mutant compared to wild type cells, with cell poles frequently being unoccupied by ParB-*oriC* complexes. Even though chromosome segregation defects upon *parA* deletion do not impair the strong correlation between *oriC* numbers and cell length, linear regression models differ significantly (**Figure 2.2B**), indicating an increase in average foci numbers in mutant compared to wild type cells. Since Δ*parA* cells do not over-initiate replication (AG Bramkamp, unpublished data), ParA likely supports ParB-*oriC* tethering or clustering between complexes at cell poles. Due to particularly high amounts of ParB clusters per cell, we further aimed to determine maximal ParB-*oriC* complex numbers by using DivIVA as a marker for cell division in wild type cells. More

precisely, DivIVA associates with cell poles and maturing septal membranes in *C. glutamicum* (Donovan et al., 2012). Here, a dual reporter strain harboring fluorescent ParB-eYFP in combination with DivIVA-mCherry was obtained by an additional allelic replacement of chromosomally encoded *divIVA* by *divIVA-mCherry*, in order to verify completion of cell division by septum closure prior to physical separation of daughter cells (**Figure 2.2C**). Growth and morphology of this strain are wild type-like, indicating functionality of combined fusion proteins (**Figure 2.1B**, **C**). Analyses of live cell imaging data revealed an average of four ParB-*oriC* complexes at pre-division stages that are distributed along a cell length of four micrometers, yet up to six foci were counted in a fraction of cells (**Figure 2.2D**). Correspondingly, newborn cells harbored mostly two to three ParB-*oriC* complexes at an average cell length of two micrometers (**Figure 2.2D**). These results are in line with preceding ParB foci-counts using the physical separation of daughter cells as measure for completed cell division. Therefore, our data indicate unexpectedly high *oriC* numbers, which result from either continuous chromosome replication that leads to overlapping replication periods or from polyploidy, where multiple copies of fully replicated chromosomes are maintained throughout generations.

In a further step, positioning of *oriC* domains was analyzed by live cell imaging in the course of one cell cycle. To this end, cellular ParB-eYFP foci were tracked by time lapse microscopy in five minute intervals, as shown in **Figure 2.3A**. We further distinguish between old and new cell poles, the latter one originating from a recent division event at the septum of the mother cell. Here, newborn cells harboring exclusively two initial ParB-*oriC* clusters were chosen for analysis, where distinct origin localization patterns could be determined throughout the cell cycle. In these cells both clusters stably localize to cell poles, while a third and a fourth ParB-*oriC* complex develops in the course of cell elongation at opposite cell poles (**Figure 2.3B**).

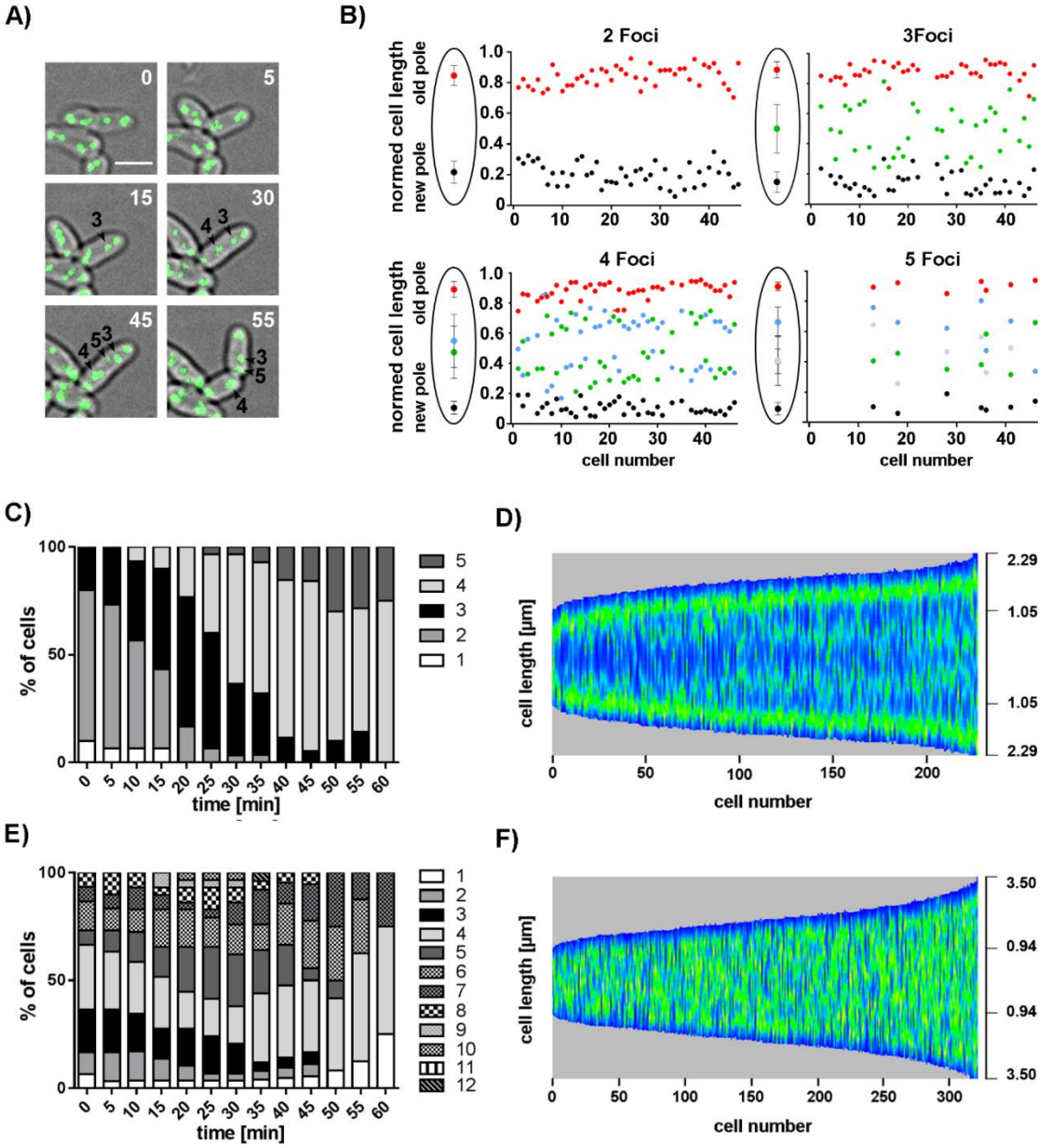

Figure 2.3: Spatiotemporal localization of ParB-*oriC* complexes throughout the cell cycle.

(**A**) Exemplary time series of ParB cluster generation over one life cycle in CBK007 (*par::parB-eYFP*). Images are taken at the time points of ParB cluster-separation (green), ParB-eYFP foci are numbered according to their order of occurrence (black label). Minutes after beginning of the cell cycle are indicated by white numbers. Scale bar, 2 µm. (**B**) Longitudinal positioning of ParB clusters within aforementioned cells at the time point of new clusters being separated (foci 3-5, n = 46). Cluster positions are illustrated by colored circles with cell lengths normalized to one; cells were oriented with the old cell poles facing downwards. Cartoons shown on the left depict average cluster positions along cell axes; error bars indicate standard deviations. (**C**) Timeline showing the cell cycle-dependent increase of ParB-*oriC* complex numbers counted in 5 min intervals in the course of one generation time (n = 30, strain CBK007); fractions of cells harboring one to five clusters are indicated. (**D**) Demograph visualized via Morpholyzer (Schubert et al., 2017) illustrates ParB-eYFP fluorescence profiles (green) extracted from still microscopy images and

sorted according to length (in µm, y-axis) of CBK007 cells (n > 200). (**E**) Analysis of ParB-*oriC* clusters in Δ*parA* cells (CBK072) as in (**C**). (**F**) Cellular fluorescence profiles of ParB-eYFP foci depicted as in (**D**) upon *parA* deletion (CBK072, n > 300).

These complexes progressively relocate towards midcell positions, yet remain located within their initial cell half. Eventually, a fifth focus may form at late cell cycle stages. Notably, all newly formed ParB foci emerge randomly at new or old cell poles, indicated by a localization average of foci tracks around midcell positions. Therefore, the timing of *oriC* firing and segregation is unbiased between both cell poles. In addition, temporal appearances of ParB-*oriC* clusters are summarized in **Figure 2.3C**. An increase of clusters could be observed in the course of growth progression, therefore, *oriC* numbers per cell are further associated with the cell cycle. Already at early generation stages one third of cells analyzed harbor more than two clusters, while four up to five clusters were observed in the majority of cells after half of the average generation time (~ 30 minutes).

In order to confirm spatiotemporal ParB-*oriC* localizations, automated analysis of still microscopy images was applied. To this end, a Fiji software plug-in termed Morpholyzer was utilized that allows automated detection of cells and displays their fluorescence profiles sorted by cell length (Schubert et al., 2017). Resulting demographs are illustrated in **Figure 2.3D**, showing stable ParB-*oriC* complex anchoring to both cell poles throughout progression of cell growth. Newly replicated *oriC*s start separating from polar sisters at one third of the cell cycle. Complexes further relocate towards cell quarter positions and finally localize in long cells to future division sites at midcell. These data confirm the preceding manual evaluation of time-lapse data and are in line with *oriC*-dynamics identified before in *M. xanthus*, *C. crescentus*, *M. smegmatis* and *V. cholerae* (Fogel and Waldor, 2006; Harms et al., 2013; Santi and McKinney, 2015; Thanbichler and Shapiro, 2006; Trojanowski et al., 2015). In comparison to wild type, impeding chromosome segregation by *parA* deletion results in an increased formation of ParB-*oriC* complexes throughout the cell cycle, while a majority of cells start with more than two initial *oriC* complexes (**Figure 2.3E**). Besides, ParB foci localize without a clear site of preference within cells, with fluorescence signals being detected at random positions along the longitudinal cell axis (**Figure 2.3F**). Our data illustrate the effect of a *parA* deletion on *oriC* positioning, underlining the essentiality of ParA in control of *oriC* domain segregation and polar ParB-*oriC* tethering.

Timing of replication initiation at old and young cell poles was further investigated via automated analysis of microscopy images. For this, we made use of the DivIVA-mCherry reporter strain to

distinguish between both cell poles in still images. In *C. glutamicum* an increased amount of peptidoglycan is incorporated at the old cell pole compared to the young pole (Sieger et al., 2013), a phenomenon that is directly linked to the polar asymmetry of DivIVA assembly (Schubert et al., 2017). Cells were aligned in demographs with cell poles of higher DivIVA-mCherry fluorescence intensities facing downwards (**Figure 2.4A**). Fluorescence profiles indicate that ParB-*oriC* complexes segregate evenly from sister complexes at both cell poles, without any bias for old or young cell pole. Therefore, even though ParB-*oriC* complexes have been shown to interact with polar DivIVA (Donovan et al., 2012), timing of replication and segregation of sister *oriC*s are not coupled to disparities in polar DivIVA-accumulation.

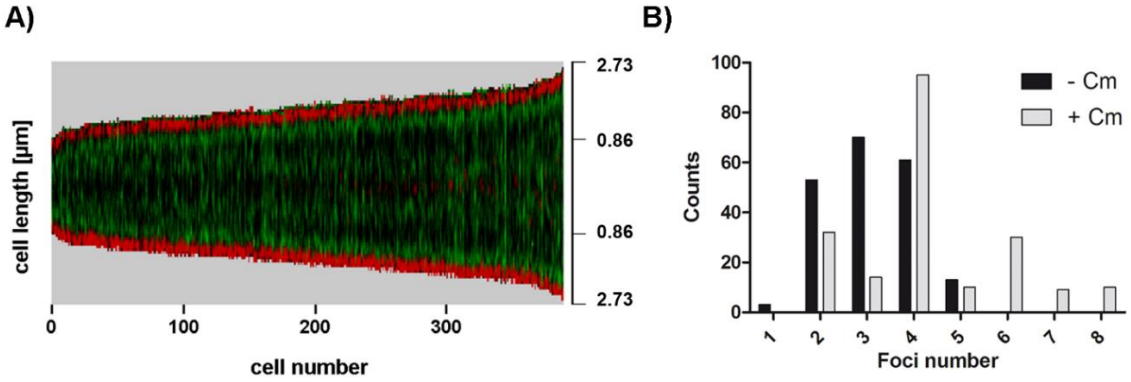

Figure 2.4: Sister *oriC* complexes synchronize replication and segregation events.

(**A**) Uniform segregation of ParB-*oriC* complexes at old (facing downwards) and young cell poles (facing upwards). Automated image analysis of strain CBK061 pictures DivIVA-mCherry (red) and ParB-eYFP fluorescence profiles (green) in a demograph sorted according to cell length in µm. (**B**) Comparison of ParB-*oriC* complex counts in chloramphenicol-treated cells (+ Cm) analyzed by z-stacking of microscopic images and in non-treated cells using standard analysis (- Cm, n = 200).

Finally, due to uneven numbers of ParB-*oriC* complexes in a large fraction of cells, analysis was performed to verify whether timing of replication initiation is asymmetric amongst *oriC*s within one cell. Detachment from cell poles and enhanced separation of ParB-*oriC* complexes was achieved by chloramphenicol treatment. Z-stacking of microscopic images further served to determine ParB-*oriC* clusters per cell more accurately (**Figure 2.4B**). Here, ParB-*oriC* analysis revealed primarily even complex numbers compared to foci counts with previous experiment settings. Notably, up to eight ParB clusters were determined per cell. Therefore, replication initiation is synchronized amongst *oriC*s, while uneven cluster numbers determined

microscopically result from variable colocalization periods of sister *oriC*s. Additionally, actual *oriC* numbers may have been underestimated by microscopic analyses.

Conclusively, ParB-*oriC* complex numbers appear to be exceptionally high and correlate with cell length in a ParA-independent way, while *oriC* domains segregate uniformly from old and young cell pole in distinct spatiotemporal localization patterns along the longitudinal cell axis.

2.1.2. Longitudinal chromosome arrangement

In addition to cellular localization of *oriC* domains, information about the positioning of replication termini was needed to explicitly elucidate chromosome orientation in *C. glutamicum*. Since ParB-*oriC* clusters attach to cell poles, *terC* domains likely face towards midcell positions. In order to confirm a longitudinal chromosome arrangement, *terC*-positioning was analyzed microscopically. A Lac Operator (*lacO*)/Lac Repressor (LacI) FROS system was used to fluorescently label *terC* domains in cells that additionally form *oriC*-proximal ParB-eYFP clusters, where extrachromosomal *lacI-CFP* expression was induced by tetracycline. FROS-labeled *terC* domains form large fluorescent foci within *C. glutamicum* cells, that indeed mainly localize to midcell positions (**Figure 2.5A**). On average two *terC*-foci could be determined per cell (**Figure 2.5B**). At fast growth in standard growth medium between one and five *terC*-foci were counted per cell, where numbers increase with cell length, similar to ParB-*oriC* complexes (**Figure 2.5B, C**). In line with these results, *terC* counts correlate with ParB-*oriC* complex numbers per cell (**Figure 2.5C**). To further investigate the cell cycle-dependent localization of termini relative to *oriC* domains, ParB-*oriC* and *terC* fluorescence patterns were analyzed in still microscopy images by application of the Morpholyzer tool. The resulting demograph pictures continuous *terC*-localization at midcell throughout cell elongation (**Figure 2.5D**). Notably, ParB-*oriC* complexes move upon duplication at cell poles towards *terC* domains, which still do not relocate to cell quarter positions before cytokinesis. These data prove a longitudinal *ori-ter-ter-ori* chromosome organization in *C. glutamicum*.

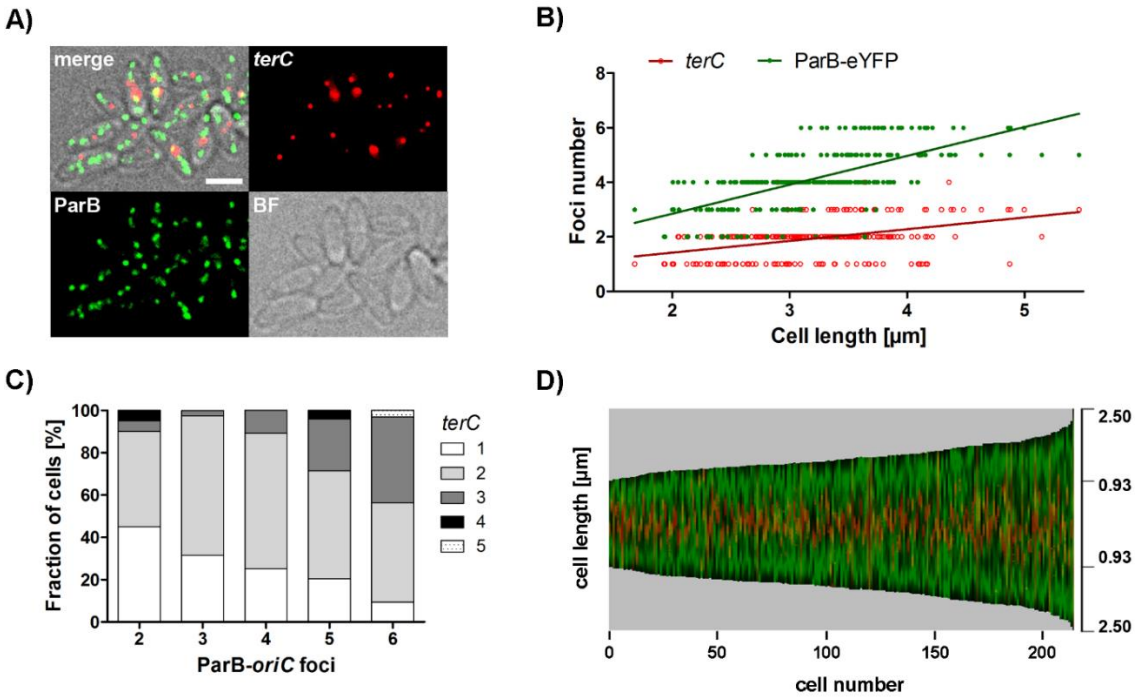

Figure 2.5: Multiple replication termini steadily position at midcell opposite to *oriC* domains.

(**A**) Cellular localization of ParB-*oriC* complexes and FROS-labeled *terC* domains in strain CBK065. Microscopy images show ParB-eYFP (green) and LacI-CFP fluorescence (*terC*, red) together with bright field (BF) and merged channels. Scale bar, 2 µm. (**B**) Correlation of *oriC* and *terC* numbers per cell with cell length (n = 250, CBK065). Linear regression lines are indicated, with r (*oriC*) = 0.64 and r (*terC*) = 0.40. (**C**) Dependence of *terC* counts on ParB-*oriC* complex numbers per cell. Fractions of cells with one to five *ter*Cs were determined and sorted according to *oriC* numbers (n = 250). (**D**) Automated image analysis of CBK065 cells sorted according to cell length with ParB and LacI-CFP (*terC*) fluorescence profiles shown in green and red; y-axis displays cell length in µm (n > 200).

Most strikingly, even at any slower growth mode in various minimal media (**Figure 2.6A**), cells reached between one up to four *ter*Cs (**Figure 2.6B**, **C**), where frequency distributions are comparable amongst all conditions tested. Hence, *terC* numbers are likely underestimated by microscopic approaches due to domain-colocalization of opposing chromosomes. Multiple *terC* counts indicate that more than two chromosomes are commonly present per cell in the course of a life cycle and supports exceptionally high numbers of ParB-*oriC* complexes determined before.

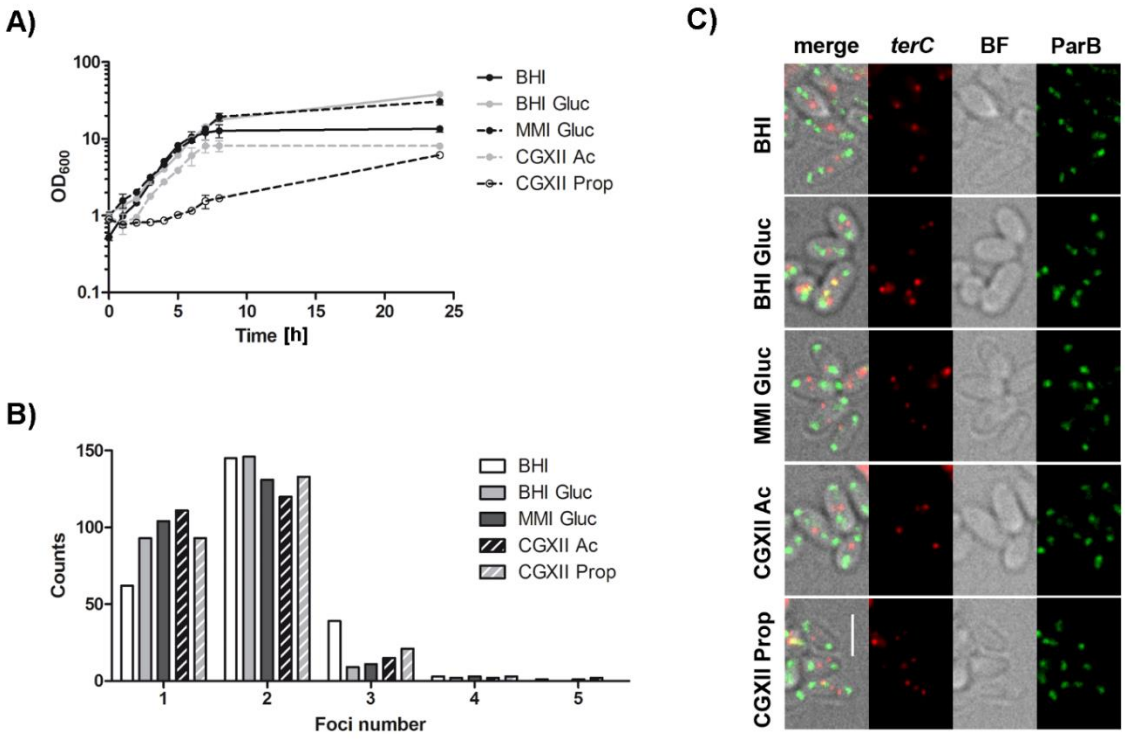

Figure 2.6: Replication termini per cell are constant amongst various growth conditions.

(**A**) Growth curves of strain CBK065 harboring FROS-labeled *terC* domains (*lacO*/LacI-CFP) in combination with ParB-eYFP at the native genomic locus. Cells were grown in BHI complex medium (μ = 0.62), BHI (μ = 0.43 h^{-1}) or minimal salt medium (MMI) medium supplemented with glucose (μ = 0.37 h^{-1}), minimal salt medium CGXII medium supplemented with acetate (μ = 0.39 h^{-1}) or propionate (μ = 0.15 h^{-1}). Values derive from duplicates. (**B**) Cell fractions with one to five *terC* foci shown for above-named strain and media; average *terC* numbers: $\bar{x}$ (BHI) = 1.94, $\bar{x}$ (BHI Gluc) = 1.68, $\bar{x}$ (MMI Gluc) = 1.66, $\bar{x}$ (CGXII Ac) = 1.66, $\bar{x}$ (CGXII Prop) = 1.74 (n = 250). (**C**) Representative CBK065 cells grown in media as indicated. Microscopy images display bright field, CFP and eYFP channels (BF, *terC*, ParB) together with the corresponding merged image (merge). Scale bar, 2 µm.

Moreover, FROS-labeling of the 90° position on the right chromosomal arm in *C. glutamicum* was performed in an analogous manner to the visualization of *terC* domains described before. Assuming that replichores evenly distribute in length along the longitudinal axis from one cell pole to midcell, 90° positions are expected to localize at cell quarters. Interestingly, these genomic regions between *oriC*s and *terC*s rather position at midcell and are grouped in up to four fluorescent foci (**Figure 2.7A, B**).

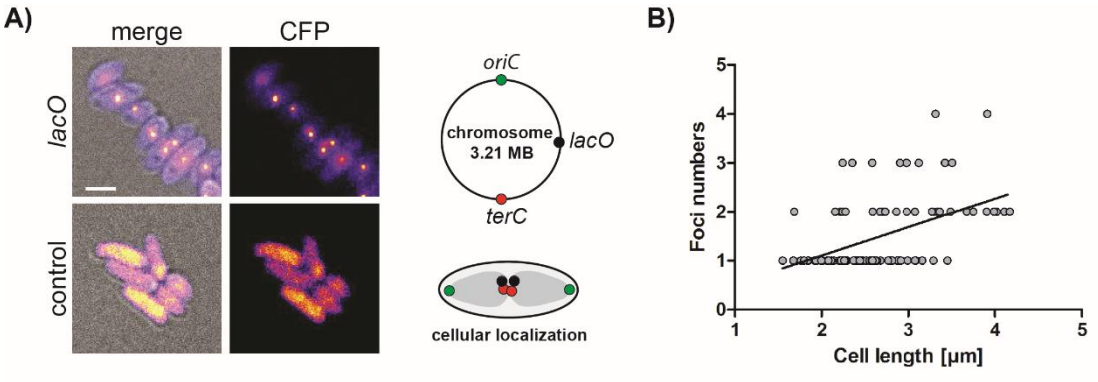

Figure 2.7: FROS-labeling of the right chromosomal arm.

(A) Left: Microscopy images show LacI-CFP fluorescence and overlays of CFP and bright field channels (merge) of cells in presence or absence of *lacO* arrays at 90° chromosomal positions (*lacO*, CBK067; control, CBK068); scale bar, 2 µm. Cartoon showing region of chromosomal *lacO* insertion and common cellular fluorescence localization of *lacO*/LacI-CFP foci; nucleoids are indicated by grey ovals. (B) *lacO*-LacI-CFP foci numbers depend on cell length (n = 100); linear regression is indicated by black line (r = 0.48).

Expression of *lacI-CFP* in absence of *lacO* arrays yields in dispersed CFP-fluorescence signals within cells, validating an accurate representation of domain localization by FROS in *C. glutamicum* (**Figure 2.7A**). This result indicates that chromosomal arms may spread non-uniformly between *ori* and *terC* domains, yet in-depth analyses including domain labeling of the left arm will be needed to further elucidate cellular replichore positioning in detail.

2.1.3. Multiple replication forks combine with flexible origin cohesion times

High abundance of chromosomal domains per cell shown before hints to maintenance of large genomic contents in *C. glutamicum* cells, nevertheless spatial organization and segregation of *oriC* and *terC* regions are timely organized throughout their generation cycles. On the basis of these data, we further investigated dynamics of DNA replication by tracking replisomes *in vivo*. A fully functional fluorescent fusion of the replisome sliding clamp DnaN with mCherry was constructed, not impacting on cell growth, morphology and DNA segregation (**Figure 2.8A**, **B, Table S1**). Stability of full-length DnaN-mCherry protein in cell lysates was further verified by western blotting (**Figure 2.1A**).

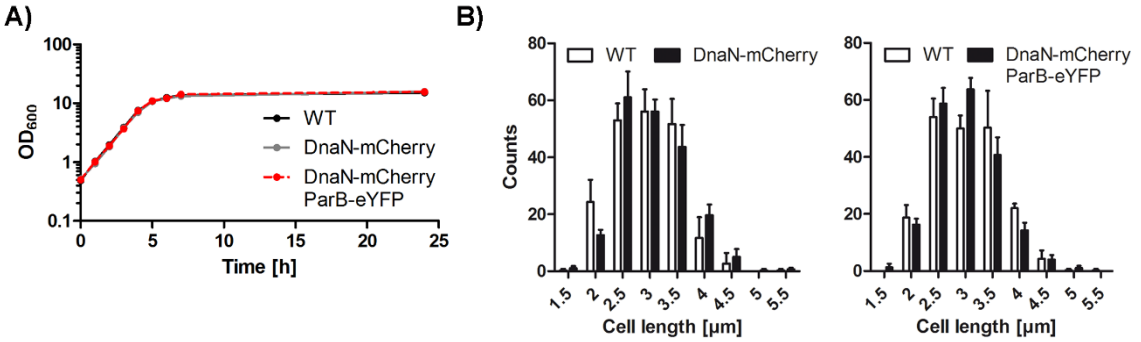

Figure 2.8: Characterization of *C. glutamicum dnaN::dnaN-mCherry* mutant phenotypes.

(**A**) Growth curves of *C. glutamicum* wild type ($\mu = 0.68\ h^{-1}$) and mutant strains CBK062 (DnaN-mCherry, $\mu = 0.67\ h^{-1}$), CBK063 (DnaN-mCherry ParB-eYFP, $\mu = 0.69\ h^{-1}$). Cells were grown in BHI medium; error bars indicate standard deviations of biological triplicates. (**B**) Cell length distributions of aforementioned strains grown and analyzed as in (**A**), n = 200.

DnaN-mCherry fluorescence accumulates in several bright foci within the cellular nucleoids (**Figure 2.9A**). In order to identify distinct localization patterns of replication events, analysis of still microscopy images was performed using this reporter strain. The resulting demograph (**Figure 2.9B**) reveals high mCherry fluorescence intensities in a wide central region in newborn cells. After approximately one third of the cell cycle replication hubs form in broad ranges at cell quarter positions, where they remain localized until cell division (**Figure 2.9B**). Here, replication transition to cell quarter positions is a fluent process. In the course of polar cell elongation, replisome accumulation tends to relocate further away from the cell poles.

Therefore, we questioned whether replisomes actively translocate at replication forks towards midcell or whether passive relocation occurs due to cell elongation from cell poles. Time-lapse microscopy was performed, where newly formed DnaN-mCherry foci were tracked in conjunction with cell length increase until cytokinesis via live cell imaging. Subtracting half the increment of cell length from the distance covered by the replisome yielded in an average track-difference of zero (**Figure 2.9C**). These data suggest a passive relocation of replication forks towards midcell with replisomes of rather static nature. Subsequently, replisome counts per cell were monitored over entire cell cycles (**Figure 2.9D**). Directly after cell division, one up to three DnaN-mCherry foci were counted per cell, while numbers increase during cell cycle progression with mainly more than two foci being present per cell. At maximum, up to six clusters could be distinguished, indicating that at least three replication events take place simultaneously. Due to the high number and frequent splitting and merging events of replication forks (shown hereafter), overlaying replisome signals cannot be excluded.

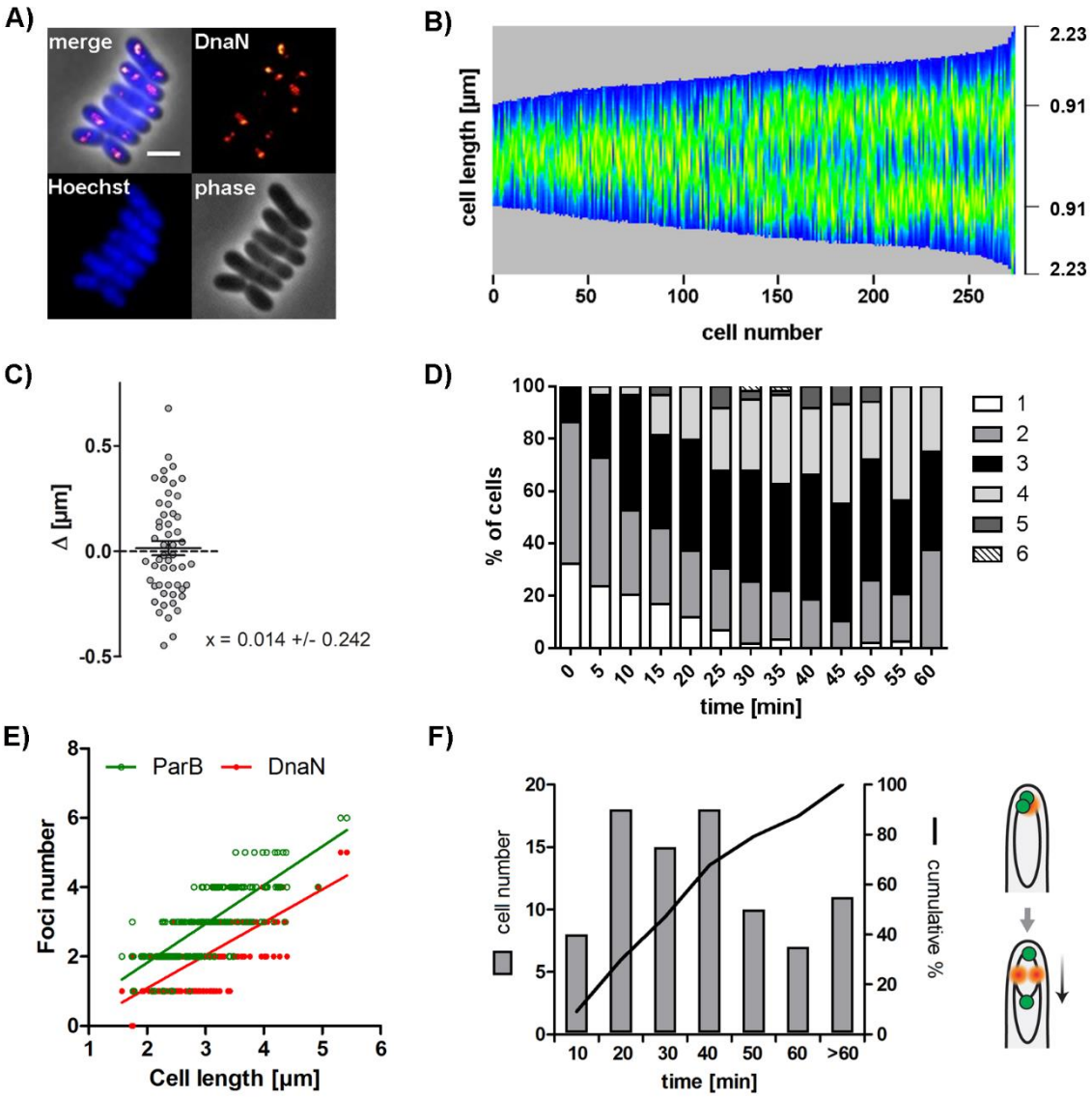

Figure 2.9: Multiple replisomes localize in replication hubs at cell quarter positions.

(**A**) Cellular localization of fluorescently labeled replisome component DnaN-mCherry (CBK062). Shown are phase contrast (phase), mCherry fluorescence (DnaN) and DNA stain (Hoechst) in separate channels and as overlay image (merge). Scale bar, 2 µm. (**B**) Heat map of cell cycle-dependent DnaN-mCherry fluorescence profiles along the longitudinal axis of CBK062 cells. Cells are sorted by length with high fluorescence intensities indicated in green (n > 250). (**C**) Time lapse microscopy of strain CBK063 was applied to investigate differences (Δ) between polar elongation (cell length increase divided by two) and distances covered by the replisome measured from appearance of DnaN foci until cell division, $\bar{x}$ = 0.014, SD = 0.242 (n = 52) (**D**) Replisome numbers increase in the course of one cell cycle. One up to six DnaN-spots were detected per cell; cell fractions are indicated as percentage of total cell number for each time frame (n = 59, CBK062). (**E**) ParB-eYFP and DnaN-mCherry foci numbers per cell in relation to cell length (CBK063, n = 200). Linear regression lines are shown; r (ParB-eYFP/DnaN-mCherry) = 0.65. (**F**) Cohesion periods of sister *oriC*s analyzed by time lapse microscopy of strain CBK063. Left: ParB-*oriC* colocalization intervals are shown together with the cumulative skew of sample data (n = 88). Right: Scheme of cell halves

of CBK063 indicating localization of ParB-*oriC* (green) and DnaN foci (red) associated with chromosomal DNA (black lines) at the time point of replication initiation and at subsequent *oriC*-segregation.

In order to verify replication initiation at ParB-*oriC* complexes a strain harboring a combination of functional DnaN-mCherry and ParB-eYFP fusions was constructed (**Figure 2.8A**, **B**). The dependence of ParB-eYFP and DnaN-mCherry foci numbers on cell length has been validated (**Figure 2.9E**). On average less replisomes than ParB-*oriC* clusters were counted per cell, yet the numbers of replication forks and *oriC*s per cell moderately correlate with each other. Further, cohesion times of sister *oriC*s were analyzed by determining the time frame from replication initiation at ParB-*oriC* foci to splitting of descended sister *oriC* domains into two distinct fluorescent signals (**Figure 2.9F**, **Figure 2.10**). Time intervals of *oriC*-cohesions appear to be highly variable, ranging from 5 to 80 minutes. On average, *oriC* domains colocalized for 36 minutes, which is in line with an *oriC*-colocalization of 40 minutes determined for *E. coli* cells at fast growth (Fossum et al., 2007). However, different to *E. coli*, *C. glutamicum oriC*-cohesions are distributed relatively homogeneously across the time span of more than one hour, indicating that a tight regulation of sister ParB-*oriC* complex segregation might be absent (**Figure 2.9F**). Besides this, replication initiates frequently in mother generations, where ParB-*oriC* complexes do not separate before they passed through large parts of the daughter cell cycles (**Figure 2.10**). Notably, tracking of DnaN-foci indicates that ongoing replication events can be prolonged beyond initiation of new C-periods at polar as well at midcell-positioned ParB-*oriC* complexes (exemplified in **Figure 2.10**). Therefore, live cell imaging provides further evidence that C-periods follow each other in very quick succession or may even overlap. This observation is in line with the large-scale localization analysis of DnaN-mCherry signals in still microscopy images shown before (**Figure 2.9B**), where newly formed replication hubs at cell quarter positions cannot be separated from previous fluorescence signals at midcell positions. Unlike demographs showing cellular DnaN-mCherry fluorescence profiles (**Figure 2.9B**), live cell imaging clearly points to replisome formation at polar and septal positions, followed by a progressive movement away from ParB-*oriC* domains (**Figure 2.10**). Such replisome localization patterns are not clearly obtained by demograph visualization, likely due to divergent replisome dynamics and variable timing of replication initiation between cells of comparable sizes. In summary, replisome analyses reveal variable cohesion times of ParB-*oriC* complexes and the presence of multiple replication forks per cell that prolong over two generations and originate from replisome assembly at polar or septal *oriC* domains.

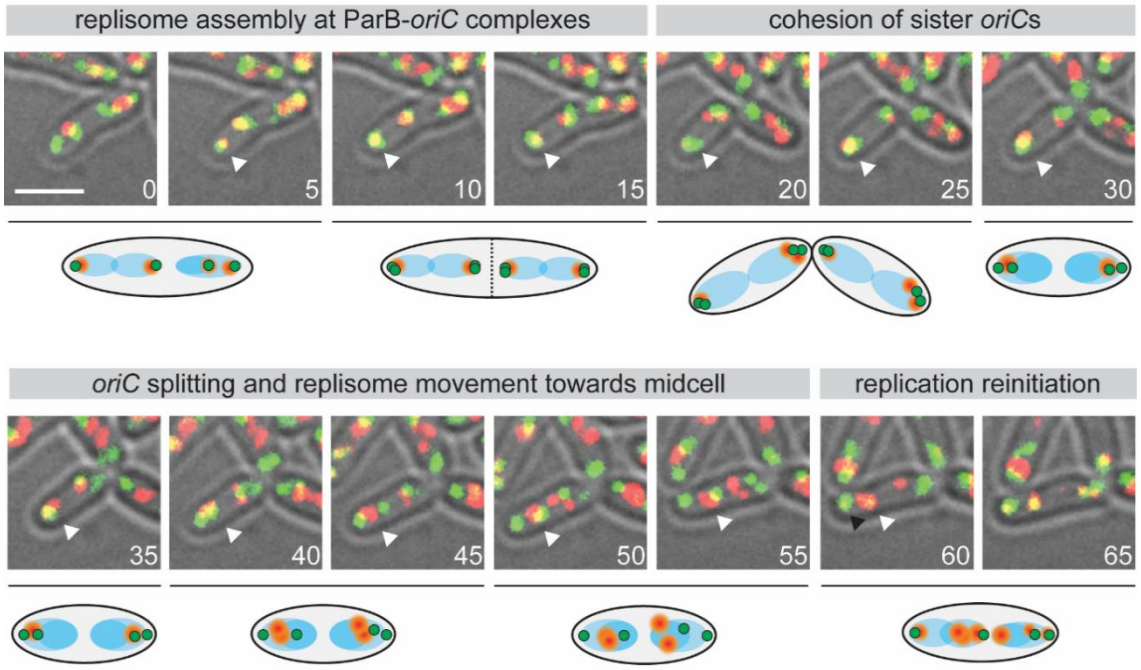

Figure 2.10: Coordination of replisome dynamics with subcellular ParB-*oriC* positioning.

Time-lapse microscopy series of CBK063 cells. ParB-*oriC* and DnaN-mCherry fluorescence are shown in green and red (overlay in yellow) merged with bright field channels. Replisome tracking (white arrowhead) from polar assembly, relocalization towards midcell until replication re-initiation (black arrowhead) prior to termination of the previous round takes place within two cell generations. Newly replicated sister *oriC*s colocalize up to 40 minutes; sister replisomes merge in one fluorescent spot, yet replisomes of opposing cell half split at 50 and 55 minutes (see cartoon of cells below images with nucleoids indicated by blue spheres). Images were taken in 5 minute intervals (white captions, bottom right corners); scale bar, 2 µm.

2.2. The cell cycle of *C. glutamicum*

Data of this study shown so far reveal highly organized localization patterns of chromosomal macrodomains and replication forks, where their positioning along the longitudinal cell axis depends on cell growth and the timely progression of the cell cycle. However, precise cell cycle parameters have not been determined before in *C. glutamicum*. In order to put spatiotemporal localization of chromosomal structures in the context of distinct cell cycle stages, we subsequently resolved C- and D-periods and determined overall DNA contents per cell at different growth rates.

2.2.1. Overlapping replication periods allow for fast growth

ParABS systems and multifork replication were hypothesized to be mutually exclusive (Lutkenhaus, 2012), because multifork replication had been initially attributed to fast-growing bacteria *E. coli* that lacks ParABS and *B. subtilis*, where ParAB homologues Soj/Spo0J are primarily required for DNA-segregation during sporulation. However, due to detection of multiple ParB-*oriC* complexes and replication forks per *C. glutamicum* cell, we aimed to challenge this assumption. Here, we investigated whether new rounds of replication may be initiated prior to termination of previous ones.

Marker frequency analyses were carried out to determine growth rate-dependent replication modes in *C. glutamicum*. Average ratios of *oriC* to *terC* per cell were analyzed in non-synchronized wild type cultures by amplification of chromosomal loci close to *oriC* and *terC* domains (**Figure 2.11A**) by qPCR. Three different growth media were utilized (BHI, BHI Gluc or MMI), which allow for fast, intermediate and slow growth (**Figure 2.11B**). In principle, multifork replication yields *oriC*/*terC* ratios above values of two, as shown for exponentially grown *B. subtilis* cells (**Figure 2.11B**) that undergo clear multifork replication (Yoshikawa et al., 1964). For *C. glutamicum* qPCR data of two different marker combinations result in comparable *oriC*/*terC* ratios (**Figure 2.11A**). For exponential cultures in BHI and BHI Gluc complex media *oriC*/*terC* ratios between values of two and three were obtained, indicating a moderate degree of nested replication forks at fast growth. On the contrary, significantly lower *oriC*/*terC* ratios with average values of 1.5 to 1.7 were determined for slow growth conditions in MMI medium. These ratios do not differ significantly from the ones obtained for cells in stationary growth phases (**Figure 2.11A**). Inhibition of replication initiation by antibiotic treatment resulted in cells with fully replicated chromosomes that served as a control. These replication run-outs resulted in *oriC*/*terC* ratios close to one (data not shown). Therefore, values of stationary cells indeed indicate the presence of incomplete replication events. Likewise, active replication forks were observed in around 24 % of stationary *M. smegmatis* cells (Trojanowski et al., 2015).

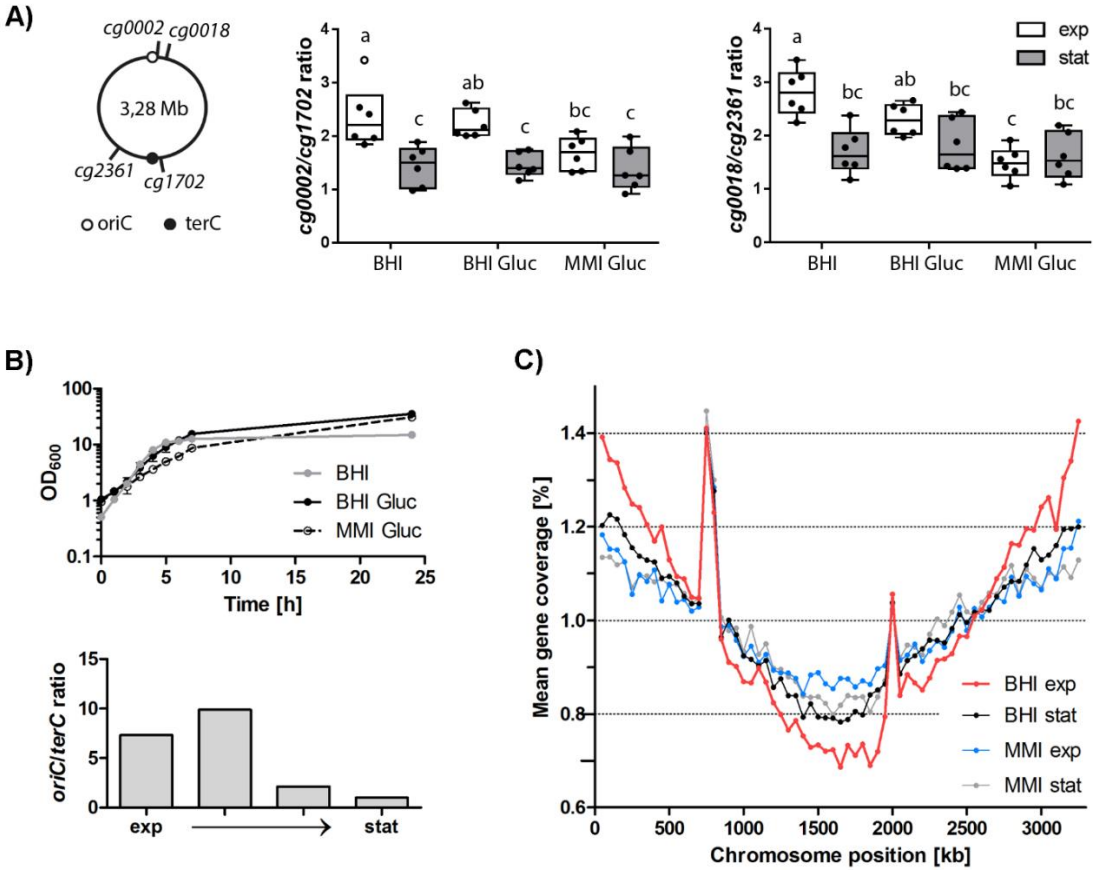

Figure 2.11: Growth rate-regulated timing of chromosomal replication re-initiations.

(**A**) Marker frequency analysis of *oriC*/*terC* regions in *C. glutamicum* RES167 wild type. Left: Positioning of qPCR markers along the *C. glutamicum* chromosome. Middle and right: Estimates of *oriC*/*terC* ratios determined by qPCR using marker combinations *cg0002*/*cg1702* and *cg0018*/*cg2361* for exponential (exp) or stationary (stat) growth phases, media: BHI, BHI supplemented with glucose or MMI supplemented with glucose. Boxplots show medians and whiskers of 1.5 × interquartile range (n = 6); outliers are indicated by open circles. An ANOVA yields significant variation for ratios *cg0002*/*cg1702* amongst growth phases ($F(1, 30) = 28.00$, $p < .0001$) and media ($F(2, 30) = 3.43$, $p < .05$). Similarly, an ANOVA reveals an effect of growth phases ($F(1, 30) = 13.41$, $p<.001$), of media ($F(2, 30) = 9.77$, $p < .001$) and of the combination growth phase and medium ($F(2, 30) = 7.17$, $p < .01$) on ratios *cg0018*/*cg2361*. Letters indicate significant differences between data sets, Post-hoc Bonferroni analysis at $p < .05$. (**B**) Top: Growth curves of *C. glutamicum* RES167 wild type strain grown in above-named media: BHI ($\mu = 0.66\ h^{-1}$), BHI Gluc ($\mu = 0.50\ h^{-1}$), MMI Gluc ($\mu = 0.32\ h^{-1}$). Values derive from triplicates; standard deviations are indicated. Below: Marker frequency analysis using DNA of *B. subtilis* 168 grown in LB medium at time points of exponential (exp) to stationary growth (stat). (**C**) Sequencing coverage of genomic DNA of *C. glutamicum* RES167 wild type grown as described above. Sequencing reads were mapped accordingly (GeneBankID: BX927147.1); data are displayed as the mean gene coverage in % of each 50 Kb sliding window of the total mean coverage per sample; *terC*-centered. RES167 used in this study harbors an *ISCg14* mediated 5 × tandem amplification of the trehalose uptake system (*cg0830-cg0835*)-genes (peaks at approx. 750 and 2000 Kb positions); loci were excluded from analysis.

These results were further confirmed by analysis of whole-genome sequencing data obtained from DNA isolated from *C. glutamicum* cells grown in corresponding rich and minimal media (BHI and MMI). Read coverages were compared between growth conditions and between exponential and stationary growth phases (**Figure 2.11C**). At any condition tested, replication forks progress symmetrically along both replichores from *oriC* towards the *terC* domain. During fast growth the mean gene coverage at *oriC* is 2.1-fold higher than the one at *terC*-proximal regions. Since these data display averaged *oriC*/*terC* values that derive from non-synchronized cell populations, *C. glutamicum* is capable to re-initiate replication prior to termination of an ongoing replication event at least during certain time periods of the cell cycle. These results are in line with marker frequency data and with remarkably high replisome numbers per cell determined before. Sequencing ratios of *oriC*- to *terC*-proximal genome regions in slowly-growing cells yield a value of 1.5, which is comparable to ratios of cells in stationary growth phases (**Figure 2.11C**). Again, these data are in line with marker frequency analyses. In summary, we provide evidence for multifork replication in *C. glutamicum* that allows for a reduction of generation times at fast growth. Further, marker frequency analyses and genome sequencing results point to distinct growth rate-dependent replication cycles.

2.2.2. Multiple chromosome equivalents at varying growth rates

In the following, the relatively high *oriC* frequency compared to *terC* domains was quantified more precisely in absolute *oriC* numbers per cell by application of flow cytometry. Similar to preceding marker frequency analyses, DNA content per cell was determined in *C. glutamicum* wild type cells cultured in different media that enable for fast, intermediate and slow growth. Here, replication run-outs were performed at exponential growth phases by chloramphenicol treatment, that allows for completion of ongoing rounds of replication but inhibits replication re-initiations. Consequently, cells end up with fully replicated chromosomes, where total genome copies correspond to initial *oriC* numbers per cell.

First of all, absolute DNA content was assigned according to an internal standard in flow cytometry measurements. To this end, *B. subtilis* cells of known DNA content (Hill et al., 2012) were included in samples of *C. glutamicum* cells after applying click chemistry reactions for cell wall staining with Carboxyrhodamine (see Materials and Methods). In order to detect nucleoids in cell mixtures, samples were additionally stained with Hoechst (**Figure 2.12A**). *C. glutamicum* and *B. subtilis* subpopulations were distinguished by their green fluorescence intensity and DNA

fluorescence intensities of *C. glutamicum* cells could be assigned to chromosome numbers according to the *B. subtilis* standard (**Figure 2.12B**).

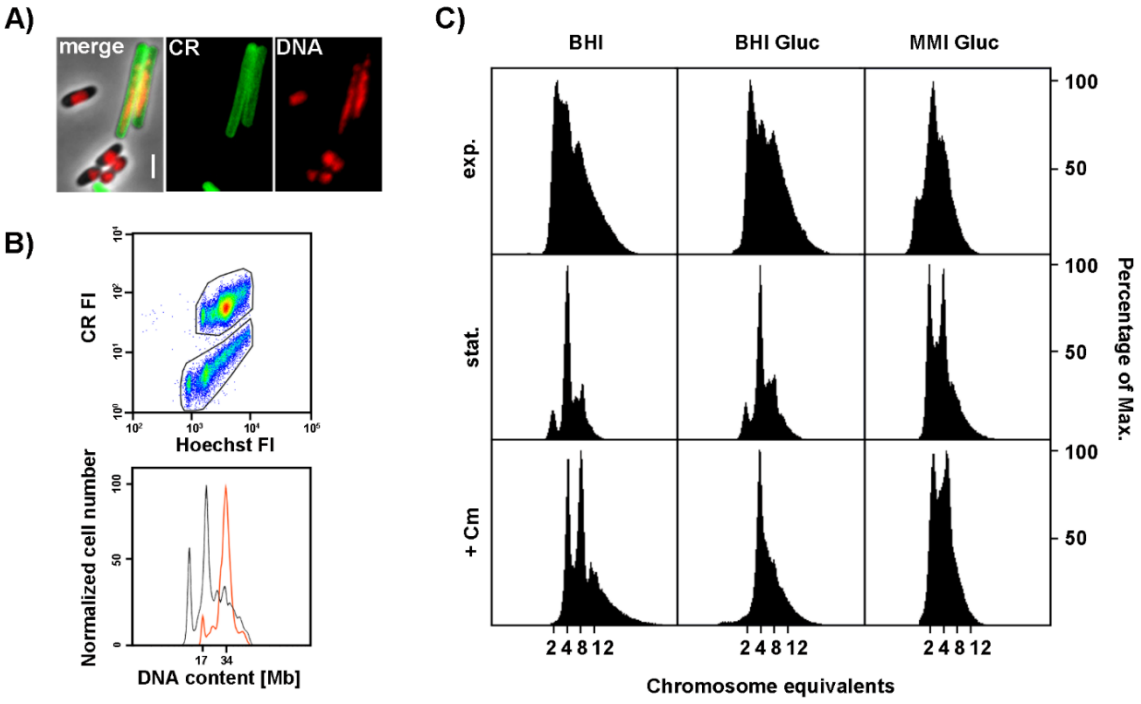

Figure 2.12: Population-based measurements of absolute *oriC* numbers per cell.

(**A**) Representative *C. glutamicum* RES167 wild type cells grown at fast rates and *B. subtilis* 168 cells used as calibration of DNA measurements. Microscopy images show the overlay (merge) of Carboxyrhodamine (green) and Hoechst fluorescence (false-colored, red) with the phase contrast image and individual fluorescence channels (CR, DNA). Scale bar, 2 µm. (**B**) Gating strategy exemplified using above-named sample cells. Top: *C. glutamicum* and *B. subtilis* subpopulations were identified in density plots of the Carboxyrhodamine (CR FI, arbitrary units) versus the Hoechst channel (Hoechst FI, arbitrary units). Below: Determination of *C. glutamicum* chromosome numbers (black) according to the *B. subtilis* standard (red) in histograms versus DNA quantity. (**C**) Flow cytometry analysis of DNA contents in *C. glutamicum* wild type cells grown at high (BHI), intermediate (BHI Gluc) or low rates (MMI Gluc). Cultures were analyzed in exponential (exp.) and stationary growth phases (stat.), or after replication run-outs (+Cm); numbers of chromosome equivalents are indicated below graphs.

Subsequent measurements of *C. glutamicum* DNA content were performed by usage of SYBR® Green I dye. DNA histograms of cells at exponential or stationary growth phases not subjected to antibiotic treatment are shown together with replication run-outs (**Figure 2.12C**). *C. glutamicum* populations at log phase exhibit widespread DNA fluorescence profiles for all growth conditions tested, while peaks of distinct DNA-fluorescence intensities form at stationary growth phases.

These transitions in fluorescence intensity reflect the increasing amount of terminated replication events that yields in fully replicated chromosomes in a pre-divisional state at stationary growth phases. Notably, these observations are in line with DNA fluorescence patterns of *C. glutamicum* cells shown in previous flow cytometry measurements (Neumeyer et al., 2013). DNA content distributions of chloramphenicol-treated cells show the number of fully replicated chromosomes, which equal the cellular origin numbers at the time point of antibiotic treatment at different growth rates (**Figure 2.12C**). Upon replication run-out cells mainly contained four and eight chromosome equivalents at fast and intermediate growth rates, while a small fraction of cells contained ten and twelve chromosome equivalents. At slow growth, most cells harbored two or four chromosomes, yet eight chromosome equivalents were detected in a small subpopulation. Prior to replication run-outs, average *oriC* numbers of 5.90, 5.17 and 3.85 were maintained per cell during log-phase at fast, intermediate or slow growth, respectively. Strikingly, monoploid subpopulations were absent for all conditions tested during exponential growth.

Overall, the *oriC* content per cell determined by flow cytometry considerably exceeds the expectations based on marker frequency data. Further, flow cytometry results are markedly supported by microscopy analyses of ParB-*oriC* complex numbers and replisome counts per cell. The latter one was investigated using *dnaN-mCherry*-expressing *C. glutamicum* cells. Replisome abundance was determined for corresponding media, indicating a dependency on growth rate and cell length (**Figure 2.13A**, **B**). Fast growth allows for one up to six DnaN-mCherry spots per cell, whereas zero up to four foci per cell were counted at slow growth conditions (**Figure 2.13B**, **C**). Cells harboring fluorescent ParB-eYFP fusions were grown at various rates, two of which even fall below the ones analyzed in flow cytometry and marker frequency studies (**Figure 2.13D**). Similar to replisome counts, the abundance of ParB-*oriC* complexes per cell depends on growth rate, nonetheless, fractions of cells with less than two ParB-*oriC* foci were mostly absent in any case (**Figure 2.13E**).

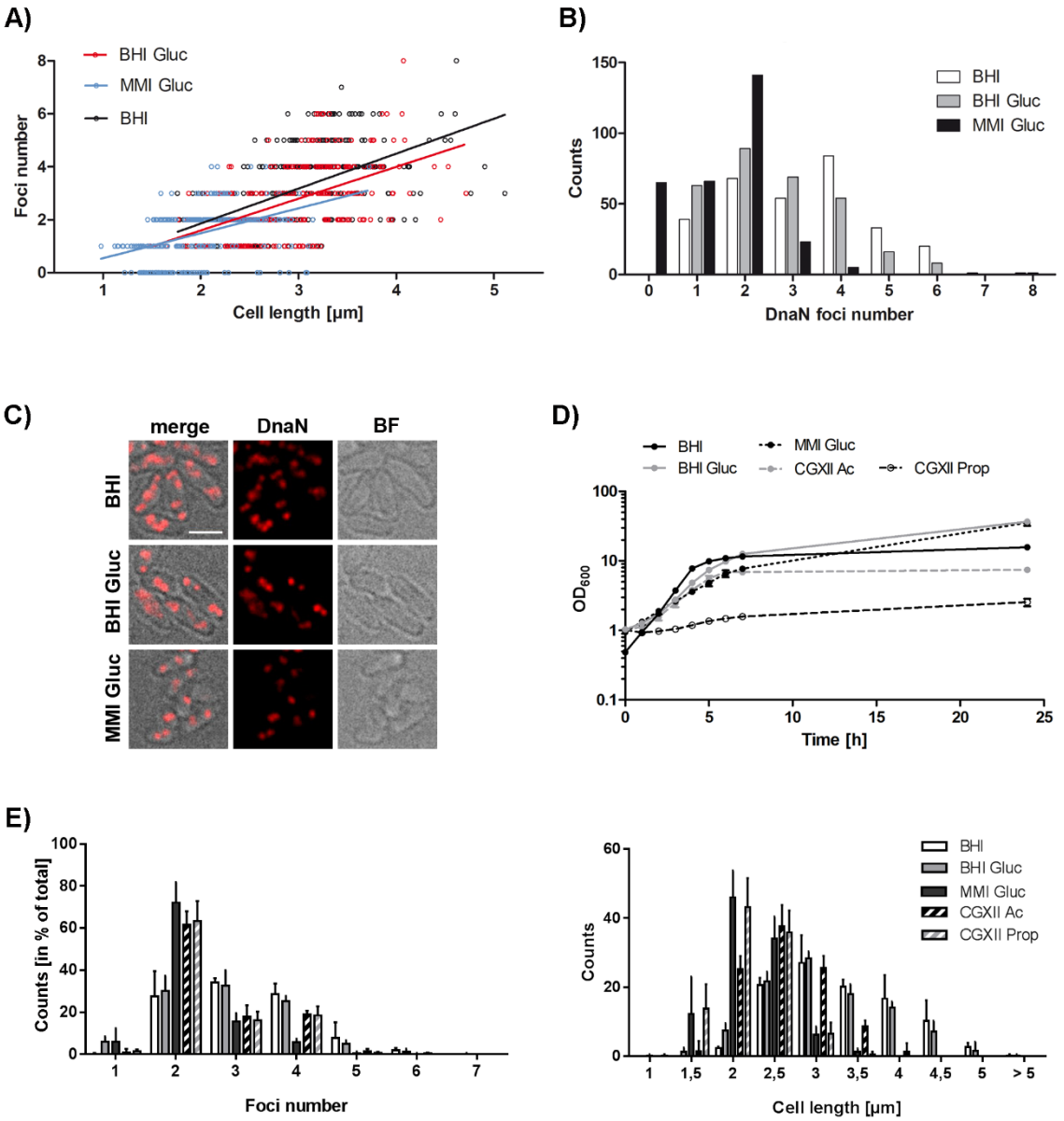

Figure 2.13: Growth rates impact on replisome and ParB-*oriC* cluster numbers per cell.

(**A**-**C**) *C. glutamicum dnaN::dnaN-mCherry* cells (CBK062) were grown exponentially in BHI medium (BHI) and BHI or MMI medium each supplemented with glucose (BHI Gluc, MMI Gluc). (**A**) Replisome numbers are cell length-dependent at any growth rate (n = 300); linear regression lines are shown, r(BHI) = 0.54, r (BHI Gluc) = 0.55, r (MMI Gluc) = 0.42. (**B**) Zero up to eight replisomes were determined microscopically per cell, n = 300. (**C**) Images exemplify replisome localization; bright field images (BF), mCherry fluorescence (DnaN) and overlays of both channels (merge) are shown. Scale bar, 2 µm. (**D**) Growth curves of strain CBK007 harboring fluorescent ParB-eYFP cultivated in BHI ($\mu = 0.62\ h^{-1}$), BHI ($\mu = 0.49\ h^{-1}$) or MMI supplemented with glucose ($\mu = 0.32\ h^{-1}$), and CGXII supplemented with acetate ($\mu = 0.41\ h^{-1}$) or propionate ($\mu = 0.13\ h^{-1}$). Experiments were performed in triplicates; error bars display standard deviations. (**E**) ParB-eYFP foci counts per cell and cell length distributions of CBK007 at use of different carbon sources (n = 200).

Therefore, *C. glutamicum* is at least diploid and appears to support even oligoploid cell cycle stages at varying growth rates, with two ParB-*oriC* complexes being stably attached to the cell poles. Nutrient-rich media support fast growth and accelerate the process of replication-initiation, leading to multi-forked chromosomes.

2.2.3. Growth rate-dependent cell cycle models

Previous analyses of replication timing and DNA content per cell provide relevant information to finally formulate complete cell cycle models for different growth rates in *C. glutamicum*. To this end, the time intervals of C- and D- periods were calculated based on *oriC*/*terC* ratios obtained from marker frequency analyses, the average *oriC* and *terC* numbers per cell obtained by flow cytometry and doubling times for each growth condition (**Table 1**, for formula see Materials and Methods).

Table 1: Cell cycle parameters of *C. glutamicum* grown at three different rates.

Growth medium	T_d [min][1]	*oriC*/*terC*[2]	*oriC*/cell[2]	C [min]	D [min]
BHI	63	2.36 ± 0.54	5.90 ± 0.03	78	20
BHI + glucose	83	2.23 ± 0.21	5.17 ± 0.02	96	18
MMI + glucose	130	1.68 ± 0.28	3.85 ± 0.16	97	26

[1] T_d: doubling time

[2] Averaged values are displayed including standard deviations

On average, fast-growing cells cultivated in BHI medium replicate one chromosome of 3.21 Mb in size within 78 minutes. In comparison, C-periods during intermediate and slow growth in BHI or minimal medium supplemented with glucose are approximately 20 % longer. These values result in moderate replisome velocities that range from 280 to 340 bases per second in *C. glutamicum* and are comparable to replication speeds reported for *C. crescentus*, *M. xanthus* and the related actinobacterium *M. smegmatis* (**Table 2**). By contrast, the chromosome replication speed of the slowly-growing *M. tuberculosis* is six times lower, while *V. cholerae*, *E. coli* and *B. subtilis* can speed up replisome velocities growth rate-dependently to more than twice the value determined for *C. glutamicum* (**Table 2**).

Table 2: Summary of distinct DNA replication speeds observed in different model organisms.

Organism[1]	Genome size [Mb]	C-period [min]	Repl. speed[2] [bases/sec]	Reference
Cgb	3.21	78	340	this study
Mtu	4.42	660	50	(Nair et al., 2009)
Msm	6.99	140	400	(Santi and McKinney, 2015; Trojanowski et al., 2015)
Mxa	9.14	200	380	(Harms et al., 2013; Zusman and Rosenberg, 1970)
Ccr	4.02	95	350	(Dingwall and Shapiro, 1989)
Vch[3]	2.96	30-50	490-820	(Rasmussen et al., 2007; Stokke et al., 2011)
Bsu	4.22	50-60	600-700	(Hill et al., 2012; Sharpe et al., 1998)
Eco	4.64	40-200	200-1000	(Cooper and Helmstetter, 1968; Michelsen et al., 2003)

[1]Cgb: *C. glutamicum* RES167, Mtu: *M. tuberculosis*, Msm: *M. smegmatis*, Mxa: *M. xanthus*, Ccr: *C. crescentus*, Vch: *V. cholerae*, Bsu: *B. subtilis*

[2]Replication speed, [3]Shown are parameters for chromosome I only.

Furthermore, equations for the calculation of D-periods reported before (Hill et al., 2012) yield in time intervals that are longer than the generation times for each of the three growth conditions analyzed. In general, these time frames comprise the period of replication termination to separation of the newly replicated sister chromosomes by cell division. However, due to diploidy of *C. glutamicum* cell, newly replicated chromosomes separate to daughter cells with a delay of one generation time. Therefore, calculations of D-periods were adapted to a diploid organism (see Material and Methods), comprising time intervals from completion of the latest replication to subsequent cell division. Here, D-periods remained relatively unaltered in *C. glutamicum* with 20 and 18 minutes at high and intermediate growth rates, respectively (**Table 1**). However, slow growth in minimal medium leads to an extended continuation of the pre-divisional state. Based on these parameters, we developed cell cycle models that are shown below for fast and slow growth conditions (**Figure 2.14**).

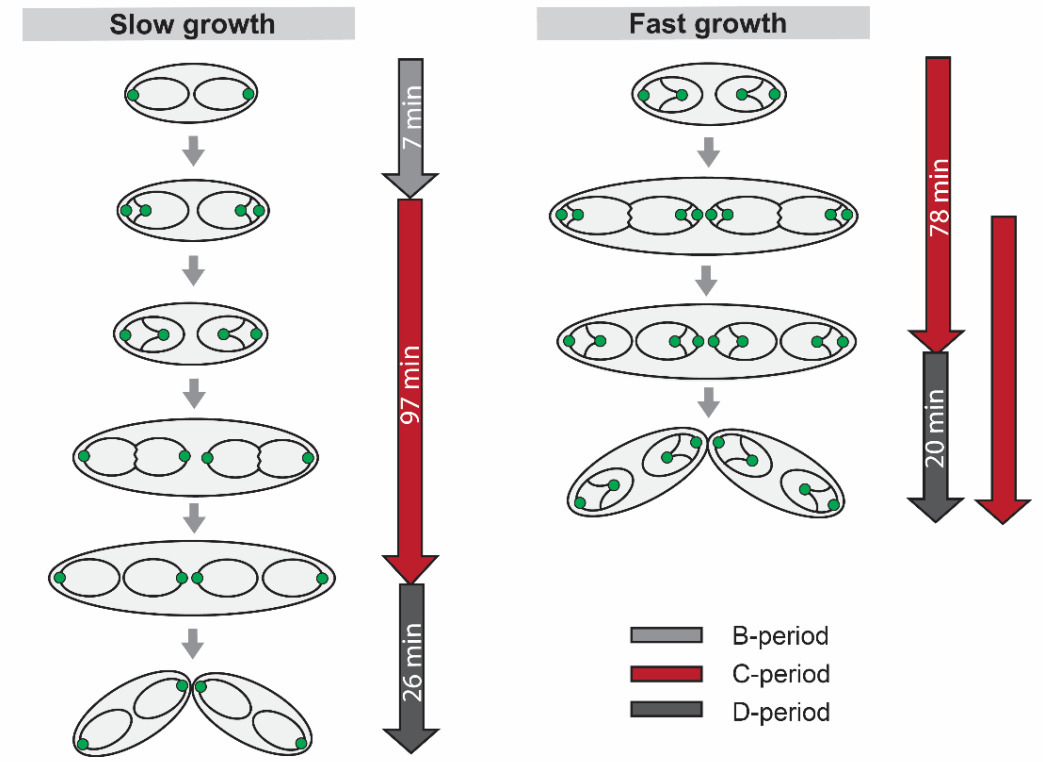

Figure 2.14: Spatiotemporal chromosome organization of *C. glutamicum*.

Cell cycle modes for short and long generation times. Chromosomes are depicted as black lines with *oriCs* indicated by green circles. Notably, stages with single chromosomes per cell are absent at any growth rate and replication cycles of at least two sister chromosomes take place simultaneously. Left: Cell cycle of slow-growing cells in MMI medium supplemented with 4 % glucose (doubling time = 130 min). Right: Life cycle of BHI-grown cells (doubling time = 63 min).

Newborn cells harbor two fully replicated chromosome copies, which tether ParB-*oriC* complexes to one cell pole each and position longitudinally within the cells. Replicated sister *oriC* domains segregate towards midcell positions. At slow growth one round of genome duplication is achieved in the course of an average generation time of 130 minutes. This growth mode further features a short B-period of seven minutes, which is the time interval that precedes replication initiation. By contrast, short doubling times of 63 minutes are characterized by overlapping replication periods. Newborn cells inherit chromosomes, where replication of both copies commenced in the previous generation. A new round of replication initiates at *oriC* domains 28 minutes after cell division, while the preceding replication event terminates 15 minutes later. Consequently, at fast growth mainly four up to eight ParB-*oriC* clusters and at slow growth two to four ParB-*oriC* clusters are present per cell. Notably, these data are in line with microscopy data shown before (**Figure 2.4B**, **Figure 2.13E**). Further, high replisome numbers with up to six DnaN-mCherry foci per cell were

determined microscopically (**Figure 2.9D**, **Figure 2.13B**). These results are confirmed by the cell cycle model, where up to six replication events may occur simultaneously during replication overlap at fast growth, which give rise to up to 12 replisomes per cell. Likely, microscopy analyses of DnaN-mCherry foci underestimate replication events per cell due to colocalization of replication forks. At both, high and low growth rates newly replicated sister chromosomes are not separated from each other before cytokinesis of daughter cells.

Conclusively, comprehensive cell cycles models described here point to diploidy combined with growth rate-dependent replication timing in *C. glutamicum*, where overlapping replication events allow for fast growth.

2.3. Impact of *parS* sites on chromosomal architecture in *C. glutamicum*

Preceding studies on spatiotemporal chromosome organization in *C. glutamicum* have exploited ParB-*parS* interactions to track *oriC* domains in the course of the cell cycle (Böhm et al., 2017), building on the colocalization of ParB clusters with *oriC* domains (Donovan et al., 2010). Nonetheless, the conservation of *parS* motifs and their precise positioning on the *C. glutamicum* chromosome had not been characterized, yet. Moreover, these motifs do not only act as a basis for ParAB-mediated DNA segregation, but have also been shown to impact on overall chromosome folding in *B. subtilis*, *C. crescentus* and *P. aeruginosa* (Lagage et al., 2016; Tran et al., 2018; Wang et al., 2015). Hereafter we follow up on identification of *parS* sites in *C. glutamicum* and further elucidate their impact on ParB complex formation, overall chromosome folding and DNA segregation.

2.3.1. An *oriC*-proximal *parS* cluster flags the hub of chromosome organization

Chromosomal *parS* sites had first been described in *B. subtilis*, where they consist of a distinct consensus motif that may be slightly degenerated in sequence and localize within an *oriC*-proximal region that accounts for 20 % of the chromosomal length (Lin and Grossman, 1998). Based on the *B. subtilis* 16 bp sequence motif, four up to eight putative *parS* sites were initially predicted in the genus *Corynebacterium*, (Livny et al., 2007). However, we identified ten corresponding *parS* sites in *C. glutamicum* using blast. They cluster within a 35 Kb region comprising 1 % of the 3.21 Mb-sized chromosome, 73 Kb distant to the *oriC* (**Figure 2.15A**). Solely one *parS* site, located farthermost from *oriC* (*parS*1), positions within an open reading

frame (*cg3362*, *trpCF*). All other *parS* sequences that are from now on termed *parS*2-10 lie within intergenic regions. In addition, several putative *parS* motifs that exhibit at least three bp mismatches locate separately at *oriC*-distant genome regions, for example 5' of *cg0146* and within *fusA* and *cg1994* coding regions. In order to test whether these hypothetical *parS* sites are responsible for ParB recruitment, *in vivo* chromatin immunoprecipitations (ChIP) have been carried out. A mCherry-tagged version of the native ParB was precipitated using α-mCherry antibodies. As before, this mutant strain derives from a clean allelic replacement and has a wild type-like phenotype (**Figure 2.1B**, **C**). Analyses of ChIP combined with deep-sequencing (ChIP-seq) result in highly reproducible ParB-enrichment signals at the 3.16 Mb genomic position in *oriC*-proximity (**Figure 2.15B**). These signals coincide with chromosomal *parS*1-10 positions. Besides, comparably weaker enrichment peaks were detected at highly transcribed genes, in particular at ribosomal DNA (rDNA) and transfer RNA (tRNA)-gene clusters (**Figure 2.15B**). A scale-up of the pronounced ParB-binding signal close to *oriC* reveals three distinct ParB propagation zones that span over *parS*1-4, *parS*5-8 and *parS*9-10 sites, respectively (**Figure 2.15C**). Notably, ParB is recruited in decreasing amounts to these regions, exhibiting high protein enrichment at *parS1-4* to comparably reduced enrichment at *parS9*-10. However, *parS*1-10 sites are identical in sequence. Therefore, deviant ParB-recruitments by each of the sub-clusters likely result from local DNA folding patterns or *parS* numbers and differing distances between *parS* sites, which may alter the binding probabilities of ParB to DNA. Likewise, sharp dips between ParB-recruitment zones presumably reflect local roadblocks, likely caused by nucleoid-associated proteins or other chromosomal topologies. By contrast, degenerated *parS* sequences identified beforehand by blast comparison failed to recruit ParB.

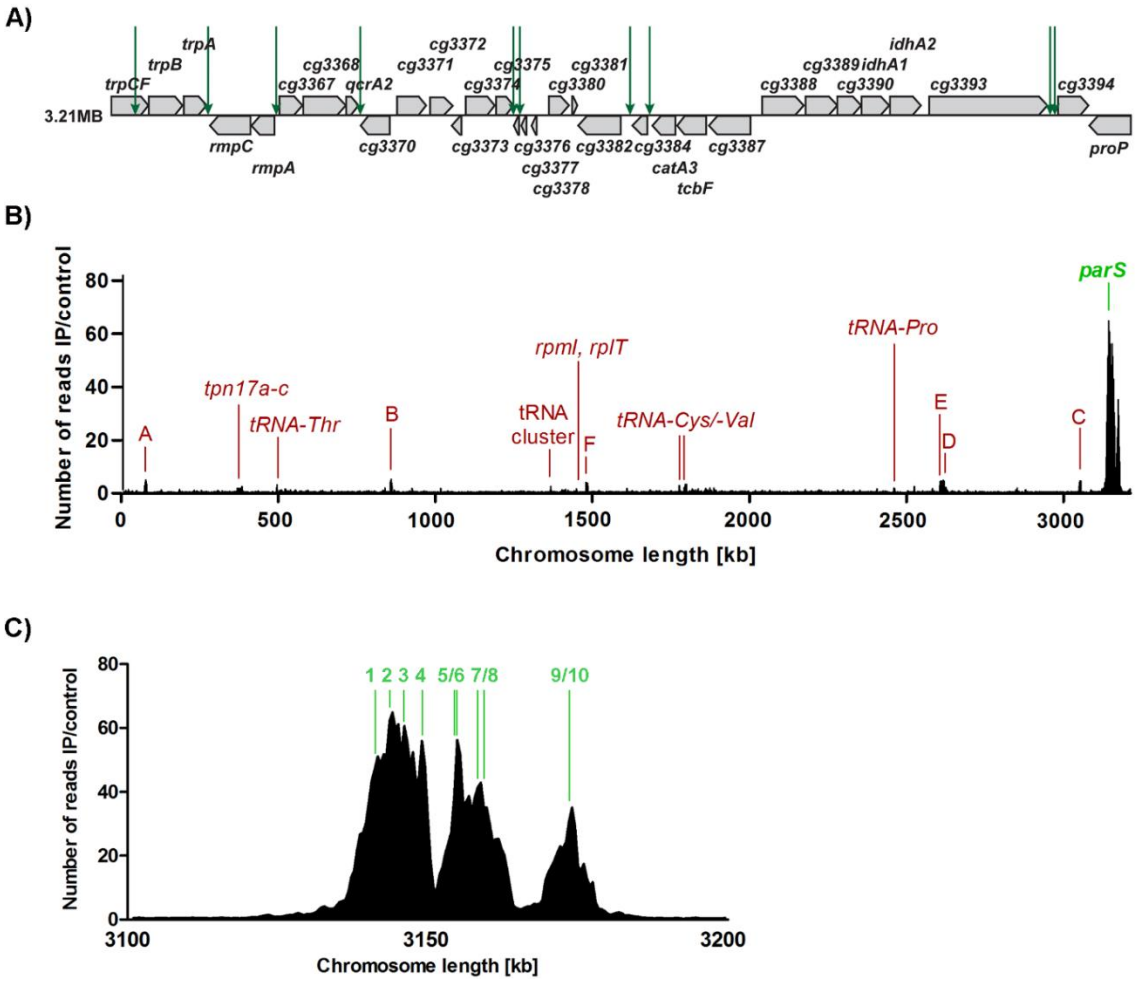

Figure 2.15: ParB is recruited by ten *parS* sites in *oriC*-proximity.

(**A**) Genome section including ten *parS* sites of 16 bp consensus sequence each. (**B**) ChIP-seq enrichments of fluorescently tagged ParB-mCherry protein along the *C. glutamicum* chromosome. Signals derive from *in vivo* ChIP analysis using strain CBK006 at exponential growth. Data are presented as fold-enrichment of ChIP sequencing reads versus a control (IP/control) in 0.5 Kb bins; *terC*- centered. Minor enrichment signals at highly transcribed regions, like rDNA operons (letters A-F), are indicate by red labels. (**C**) ChIP-seq signals at chromosomal region 3.1 - 3.2 Mb; *parS* sites 1-10 are indicated by green letters.

Having identified the genomic location of functional *parS* sites in *C. glutamicum*, we next aimed to investigate whether these loci are characteristic features of the overall chromosome conformation. For instance, chromosome folding in *B. subtilis* initiates at ParB-*parS* clusters surrounding *oriC* (Marbouty et al., 2015; Wang et al., 2015). Here, SMC is recruited by ParB-*parS* complexes, mediating the alignment of right and left chromosomal arm. Therefore, we analyzed higher-order chromosome folding in *C. glutamicum*, using chromosome conformation capture to exponentially growing wild type cells (see Materials and Methods). In short, average distances

between genomic loci are determined by chemical crosslinking of neighboring DNA regions coupled with deep-sequencing approaches. Subsequent analyses of interaction frequencies picture genome-wide DNA-folding patterns at multiple scales. Chromosome conformation capture analyses were performed in collaboration with Dr. Martial Marbouty and Prof. Dr. Romain Koszul from the Institut Pasteur in Paris.

The contact map depicted below represents the average contact frequencies between all 5 Kb segments within the *C. glutamicum* wild type chromosome (**Figure 2.16**) and unveils the following features of DNA folding. First of all, frequent short-range contacts between adjacent DNA loci located within the same genomic region are represented by the strong and broad main diagonal, which is subdivided into differently-sized squares. These signals picture distinct interaction domains along the chromosome that correspond to genomic regions forming frequent contacts within themselves. Further, domains are separated from each other by abrupt boundaries as shown for other bacterial chromosomes (Le et al., 2013; Lioy et al., 2018; Marbouty et al., 2015; Val et al., 2016; Wang et al., 2015), which were classified statistically by directional index analysis (Dixon et al., 2012). Chromosomal interaction domains range from sizes of 125 to 500 Kb. Interaction borders often coincide with high transcriptional activity in *B. subtilis* and *C. crescentus* (Le et al., 2013; Marbouty et al., 2015) In *C. glutamicum* only 6 out of 11 boundaries are associated with high transcriptional activity or gene lengths (3 out of 11). Other roadblocks like nucleoid-associated proteins might play a major role in confining chromosomal interaction domains. Short-range interaction domains are mainly present at *terC*-proximal regions, while interaction ranges tend to increase towards the central *oriC*, indicating a looser DNA-packing surrounding this domain. Apart from that, a secondary diagonal of comparably lower interaction frequencies is displayed perpendicular to the main one. Both diagonals cross each other at the 35 Kb *parS* cluster close to *oriC* and extend towards *terC* regions, indicating that chromosomal arms are bridged all along their length. Here, folding originates from *parS* sites, analogous to *B. subtilis* and *C. crescentus* chromosomes (Le et al., 2013; Marbouty et al., 2015; Wang et al., 2015).

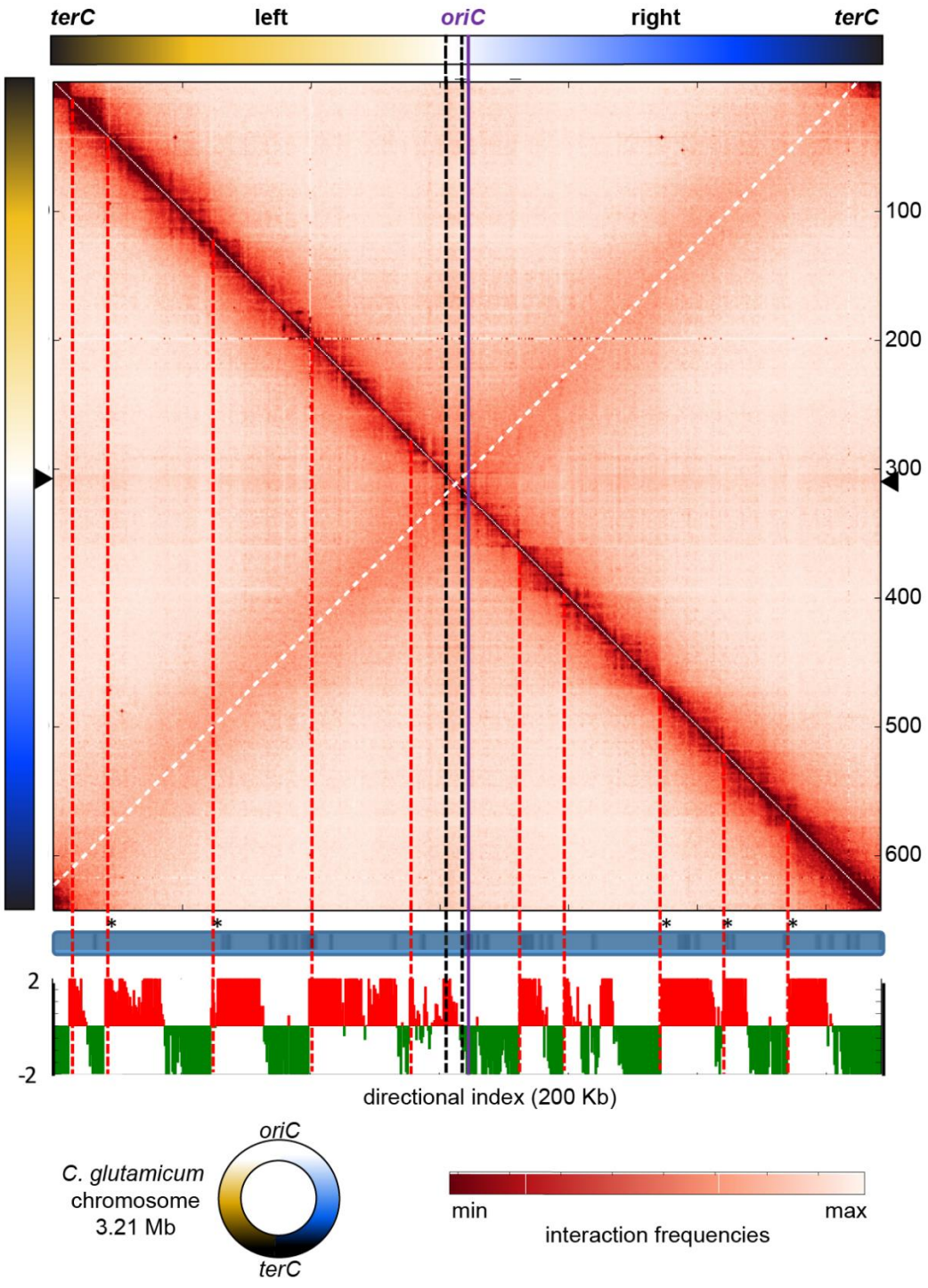

Figure 2.16: High-resolution chromosome folding in *C. glutamicum*.

Normalized chromosome contact map of asynchronously grown *C. glutamicum* RES167 wild type cells; x- and y-axes represent chromosomal arms, as illustrated schematically (bottom left); *oriC*-centered. Contact frequencies are mapped in 5 Kb bins (color gradient, red to white). Barriers between domains, *parS* sites and the secondary diagonal are indicated by red, black and white dotted lines; replication signals are emphasized by black triangles. Highly expressed genes (blue bars) are depicted above directional index analysis that indicates down- (red) and upstream (green) biases of corresponding genomic regions.

Finally, the contact map shows faint signals of a vertical and a horizontal line, both crossing each other at the *parS* cluster (clearly attenuated in differential maps presented in the following chapter). Chromosomal contacts correspond to interactions captured between the *oriC* region with all other chromosomal loci, which have been described before in *B. subtilis* (Wang et al., 2015). These replication signals reflect the translocation of polar ParB-*oriC* complexes across the whole nucleoid towards midcell positions in the course of chromosome segregation. In sum, chromosomal conformation capture analysis reveals characteristic features of chromosome folding in *C. glutamicum*, which collectively point to an organizational hub located at *parS* sites.

2.3.2. One *parS* site maintains ParB complex formation and global DNA-folding

Considering the very close proximity of all *parS* sites on the *C. glutamicum* chromosome, we tested the influence of ParB-*parS* complex quantity on the overall chromosome organization in a next step. For this purpose, *parS*1-10 were subsequently mutated markerless by silent point mutations (**Figure 2.17A**). Mutant cells harboring chromosomes that carry only one *parS* site (*parS*1) grow and divide wild type-like (**Figure 2.17B**, **C**). However, a complete lack of *parS* sites results in a wide range of cell lengths (**Figure 2.17B**) with more than 20 % of DNA-free minicells, hinting to impaired nucleoid segregation similar to the Δ*parB* phenotype (**Figure 2.17B**, **C**, **Table S1**). Notably, this phenotype confirms the detection of all relevant ParB-binding motifs by previous ChIP-seq analysis.

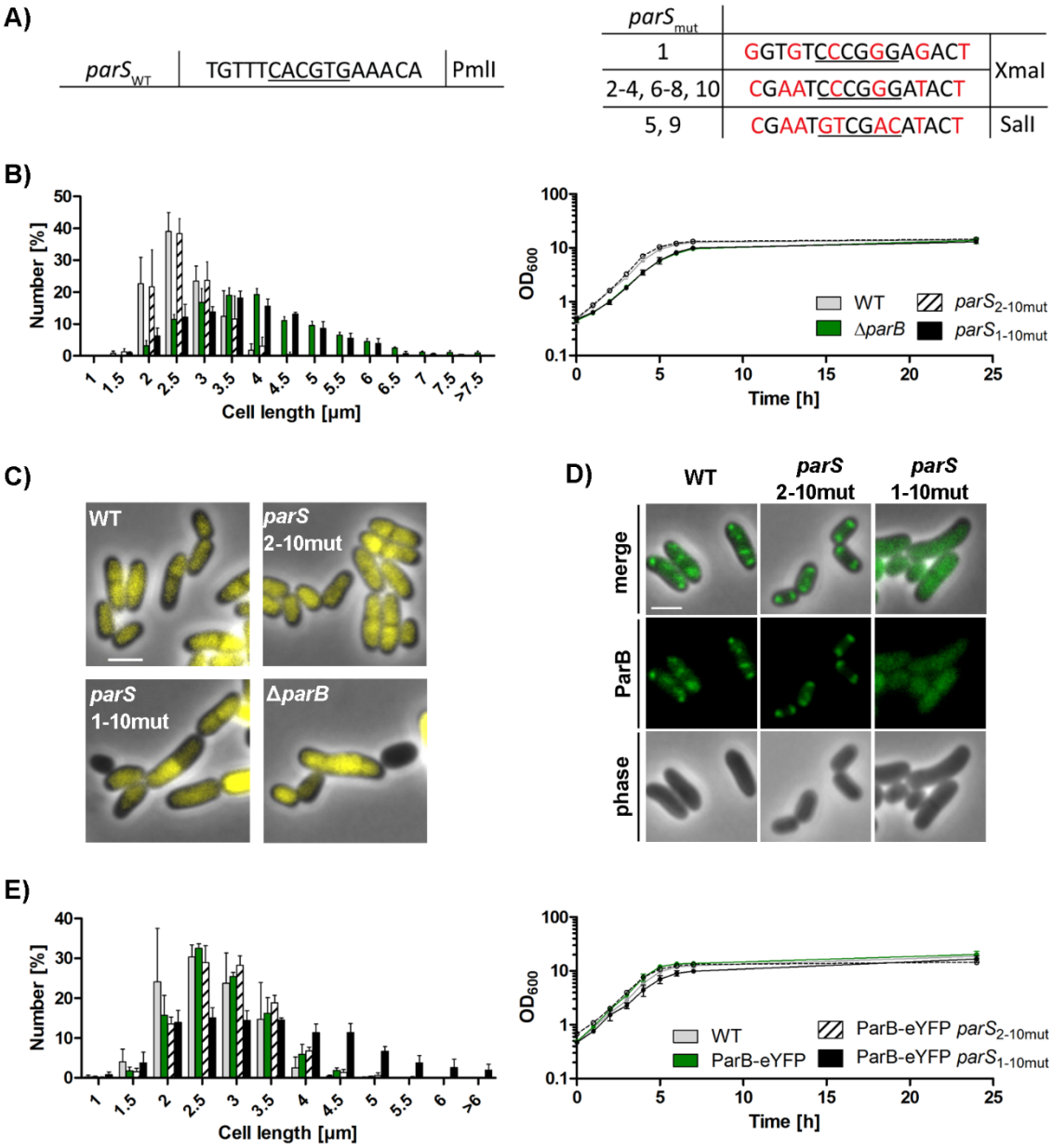

Figure 2.17: A single *parS* site suffices wild type-like chromosome segregation.

(**A**) Point mutations of *parS* sequences; bp exchanges (red letters) and (newly created) restriction sites (underscored) are indicated. (**B**) Comparison of cell length distributions and growth curves of *parS* and *parB* mutants in BHI medium measured in triplicates: wild type ($\mu = 0.65\ h^{-1}$), CDC003 (Δ*parB*, $\mu = 0.57\ h^{-1}$), CBK023 ($parS_{2\text{-}10mut}$, $\mu = 0.69\ h^{-1}$), CBK024 ($parS_{1\text{-}10mut}$, $\mu = 0.57\ h^{-1}$). (**C**) Microscopy images exemplify *C. glutamicum* cells harboring either all (wild type RES167), one ($parS_{2\text{-}10mut}$, CBK023) or none ($parS_{1\text{-}10mut}$, CBK024) *parS* site(s) or lacking *parB* (Δ*parB*, CDC003). DNA is stained with Hoechst dye (false-colored, yellow). Scale bar, 2 µm. (**D**) Cellular fluorescence of ParB-mCherry (false-colored, green) in the wild type background (WT, CBK006) and mutant cells harboring only one *parS* site ($parS_{2\text{-}10mut}$, CBK027) or none *parS* site ($parS_{1\text{-}10mut}$, CBK028). Shown are phase contrast, ParB-mCherry fluorescence and merge images; scale bar, 2 µm. (**E**) Growth analyses of ParB-eYFP-containing wild type and *parS* mutant strains were performed in biological triplicates and yield in growth curves (right) with the following growth rates:

CBK007 ($\mu = 0.65\ h^{-1}$, ParB-eYFP), CBK025 ($\mu = 0.59\ h^{-1}$, ParB-eYFP *parS*$_{2\text{-}10mut}$), CBK026 ($\mu = 0.55\ h^{-1}$, ParB-eYFP *parS*$_{1\text{-}10mut}$); corresponding cell length distributions are shown on the left.

First of all, we analyzed recruitment of fluorescent ParB-mCherry in mutant strains harboring one or none *parS* site. Similar to wild type cells, ParB-mCherry localizes in distinct clusters at cell poles and division septa in presence of only one *parS* site (**Figure 2.17D**). By contrast, mutation of all *parS* sites leads to a diffuse ParB localization throughout the cells, without formation of fluorescent foci (**Figure 2.17D**). Interestingly, cells with only one functional *parS* site per chromosome expressing *parB-eYFP* show DNA segregation defects, with a cell fraction of 7 % being anucleate (**Table S1**). Since *parB-eYFP* phenotypes are absent in presence of all *parS* sites (**Figure 2.17E**), the high abundance of *parS* sites likely evolved to reduce the susceptibility of the segregation machinery to disturbances. Otherwise, growth rates and cell-length distributions are not affected by fluorescently tagged ParB.

Accordingly, ParB ChIP-qPCR signals of locus *parS*1 were similar in both wild type and the mutant strain harboring only *parS*1, while no signal was detected in a mutant lacking all *parS* sites (**Figure 2.18A**). ParB spreading around a single *parS* site was further characterized by ChIP-seq analysis (**Figure 2.18B**, **C**). Here, ParB-binding was maximum within 2 Kb windows on either side of *parS*1, while spreading out extensively up to 16 Kb away from *parS*. Similar maximum spreading distances along *parS* were determined for the *B. subtilis* ParB homologue Spo0J (Breier and Grossman, 2007). These data show that one *parS* site recruits a considerable amount of ParB and supports the assembly of a ParB-*oriC* complex that is sufficiently large to allow for reliable chromosome partitioning. Strikingly, *C. glutamicum* ParB does not accumulate evenly around *parS*1, since the enrichment signal displays a one-sided shoulder downstream of *parS*1 (**Figure 2.18B**). Moreover, ParB deposition is confined to the same distinct border region downstream of *parS*4 (9 Kb away from *parS*1) that was identified before for wild type cells harboring all *parS* sites, suggesting that DNA properties accounting for ParB propagation are independent of *parS*-distribution along the nucleation zone. This observation was further confirmed by including a mutant that contains chromosomal *parS*1 in combination with the farthermost localized *parS*10 site in ChIP-seq analyses (**Figure 2.18B**). Likewise, ParB spreading was restricted by the same border regions between *parS*4 and *parS*5 and between *parS*8 and *parS*9 (6 Kb away from *parS*10) that were detected in wild type before. Therefore, the striking ParB confinement to distinct nucleation zones is independent of the number and the distribution of *parS* sites along this region.

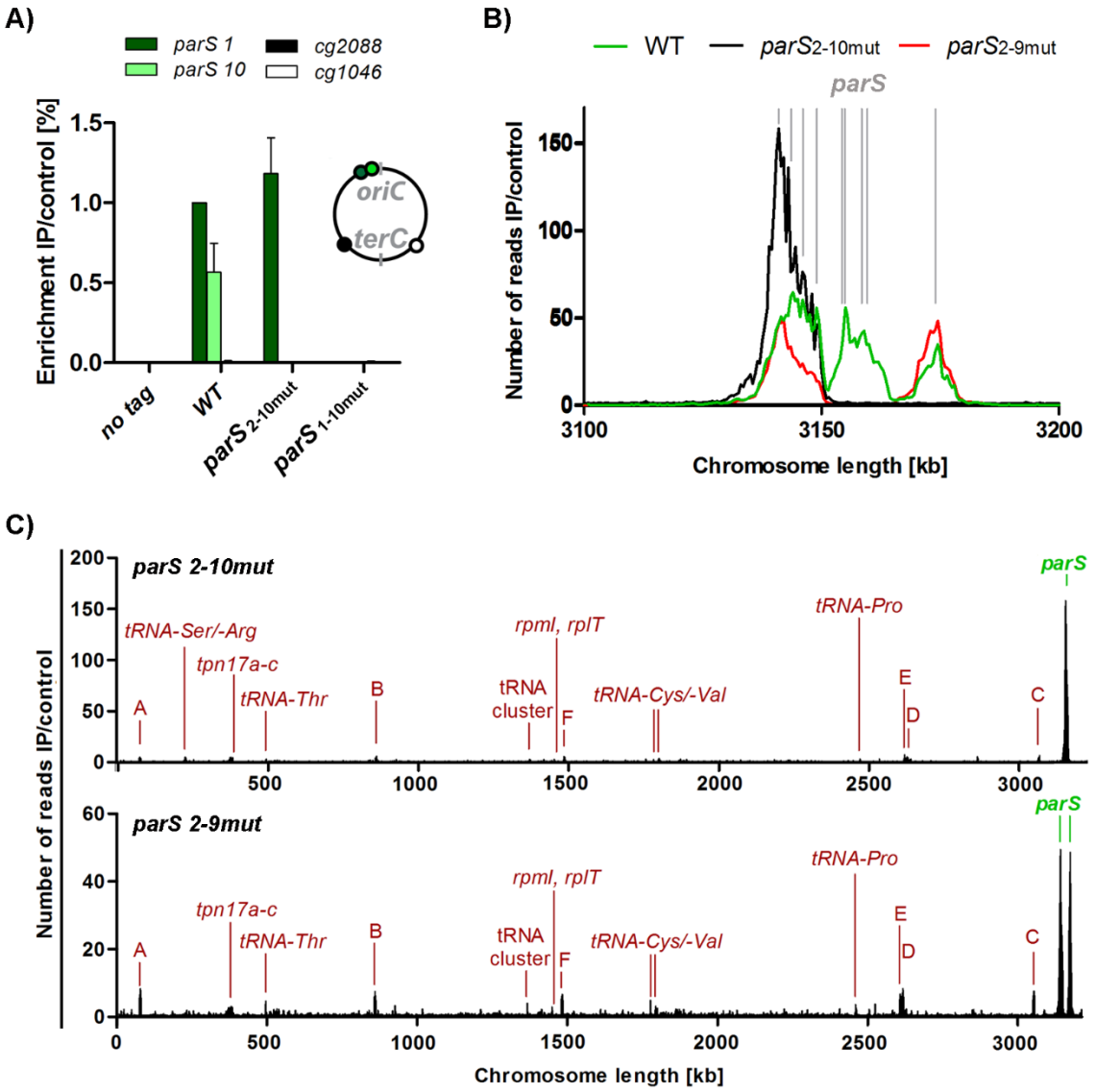

Figure 2.18: Single *parS* sites allow for substantial ParB propagation within distinct zones.

(**A**) ChIP-qPCR for *C. glutamicum* wild type (no tag) and strains harboring ParB-mCherry in wild type (WT, CBK006) and mutant backgrounds with one ($parS_{2\text{-}10mut}$, CBK027) or none *parS* site ($parS_{1\text{-}10mut}$, CBK028) per chromosome; data are normalized to the wild type signal at locus *parS*1. Error bars indicate standard deviations derived from biological triplicates. (**B**) Comparison of ParB-mCherry propagation in wild type (WT) and mutant cells containing only one *parS* site per chromosome ($parS_{2\text{-}10mut}$, CBK027) or two *parS* sites per chromosome ($parS_{2\text{-}9mut}$, CBK030) by ChIP-seq within chromosomal range of 3.1 - 3.2 Mb; bin size 0.5 Kb. Gray lines indicate positions of *parS* that are present in wild type or mutant chromosomes. (**C**) Whole-genome ParB-mCherry-ChIP-seq analyses of strains *parB::parB-mCherry* $parS_{2\text{-}10mut}$ (CBK029) and *parB::parB-mCherry* $parS_{2\text{-}9mut}$ (CBK030) show fold-enrichments of immunoprecipitation relative to extract samples (IP/control) in 0.5 Kb bins; x-axes *terC*-centered; enrichments at *parS* sites (green) and highly transcribed genes (red) are labeled.

In order to investigate the influence of ParB and *parS* sites on multi-scale chromosome folding in *C. glutamicum*, chromosome conformation capture was performed with a *parB* mutant and strains harboring either one or none *parS* site. **Figure 2.19** pictures contact maps and corresponding differential maps.

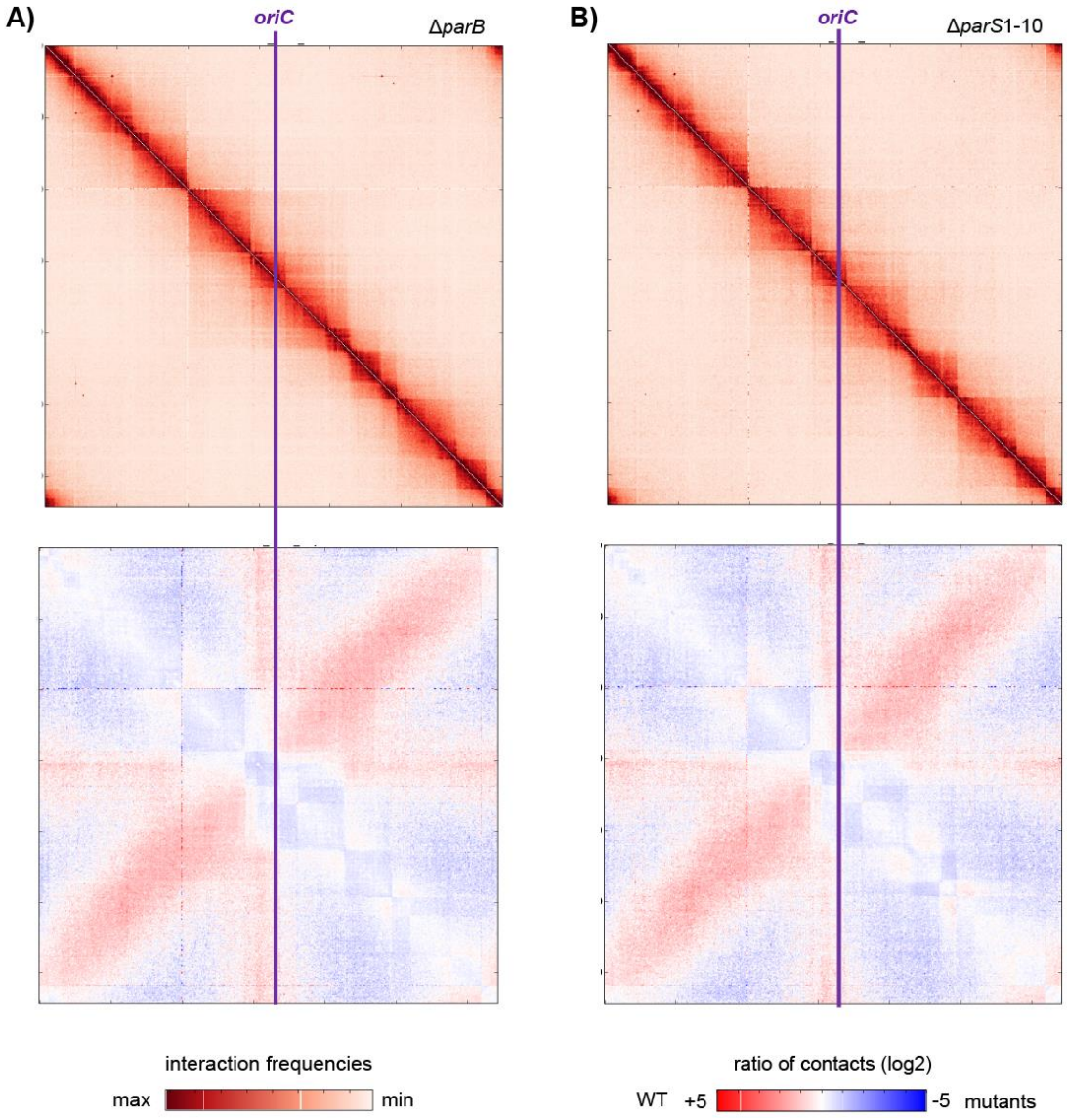

Figure 2.19: Chromosomal replichore cohesion is mediated by ParB-*parS* complexes.

(**A**, **B**) Normalized contact maps of Δ*parB* (CDC003) and $parS_{1\text{-}10mut}$ (CBK024) mutants centered at *oriC*. Contact frequencies are mapped in 5 Kb bins; color codes as in **Figure 2.16** were applied. Differential maps correspond to the log2 of normalized contact frequencies of the wild type relative to the ones of the corresponding mutant strain. Color scales indicate contact enrichment in mutant (blue) or wild type (red, WT); white color indicates no differences between both strains.

This display mode compares chromosomal contact frequencies to the one in wild type maps, where signals that are lost in mutants are depicted in red and signals that are overrepresented in mutant chromosomes are shown in blue. Deletion of *parB* (**Figure 2.19A**) and mutation of all *parS* sites (**Figure 2.19B**) result in comparable DNA folding patterns, causing the following changes in chromosomal contact frequencies compared to wild type cells. First, the secondary diagonal is absent in both mutant contact maps, indicating an unfolding of chromosomal arms in absence of ParB or *parS* sites. Second, horizontal and vertical lines that cross each other at *parS* sites are equally missing in these two contact maps, reflecting the lack of ParB-*parS* cluster generation and segregation along the nucleoid.

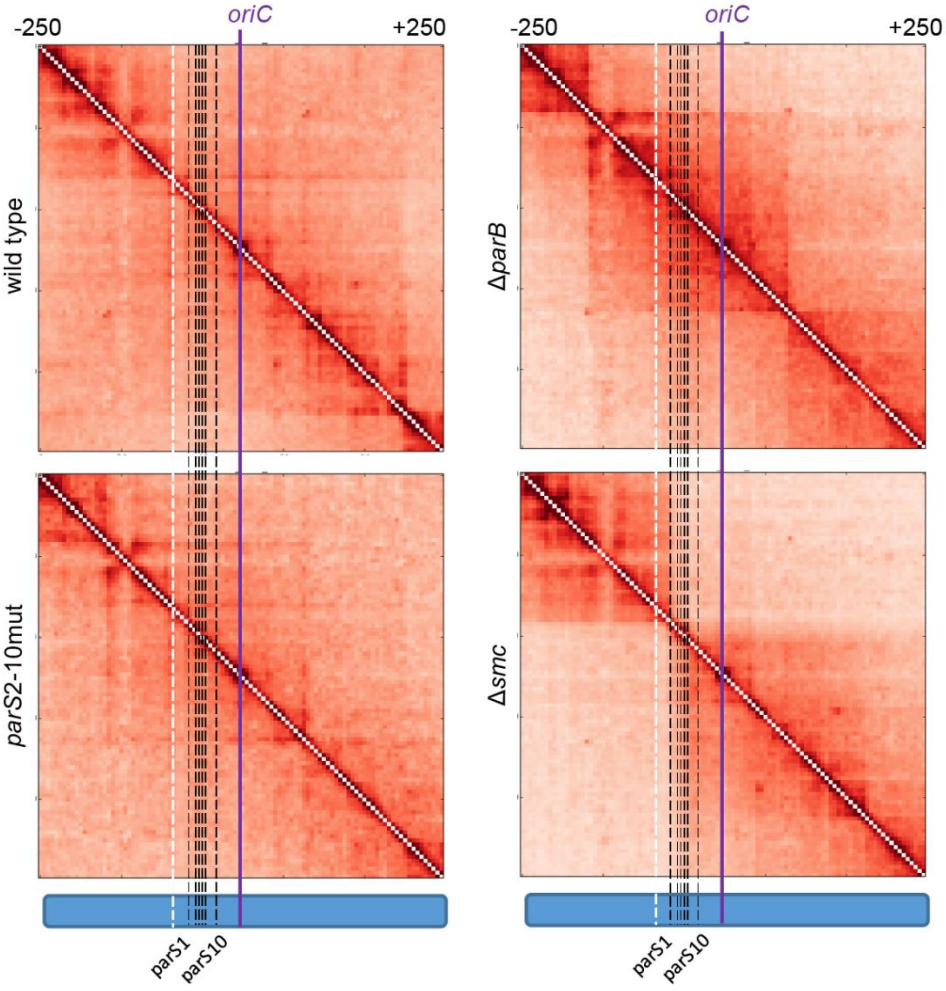

Figure 2.20: Restructuring of the *oriC* domain in *C. glutamicum* mutant strains.

Magnifications encompassing 250 Kb regions surrounding *oriC* of genomic contact maps shown in **Figure 2.16**, **Figure 2.19**, **Figure 2.21** and **Figure 2.32**; *parS* sites and location of SMC-roadblock (described in chapter **2.4.3**) are indicated by black and white dashed lines, respectively.

Lastly, the level of short-range contacts within interaction domains surrounding *oriC* appears to be increased in mutant chromosomes (**Figure 2.19**, **Figure 2.20**). These results show that ParB and the *parS* cluster are major structural components in the overall chromosome organization. The combination of both elements recruits downstream factors responsible for chromosome folding emanating from *parS* sites, bridging the two replichores together down to the *terC* region and for the establishment of long-range interactions at loci surrounding *oriC*.

In contrast, cells mutated in *parS*2-10 sequences, but carrying functional *parS*1 display wild type-like chromosomal interaction contacts including a secondary diagonal and *oriC*-segregation signals (**Figure 2.21**). This mutant exhibits only slightly stronger interaction patterns around the *oriC* domain, which appear to be more confined than in wild type (**Figure 2.20**). Therefore, a single *parS* site sustains sufficient ParB-binding for ParB-*parS* complexes formation mediating the zip-up interaction of chromosomal arms and maintaining overall chromosome architecture, yet minor alterations in chromosomal contacts are detectable at *parS*.

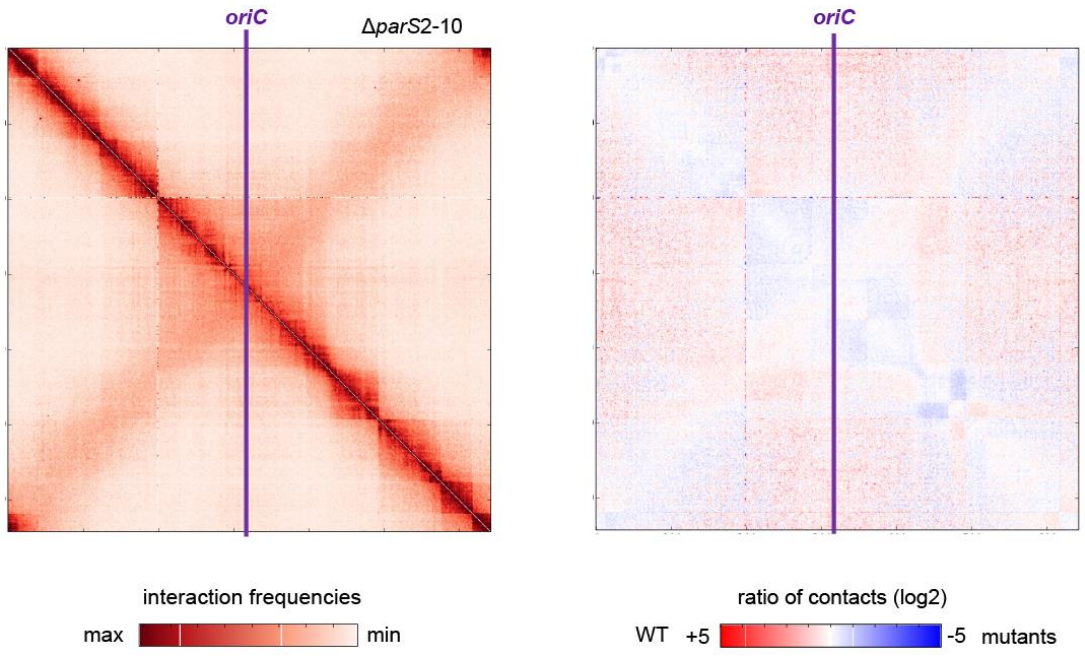

Figure 2.21: Redundancy of *parS* sites in chromosome folding.

Normalized contact map and differential map of mutant $parS_{2\text{-}10mut}$ (CBK023) displayed as in **Figure 2.19**.

2.3.3. Chromosome segregation requires confined *parS*-positioning

Having shown that one *parS* site maintains wild type-like chromosome homeostasis, we further investigated the impact of chromosomal *parS*-positioning on cellular ParB-*parS* localization and on chromosome segregation. A single *parS* site was repositioned at different genomic regions in mutants that otherwise lack *parS* sites at its native locus. Cells harboring an ectopic *parS* site at 9.5°, 90°, 180° or 270° positions relative to *oriC* were viable (**Figure 2.22A**), yet 25 % of DNA-free mini cells were detected in all mutants (**Table S1**). Unlike in cells harboring one *parS* site at its original position, where ParB-*parS* complexes localize to cell poles and division septa, all of these mutant cells distribute ParB foci randomly along their longitudinal cell axis (**Figure 2.22B**). Here, ParB spots commonly appear to have reduced fluorescence intensities compared to the ones in wild type cells and cell poles are frequently devoid of ParB-*parS* complexes. All *parS* mutants further display a cell length phenotype with cell lengths of up to seven micrometers and increased ParB-*parS* foci numbers per cell (**Figure 2.22C, D**), similar to the Δ*parA* phenotype characterized before (see **Figure 2.2**). Therefore, none of these *parS*-shifts restores controlled nucleoid segregation, while the severity of chromosome segregation defects does not markedly differ amongst varying *parS*-distances from *oriC*. The number of ParB foci nevertheless correlate well to cell length (**Figure 2.22D**), excluding replication initiation deficiencies. In order to confirm ParB recruitment by aberrant *parS* sequences, we exemplarily detected ParB-binding to a *parS* sequence located at the 90° chromosomal position (locus *cg0904*, strain CBK042) by ChIP-seq. ParB deposition was identified in a comparably little range of 9 Kb on either side of *parS* (**Figure 2.22E, F**), which covers approximately only half the ParB propagation-distance determined for cells harboring one *parS* at its native locus.

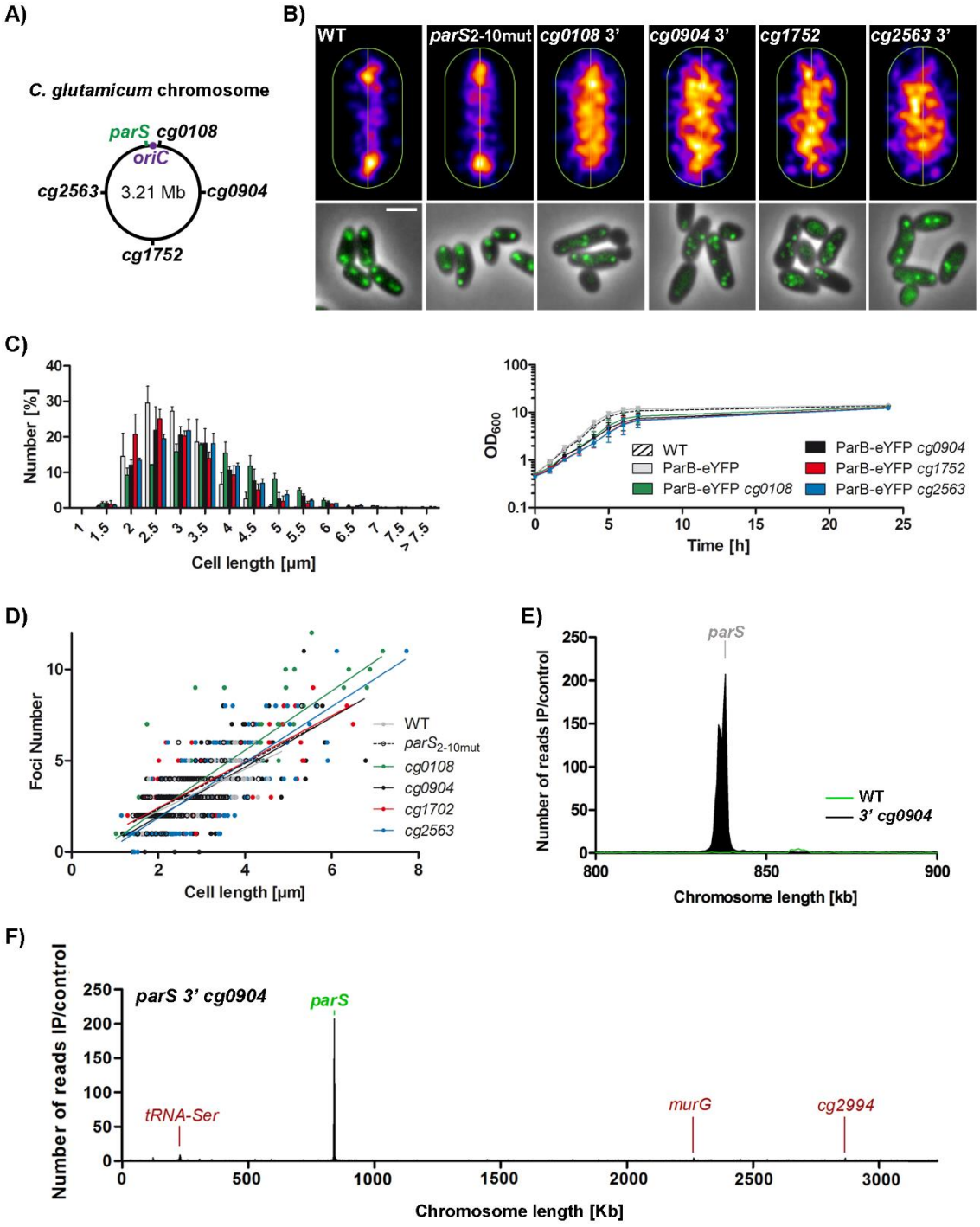

Figure 2.22: The genomic positioning of *parS* impacts on chromosome segregation.

(**A**) Scheme of chromosomal *parS* insertions with native *parS* cluster shown in green and *parS* shifted to intergenic regions 3' of *cg0108*, 3' of *cg0904*, 3' of *cg2563* or *cg1705::parS* (CBK040, CBK041, CBK043, CBK044). (**B**) Top: Average cellular ParB-eYFP fluorescence normed to cell length illustrated via MicrobeJ (Ducret et al., 2016) as heat maps for wild type (WT, CBK007), for cells harboring one *parS* site ($parS_{2\text{-}10mut}$, CBK025) and for above-named mutant cells; color scale indicates low (blue) to high fluorescence intensities (yellow); n > 250. Below: ParB-eYFP fluorescence (green) merged with phase contrast images of representative cells named above. Scale bar, 2 µm. (**C**) Cell length distributions and growth rates in above-

named strains, growth rates: wild type (μ = 0.57 h^{-1}), ParB-eYFP (μ = 0.61 h^{-1}), ParB-eYFP *parS* 3' *cg0108* (μ = 0.46 h^{-1}), ParB-eYFP *parS* 3' *cg904* (μ = 0.46 h^{-1}), ParB-eYFP *cg1752* (μ = 0.40 h^{-1}), ParB-eYFP *parS* 3' *cg2563* (μ = 0.41 h^{-1}). (**D**) Dependence of ParB-*parS* cluster numbers on cell length in strains named in (**B**), n > 150. Linear regression lines are shown; r (WT) = 0.71, r ($parS_{2\text{-}10mut}$) = 0.74, r (*cg0108*) = 0.86, r (*cg0904*) = 0.68, r (*cg1752*) = 0.75, r (*cg2563*) = 0.79. (**E**) ChIP-seq of ParB-mCherry in strain CBK042, harboring *parS* 3' of *cg0904* and in wild type (CBK006). ParB enrichment signals are displayed in 0.5 Kb bins within the 0.8 - 0.9 Mb chromosomal range. (**F**) Whole-genome ChIP-seq data of analysis show described in (**E**), x-axis *terC*-centered; enrichments at *parS* site (green) and other genes (red) are labeled.

We next investigated the effect of misplaced *parS* to the 90° genomic position on overall chromosome folding by conformation capture analysis. The resulting contact map features a secondary diagonal, which crosses the primary one at the position of the aberrant *parS* site on the right chromosomal arm (**Figure 2.23**). Therefore, ParB recruitment promotes folding of the chromosomal arms emanating from this position as well as local folding of the chromosome, shown by the formation of one large interaction domain surrounding *parS*. However, this loading appears insufficient to fold the whole chromosome and to cohese the two chromosome arms over their entire length. DNA topology and overall chromosomal localization might hereby determine *parS*-distant ParB-DNA interaction.

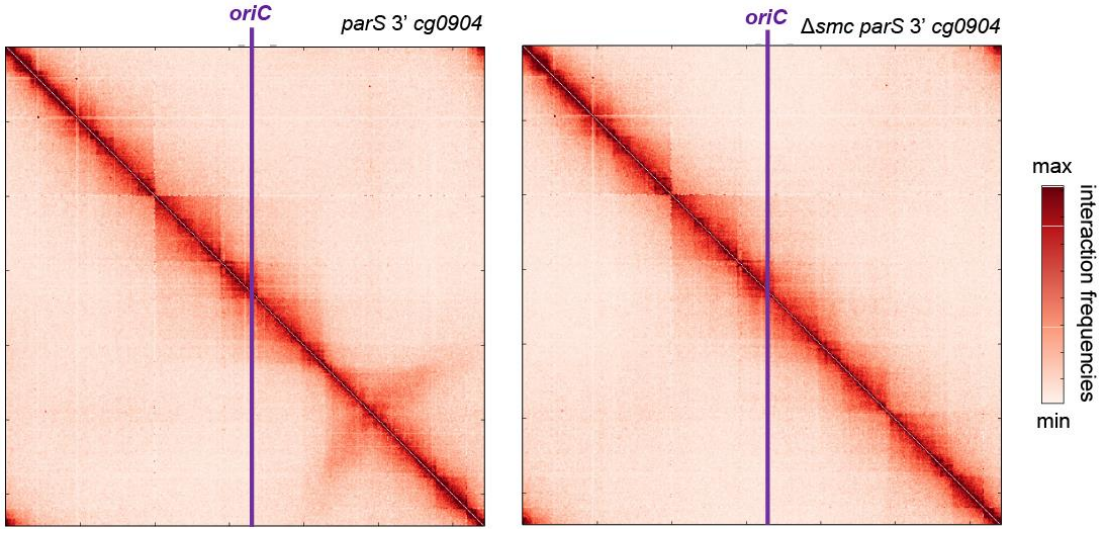

Figure 2.23: Folding of chromosomal arms emanates from genomic *parS* position.

Normalized contact maps of cells containing a single *parS* motif per chromosome, inserted *3'* of *cg0904* in a wild type (CBK037) and in a Δ*smc* background (CBK046). Chromosomal contacts are displayed as described before.

Moreover, the secondary diagonal rather presents a "bow shape" motif bent towards the *terC* region. This pattern reflects an asymmetry in arm interaction, which has been shown before in *B. subtilis* and *C. crescentus* (Tran et al., 2017; Wang et al., 2015). Here, zip-up of chromosomal arms originating from *oriC*-distal loci was assumed to be attenuated by conflicts with transcription of highly expressed genes that are to large parts co-oriented with replication. Upon deletion of SMC, a downstream factor of ParB-*parS* characterized in detail later on, this chromosomal interaction motif is lost (**Figure 2.23**). Besides this, similar to wild type faint horizontal and vertical lines cross each other at the misplaced *parS* site, indicating the formation of contacts between DNA loci at ParB-*parS* with the rest of the chromosome. These data show that *parS* sites located at any chromosomal position can recruit ParB to a certain extent that may partially recover typical features of chromosome folding emanating from the genomic *parS* position. Nonetheless, none of the *parS*-shifts analyzed here restores controlled chromosome segregation, which is likely dependent on *parS*-positioning to a confined *oriC*-proximal region.

2.3.4. ParB sub-clusters reflect propagation zones along *parS* sites

Apart from ChIP-seq assays, we aimed to directly characterize *oriC* domain structuring based on ParB-*parS* interactions by application of photoactivated localization microscopy (PALM). PALM microscopy was performed in collaboration with Giacomo Giacomelli (AG Bramkamp, LMU Munich). Here, we visualize individual ParB-PAmCherry molecules with nanometer resolution in mutant cells, which harbor one, two or all *parS* sites at their native genomic loci. PALM unveiled distinct ParB-dense regions at cell poles and cell quarter positions, similar to foci observed via diffraction limited epifluorescence microscopy (**Figure 2.24**). These ParB-enriched regions (macro-clusters) are characterized by heterogeneous densities, each containing variable numbers of higher density zones (sub-clusters). Macro- and sub-clusters have been identified via the Optics algorithm (Ankerst et al., 1999; Team, 2014). For detailed parameters and workflow of cluster analysis see Materials and Methods.

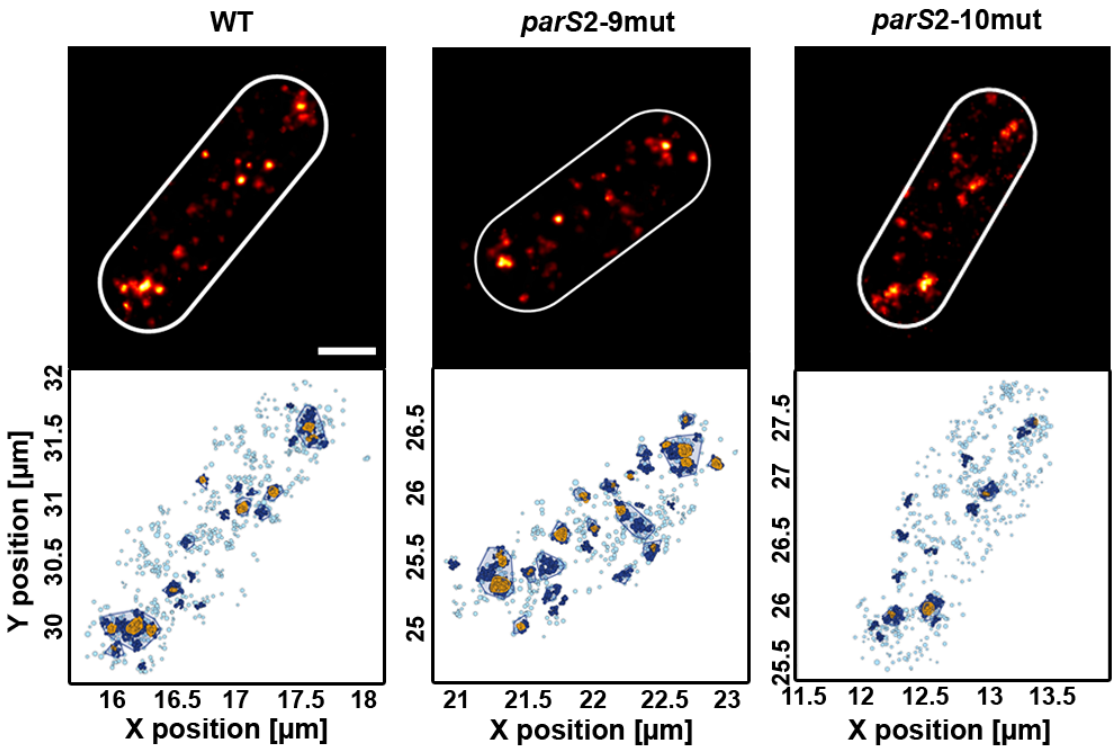

Figure 2.24: ParB-nucleoprotein complexes are sub-structured into ParB-dense clusters.

Single-molecule localization microscopy of representative wild type, *parS*$_{2\text{-}9mut}$ and *parS*$_{2\text{-}10mut}$ cells harboring ParB-PAmCherry (CBK009, CBK029, CBK031). Top: Gaussian rendering of ParB-signals (0.71 point spread function (PSF), 1 px = 10 nm), below: Color-coded representation of ParB-events within corresponding cells with macro-clusters (dark blue), sub-clusters (yellow) and events that are outside of dense clusters (light blue) being indicated. Scale bar, 0.5 µm.

Colocalization of *oriC*s may occur in fast-growing cells due to high chromosome numbers per cell (Böhm et al., 2017). In order to estimate ParB clusters more accurately, we performed PALM analysis using slow-growing cells with significantly fewer macro-clusters per cell (**Figure 2.25A**). Besides this, segregation of *oriC* complexes might alter their DNA compaction and thus, we restrict analyses on the two biggest macro-clusters per cell, which are commonly the ones being stably tethered to cell poles.

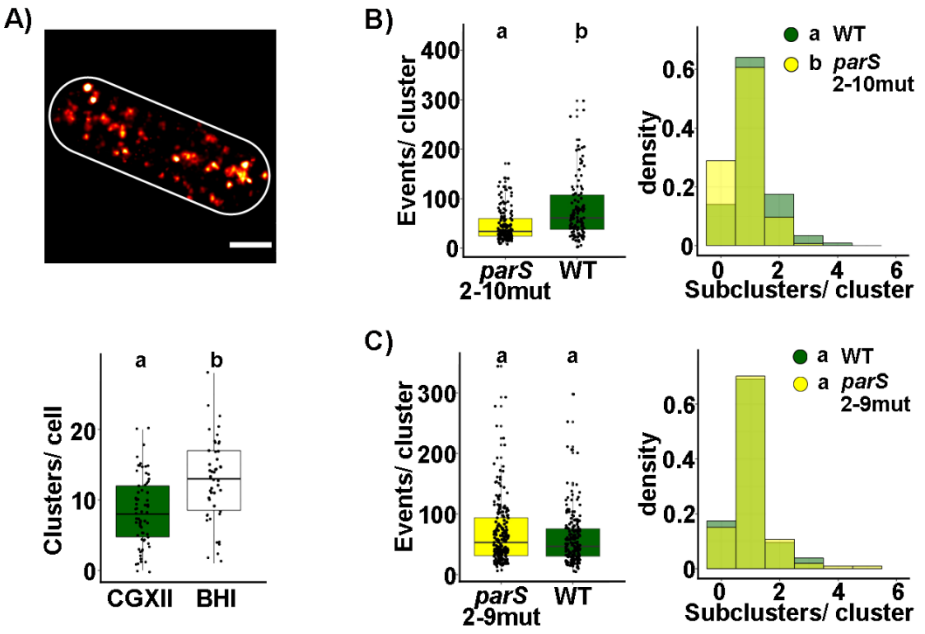

Figure 2.25: ParB sub-clusters reflect ParB deposition at *parS* sites.

(**A**) Top: Gaussian rendered PALM microscopy image (0.71 PSF, 1 px = 10 nM) exemplifying ParB-PAmCherry localization in fast-grown cell (CBK009). Scale bar, 0.5 µm. Below: Significantly more ParB macro-clusters are present in fast- (BHI) compared to slow-growing cells (CGXII) indicated by letters above data sets, (H test: chi-squared = 5.6107, df = 1, $p < 0.05$, $cells_{BHI}$: n = 47, $cells_{CGXII}$: n = 68). (**B**) ParB-PAmCherry events within each of the two biggest macro-cluster per cell (n > 100). Left: Solid lines indicate medians; whiskers mark 1.5 interquartile ranges. Macro-cluster sizes differ significantly between wild type (WT) and $parS_{2\text{-}10mut}$ (H test: chi-squared = 27.582, df = 1, $p < 0.05$). Right: Sub-cluster numbers per macro-cluster shown as overlay bar charts. Significantly more sub-clusters are present in wild type compared to $parS_{2\text{-}10mut}$ macro-clusters (H test: chi-squared = 12.284, df = 1, $p < 0.05$). (**C**) Cluster analysis as depicted in (**B**): No difference is detected in cluster size between wild type and $parS_{2\text{-}9mut}$ mutant cells (H test: chi-squared = 1.7848, df = 1, p = 0.18) and H test yielded no significant differences of sub-cluster numbers amongst both strain backgrounds (chi-squared = 0.38145, df = 1, p = 0.54).

The amount of ParB contained within each macro-cluster in a wild type background is significantly higher than the one observed in cells containing a single *parS* site (**Figure 2.25B**). These data are in line with the varying ranges of ParB propagation observed via Chip-seq for corresponding strains. PALM analysis of sub-cluster numbers per macro-cluster further reflects zones of ParB deposition revealed by ChIP-seq. In particular, multiple ParB nucleation zones are present on wild type chromosomes, while a single propagation zone forms in presence of one *parS* site shown before by ChIP-seq (**Figure 2.18B**). Accordingly, significantly higher sub-cluster numbers are found per wild type than per mutant macro-cluster, where the fraction of macro-clusters consisting of only one sub-cluster is markedly increased in the mutant strain (**Figure**

2.25B). However, these differences cannot be observed when comparing cells harboring all or two *parS* sites (**Figure 2.25C**), indicating that variances in ParB-recruitment and complex formation between these two strains are too little to be differentiated microscopically. Note that repetition of analyses including all macro-clusters per cell yield comparable differences between wild type and both *parS* mutant strains (**Figure 2.26A**, **B**).

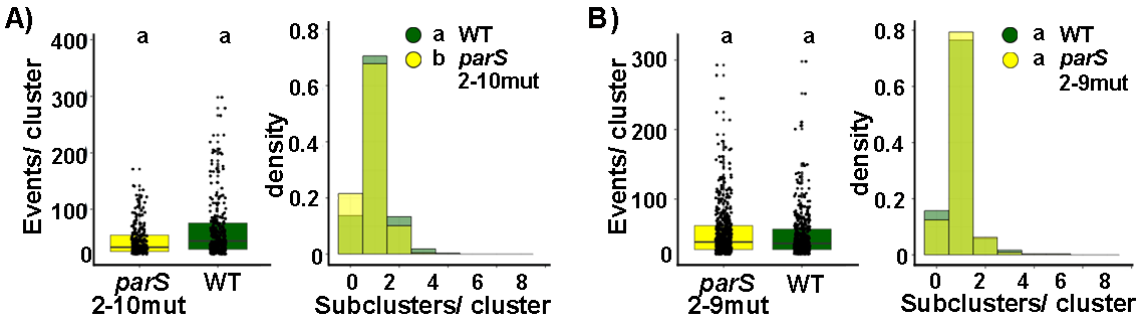

Figure 2.26: Analyses of all ParB macro-clusters per cell in *parS* mutants.

(**A**) ParB cluster-properties of wild type and $parS_{2\text{-}10mut}$ cells (CBK009, CBK029) including all macro-clusters per cell. Mean macro-cluster size (left, H test: chi-squared = 18.923, df = 1, p-value < 0.05) and sub-cluster numbers per macro-cluster (right, H test: chi-squared = 6.8861, df = 1, p < 0.05) are significantly higher in presence of all *parS* sites. (**B**) ParB clusters per cell compared between wild type and $parS_{2\text{-}9mut}$ mutant (CBK031). Differences of events per macro-clusters (left, H test: chi-squared = 1.9737, df = 1, p-value = 0.16) or sub-cluster numbers per macro-cluster (right, H test: chi-squared = 1.5435, df = 1, p-value = 0.2141) amongst strain backgrounds are not significant.

These observations can explain the differences between contact matrices shown before (**Figure 2.20**, **Figure 2.21**), where an enhanced *oriC*-structuring appears in the mutant strain containing one *parS* site compared to the *oriC* domain of the wild type. We conclude a *parS*-dependent sub-structuring of *C. glutamicum* partition complexes.

2.4. Functional characterization of two condensin paralogs

Apart from *oriC*-organizing ParB clusters, most bacteria rely on condensin complex SMC/ScpAB and enterobacteria on the complex MukBEF to structure their chromosomes. Condensin-mediated nucleoid folding just started being characterized (Lioy et al., 2018; Marbouty et al., 2015;

Wang et al., 2015), while an additional condensin MksBEF of yet unknown function was recently identified in a fraction of bacterial genomes (Petrushenko 2011). Accordingly, we identified two condensin complexes in *C. glutamicum*. Since SMC contributes cooperatively with ParB-*parS* complexes to structure chromosomes in *B. subtilis* and *C. crescentus* (Marbouty et al., 2015; Tran et al., 2017; Wang et al., 2015), we further challenged their interaction with ParB. Moreover, roles in genome folding are described in the following, where we characterize fundamental differences in function between both complexes.

2.4.1. Identification of SMC/ScpAB and MksBEFG complexes

Condensin complexes are key chromosome organizing structures in standard model organisms like *B. subtilis* and *E. coli* (Lioy et al., 2018; Wang et al., 2015). However, condensins of *C. glutamicum* had not been studied yet. A sequence homology search pointed to the co-existence of both SMC/ScpAB and MksBEFG in *C. glutamicum*. Their genomic coding regions are illustrated in **Figure 2.27A**: the SMC/kleisin complex is encoded by *cg2265* (*smc*), *cg1611* (*scpA*) and *cg1614* (*scpB*), whereas *mks* subunits are organized in a conserved operon structure as described before (Petrushenko et al., 2011) comprising genes *cg3103-cg3106* (*mksGBEF*). Notably, subunit *mksG* may not always be present in bacterial *mks* operons and was suggested to act in complex with MksBEF (Petrushenko et al., 2011). In *C. glutamicum* the coding region for an adenosylhomocysteine nucleosidase (*cg3102*) involved in methionine metabolism is part of the operon.

To characterize condensin complex formation *in vivo*, we combined co-immunoprecipitations of SMC and MksB with mass spectrometry. Mass spectrometry was performed in collaboration with Dr. Andreas Schmidt and Prof. Dr. Axel Imhof from the Biomedical Center in Munich. Here, whole cell lysates containing SMC-mCherry and MksB-mCherry baits were utilized in anti-mCherry pull-down experiments. Cell lysate comprising free mCherry was included as negative control. Stability of fluorescent fusion proteins and absence of growth phenotypes in both mutant strains were confirmed (**Figure 2.27B**, **C**). Kleisin subunit ScpA and the accessory ScpB co-precipitated in significant amounts with SMC compared to the negative control (**Figure 2.27D**). Likewise, subunits MksF and MksE, but not MksG, were substantially enriched in the pull-down experiments with MksB (**Figure 2.27D**).

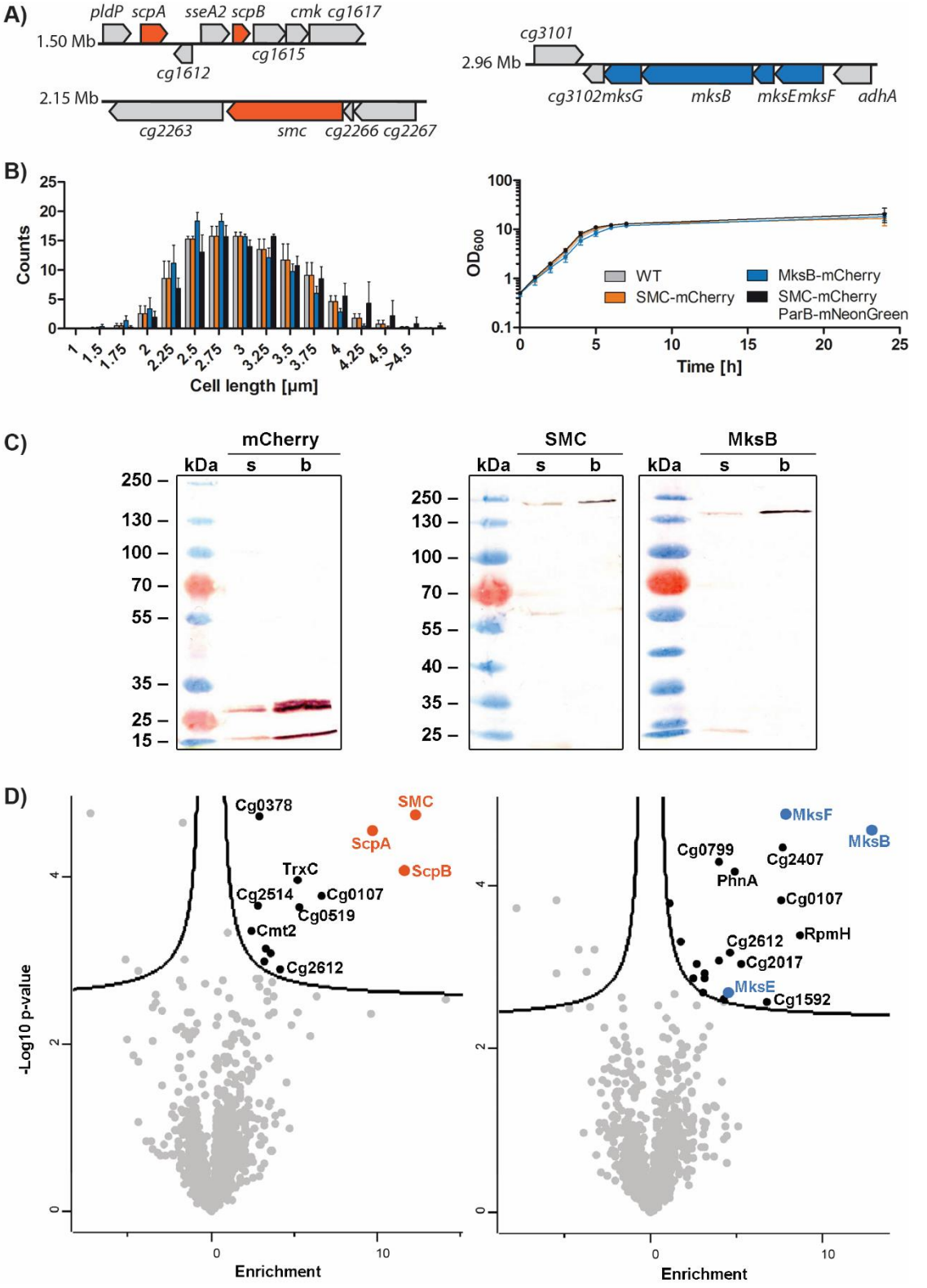

Figure 2.27: Identification of two condensin paralogs in *C. glutamicum*.

(**A**) Chromosomal loci of *C. glutamicum* coding for condensin subunits. (**B**) Cell length distributions and growth curves of BHI-grown *C. glutamicum* strains: wild type ($\mu = 0.64\ h^{-1}$), SMC-mCherry ($\mu = 0.67\ h^{-1}$, CBK012), MksB-mCherry ($\mu = 0.60\ h^{-1}$, CBK015), SMC-mCherry ParB-mNeonGreen ($\mu = 0.68\ h^{-1}$,

CBK013). Values derive from triplicates; standard deviations are displayed (n > 1000). (**C**) Immunoprecipitated full length protein fusions were validated via western blots, showing SMC-mCherry (155 kDa, CBK012), MksB-mCherry (151 kDa, CBK015) and mCherry (26.7 kDa, CBK052) in whole cell lysate of respective *C. glutamicum* strains. 10 µl magnetic RFP-Trap® beads (b) and 10 µl supernatant (s) were loaded, proteins were detected using α-mCherry antibody with identical incubation times for all experiments. (**D**) Anti-mCherry co-immunoprecipitations of condensin core subunits SMC-mCherry and MksB-mCherry combined with mass spectrometry reveal condensin subunit interactions. Cell lysates of CBK012, CBK015 and of the negative control strain (CBK052) were utilized. Volcano plots picture the difference in mean enrichments plotted against the -log10 adjusted p-value for each protein identified; condensin subunits are highlighted respectively. Cutoff curves indicate significant hits (two-tailed t-test, $p < 0.05$, fold change > 0.1).

Notably, the complete lack of MksG in immunoprecipitations may result from a compromised MksBEFG complex formation caused by a functionally impaired MksB-mCherry fusion or from reduced MksG levels due to non-compliance of the *mCherry* insertion with the 5' untranslated region of *mksG*. ParB, which mediates SMC-loading onto DNA in *B. subtilis* and *S. pneumoniae* (Gruber and Errington, 2009; Minnen et al., 2011; Sullivan et al., 2009), was not immunoprecipitated with SMC in any of the experiments. Instead, both SMC and MksB immunoprecipitated with few additional proteins in significant amounts (**Figure 2.27D**, **Table 3**). Those are mainly proteins of unknown function or functions that are not directly linked to DNA homeostasis, like carbon metabolism, cell wall biogenesis and ABC-type transport. Particularly MksB co-immunoprecipitated with proteins involved in amino acid biosynthesis (AnsA, LeuD, NifS2). Whether these proteins are indeed interaction partners of condensin complexes remains to be shown.

Table 3: SMC and MksB co-immunoprecipitate significantly with proteins shown below.

Difference	Protein	Description
SMC immunoprecipitate		
12.32	**SMC**	Chromosome segregation ATPase
11.63	**ScpB**	Kleisin-associated protein
9.75	**ScpA**	Kleisin subunit of SMC
6.69	**Cg0107**	Putative secreted protein
3.60	**Cg0405**	Fe3+-siderophore transport system, secreted component
5.31	**Cg0519**	Putative phosphoglycerate mutase
5.26	**TrxC**	Thioredoxin

4.16	**Cg2612**	Cytokinin riboside 5'-monophosphate phosphoribohydrolase
3.26	**DacB**	Serine-type D-Ala-D-Ala carboxypeptidase
2.89	**Cg0378**	Putative phage-associated protein
3.23	**Cg1065**	ABC-type urea transporter, ATPase component
2.86	**Cg2514**	16S rRNA Methyltransferase
2.41	**Cmt2**	Mycolyltransferase
MksB immunoprecipitate		
12.81	**MksB**	ATPase involved in plasmid restriction
8.68	**RpmH**	50S ribosomal protein L34
7.89	**MksF**	Kleisin subunit of MksB
7.66	**Cg2407**	Uncharacterized protein
7.56	**Cg0107**	Putative secreted protein
6.77	**Cg1592**	Uncharacterized protein
5.23	**Cg2017**	Uncharacterized protein
4.91	**PhnA**	Phosphonoacetate hydrolase
4.60	**Cg2612**	Cytokinin riboside 5'-monophosphate phosphoribohydrolase
4.56	**MksE**	Kleisin-associated protein
4.24	**NifS2**	Cysteine desulfurase
3.96	**AnsA**	L-asparaginase
3.95	**Cg0799**	Conserved hypothetical protein
3.13	**Cmt2**	Mycolyltransferase
3.13	**Pbp**	D-alanyl-D-alanine carboxypeptidase
3.07	**Cg2430**	Uncharacterized protein
2.72	**Rpf2**	Resuscitation-promoting factor
2.50	**Cg2688**	ABC-type molybdenum transporter, ATPase component
1.76	**Cg2906**	Uncharacterized protein
1.14	**LeuD**	3-isopropylmalate dehydratase small subunit

In order to confirm mass spectrometry results bacterial two-hybrid analyses were performed with condensin subunits, ParB, and the polar scaffold DivIVA (**Figure 2.28A**). Our data point at the complex formation of SMC/ScpAB and MksBEFG (**Figure 2.28B**).

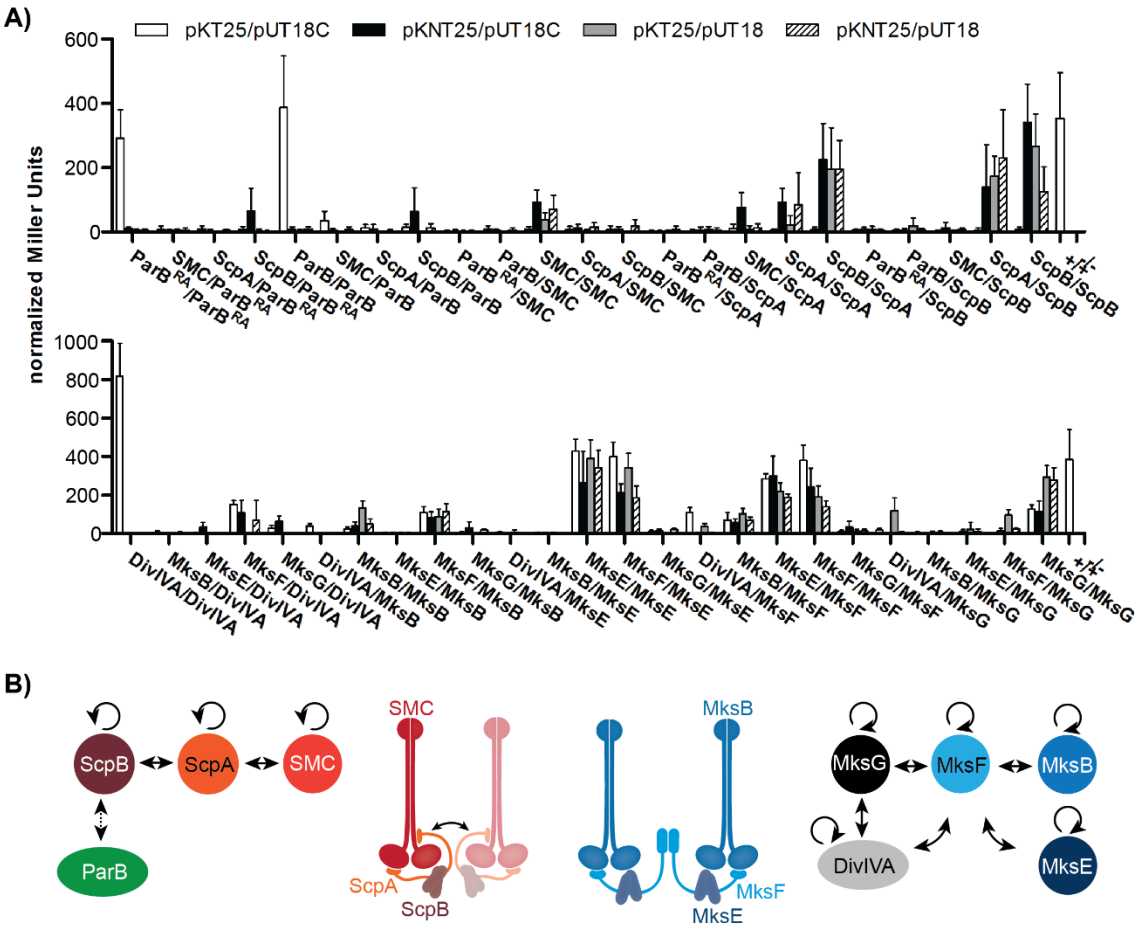

Figure 2.28 Confirmation of condensin complex compositions.

(**A**) Analysis of protein-protein interactions via bacterial two-hybrid screens. Interactions were quantified by β-galactosidase assays in all combinations of hybrid proteins: C/C- (pKT25/pUT18C), C/N- (pKNT25/pUT18C), N/C- (pKT25/pUT18), and N/N- (pKNT25/pUT18) terminal fusions of adenylate cyclase fragments ($ParB^{RA}$: ParB mutant R175A described in chapter **2.4.3**); error bars indicate standard deviations of biological triplicates. (**B**) Illustration of SMC/ScpAB and MksBEFG subunit interactions based on bacterial two-hybrid data; cartoons indicate condensin complex formations.

No significant SMC/ScpAB-ParB interactions were detected. We further observe ScpA-ScpA self-interaction signals well above background, which have not been shown before. Nonetheless, they are in line with a previously suggested handcuffing model in *B. subtilis*, where two SMC/ScpAB complexes might be physically coupled together (Wang et al., 2017). Moreover, MksG connects to the MksBEF complex via interaction with MksF, while MksF and MksG subunits further interact with the *C. glutamicum* polar scaffold protein DivIVA.

2.4.2. SMC mediates replichore-cohesion ParB-dependently

First of all, we aimed to functionally characterize *C. glutamicum* condensin SMC/ScpAB. In *B. subtilis*, absence of SMC leads to failure of chromosome segregation, resulting in a conditionally lethal phenotype, in particular at fast growth (Britton et al., 1998). By contrast, *smc* deletion in *C. glutamicum* did not result in DNA segregation-phenotypes (**Table S1**), similar to *M. smegmatis* or *M. tuberculosis* (Güthlein et al., 2008). Further, growth, cell length distributions and morphologies were comparable to the wild type at slow and fast growth rates (**Figure 2.29A**).

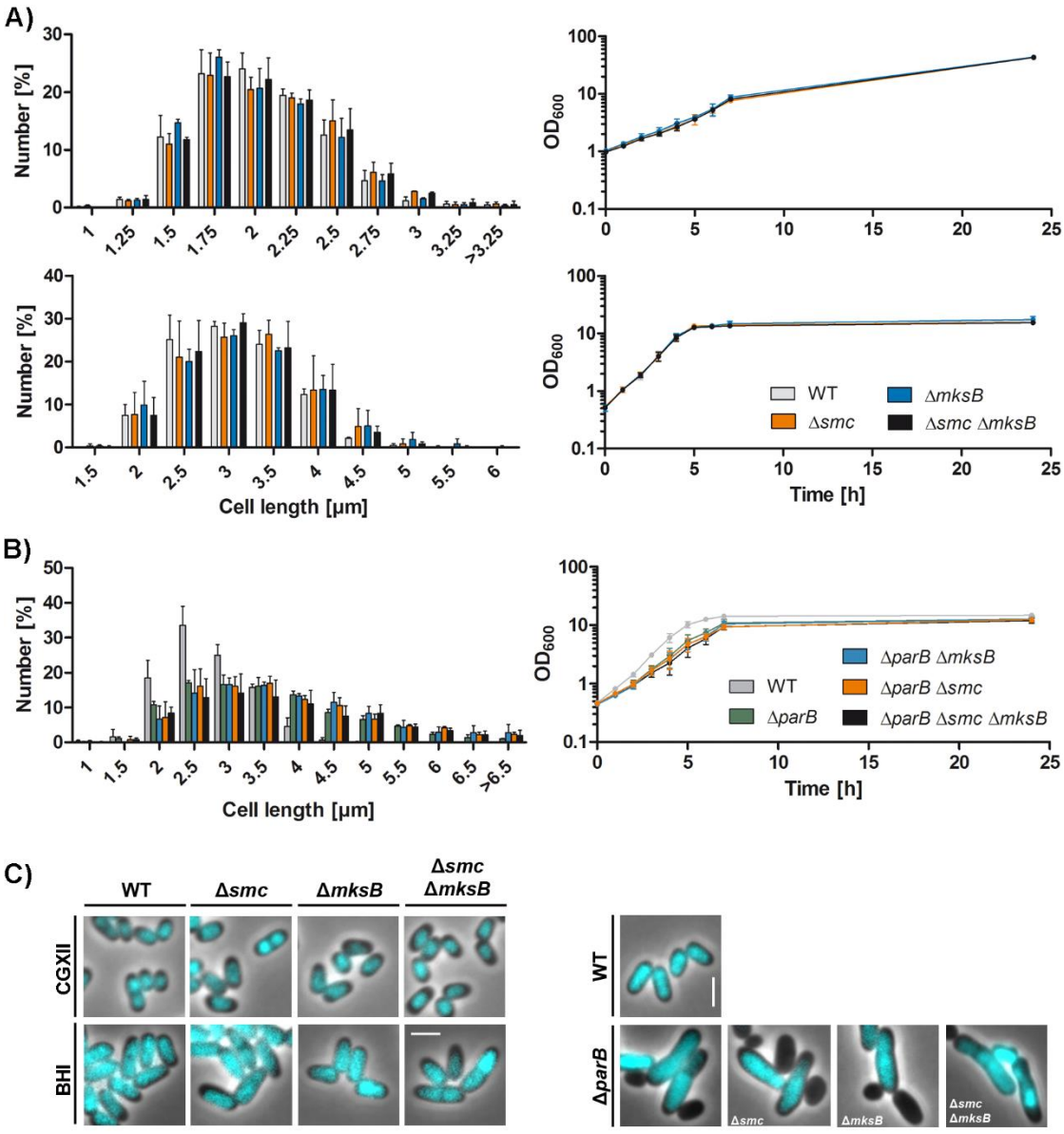

Figure 2.29: Condensin deletions do not impact on chromosome segregation.

(**A**, **B**) Growth curves and cell length distributions (n > 1000) of *C. glutamicum* mutants determined in biological triplicates; error bars indicate standard deviations. (**A**) Growth experiments performed in CGXII medium (top): wild type (μ = 0.26 h^{-1}), Δ*smc* (μ = 0.22 h^{-1}, CDC026), Δ*mksB* (μ = 0.27 h^{-1}, CBK001), Δ*smc* Δ*mksB* (μ = 0.25 h^{-1}, CBK004) and in BHI medium (below): wild type (μ = 0.71 h^{-1}), Δ*smc* (μ = 0.70 h^{-1}), Δ*mksB* (μ= 0.72 h^{-1}), Δ*smc*Δ*mksB* (μ = 0.70 h^{-1}). (**B**) Growth of mutant strains in BHI medium as indicated: wild type (μ = 0.67 h^{-1}), Δ*parB* (μ = 0.51 h^{-1}, CDC003), Δ*parB* Δ*smc* (μ = 0.46 h^{-1}, CBK002), Δ*parB* Δ*mksB* (μ = 0.49 h^{-1}, CBK003), Δ*parB* Δ*smc* Δ*mksB* (μ = 0.43 h^{-1}, CBK005). (**C**) Microscopy images exemplify above-named *C. glutamicum* mutant cells in overlays of Hoechst-stained DNA (cyan) and phase contrast images. Scale bar, 2 μm.

Besides, a *parB smc* double deletion did not exacerbate the *parB* phenotype (**Figure 2.29B**, **C**, **Table S1**). However, the combination of genetic backgrounds *parB::parB-eYFP* and Δ*smc* yield a fraction of 4-5 % anucleate cells (**Table S1**, **Figure 2.30**), indicating that fluorescently tagged ParB is partially impaired in function upon *smc* deletion. Hence, both proteins likely function in the same pathway, whereby *parB* is epistatic to *smc*.

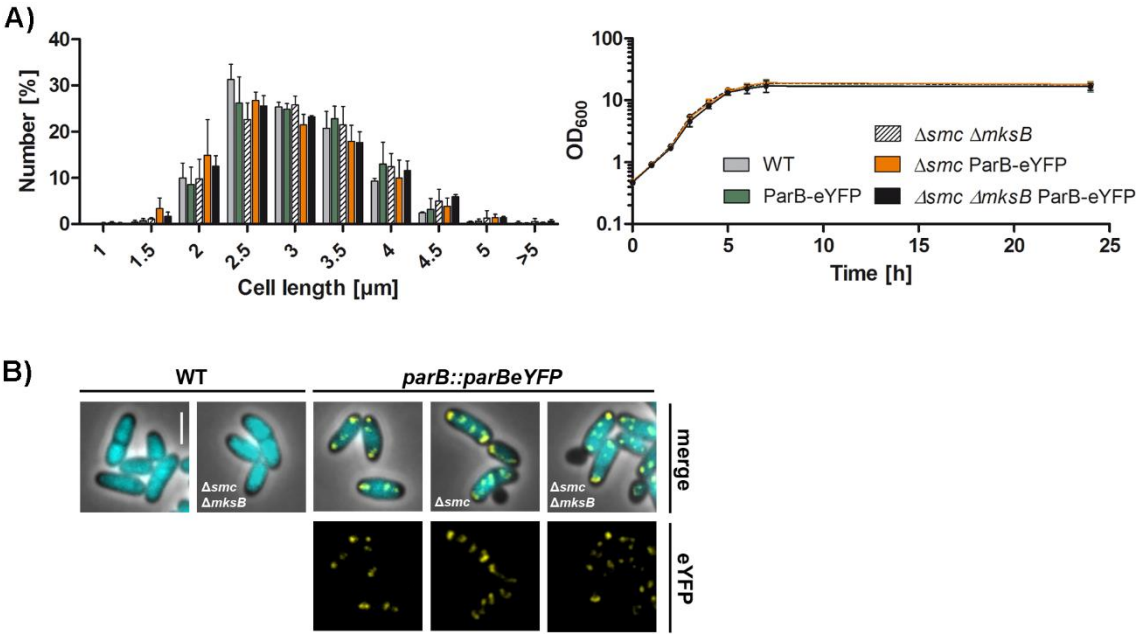

Figure 2.30: Mild *smc*-phenotype in combination with ParB-eYFP modifications.

(**A**) Growth and cell length analysis of *C. glutamicum* Δ*smc* mutants in BHI medium as in **Figure 2.29**; growth rates: wild type (μ = 0.70 h^{-1}), ParB-eYFP (μ = 0.69 h^{-1}, CBK007), Δ*smc*Δ*mksB* (μ = 0.72 h^{-1}, CBK004), Δ*smc* ParBeYFP (μ = 0.70 h^{-1}, CBK010), Δ*smc* Δ*mksB* ParBeYFP (μ = 0.71 h^{-1}, CBK011). (**B**) Microscopy images of strains characterized in (**A**) showing overlays of DNA stained with Hoechst (cyan), phase contrast and ParB-eYFP fluorescence (yellow). The YFP channel is additionally depicted in separate images. Scale bar, 2 μm.

In order to further investigate whether SMC functionally interacts with ParB in regulating chromosome organization, we determined cellular localization of SMC. To this end, a strain harboring a fluorescently tagged SMC-mCherry was imaged, revealing the formation of SMC clusters along the entire longitudinal axis of the cell resembling subcellular localization of ParB-*parS* clusters (**Figure 2.31A**). Therefore, subcellular localizations of SMC and ParB foci were analyzed in a strain carrying allelic replacements of both proteins by fluorescent fusions (**Figure 2.31B**) that harbors a wild type-like growth and cell length phenotype (**Figure 2.27B**, **Table S1**). Here, ParB-mNeonGreen and SMC-mCherry clusters are often proximal but do not co-localize, while foci numbers correlate with cell length in each case. Up to eight SMC-mCherry spots were detected per cell, yet on average cells contained fewer SMC clusters than ParB-*parS* complexes (**Figure 2.31B**, **C**).

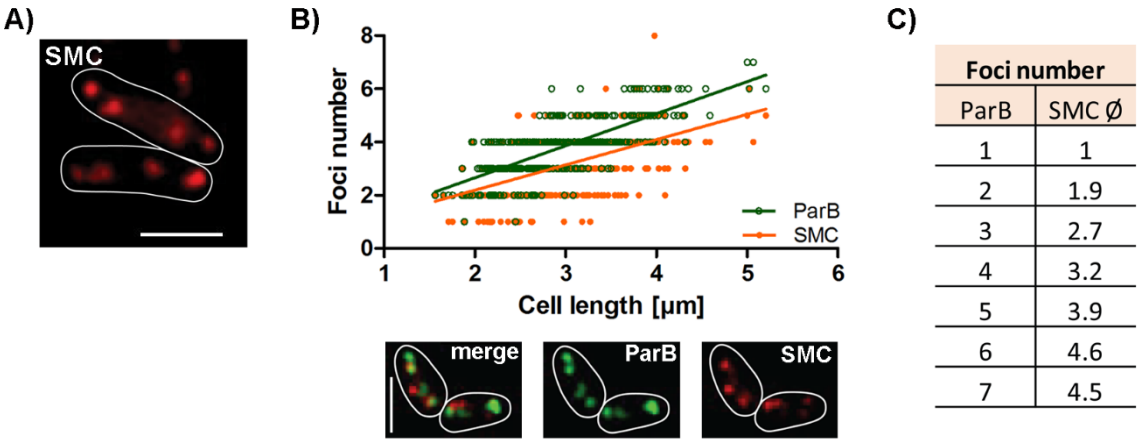

Foci number	
ParB	SMC Ø
1	1
2	1.9
3	2.7
4	3.2
5	3.9
6	4.6
7	4.5

Figure 2.31: SMC accumulates ParB-like in distinct foci along the longitudinal cell axis.

(**A**) Microscopy image exemplifies localization of cellular SMC-mCherry fluorescence (red) in *C. glutamicum* strain CBK012; white lines indicate cell outlines. Scale bar, 2 µm. (**B**) Localization analysis of SMC-mCherry and ParB-mNeonGreen in strain CBK013. Left: SMC and ParB foci numbers positively correlate with cell length, r(ParB) = 0.74, r(SMC) = 0.53; n > 350. Right: Subcellular localization of ParB and SMC is shown in representative cells as overlays of mNeonGreen and mCherry fluorescence and in separate channels. Scale bar, 2 µm. (**C**) Average SMC-mCherry foci numbers in dependence of ParB-mNeonGreen clusters per cell (CBK013, n > 200).

Finally, we generated chromosome conformation contact maps of the *smc* mutant (**Figure 2.32A**) to analyze the role of condensin in overall chromosome folding. Deletion of *smc* leads to a loss of the secondary diagonal. Moreover, we noticed the formation of a clear boundary at the *parS*

cluster in absence of SMC (**Figure 2.32A**, **Figure 2.20**). Short-range contacts between genomic loci on the same chromosomal arm remained otherwise largely unaffected (**Figure 2.32A**).

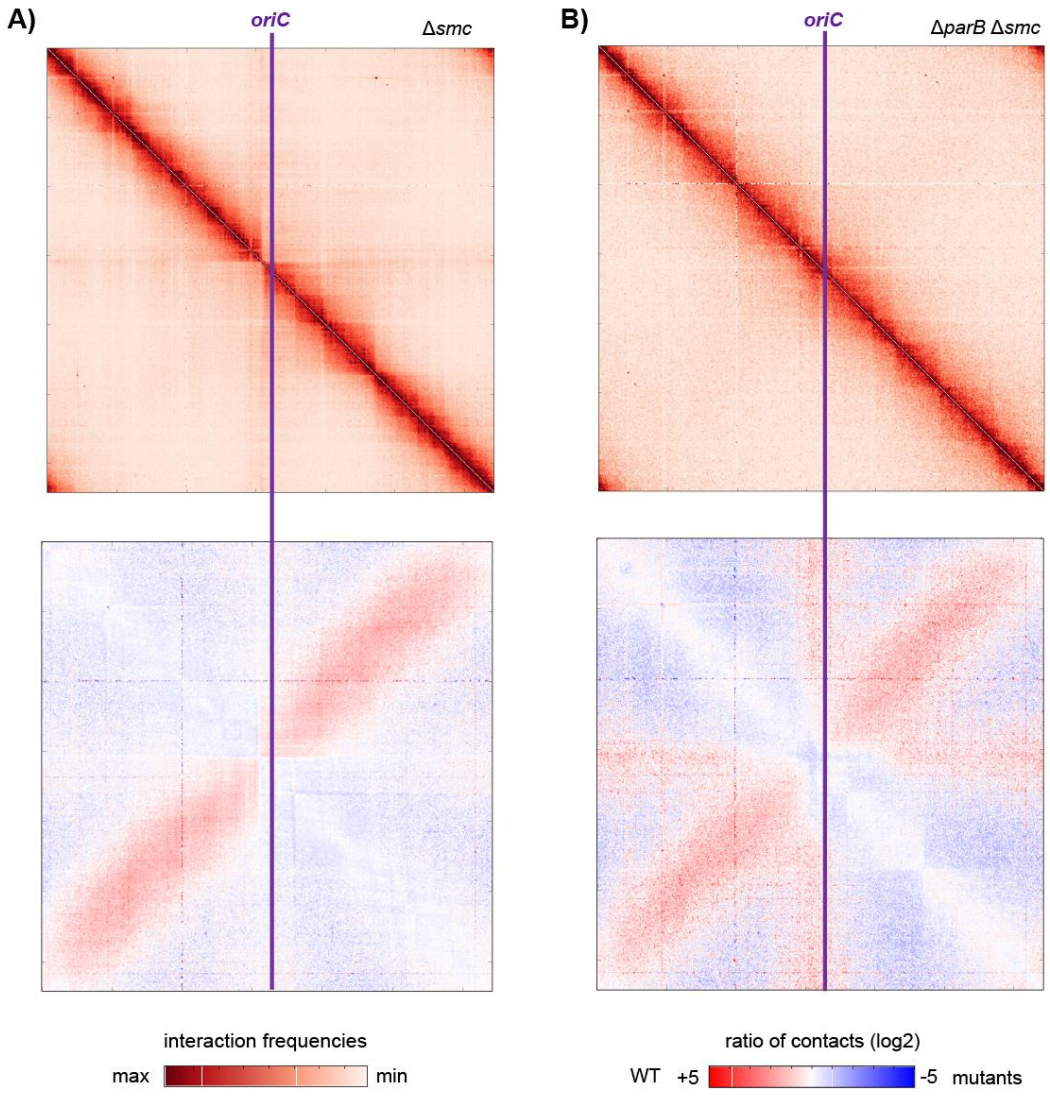

Figure 2.32: Bridging of chromosomal arms requires SMC.

Normalized contact maps of Δ*smc* (CDC026, **A**) and Δ*parB*/Δ*smc* mutants (CBK002, **B**), as shown in **Figure 2.19**. Contacts are binned in 5 Kb; differential maps indicate the log2 of the ratio (wild type normalized/mutant normalized).

The combination of *smc* and *parB* mutations mimics *parB* and *parS* phenotypes described before (**Figure 2.32B**, **Figure 2.19A**, **B**), equally resulting in the loss of chromosomal inter-arm contacts and in the loss of *oriC* interactions with loci along the whole chromosome. Therefore, global *oriC* interactions are solely maintained by ParB-*parS* complex formation, while folding of right and

left replichores is mediated by SMC/ScpAB in concert with ParB. Our data demonstrate that the conserved role for SMC in chromosome organization (Le et al., 2013; Marbouty et al., 2015; Tran et al., 2017; Wang et al., 2015) is also maintained in presence of a second condensin complex.

2.4.3. Chromosomal SMC-loading at ParB-*parS* complexes

Since SMC/ScpAB complexes accumulate ParB-like in several clusters per cell, we next aimed to identify distinct binding sites of SMC-mCherry on the *C. glutamicum* chromosome via anti-mCherry ChIP-seq. In model organisms *B. subtilis*, *C. crescentus* and *S. pneumoniae* SMC is specifically recruited to *parS* sites for chromosomal loading (Gruber and Errington, 2009; Minnen et al., 2011; Tran et al., 2017). Accordingly, whole-genome screens for SMC-binding sites revealed minor SMC enrichment at the *parS*1-10 cluster and in near surroundings, with signals being more than ten-fold lower than detected for ParB-ChIPs (**Figure 2.33**). Most strikingly, a genomic region 13 Kb upstream of *parS*1 recruited a higher amount of SMC than the *parS* cluster (**Figure 2.33**).

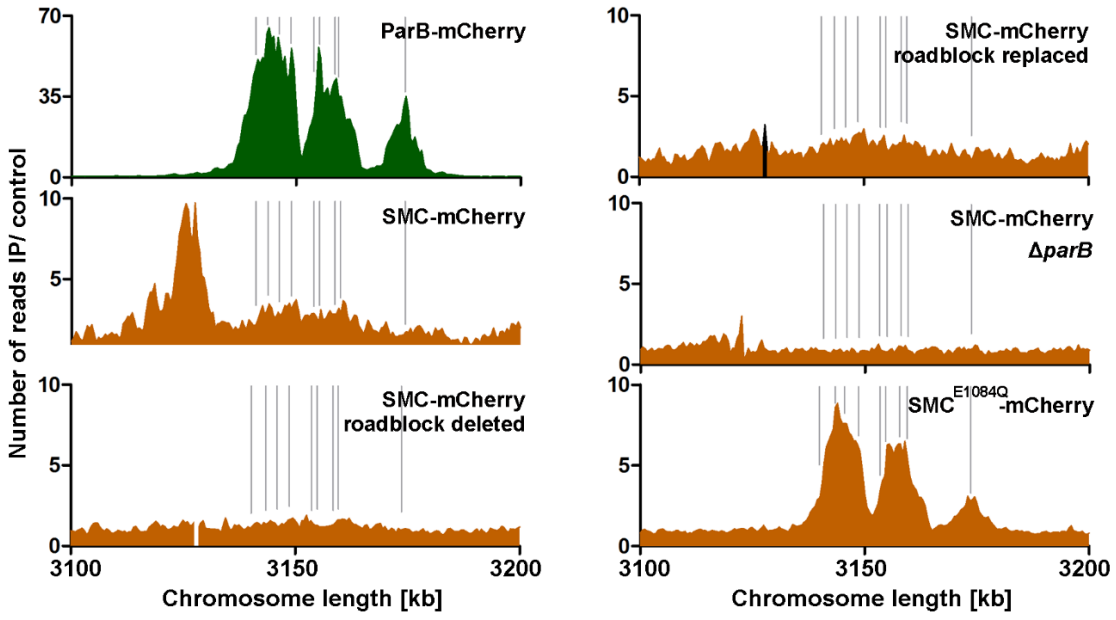

Figure 2.33: SMC loads at ParB-*parS* complexes onto the chromosome.

ChIP-seq of ParB-mCherry (green, CBK006) and SMC-mCherry in strain backgrounds as indicated (orange, CBK012, CBK034, CBK035, CBK014, CBK051). Enrichment signals at *parS* sites (gray lines) are shown in a genomic range of 3.1-3.2 Mb; bin size 0.5 Kb. Signals in black indicate genomic region of DNA replacement.

In order to determine whether this locus directly recruits SMC or whether it blocks relocation of SMC that was initially recruited at *parS*, we mutated this site as follows. The locus was either partially deleted and reinserted at another genomic position (CBK034) or substituted by a random DNA sequence of *B. subtilis* of identical size (CBK035) (**Figure 2.34A**). Both mutants grow and divide wild type-like (**Figure 2.34B**).

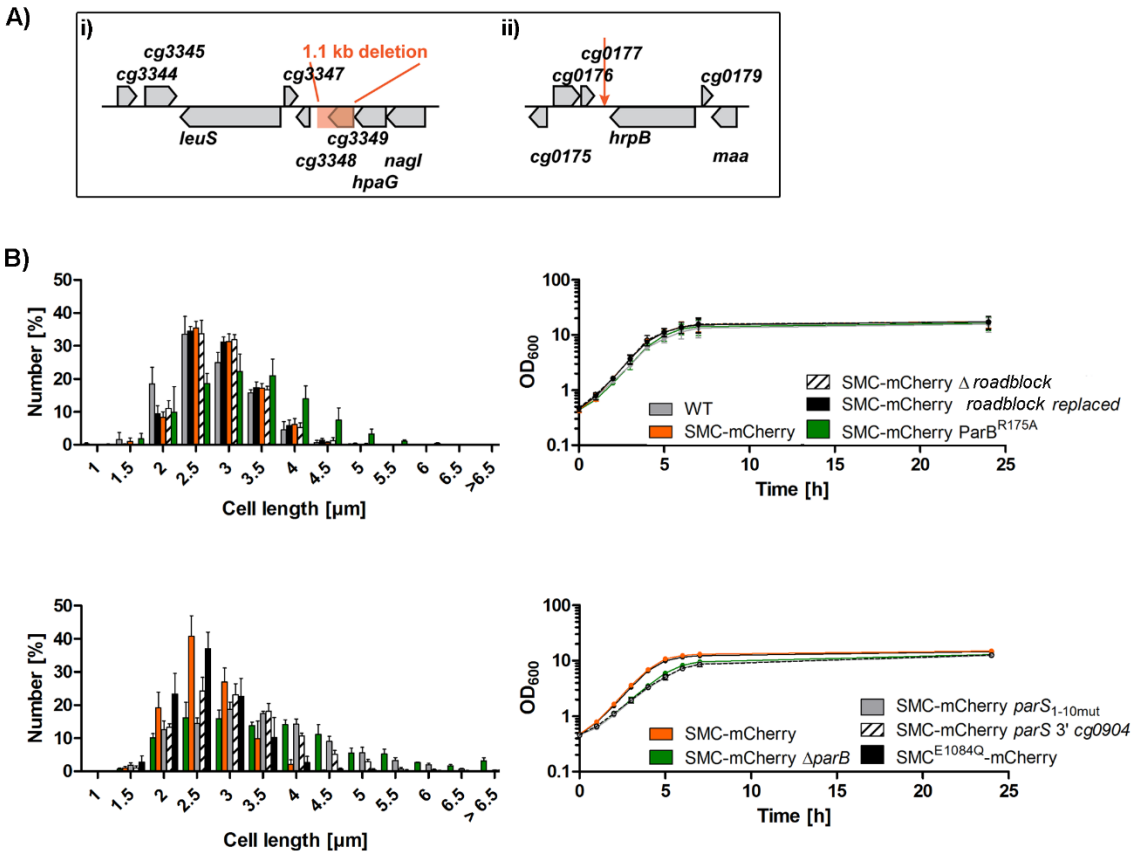

Figure 2.34: Growth analyses of *smc::smc-mCherry* mutant strains.

(**A**) Illustration of mutation sites within the *C. glutamicum* CBK034 and CBK035 genomes with a partially deleted SMC enrichment region (1.1 Kb) upstream of *parS* including the non-essential gene *cg3349* (i). This region was reinserted into intergenic region 3' of *cg0177* in CBK034 (ii) or replaced by a non-coding *B. subtilis* sequence of identical size (not shown). (**B**) Cell lengths distributions (left) and growth curves (right) of *smc::smc-mCherry* mutant strains. Error bars indicate standard deviations (biological triplicates, n > 1000). Top: Shown are data for indicated strains including the following growth rates: wild type (μ = 0.63 h^{-1}), SMC-mCherry (μ = 0.69 h^{-1}, CBK012), SMC-mCherry Δ*roadblock* (μ = 0.68 h^{-1}, CBK034), SMC-mCherry *roadblock replaced* (μ = 0.68 h^{-1}, CBK035), SMC-mCherry $ParB^{R175A}$ (μ = 0.69 h^{-1}, CBK049). Below: Growth analyses as described before; growth rates: SMC-mCherry (μ = 0.71 h^{-1}, CBK012), SMC-mCherry Δ*parB* (μ = 0.60 h^{-1}, CBK014), SMC-mCherry $parS_{1\text{-}10mut}$ (μ = 0.56 h^{-1}, CBK032), SMC-mCherry *parS* 3' cg0904 (μ = 0.55 h^{-1}, CBK045), SMC-mCherry^{E1084Q} (μ = 0.72 h^{-1}, CBK050).

In both strains SMC-deposition was completely lost at this region and did not reappear at the genomic site of reinsertion (**Figure 2.33**, **Figure 2.35**).

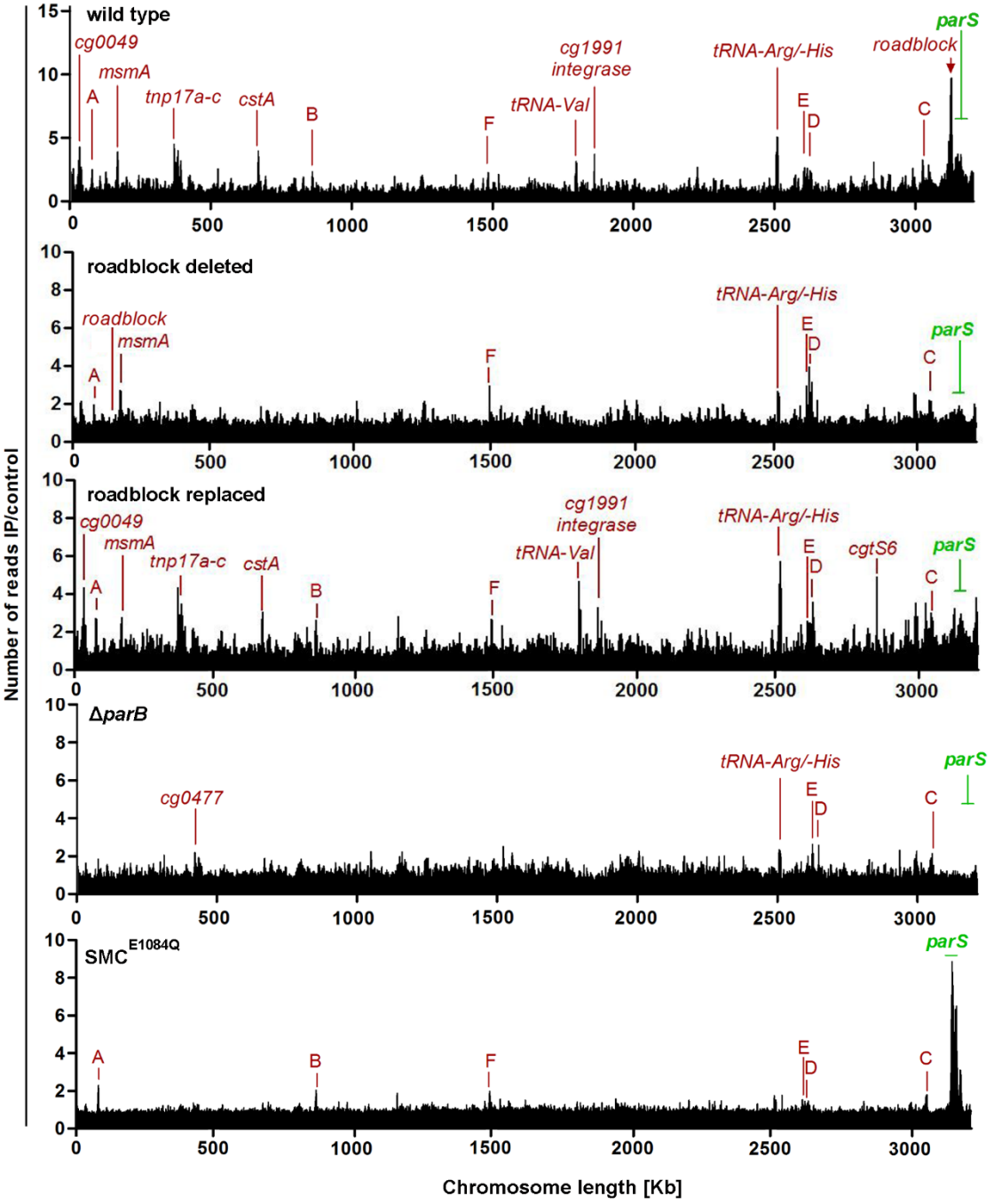

Figure 2.35: Whole-genome SMC-ChIP-seq enrichment.

ChIP-seq analyses of SMC-mCherry strains. Additional mutations are each indicated (top left corners). Genome-wide SMC-mCherry binding; signals at *parS* sites and at other loci (red letters), like at rDNA genes

(A-F), are illustrated in 0.5 Kb bins along the chromosome; x-axis centered at *terC*. Strains from top down are: CBK012, CBK034, CBK035, CBK014 and CBK051.

Conclusively, SMC accumulation 13 Kb upstream of *parS* sites reflects a roadblock, which explains SMC-trapping as SMC redistributes to distant chromosomal regions rather than specific SMC-binding. This hypothesis is further supported by the study of the contact map of wild type cells shown before (**Figure 2.16**). Indeed, the region of SMC enrichment appears clearly delimited by a strong border on its left (**Figure 2.20**– white dashed line). SMC retention could be caused by transcriptional activity, nucleoid-associated proteins or DNA-folding. Further SMC enrichment-signals were mainly detected at sites of high transcriptional activity along the whole chromosomal length (**Figure 2.35**). Different to other mutant strains, subcellular SMC-mCherry foci are less frequent in absence of ParB or *parS*, while dispersed mCherry signals increase within cells (**Figure 2.36A**). Further, ChIP-seq and ChIP-qPCR analyses reveal that SMC binding at *parS* sites is completely absent upon *parB* or *parS* deletion (**Figure 2.33**, **Figure 2.35**, **Figure 2.36B**). These findings demonstrate a ParB- and *parS*-aided SMC-loading at *oriC*-proximal sites.

To unambiguously demonstrate chromosomal SMC-loading at ParB-*parS* clusters, we made use of a well-characterized SMC ATP-hydrolysis mutant E1084Q (Hirano and Hirano, 2004; Hirano and Hirano, 2006; Minnen et al., 2016; Schwartz and Shapiro, 2011). This mutation allows for DNA-binding but prevents subsequent SMC-migration along the chromosome. Notably, the *C. glutamicum* SMC^{E1084Q} mutant does not have growth or cell length phenotypes (**Figure 2.34B**), while SMC^{E1084Q}-mCherry localizes wild type-like in distinct foci (**Figure 2.36A**). However, compared to wild type SMC, SMC^{E1084Q} strongly accumulates at *parS* sites, mimicking a ParB-enrichment pattern (**Figure 2.33**). As expected, ChIP enrichment signals at highly transcribed genes at distant chromosomal regions and at the roadblock upstream of *parS*1 are mostly absent, indicating impaired SMC-migration along DNA (**Figure 2.35**). Conclusively, we confirm specific SMC-loading at ParB-*parS* complexes on the *C. glutamicum* chromosome.

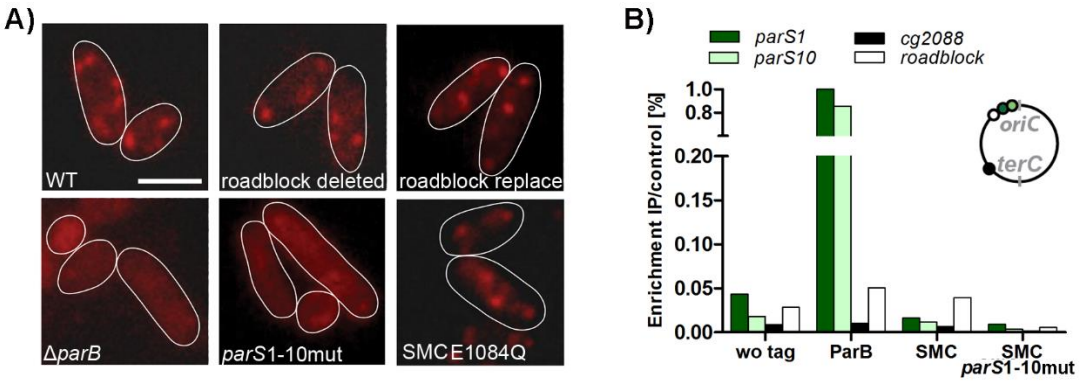

Figure 2.36: Loading of SMC depends on the presence of ParB/*parS*.

(**A**) Images show subcellular localization of SMC-mCherry fluorescence in strain backgrounds named in **Figure 2.35** and stain *smc::smc-mCherry* lacking all *parS* sites (*parS*1-10mut). Outlines of representative cells are indicated by white lines; scale bar, 2 µm. (**B**) ChIP-qPCR of wild type cells (wo tag) and cells containing ParB- or SMC-mCherry fusions in presence (SMC) or absence of *parS* (SMC $parS_{1\text{-}10mut}$). Genomic loci analyzed are indicated; values derive from biological duplicates normalized to ParB signal at *parS*1.

Moreover, SMC is also recruited via ParB to a single *parS* site inserted in an ectopic position on the *C. glutamicum* chromosome, 90° shifted from *oriC* (**Figure 2.37A**, **B**). Here, cellular SMC-mCherry foci formation is impaired in a fraction of cells, similar to Δ*parB*/*parS* mutants (**Figure 2.37A**, **Figure 2.36A**). Chromosome conformation capture analysis reveals that the genomic positioning of *parS* determines the efficiency of SMC-function in replichore cohesion, since folding of chromosomal arms is incomplete and does not extend beyond the *terC* region, as shown before (**Figure 2.23**).

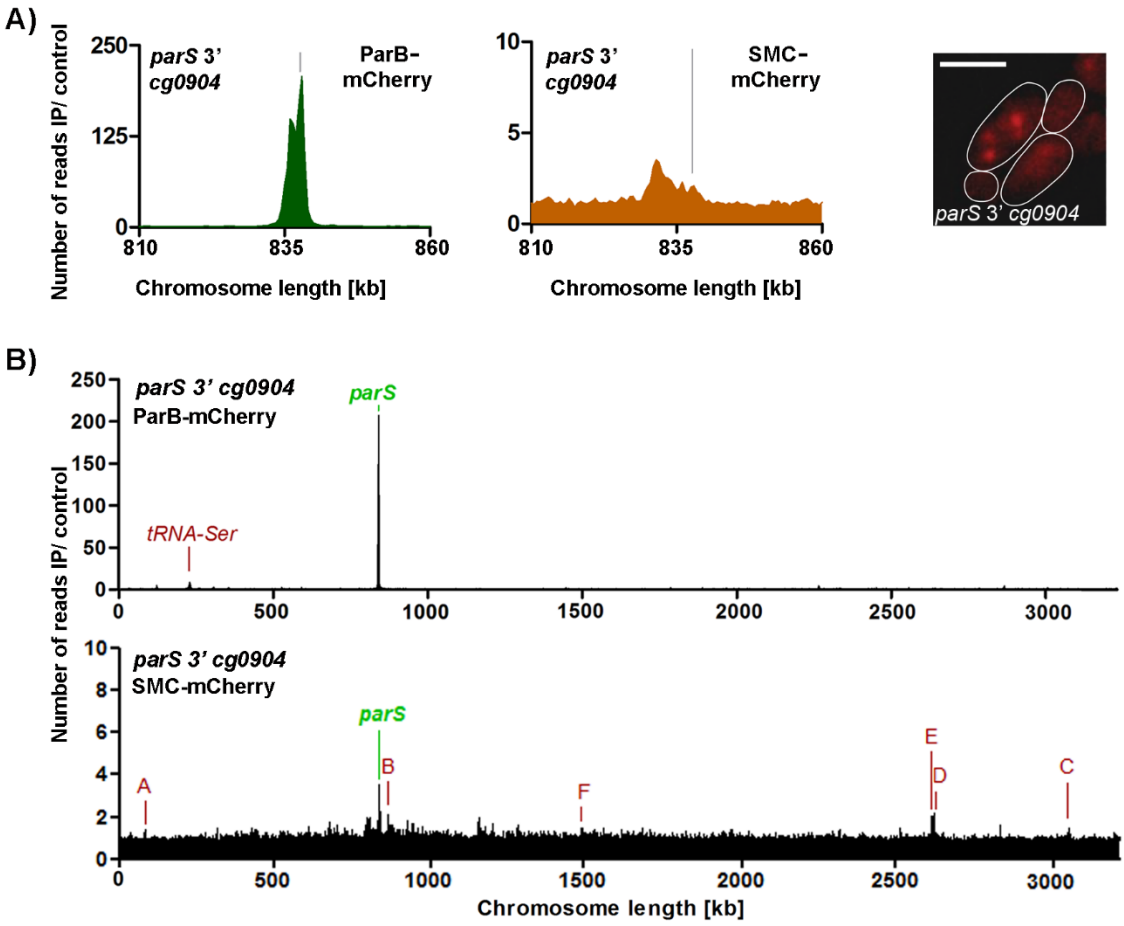

Figure 2.37: An ectopic chromosomal *parS* site allows for SMC recruitment.

(**A**) Left: ParB- (green, CBK042) and SMC-deposition (orange, CBK045) at a *parS* site inserted 3' of cg0904. ChIP-seq analyses show fold-enrichments of immunoprecipitation relative to extract samples (IP/control) binned in 5 Kb. Gray lines indicate genomic *parS* positions. Right: SMC-mCherry fluorescence in exemplary CBK045 cells with outlines indicated by white lines; scale bar, 2 µm. (**B**) Whole genome ParB- and SMC-ChIP-seq of above-named strains; *terC*-centered. Genomic localization of highly transcribed genes (rDNA genes A-F) and *parS* sites are displayed.

In addition to *parS* repositioning along the chromosome, we were able to alter chromosomal SMC recruitment by making use of the *C. glutamicum* ParB^{R175A} mutant. The R175A mutation localizes within in the N-terminal binding box II of ParB, which leads to a loss of dimer-dimer interactions in the corresponding *B. subtilis* ParB^{R79A} (Graham et al., 2014). Characterization of *C. glutamicum* ParB^{R175A} indicates an attenuated phenotype compared to *B. subtilis* ParB^{R79A}: *C. glutamicum* ChIP-analyses reveal more broadly distributed and reduced recruitment of ParB^{R175A} compared to wild type ParB surrounding the *parS* cluster or the single *parS* site (**Figure 2.38A**, **B**). Therefore, weak ParB^{R175A}-ParB^{R175A} interactions appear capable of building up diminished nucleoprotein

complexes around *parS* sites in *C. glutamicum*. Our data further confirm binding of ParB^{R175A} to exclusively *parS*-proximal genomic regions (**Figure 2.38C**).

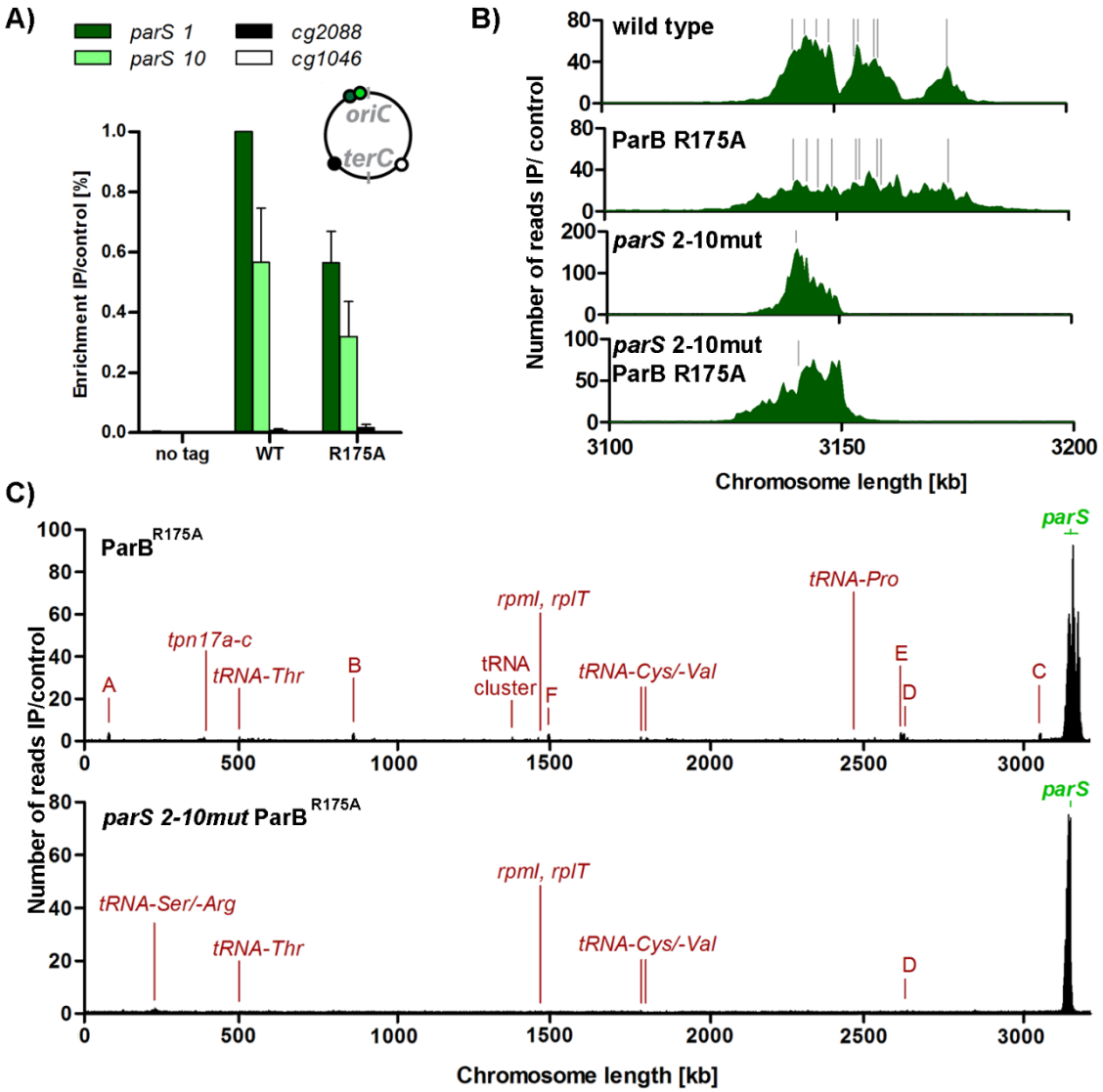

Figure 2.38: Altered ParB recruitment to *parS* sites upon R175A mutation.

(**A**) qPCR of mCherry-ChIP experiments performed with cells containing wild type (CBK006) or R175A ParB-mCherry (CBK047). Four chromosomal markers were analyzed in biological triplicates. Standard deviations are shown; data are normalized to wild type *parS*1 signals. Signals at *parS*2 yield no significant difference between wild type and R175A ParB, while signals at *parS*1 show a tendency towards statistical significance (two-tailed t-test, p = 0.17). (**B**) ChIP-seq showing recruitment of ParB- (black) or ParB^{R175A}-mCherry proteins (green) to the *parS* cluster (CBK006, CBK047) or to a single *parS*1 site (CBK027, CBK048). Enrichment signals are binned in 0.5 Kb; gray lines indicate *parS* sites. (**C**) Whole-genome ParB-ChIP-seq enrichment for strains described in (**B**); x-axes *terC*-centered. Enrichments at *parS* sites (green) and highly transcribed genes (red) are labeled.

The ParB^{R175A} mutation results in 18 or 31 % of DNA-free cells in presence of all or only one *parS* site(s) (**Table S1**). Likewise, growth rates and ParB^{R175A} cluster formation are most clearly affected in cells harboring only a single *parS* site (*parS*1) (**Figure 2.39A**, **B**). By contrast, no changes in *in vitro* DNA-binding affinities compared to wild type ParB were detected (**Figure 2.39C**) and altered binding affinity for SMC/ScpAB or self-interactions could not be verified by bacterial two-hybrid analyses (**Figure 2.28A**).

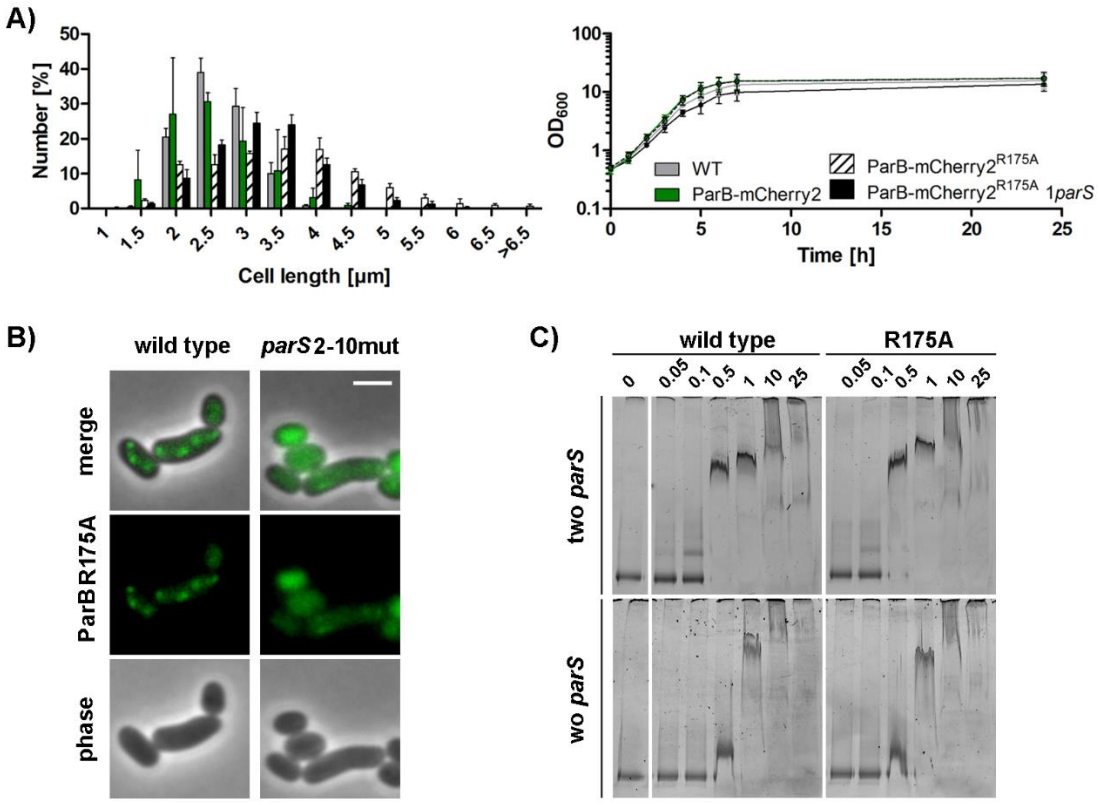

Figure 2.39: ParB R175A mutation affects ParB-*parS* cluster formation.

(**A**) Growth curves and cell length distributions of strain *parB::parB-mCherry* derivatives harboring ParB^{R175A} mutant protein; growth rates: wild type (µ = 0.63 h^{-1}), ParB-mCherry (µ = 0.69 h^{-1}, CBK006), ParB^{R175A}-mCherry (µ = 0.68 h^{-1}, CBK047), ParB^{R175A}-mCherry *parS*$_{2\text{-}10mut}$ (µ = 0.57 h^{-1}, CBK048). (**B**) ParB^{R175A}-mCherry localization in wild type and *parS*$_{2\text{-}10mut}$ mutant cells (CBK47, CBK048). Shown are phase contrast, mCherry fluorescence (false-colored, green) and an overlay of both channels. Scale bar, 2 µm. (**C**) Recombinant ParB and ParB^{R175A} proteins bind *parS* sites and nonspecific DNA. Electrophoretic mobility shift assays of ParB proteins pre-incubated with 100 ng of DNA sized 1084 bp with or without two *parS* sites.

Interestingly, ParB^{R175A} mutation results in increased SMC-binding with a striking similarity to ParB^{R175A} propagation zones (**Figure 2.40A**) that had not been described before. However, SMC-translocation along DNA is only partially impaired in this mutant, since SMC still accumulates at

the roadblock 13 Kb upstream of the *parS* cluster (**Figure 2.40A**, **B**). SMC-mCherry foci formation is frequently absent, particularly in minicells (**Figure 2.40A**).

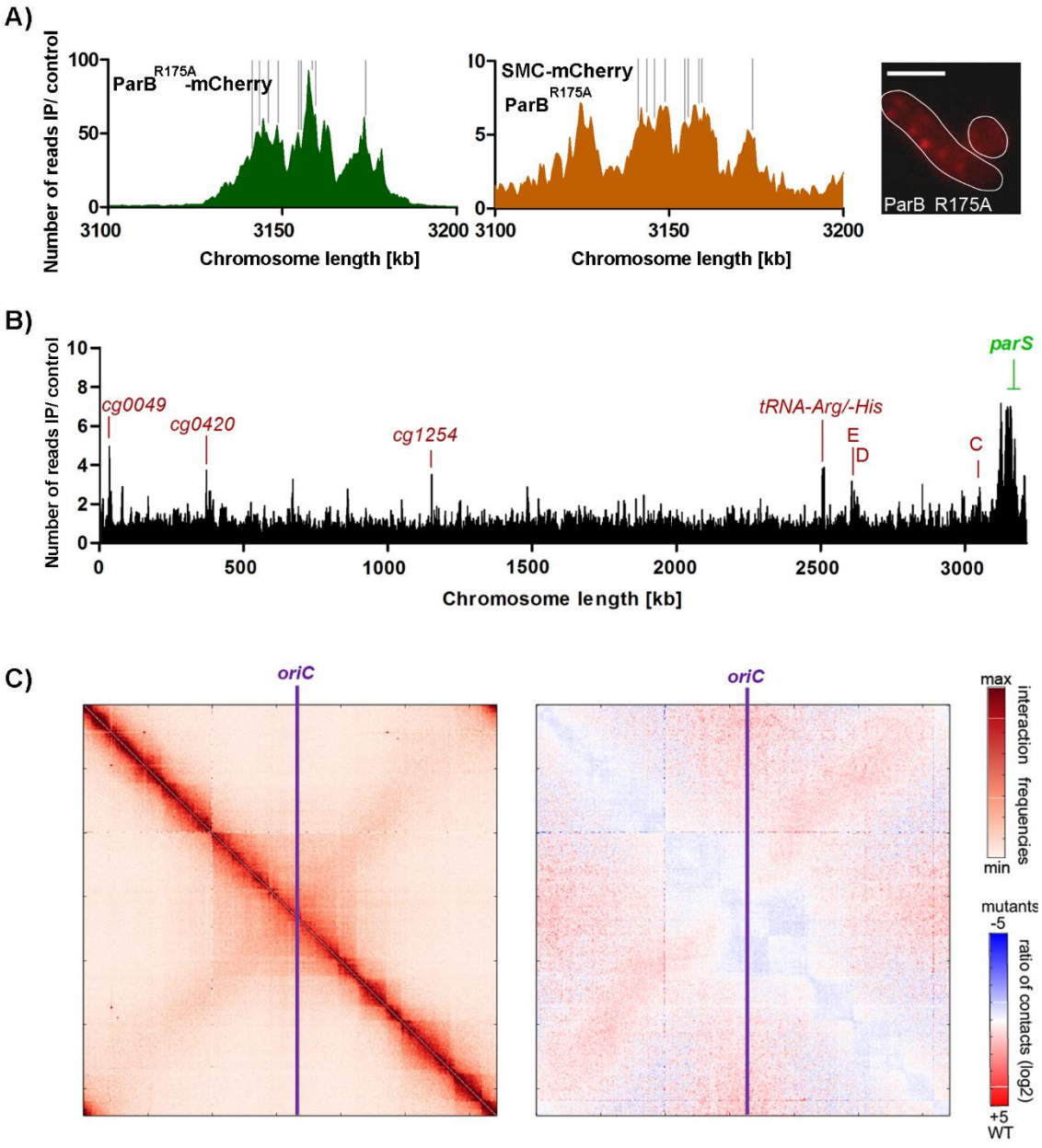

Figure 2.40: Aberrant SMC recruitment to DNA upon ParB and *parS* modifications.

(**A**) ParB- (green) and SMC-deposition (orange) at the native *parS* cluster in presence of ParB^{R175A}. Gray lines indicate genomic *parS* positions (left). SMC-mCherry fluorescence in exemplary cells with outlines indicated by white lines; scale bar, 2 µm (right). (**B**) SMC-ChIP-seq enrichment signals in CBK049 cells harboring ParB^{R175A} along the chromosome centered at *terC*. (**C**) Normalized contacts of chromosomal loci in mutant *parB::parB*^{R175A} (CBK047) depicted as described before.

Further, chromosomal inter-arm contacts are maintained, but appear less pronounced than in wild type cells (**Figure 2.40C**). Therefore, we describe a ParB^{R175A} mutation that partially locks the translocation ability of SMC/ScpAB by trapping the complexes within ParB-*parS* clusters. Altogether, out data demonstrate that the *C. glutamicum* SMC/ScpAB complex is a *Bacillus*-like condensin, which loads and migrates to distant chromosomal regions via an explicit ParB-interplay at *parS* sites.

2.4.4. MksB influences plasmid restriction at cell poles

The function of bacterial condensin MksBEFG had not yet been investigated. However, the *P. aeruginosa* MksBEF complex lacking the MksG subunit was suggested to act in chromosome organization together with SMC/ScpAB (Petrushenko et al., 2011). Therefore, we tested whether both *C. glutamicum* condensins SMC and MksB are redundant in function. To this end, mutant strains lacking the condensin core subunit Δ*mksB* or both Δ*smc* Δ*mksB* were constructed. Similar to Δ*smc*, phenotypes in growth and morphology were absent in both mutants (**Figure 2.29A**, **Table S1**). A double mutation Δ*parB* Δ*mksB* and a triple mutation Δ*parB* Δ*smc* Δ*mksB* did not aggravate the Δ*parB* phenotype (**Figure 2.29B**, **Table S1**).

Moreover, ParB-*parS* cluster numbers and their relation to cell length (**Figure 2.41A**) as well as subcellular localization of ParB foci (**Figure 2.29C**) remained unaffected by a *smc mksB* double deletion, excluding a synthetic phenotype of condensins in chromosome segregation. Fluorescence of cellular MksB-mCherry was mainly detected in dim foci at the cell poles and occasionally at midcell positions (**Figure 2.41B**), further supporting an interaction with the polar protein DivIVA. Most cells contained two MksB-mCherry clusters. Up to four distinct foci could be detected per cell, yet different to ParB and SMC clusters, MksB foci numbers do not correlate with cell length (**Figure 2.41B**). MksB-mCherry ChIP-seq analyses failed to detect specific binding or loading sites on the *C. glutamicum* chromosome (**Figure 2.41C**). Minor background signals coincide with regions of high transcriptional activity.

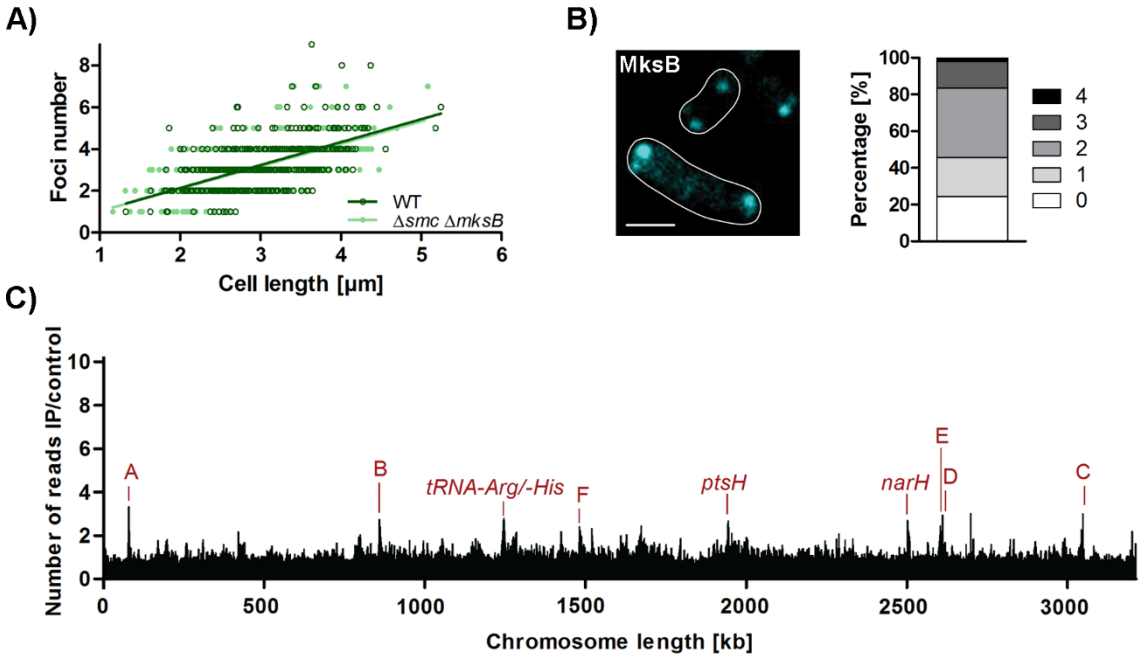

Figure 2.41: Polar MksB clusters do not reflect chromosomal binding sites.

(**A**) ParB-*oriC* cluster numbers correlate to cell length in BHI-grown *C. glutamicum* wild type (WT, CBK007) and Δ*smc* Δ*mksB* cells (ΔΔ, CBK011), n > 350. Linear regression lines and intercepts are not significantly different from each other (ANCOVA, F (1, 770) = 0.059, p > .05; ANCOVA, F (1, 771) = 0.60, p > .05); correlation coefficients: r (WT) = 0.57, r (ΔΔ) = 0.62. (**B**) Cellular localization of condensin subunits in *mksB::mksB-mCherry* cells (CBK015). Left: Microscopy image exemplifies MksB-mCherry fluorescence; white lines indicate cell outlines. Scale bar, 2 µm. Right: Cell fractions harboring 0-4 foci, n > 100. Foci numbers do not significantly correlate with cell length (F-test: F = 0.7642, df = 1, p = 0.38). (**C**) Anti-mCherry ChIP-seq analysis of MksB-mCherry, strain CBK015. Background signals like at rDNA genes (A-F) are indicated by red letters; bin size 0.5 Kb; chromosomal coordinates are *terC*-centered.

To further characterize the role of MksB in genome folding we applied chromosome conformation capture in corresponding condensin mutants (**Figure 2.42**). The ratio map comparing wild type and mutant contact frequencies hardly shows any differences (**Figure 2.42A**). Therefore, deletion of *mksB* has no effect on chromosome organization. Moreover, the Δ*smc*Δ*mksB* contact map is mostly identical to the one of Δ*smc* cells (**Figure 2.42B**, **Figure 2.32A**), showing that MksB and SMC are not involved in the same process. Conclusively, chromosome conformation capture assays support the hypothesis that MksB, unlike all other bacterial condensins studied so far, plays no direct or indirect role in *C. glutamicum* chromosome organization.

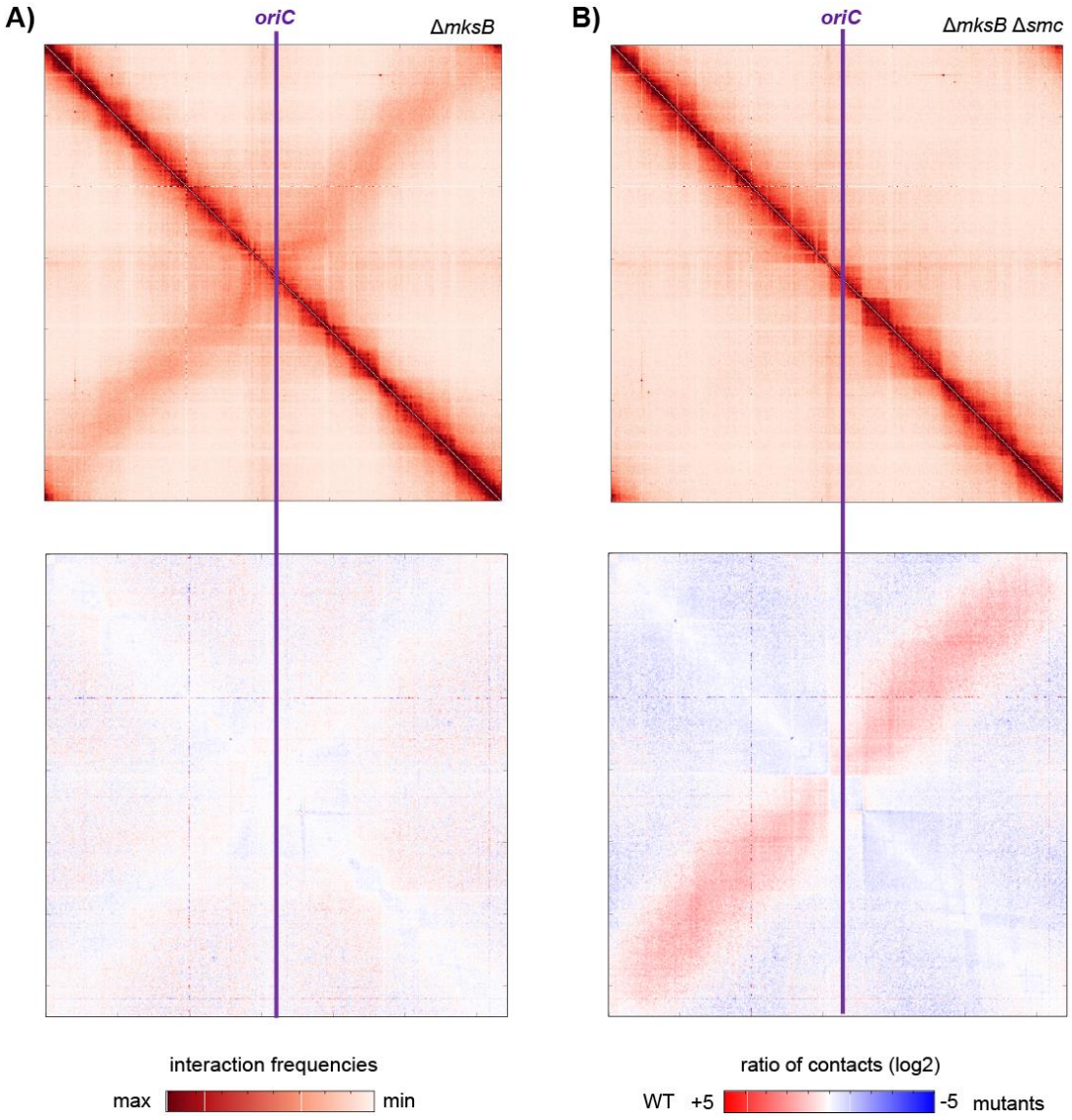

Figure 2.42: Condensin MksBEFG is not involved in chromosome folding.

(**A**) Normalized contact map of *C. glutamicum* Δ*mksB* cells (CBK001) and corresponding differential map are presented as in **Figure 2.19**. (**B**) Chromosome conformation capture analysis of Δ*mksB*/Δ*smc* mutant CBK004 as in (**A**).

We expanded our search for further putative cellular functions of MksBEFG that are not linked to chromosome folding. Since related bacterial SMC-like proteins RecN and SbcC have been shown to function in the repair of DNA double strand breaks and cleavage of DNA hairpins, we tested the influence of MksB on mitomycin C-induced DNA double strand repair and UV-damage repair (Connelly et al., 1998; Cromie and Leach, 2001; Lloyd et al., 1983; Pellegrino et al., 2012). Mitomycin C-treatment causes an aberrant cell elongation phenotype in *C. glutamicum*, while MksB-mCherry remained localized at the cell poles (**Figure 2.43A**).

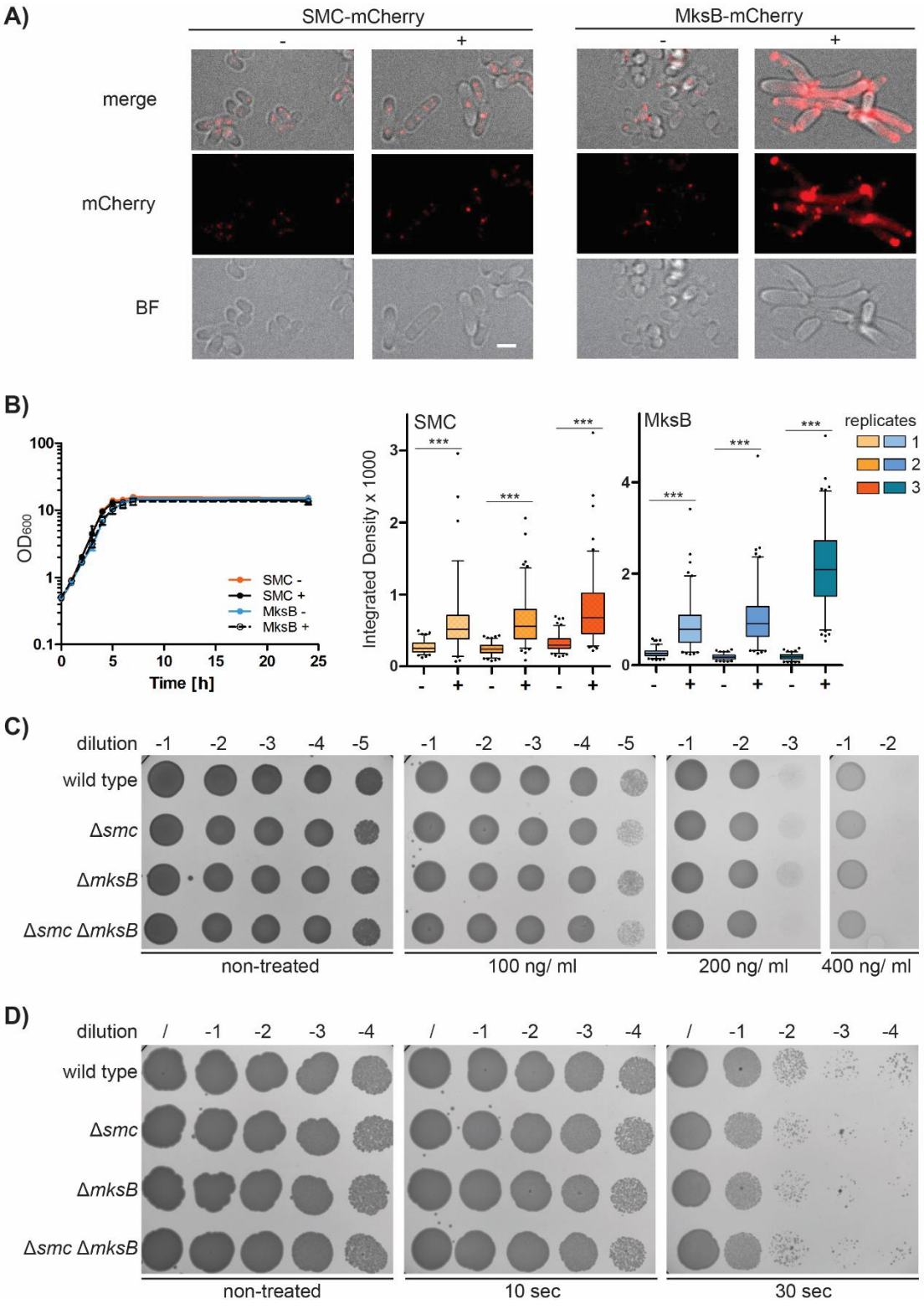

Figure 2.43: Condensins do not aid in UV- or mitomycin C- induced DNA damage repair.

(**A**) SMC- and MksB-mCherry fluorescence of strains CBK012 and CBK015 grown for 5 h in BHI medium in presence (+) or absence (-) of 200 ng/ml Mitomycin C (added 1 h after inoculation at OD_{600} = 0.5). Microscopy images show mCherry fluorescence, bright field (BF) and merged channels; scale bar, 2 µm. (**B**) Growth curves and total cellular SMC- and MksB-mCherry fluorescence for above-named growth

conditions, n > 100. Wilcoxon-tests yielded significant differences ($p < 0.001$) between treated (+) and non-treated (-) samples. Growth rates: SMC - ($\mu = 0.71\ h^{-1}$), SMC + ($\mu = 0.70\ h^{-1}$), MksB - ($\mu = 0.64\ h^{-1}$), MksB + ($\mu = 0.63\ h^{-1}$) (**C**, **D**) *C. glutamicum* wild type and condensin mutants (CDC026, CBK001, CBK004) were grown in BHI medium to $OD_{600} = 5$; ten-fold serial dilutions were plated on (**C**) BHI-agar plates containing 0 - 400 ng/ml mitomycin C and incubated overnight at 30° C or (**D**) LB-agar plates and exposed to UVB for 0 – 30 sec prior to overnight incubation. Plating assays were performed in biological triplicates; shown are representative data.

Fluorescence intensities increased significantly in presence of mitomycin C, yet similar effects were detected for SMC-mCherry in a control strain (**Figure 2.43B**). Different to the high sensitivity of *recN* mutants to DNA strand breaks in several bacterial species (Funayama et al., 1999; Kidane et al., 2004; Wang and Maier, 2008; Youssef et al., 2014), *C. glutamicum* condensin mutants did not show comparable growth defects after irradiation with UVB light or in presence of mitomycin C in concentrations ranging from 100 to 400 ng/ml compared to wild type (**Figure 2.43C**, **D**). Accordingly, we could not detect a considerable impact of *C. glutamicum* condensin MksB on DNA repair.

Therefore, we focused on the phenotypic analyses of Δ*mksB* cells in maintenance of extrachromosomal DNA. Here, a bioinformatics screen for bacterial anti-phage/anti-plasmid defense systems supported our idea of MksBEFG complexes being involved in plasmid maintenance (Doron et al., 2018). For *C. glutamicum* a variety of plasmid vectors are available (Eggeling and Reyes, 2005). We have chosen two high-copy number plasmids pJC1 and pEK0 with 140 and 30 copies per cell and two low copy number vectors with one to two copies per cell for the following experiments. First, plasmid copy numbers were analyzed relative to genomic loci close to *oriC* by qPCR (**Figure 2.44A**). Cell growth in absence of plasmid selection marker yielded at least a ten-fold enrichment of low-copy number plasmids in Δ*mksB* mutants compared to wild type cells. By contrast, the quantity of high copy number vectors per chromosome was hardly influenced by *mksB* deletions (**Figure 2.44A**). These findings were confirmed by plasmid extractions from *C. glutamicum* wild type and Δ*mksB* strains. Cells lacking MksB contained exceptionally high amounts of pBHK18 and pWK0 compared to wild type cells (**Figure 2.44B**), thus pBHK18 and pWK0 were turned into high copy number plasmids in absence of MksB. On the contrary, pJC1 and pEK0 copy numbers did not markedly differ in *mksB* mutants compared to control strains (**Figure 2.44B**). These analyses show a MksB-dependent decrease in plasmid level, in particular of low-copy number plasmids. Notably, the study of *C. glutamicum* MksB in its native host cells is in line with a recent study, where the heterologous expression of *mksBEFG*

subunits of *Bacillus* species equally affected the maintenance of a *B. subtilis* plasmid (Doron et al., 2018).

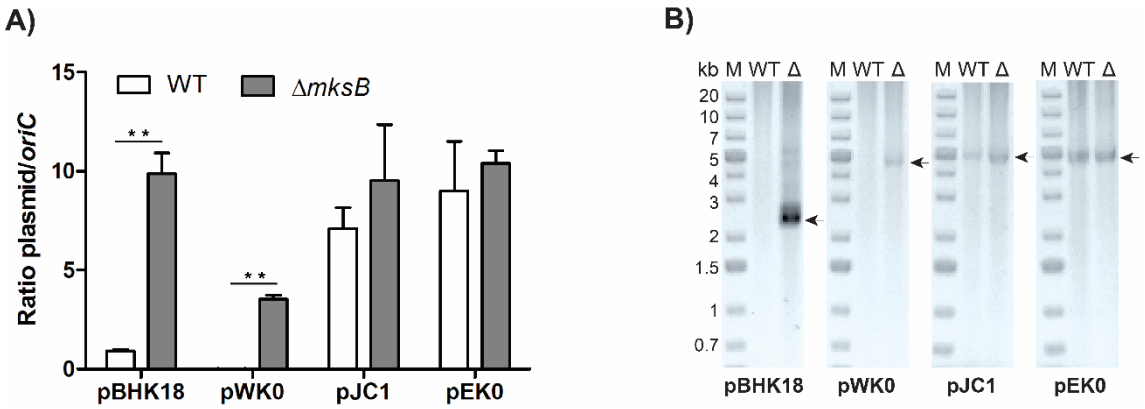

Figure 2.44: MksB restricts plasmid copy numbers.

(**A**) qPCR analyses of low copy (pBHK18 and pWK0) and high copy number vectors (pJC1 and pEK0) relative to *oriC* numbers per cell. Ratios were compared between *C. glutamicum* wild type and Δ*mksB* mutant cells (CBK053-CBK060); significant differences between ratios are indicated (two-tailed t-test, df = 2, $p < 0.01$). Cells were grown in BHI medium without addition of plasmid selection antibiotic after overnight pre-incubation with antibiotic, error bars display standard deviations (n = 3). (**B**) Extraction of above-named plasmids from *C. glutamicum* wild type (WT) and Δ*mksB* (Δ) strains grown in presence of selection antibiotic. Extracted plasmids (arrows), corresponding to yield from approximately 1 x 10^9 cells each, is visualized on 1 % agarose gels.

Together, our data show that the two *C. glutamicum* condensins evolved very different functions: whereas SMC/ScpAB acts in concert with ParB to promote cohesion of chromosomal arms and origin domain organization, MksBEFG does not impact on chromosomal architecture. Instead, this condensin complex seems involved in plasmid replication through a mechanism that remains to be characterized.

2.5. Localization interplay of the ParABS system in *C. glutamicum*

Initial characterizations of the *C. glutamicum* ParABS system revealed a crucial role for Par proteins in chromosome segregation, where their cellular localization was determined by still microscopy images (Donovan et al., 2013; Donovan et al., 2010). To date, chromosomal ParAB dynamics were generally investigated in monoploid bacteria that contain one and two chromosomes per life cycle. Since *C. glutamicum* cells are diploid and contain remarkably high

DNA contents at fast growth (Böhm et al., 2017), we aimed to investigate features of spatiotemporal ParA localization that underlie this genetic complexity by live cell imaging. In the following chapters we further demonstrate the interplay of cellular ParAB localization in dependence on each other and on *parS* sites, revealing self-sustained localization patterns of the *C. glutamicum* ParABS system.

2.5.1. ParA-association with nucleoids and cell poles

C. glutamicum ATPase ParA had been shown to localize at cell poles and throughout the cell (Donovan et al., 2010). In this study we constructed a strain with an allelic replacement of ParA by a fluorescent ParA-eYFP fusion to reinvestigate the cellular localization, in particular for analysis via time-lapse microscopy. Characterization of strain *parA::parA-eYFP* reveals wild type-like growth and cell length distributions, confirming full functionality of the ParA fusion construct (**Table S1**, **Figure 2.45A**). Cellular ParA-eYFP fluorescence was investigated microscopically: cellular ParA localizes in diffuse patches along the cell length and in bright and distinct polar foci (**Figure 2.45B**). These broadly distributed fluorescence signals likely represent ParA molecules that are bound to the *C. glutamicum* chromosome. Two to four ParA-eYFP foci could be observed per cell. Two ParA-foci localize to cell poles, while a third and fourth focus establishes at midcell positions (**Figure 2.45C**), matching septal DivIVA or ParB cluster-localizations shown before in chapter **2.1.1**. In order to distinguish cytoplasmic ParA fractions from DNA-associated ParA, we treated cells with 50 µg/ml chloramphenicol that results in nucleoid condensation at central regions of the cells (**Figure 2.45B**). Here, ParA-eYFP colocalizes in central patches with the compacted nucleoids, indicating that the protein indeed mostly associates with the chromosome. ParA-binding within these fluorescent patches was most pronounced at polarly-facing tips of the condensed nucleoids. Further, a minor protein fraction remains localized at cell poles, not being associated with DNA. Focal fluorescence enrichments at nucleoid edges likely represent ParA interactions with ParB complexes, shown before by bacterial two hybrid analysis (Donovan et al., 2010). Fluorescence at cell poles might derive from a ParA interaction with the polar DivIVA, similar to ParA interactions with DivIVA homologue Wag31 in *M. smegmatis* or Scy in *S. coelicolor* (Ditkowski et al., 2013; Ginda et al., 2013). However, a direct ParA-DivIVA interaction could not be evidenced via bacterial two-hybrid analysis (**Figure 2.45D**).

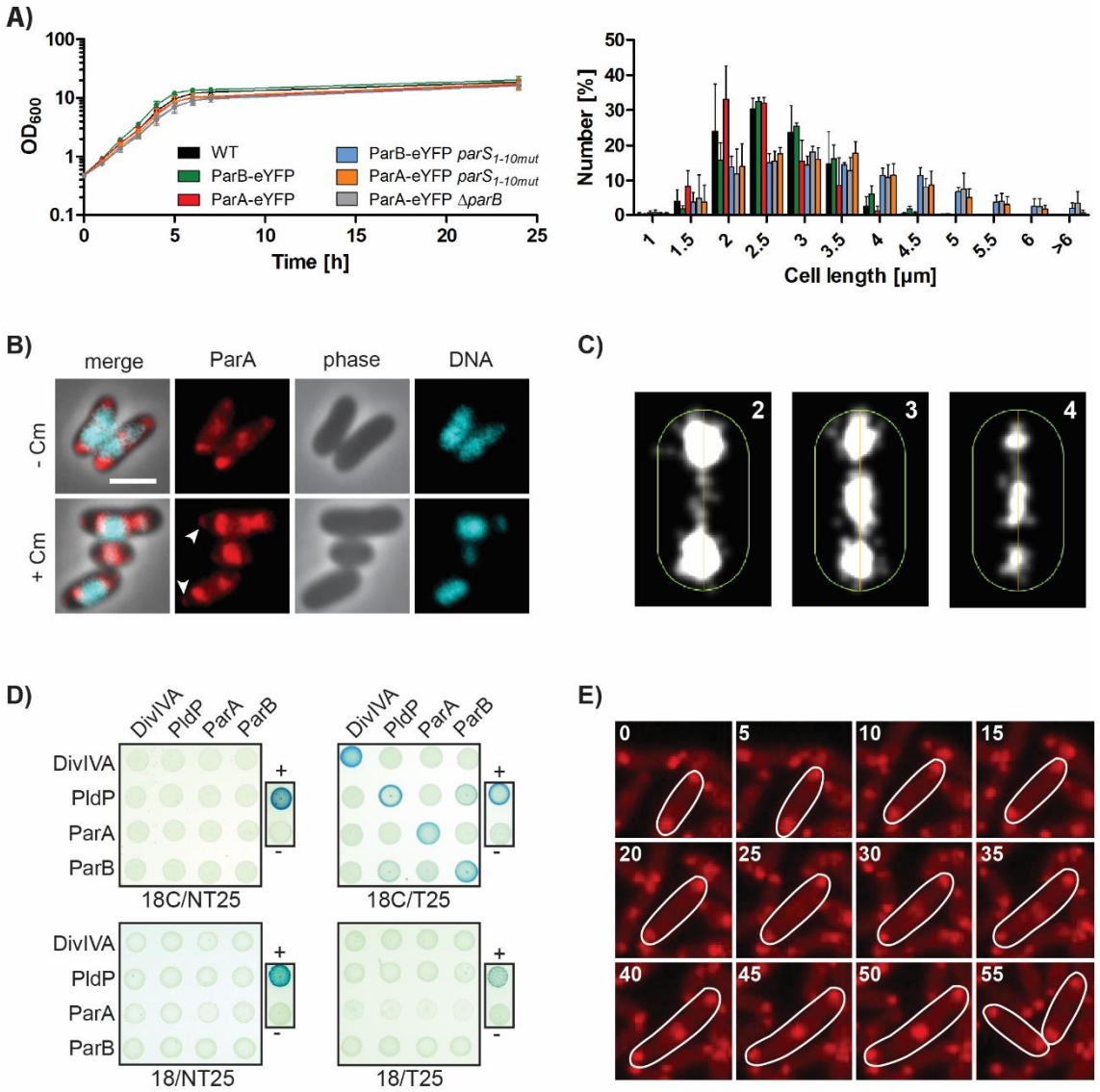

Figure 2.45 ParA localizes along the nucleoid and is steadily recruited to cell poles.

(**A**) Growth curves and cell length distributions of *C. glutamicum parA* and *parB* mutant strains harboring fluorescent ParA or ParB fusion constructs as indicated; growth rates: wild type (μ = 0.61 h^{-1}), ParB-eYFP (μ= 0.63 h^{-1}, CBK007), ParA-eYFP (μ = 0.59 h^{-1}, CBK069), ParB-eYFP *parS*$_{1\text{-}10mut}$ (μ = 0.55 h^{-1}, CBK026), ParA-eYFP *parS*$_{1\text{-}10mut}$ (μ = 0.60 h^{-1}, CBK074), ParA-eYFP Δ*parB* (μ = 0.60 h^{-1}, CBK073). (**B**) ParA-DNA colocalization in exemplary CBK069 cells. Microscopy pictures show ParA-eYFP (false colored, red) and Hoechst fluorescence (cyan), phase contrast and merge images in presence (+ CM) or absence (- CM) of chloramphenicol; white arrows point to polar ParA deposition. Scale bar, 2 µm. (**C**) Average localization of ParA-eYFP fluorescence in cells containing two to four foci (n > 100); cell lengths are normed. Illustration was performed using MicrobeJ (Ducret et al., 2016). (**D**) Bacterial two-hybrid ParA-DivIVA interaction assay. All combinations of hybrid protein C/N- (18C/NT25), C/C- (18C/T25), N/N- (18/NT25) and N/C- (18/T25) terminal fusions of adenylate cyclase fragments were investigated. (**E**) Time-lapse microscopy showing ParA-eYFP dynamics (red); cell outlines are indicated by white lines and letters show time intervals in min. Scale bar, 2 µm.

To track ParA dynamics throughout the cell cycle live cell imaging was performed with cells expressing ParA-eYFP (*parA::parA-eYFP*) as single ParA copy (**Figure 2.45E**). Newborn cells usually contain two ParA foci, which are stably retained at cell poles throughout the cell cycle. Dynamic ParA gradients emanate from each polar ParA cluster. Additional ParA patches assemble gradually in the course of cell elongation at septal positions and become polar foci at young cell poles upon cytokinesis in daughter generations.

2.5.2. ParAB dynamics during diploid cell cycles

Monoploid model bacteria *M. smegmatis*, *C. crescentus* or *M. xanthus* translocate polar ParB-*parS* complexes along a ParA gradient across the whole longitudinal cell axis to opposing cell poles (Ginda et al., 2013; Iniesta, 2014; Ptacin et al., 2010). In contrast, ParB-*parS* clusters of diploid *C. glutamicum* cells remain within their original cell half due to initial occupancy of the opposing pole by a second *oriC* complex (Böhm et al., 2017). To relate cellular ParA dynamics to spatiotemporal ParB localization in the context of the uncommon chromosome configuration of *C. glutamicum*, we constructed a dual reporter strain *parA::parA-mCherry parB::parB-eYFP*. Fluorescent tags did not impair chromosome segregation (**Figure 2.46A**) and ParB foci as well as ParA gradients formed along DNA similar to separate fluorophore fusions characterized before (**Figure 2.46B**).

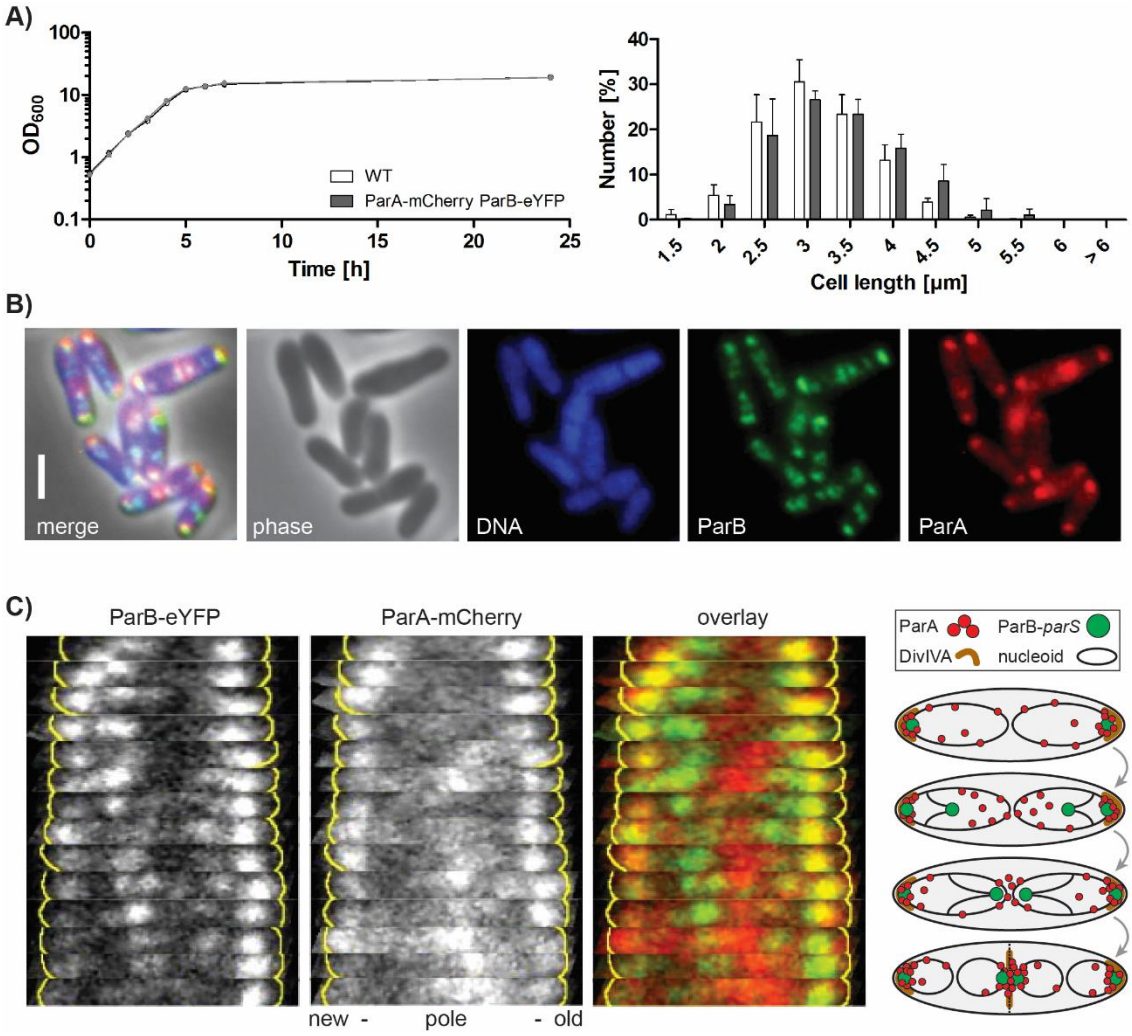

Figure 2.46: ParB-*parS* complexes segregate along dynamic ParA gradients.

(**A**) Phenotypic characterization of *C. glutamicum* dual reporter strain containing ParB-mCherry and ParB-eYFP (CBK071). Growth curves and cell length distributions are displayed with standard deviations obtained from biological triplicates; growth rates: wild type ($\mu = 0.61\ h^{-1}$), ParA-mCherry ParB- eYFP ($\mu = 0.66\ h^{-1}$). (**B**) Microscopy images of strain CBK071: phase contrast, Hoechst (DNA), ParB-eYFP and ParA-mCherry fluorescence are shown in separate channels and as overlay image. Scale bar, 2 µm. (**C**) Left: Cellular fluorescence profiles of ParB-eYFP (green) and ParA-mCherry (red) throughout one cell cycle (CBK071) shown as kymographs in 5 min intervals. Right: Cell cycle scheme illustrating spatiotemporal ParAB localization.

This strain confirms a colocalization of bright ParA foci at cell poles and at midcell positions with ParB-*parS* complexes (**Figure 2.46B**). Time-lapse microscopy reveals the formation of separate dynamic ParA gradients within both cell halves emanating from ParA foci at cell poles at the beginning of the cell cycle (**Figure 2.46C**). ParB-*oriC* complexes segregate via a distinct ParA-movement in diploid *C. glutamicum* cells: ParB-*oriC* clusters translocate from both cell poles

towards midcell effectively removing ParA from the DNA, thereby relocating ParA towards septal positions (**Figure 2.46C**). In contrast to closely related *M. smegmatis*, where ParB complexes at quarter cell positions do not colocalize with ParA foci at the outermost polar region of the cell (Ginda et al., 2013), polar fractions of *C. glutamicum* ParA associate with ParB-*oriC* complexes throughout the cell cycle. Furthermore, different to monoploid bacteria, multiple ParB-*oriC* complexes segregate from each other towards midcell by establishing several dynamic ParA gradients along the *C. glutamicum* cell axis.

2.5.3. Cellular ParABS localizations are interdependent

Having characterized subcellular ParAB localizations we further investigated the impact of *parA*, *parB* or *parS* deletions on the cellular localization on the remaining Par protein(s). All *par* mutations described below yield in severe chromosome segregation defects with approximately 25 % DNA-free mini cells and fractions of drastically elongated cells (**Table S1**, **Figure 2.1C**, **Figure 2.17E**, **Figure 2.45A**).

Specific ParB-DNA binding is lost in absence of *parS* sites, impeding ParB-nucleoprotein complex formation (**Figure 2.47**, also see chapter **2.3.2**). The homogeneous ParB-eYFP distribution likely reflects fractions of cytoplasmic ParB and ParB bound non-specifically to the nucleoid (**Figure 2.39C**). In turn, absence of distinct ParB-*parS* complexes abolishes the formation of ParA-eYFP gradients along DNA (**Figure 2.47**). Here, ParA exclusively clusters at cell poles, while midcell positions are mainly devoid of ParA fluorescence. Conclusively, homogeneously distributed ParB results in ParA-depletion from nucleoids, while recruitment to cell poles might be actively mediated by a yet unknown factor, or due to nucleoid exclusion.

Upon deletion of *parA* ParB-eYFP clusters increase in numbers per cell and distribute disorderedly along the cell axis compared to wild type (**Figure 2.47**, also see chapter **2.1.1**). Furthermore, these mutants frequently lack ParB foci at cell poles, confirming a previous study (Donovan et al., 2010). Therefore, the polar tethering of ParB-*parS* complexes relies on the presence of ParA. Finally, a *parA::parA-eYFP* Δ*parB* mutant exhibits homogenous ParA-dispersal along the nucleoid (**Figure 2.47**). This phenotype confirms that the formation of polar ParA localization in distinct foci depends on the presence of ParB, irrespective of whether ParB is distributed diffusely throughout the cell or is bound by *parS* sites.

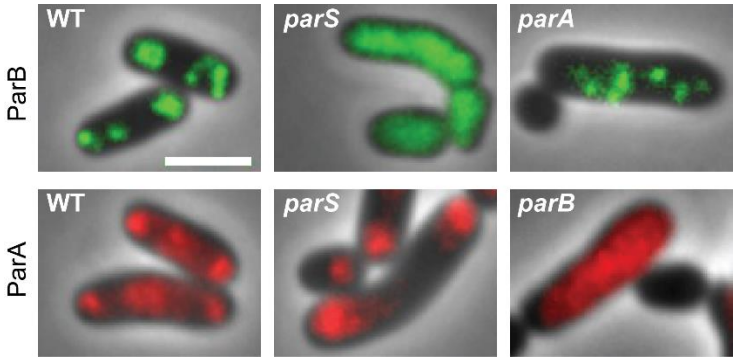

Figure 2.47: Formation of ParA and ParB clusters at cell poles are interdependent.

Microscopy images exemplify localization of ParB-eYFP (green) and ParA-eYFP (red) fluorescence in wild type (WT; CBK007, CBK069), *parS* (CBK026, CBK074), *parA* (CBK072) and *parB* (CBK073) mutant cells. Scale bar, 2 µm.

In sum, the integrity of the *C. glutamicum* ParABS system is a tripartite cooperation, where subcellular localizations of individual components are interdependent.

2.6. Functional divergence of ParA and the ParA-like ATPase PldP

Members of the ParA-family of proteins are not exclusively required for chromosome segregation. Orphan ParAs have been described in different bacterial species, where they mediate positioning of other cellular structures, like chemotaxis proteins or type IV pili components (reviewed in Lutkenhaus, 2012). In addition to ParA, a second ParA-like ATPase PldP is encoded on the *C. glutamicum* chromosome distant to the *parAB* operon (Donovan et al., 2010). PldP harbors basic residues that are highly conserved amongst bacterial ParA homologues and are likely responsible for DNA binding (Hester and Lutkenhaus, 2007). Previous work had shown that PldP localizes to the future site of septation and a *pldP* deletion resulted in misplaced division septa that caused a mild cell length phenotype compared to *parAB* mutants (Donovan et al., 2010). Therefore, PldP was suggested to act as putative regulator of division septum placement. However, the mechanism of septal PldP localization and its exact role in cell division had not yet been investigated. The following chapter covers further PldP-characterization in *C. glutamicum* with respect to spatiotemporal localization and its dependence on the ParABS system. Besides this, potential roles in DNA segregation and in division septum placement were further investigated.

2.6.1. The growth phase determines spatiotemporal PldP positioning

To characterize PldP localization in more detail an allelic replacement of *pldP* by *pldP-eYFP* was constructed. The resulting *C. glutamicum* strain grows and divides wild type-like, suggesting functionality of the fluorescent fusion construct (**Figure 2.48A**, **Table S1**). PldP-eYFP localizes throughout the cell and accumulates particularly in a wide area around midcell (**Figure 2.48B**). Further, fluorescence signals are frequently enriched at quarter cell positions in long cells. Band-like signals at midcell that were described before as distinctive PldP localization patterns (Donovan et al., 2010) were primarily observed in stationary cells and in cells grown on agar plates, but were rarely present in exponentially grown cells (**Figure 2.48B**).

We further aimed to compare cellular ParA and PldP localizations in a dual labeled reporter strain *pldP::pldP-eYFP parA::parA-mCherry*. Absence of major growth phenotypes and DNA segregation defects were confirmed and microscopy analysis revealed that both ParA-like ATPases do not strictly colocalize and localization patterns also do not exclude each other (**Figure 2.48C**, **D**, **Table S1**). Therefore, while ParA localization is determined by ParB-*parS*, the chromosome and a polar factor like DivIVA, localization of PldP is at least partially defined by other or additional interactors.

Since PldP-eYFP localization strikingly differed within a population of exponentially grown cells accumulating in either one or two zones per cell, PldP fluorescence was tracked throughout generations. To this end, time-lapse microscopy was carried out using strain *pldP::pldP-eYFP*. An exemplary time-series covering one life cycle of sister cells is shown in **Figure 2.48E**.

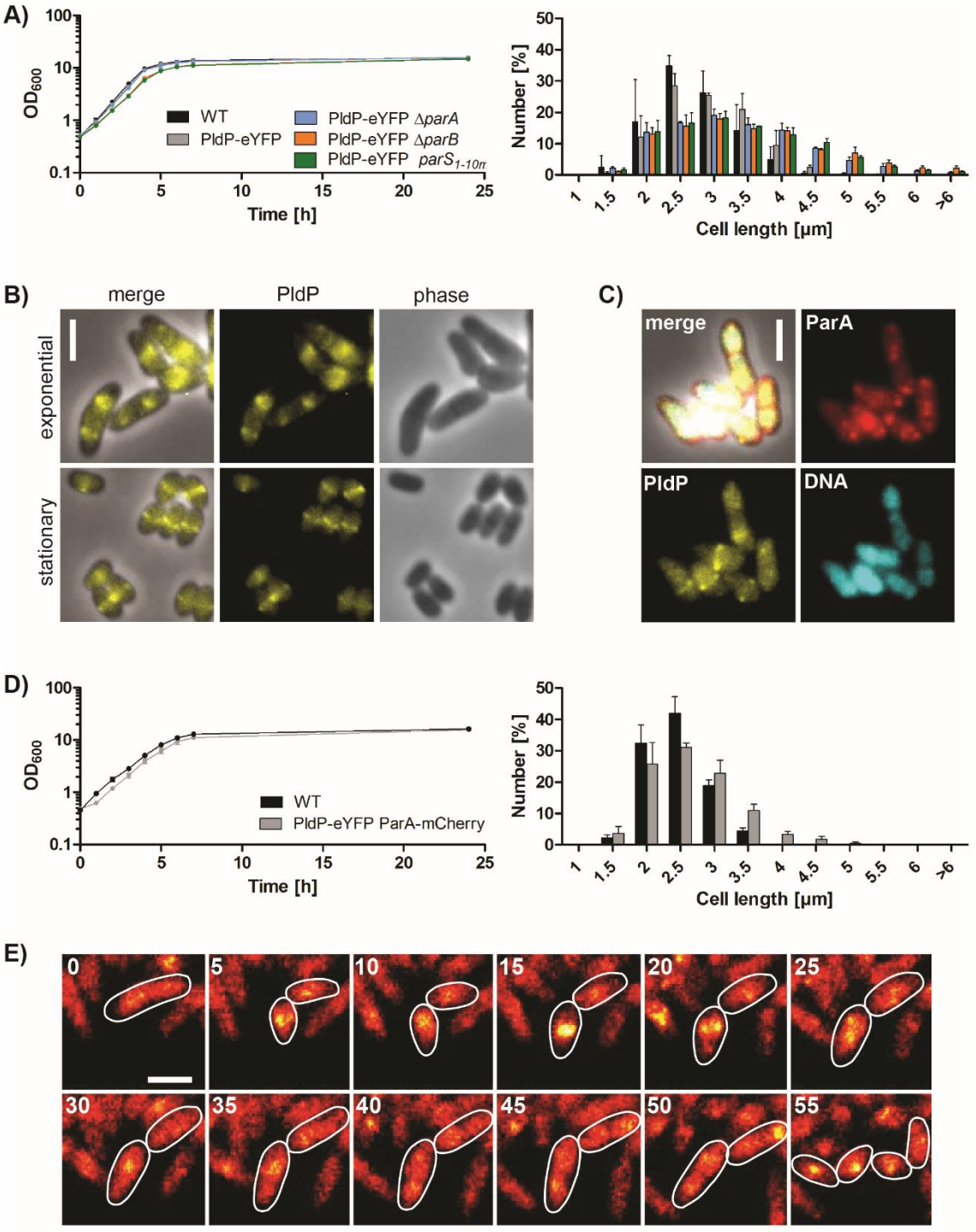

Figure 2.48: Cell cycle-dependent PldP localization to cell quarter positions and septa.

(**A**) Growth curves and cell length distributions of *C. glutamicum* wild type (WT) and strains harboring PldP-eYFP in combination with *par* mutations; growth rates: wild type ($\mu = 0.67\ h^{-1}$), PldP-eYFP ($\mu = 0.67\ h^{-1}$; CBK75), PldP-eYFP Δ*parA* ($\mu = 0.65\ h^{-1}$, CBK078), PldP-eYFP Δ*parB* ($\mu = 0.61\ h^{-1}$, CBK077), PldP-eYFP $parS_{1\text{-}10mut}$ ($\mu = 0.60\ h^{-1}$, CBK079). Error bars display standard deviations of biological triplicates. (**B**) Microscopy images of CBK075 cells at exponential (top) and stationary growth (below), showing PldP-eYFP fluorescence (false colored, yellow), phase contrast and merged channels. Scale bar, 2 µm. (**C**) ParA-

mCherry (red) and PldP-eYFP (yellow) fluorescence are exemplified in representative CBK080 cells; DNA stain (Hoechst, cyan) and an overlay of all channels are shown in addition. Scale bar, 2 µm. (**D**) Phenotypic characterization of *C. glutamicum* dual reporter strain harboring PldP-eYFP and ParA-mCherry (CBK080) as in (**A**); wild type (μ = 0.67 h^{-1}), PldP-eYFP ParA-mCherry (μ = 0.61 h^{-1}). (**E**) Time-lapse microscopy showing PldP-eYFP localization in color gradients from low (red) to high fluorescence intensity (yellow) throughout a cell cycle (CBK075) with 5 min time intervals between images. Scale bar, 2 µm.

In newborn cells PldP usually localizes in a wide area around midcell, where fluorescence intensities are highest at central positions. Upon cell elongation PldP-eYFP disperses throughout the cell and finally accumulates in two patches in each cell quarter prior to cell division. Localization in polar foci, as observed for ParA, is absent at any cell cycle stage. Conclusively, PldP distributes uncorrelated to cellular ParA localization in broad zones around future division sites.

2.6.2. Localization crosstalk of ParABS with PldP

Having differentiated cellular PldP- from ParA- localization, we further investigated the impact of PldP on ParB-*oriC* positioning. In absence of PldP cells divide asymmetrically, yielding in aberrant cell length distributions with fractions of very long cells and minicells (**Figure 2.49A**) (Donovan et al., 2010). In contrast to a *parA* deletion, all minicells contained DNA (**Table S1**). Further, while polar tethering of ParB-eYFP clusters is absent upon *parA* deletion, ParB complexes are reliably anchored at cell poles and division septa in Δ*pldP* cells (**Figure 2.49B**, **Figure 2.2A**). ParB clusters are generally more dispersed along the longitudinal cell axis in both strains compared to wild type. Particularly in Δ*pldP* cells cohesion of ParB complexes appears to be impaired with several small clusters being localized in close proximity (**Figure 2.49B**). Live cell imaging was carried out to track ParB-*parS* complex formation throughout a cell cycle. Here, most newborn cells contained two to four ParB clusters, while ParB foci numbers increased continuously over time to mainly four up to eight foci per cell (**Figure 2.49C**). Up to 11 ParB-*parS* clusters were counted in long cells with comparably short generation times (**Figure 2.49C**). Similar to Δ*parA* cells, overall ParB cluster numbers are higher than observed in wild type (compare with **Figure 2.3 C**, **E**).

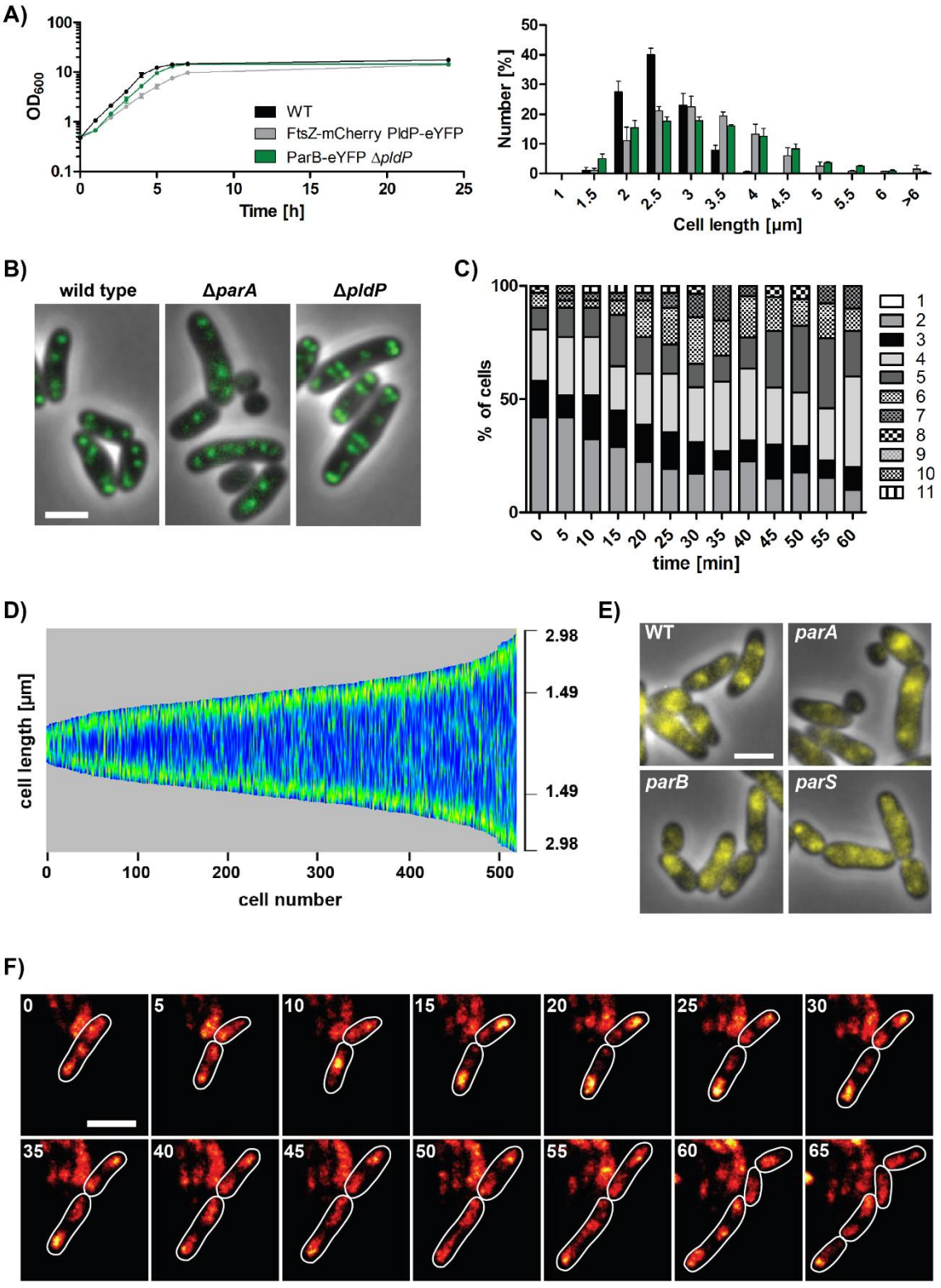

Figure 2.49: Cellular localization of PldP and ParB-*parS* complexes are interdependent.

(**A**) Growth analyses and cell length measurements of *pldP* mutant strains performed in biological triplicates; standard deviations are indicated. Growth rates: wild type (μ = 0.57 h^{-1}), FtsZ-mCherry PldP-eYFP (μ = 0.50, CBK082), ParB-eYFP Δ*pldP* (μ = 0.61, CBK081). (**B**) ParB-eYFP fluorescence in exemplary wild type (CBK007) and *parA* (CBK072) or *pldP* (CBK081) mutant cells shown as overlays of phase contrast

and YFP channels (green). Scale bar, 2 µm. (**C**) ParB-eYFP cluster numbers in Δ*pldP* cells (CBK081) counted in the course of cell elongation (n = 31). Live cell imaging was performed in 5 min time intervals; scale bar, 2 µm. (**D**) ParB-eYFP localization in dependence of cell size in a Δ*pldP* background (CBK081). The demograph illustrates cellular fluorescence profiles aligned according to cell length, with high fluorescence intensities shown in green. (**E**) Microscopy images show PldP-eYFP fluorescence (yellow) of representative wild type (CBK075), Δ*parA* (CBK078), Δ*parB* (CBK077) and *parS*1-10 mutated cells (*parS*, CBK079). Scale bar, 2 µm. (**F**) Time lapse microscopy of strain Δ*parB pldP::pldP-eYFP* (CBK077) in 5 min time frames. Shown is PldP fluorescence of two sister cells tracked for one life cycle in a color gradient as described before (**Figure 2.48**); cell outlines are indicated by white lines. Scale bar, 2 µm.

We further analyzed ParB-eYFP localization in absence of PldP in still microscopy images by plotting cellular fluorescence profiles sorted by cell lengths (**Figure 2.49D**). Similar to wild type cells, ParB clusters stably associate with cell poles, even in minicells with cell sizes below 2 µm (compare with **Figure 2.3D**). Therefore, only ParA but not PldP is needed for polar tethering of ParB protein (**Figure 2.3F**). However, in Δ*pldP* cells newly formed ParB-*parS* clusters do not segregate as directed and strictly timed with the cell cycle towards septal positions as observed for wild type (**Figure 2.3D**, **Figure 2.49D**). Conclusively, *C. glutamicum* ParA-ATPases determine positioning of ParB-*oriC* complexes to different extents, where a *pldP* mutations results in a milder phenotype and does not impact on DNA segregation.

Since PldP likely interacts with the nucleoid via residues implicated in DNA binding (Hester and Lutkenhaus, 2007), we analyzed whether the ParABS system in turn mediates cellular localization of PldP. To this end, PldP-eYFP fluorescence was determined in *par* mutant strains that are defective in DNA segregation to similar extents (**Table S1**,**Figure 2.48A**). Notably, all *par* mutants cause distinctive PldP-eYFP localization within cells (**Figure 2.49E**). In absence of ParA PldP localizes wild type-like at midcell or at quarter cell positions in a large fraction of cells, however, PldP-eYFP fluorescence also appears to be frequently dispersed throughout cells (**Figure 2.49E**). By contrast, PldP distributes mostly homogeneously throughout the cell upon *parS* mutations, while high PldP-eYFP fluorescence intensities at midcell or cell quarter positions are completely absent (**Figure 2.49E**). Deletion of *parB* causes aberrant PldP localization patterns that are ubiquitously observed in all mutant cells. Here, high PldP fluorescence intensities are detected at one or both cell poles that gradually decrease towards midcell positions (**Figure 2.49E**). To further characterize spatiotemporal PldP fluorescence in Δ*parB* cells live cell imaging was carried out. Newborn cells harbor high PldP-eYFP fluorescence intensities at one or both cell poles, however, in the course of the cell cycle PldP accumulates preferentially at old cell poles (**Figure 2.49F**). At late generation stages prior to cell division a fraction of cellular PldP localizes to the young cell

pole and particularly in long cells PldP additionally accumulates in large foci at midcell (**Figure 2.49F**). Therefore, PldP recruitment to cell quarter positions appears to be ParB-dependent, yet PldP remains highly dynamic in absence of ParB. The mechanisms behind the ordered pole-oscillation of PldP in absence of *parB* remains to be investigated. Since *parA* and *parB*/*parS* mutations lead to different degrees of PldP mislocalization, we conclude that cellular PldP positioning depends particularly on ParB-*parS* localization rather than on chromosome organization and segregation per se.

2.6.3. Potential PldP interaction partners

The precise function of *C. glutamicum* PldP is so far unknown, however, it likely positions a certain cargo within cells, as shown for other orphan ParA-ATPases (reviewed in Lutkenhaus, 2012). A bioinformatics screen revealed that a family of ParA-ATPases involved in polar localization of chemotaxis proteins is strictly encoded within corresponding chemotaxis operons (Ringgaard et al., 2011). Therefore, we examined the genomic neighborhood of *pldP* to obtain indications for putative interaction partners using IMG database (Chen et al., 2019). The occurrence of genes surrounding *pldP* is conserved amongst the genus *Corynebacterium* (**Figure 2.50A**). Chromosome-associated proteins, namely SMC kleisin subunit ScpA, SMC-like protein RecN and recombinase XerD, are encoded in close proximity. Most strikingly, *pldP* is frequently encoded in an operon with *scpA* in other *Corynebacterium* species. Anti-mCherry ChIP-seq was performed with a *C. glutamicum* strain containing a mCherry-tagged version of PldP to test whether PldP aids in loading of condensin complexes at *oriC* or positions XerCD for decatenation of sister chromosomes at *terC*-proximal regions (**Figure 2.50B**). However, no clear chromosomal PldP-binding sites were detected, supporting the notion that PldP binds non-specifically to DNA and does not position DNA-binding proteins site-specifically on the *C. glutamicum* chromosome. Besides this, unlike RecN PldP likely does not aid in DNA repair, since a Δ*pldP* strain is not sensitive to mitomycin C-induced DNA damage (AG Bramkamp, unpublished results).

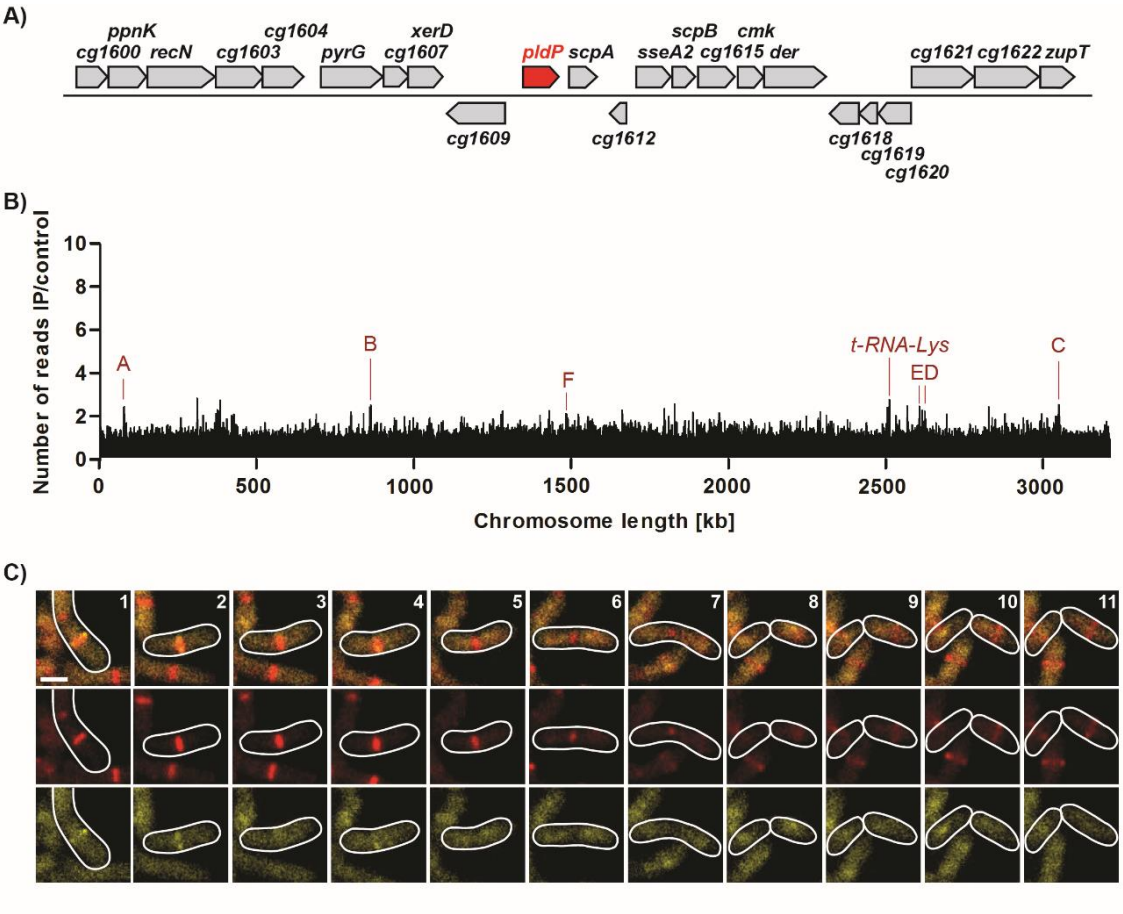

Figure 2.50: Screening for potential functions and interaction partners of PldP.

(**A**) Conserved gene configuration surrounding *pldP* on the *C. glutamicum* chromosome (at ~ 1.5 Mb). (**B**) Anti-mCherry ChIP-seq of cells containing PldP-mCherry (CBK076). Data are plotted in 0.5 Kb bins *ter*C-centered. Highly transcribed genes that coincide with minor enrichment signals are indicated by red letters (rDNA operons A-F). (**C**) Time lapse microscopy of *C. glutamicum* strain CBK082 containing PldP-eYFP (yellow) and FtsZ-mCherry (red). Images were taken in 5 min time intervals comprising one cell cycle. Shown are YFP and mCherry fluorescence and an overlay of both channels each; scale bar, 1 µm.

Since previous data hint to a role of PldP in division site selection, we further investigated PldP localization relative to Z-ring formation using a dual reporter strain *pldP::pldP-eYFP ftsZ::ftsZ-mCherry*. Notably, this strain frequently harbors misplaced Z-rings due to functional constraints of the FtsZ-mCherry fusion construct (**Figure 2.49A**, **Table S1**). Live cell imaging revealed that PldP only rarely colocalized with Z-rings upon formation of band-like structures at midcell, while otherwise being accumulated at midcell or cell quarter positions before Z-ring assembly (**Figure 2.50C**). Therefore, different to positive regulators of Z-ring formation SsgB of *S. coelicolor* or the ParA-like ATPase PomZ of *M. xanthus* (Treuner-Lange et al., 2013; Willemse et al., 2011), which colocalize with Z-rings and directly interact with FtsZ, PldP does not directly recruit FtsZ at

division sites. In order to screen for further interaction partners of PldP, we combined co-immunoprecipitations of PldP with mass spectrometry. Cell lysates containing PldP-mCherry were used in anti-mCherry immunoprecipitation assays (**Figure 2.51A**). Immunoprecipitations of free mCherry-containing lysates served as negative control.

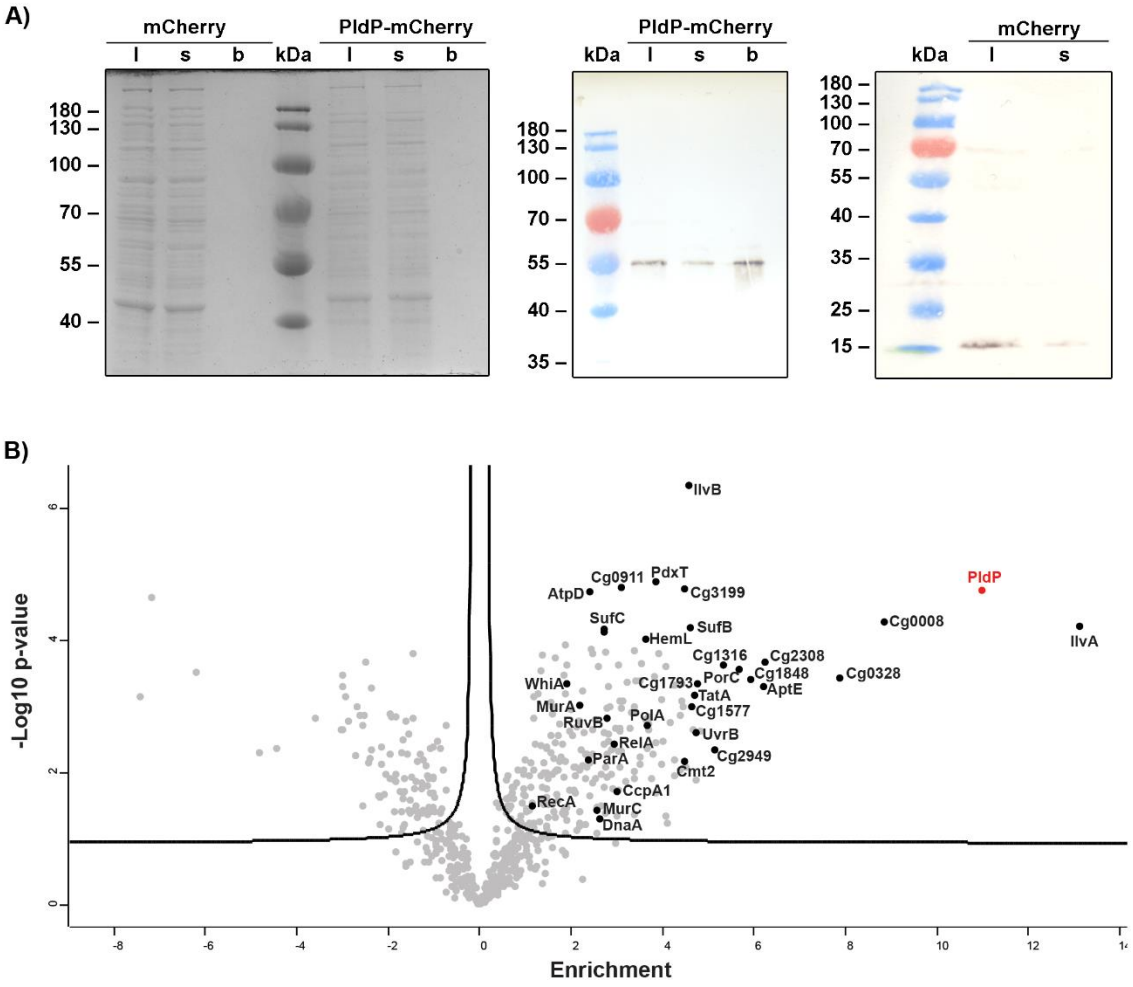

Figure 2.51: Identification of putative interaction partners of PldP.

(**A**) Detection of PldP-mCherry in cell lysates. Immunoprecipitation of full-length fusion PldP-mCherry (58 kDa) and free mCherry (27 kDa) were validated by western blotting (left); coomassie stained gel (right). 10 µl of CBK052 and CBK076 cell lysates (l), 10 µl of magnetic RFP-Trap® beads (b) and 10 µl supernatant (s) were probed; proteins were detected using an α-mCherry antibody. (**B**) Co-immunoprecipitations of PldP-mCherry or mCherry combined with mass spectrometry reveal putative PldP interaction partners (CBK076, CBK052). The difference in mean enrichment is plotted against the -log10 adjusted p-value for each identified protein. Cutoff lines (black) indicate significant enrichments (two-tailed t-test, $p < 0.05$, fold change > 0.1); selected protein names are indicated (black circles).

Out of rougly 3000 *C. glutamicum* proteins 256 proteins were significantly enriched in the PldP-mCherry-immunoprecipitate. Data are illustrated as volcano blot, where a selection of proteins are named in the graph (**Figure 2.51B**).

In addition, a list of proteins with the highest fold-changes compared to the negative control is provided (**Table 4**). Proteins identified in this analysis were further classified according to distinct cellular functions with representative examples being indicated (**Table 5**).

Table 4: Proteins co-immunoprecipitated with PldP in significant amounts.

Difference	Protein[12]	Description
13.10	**IlvA**	Threonine dehydratase
10.98	**PldP**	ParA-like ATPase
8.83	**Cg0328**	Uncharacterized protein, genomic neighborhood: *cgtS1*/*cgtR1*
7.86	**Cg0008**	Uncharacterized hydrolase, genomic neighborhood: *gyrB*
6.24	**Cg2308**	Predicted secreted protein
6.22	**AtpE**	F-type H+-transporting ATPase subunit C
5.93	**Cg1848**	N5, N10-methylene tetrahydromethanopterin reductase
5.68	**PorC**	Porin associated with mycomembrane
5.33	**Cg1316**	DNA/RNA helicase
5.15	**Cg2949**	Predicted secreted protein, genomic neighborhood: *radA*, *cgtS5*/*cgtR5*
4.83	**RbsD**	D-ribose pyranase, component of ribose ABC-type transport
4.78	**Cg1793**	Gluconeogenesis factor, in operon: *whiA*, *uvrC*, *ribX*, *rapZ*
4.75	**Cg1203**	Magnesium chelatase subunit I
4.72	**UvrB**	Excinuclease ABC subunit B
4.69	**TatA**	Component of Tat-secretion system
4.68	**DapC**	Succinyldiaminopimelate aminotransferase
4.63	**Cg1577**	Predicted secreted hydrolase
4.61	**SufB**	ABC-type transporter component
4.56	**IlvB**	Acetolactate synthase
4.51	**Cg0359**	Predicted membrane protein
4.49	**Cg3199**	Predicted hydrolase
4.46	**Cmt2**	Trehalose corynomycolyl transferase
4.45	**Cg3197**	Predicted secreted amidase

4.42	**Cg2793**	ABC-type transporter ATPase
4.41	**UdgA2**	UDP glucose 6-dehydrogenase
4.39	**Cg1968**	Uncharacterized protein
4.38	**CobT**	Nicotinate-nucleotide-dimethylbenzimidazole phosphoribosyltransferase
4.27	**Cg2675**	ABC-type transporter ATPase
4.27	**FolE**	GTP cyclohydrolase
4.27	**Cg1618**	Uncharacterized protein, putative globine YjbI homologue
4.15	**AspA**	Aspartate ammonia-lyase
4.10	**Pyc**	Pyruvate carboxylase
4.10	**Cg1995**	Predicted RNA polymerase Rpb2 domain 6
4.10	**Cg3206**	Phosphoglycerate mutase
4.00	**PutA**	Proline dehydrogenase
3.97	**Cg1340**	Predicted transcriptional regulator
3.96	**MshA**	D-inositol-3-phosphate glycosyltransferase
3.91	**SufD**	ABC-type transporter component
3.86	**SerC**	Phosphoserine transaminase
3.86	**Cg1628**	Predicted hydrolase
3.85	**Cg0899**	Glutamine amidotransferase
3.82	**Cg2678**	Substrate-binding protein of ABC-type transport systems
3.78	**Cg1905**	Predicted phosphotransferase
3.76	**GuaB1**	Inositol-Monophosphat dehydrogenase
3.70	**Cg1600**	rRNA methyltransferase
3.69	**Cg3085**	Alkanal monooxygenase
3.68	**Dld**	D-lactate dehydrogenase
3.66	**DapD**	Tetrahydrodipicolinate succinylase
3.65	**PolA**	DNA polymerase I
3.65	**Cg3128**	ABC-type transporter ATPase
3.62	**HemL**	Glutamate-1-semialdehyde 2,1-aminomutase
3.55	**ThrB**	Homoserine kinase
3.52	**RlmN**	rRNA methyltransferase
3.50	**SecA2**	Protein translocase subunit
3.50	**Cg3032**	Predicted LytR cell envelope-related transcriptional attenuator
3.41	**Mqo**	Malate dehydrogenase

3.39	**Cg3404**	ABC-type Fe^{3+}-siderophore transport, periplasmic component
3.38	**LipA**	Triacylglycerol lipase precursor
3.38	**Cg1246**	Uncharacterized protein
3.38	**TyrS**	Tyrosyl-tRNA synthetase

[1] First 60 hits with the largest fold-changes are listed.

[2] Underlined protein names: Proteins harbor signal peptide sequences that were predicted using the SignalP 5.0 server (Emanuelsson et al., 2007).

First, DNA-binding proteins were identified with functions related to DNA repair, replication and transcriptional regulation. These data are in line with PldP being a chromosome-associated protein, however, PldP interaction with proteins at specific genomic regions is unlikely as shown before by ChIP-seq (**Figure 2.50B**). We further confirm an interaction of PldP with chromosome partitioning protein ParA described before by using bacterial two-hybrid assays (Donovan et al., 2010). Despite weak ParB-PldP interaction signals in bacterial two hybrid assays shown in here and in a previous study (**Figure 2.45D**) (Donovan et al., 2010), ParB was not co-immunoprecipitated in any replicate experiment (**Figure 2.51B**).

Apart from DNA-associated proteins, several enzymes implicated in cell wall biogenesis, like mycolyltransferases and cytoplasmic Mur proteins involved in peptidoglycan synthesis were identified amongst significant hits (**Table 5**). Moreover, a notable fraction of immunoprecipitated proteins are components of different ABC-type transport systems (**Table 5**). Further membrane-associated proteins, in particular several ATP synthase subunits and components of the general secretory (Sec) pathway and the twin-arginine translocase (Tat) pathway were precipitated (**Table 5**, **Figure 2.51B**). Correspondingly, several significant protein hits with very high fold-enrichments harbor signal peptides for secretion, e.g. Cg2308, PorC, Cg2949, RbsD or Cg1577 (**Table 4**). Remarkably, FtsZ and other divisome components were not identified.

Table 5: Functional classification of proteins co-immunoprecipitated with PldP.

Cellular processes	Enzymes involved
DNA binding	DNA repair: UvrB, RecA, PolA, RuvB Replication: PolC, DnaB, Cg1316/Cg0845 DNA helicases Chromosome segregation: ParA Transcriptional regulators: e.g. CcpA1, Cg3202, Cg0156
Cell wall biogenesis	e.g. Cmt1/2 (mycolic acid layer), MurA/B1/C (peptidoglycan)
Membrane associated	ABC-type transporters: e.g. Cg3404 (iron uptake); RbsD (ribose import); Cg2812, Cg0737 (lipoprotein release) Protein export: SecA1/2, TatA/B Further proteins: e.g. PorC, AtpA/AtpD-G (ATP synthase)
Metabolism	e.g. IlvA-D, AspA (amino acid biosynthesis); Pyc, UdgA2, Mqo, Dld (carbon metabolism); CobT, FolE, PdxT (vitamin synthesis), SufB-D (Fe-S cluster biogenesis)
Cell cycle control	Cell division: WhiA, Cg1793 (gluconeogenesis factor) Stringent response: RelA Replication initiation: DnaA

Furthermore, cytosolic enzymes involved in various metabolic pathways were significantly enriched in PldP pull-downs as well as proteins implicated in cell cycle control (**Figure 2.51B**, **Table 5**). In particular, a role of PldP in timing of chromosomal replication initiation could so far be excluded by qPCR analysis (AG Bramkamp, unpublished data).

Compared to co-immunoprecipitations of condensin subunits shown before (**Figure 2.27B**), many proteins were enriched in the negative control samples. Here, mostly ribosomal proteins, chaperones like DnaK and GroE as well as FtsY, a protein adapter involved in secretory pathways, were significantly enriched.

Altogether, PldP pull-down experiments reveal a surprisingly high number of interactors with diverse cellular roles. Further analyses of these proteins will be needed to narrow down the function of PldP to (a) distinct cellular process(es).

3. Discussion

3.1. Spatiotemporal organization of multiple chromosomes

To date, bacterial chromosome organization has only been studied in a limited number of model organisms. Nonetheless, various organizational strategies have already been identified, hinting to a greater diversity in structural and regulatory characteristics than initially anticipated for prokaryotic species (Badrinarayanan et al., 2015; Randich and Brun, 2015). Here, we analyzed overall chromosome dynamics by fluorescently labeling replisomes, *oriC* and *terC* domains in *C. glutamicum*, a characteristic representative of actinomycetales serving as a model for apically growing organisms (Donovan and Bramkamp, 2014).

By tracking ParB-*oriC* complexes throughout generations we found a distinct chromosomal organization in *C. glutamicum*, resembling strategies described in other model species with important differences illustrated in **Figure 3.1A**. First of all, we confirm stable *oriC*-tethering to the cell poles throughout the *C. glutamicum* life cycle (**Figure 2.3**) (Donovan et al., 2010). Therefore, polar recruitment of ParB-*parS* complexes by the landmark protein DivIVA in *C. glutamicum* (Donovan et al., 2012; Letek et al., 2008) appears to be essentially conserved amongst related actinobacteria *M. smegmatis* and *S. coelicolor* (Ginda et al., 2013; Kois-Ostrowska et al., 2016). However, the strictly polar *oriC*-tethering being reminiscent to that of *C. crescentus* and *V. cholerae* is inconsistent with studies in *M. smegmatis*, where *oriC*s are generally more distant to cell poles and localize occasionally to central positions (Santi and McKinney, 2015; Trojanowski et al., 2015). Besides this, unlike model organisms harboring only one polar *oriC* in newborn cells (Fogel and Waldor, 2005; Ginda et al., 2013; Jensen and Shapiro, 1999), *C. glutamicum* permanently maintains at least one polar ParB-*oriC* complex at each cell pole at any growth condition (**Figure 2.3**, **Figure 2.6**). Further contrasting to monoploid bacteria, newly replicated origin domains do not migrate towards opposite cell poles in *C. glutamicum* (Fogel and Waldor, 2005; Jensen and Shapiro, 1999), and instead remain located within their originating cell half (**Figure 2.3**, **Figure 2.10**). Here, ParB-*oriC* complexes position close to septal regions after approximately half of the generation time (**Figure 2.3**), supporting a ParB interaction at the

divisome with the cell division protein FtsZ described before (Donovan et al., 2010). Besides this, spatiotemporal *oriC*-positioning of *C. glutamicum* appears to be primarily governed by the chromosome segregation protein ParA (**Figure 2.3**, further discussed in **3.5**).

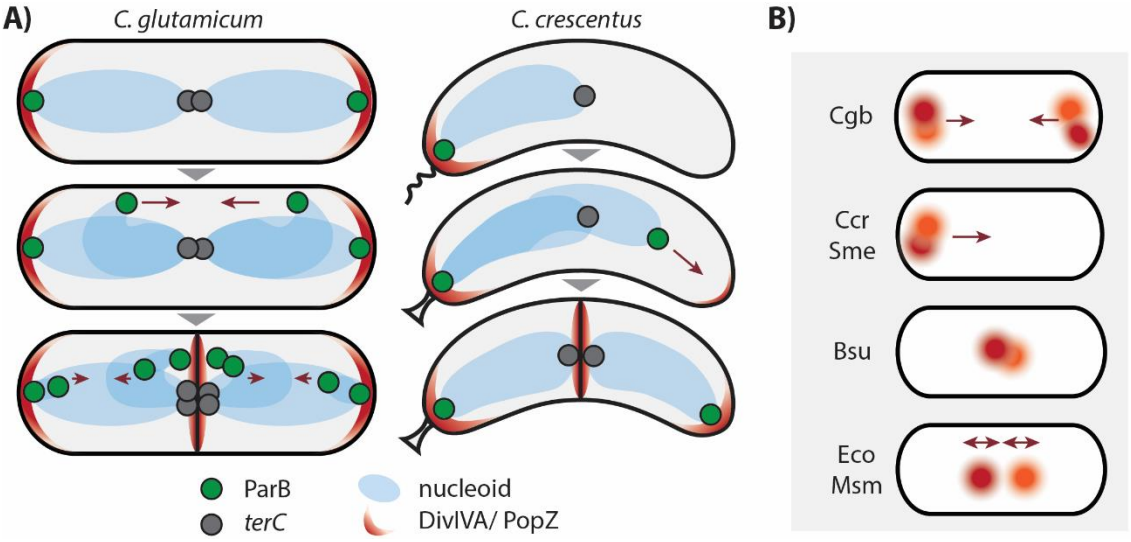

Figure 3.1: Scheme of spatiotemporal chromosome organization and replisome dynamics.

(**A**) Comparison of subcellular *oriC*- and *terC*-localization between *C. glutamicum* and *C. crescentus* life cycles. Subcellular origin migration (red arrows) and polar/septal anchoring is ensured by ParABS and polar factors DivIVA (*C. glutamicum*) and PopZ (*C. crescentus*), while *terC* domains remain at midcell. (**B**) Replisome dynamics (red arrows) in *C. glutamicum* (Cgb), *C. crescentus* (Ccr), *S. meliloti* (Sme), *B. subtilis* (Bsu), *E. coli* (Eco) and *M. smegmatis* (Msm). Replisome pairs are indicated by red and orange circles.

The combination of polar *oriC*s and central *terC* domains (**Figure 2.5**) point to a longitudinal *ori-ter-ter-ori* chromosome configuration in *C. glutamicum* (**Figure 3.1A**), similar to *C. crescentus*, *V. cholerae* and *P. aeruginosa* (David et al., 2014; Vallet-Gely and Boccard, 2013; Viollier et al., 2004). However, the continuous localization of *C. glutamicum terC*s at midcell instead at cell quarters is a surprising finding, since *oriC*s tethered at septal positions may spatially overlay with their corresponding *terC* domains. This chromosomal arrangement has not been described before and, also with regards to central localizations of the right chromosomal arms (**Figure 2.7**), challenges a strict longitudinal chromosome organization in *C. glutamicum*. Cohesion and reliable midcell positioning of sister *terC* domains in *C. glutamicum* (**Figure 2.5**, **Figure 2.6**) have been reported before in proteobacteria *E. coli* and *V. cholerae*, where both processes are coordinated by MatP/*matS* (Demarre et al., 2014; Mercier et al., 2008). However, it is so far

unknown whether organisms like *C. glutamicum* or *C. crescentus* lacking MatP position *ter*Cs centrally by comparable regulatory mechanisms (Jensen and Shapiro, 1999).

Further, replisome tracking using fluorescently labeled β-sliding clamps (**Figure 2.10**) points to replication initiation events at polar *ori*Cs, from where replisomes migrate towards midcell-positioned *ter*Cs in the course of a *C. glutamicum* life cycle (**Figure 3.1B**). Our findings comply with replication processes described in *C. crescentus* and *Sinorhizobium meliloti* (Frage et al., 2016; Jensen et al., 2001), but are in stark contrast to *M. smegmatis*. Here, studies point to midcell-positioned replisome pairs that frequently split during the replication process like shown before in *E. coli* (**Figure 3.1B**), conforming to relatively central *oriC* domains (Reyes-Lamothe et al., 2008; Santi and McKinney, 2015; Trojanowski et al., 2015). Since Corynebacteria and Mycobacteria are closely related species, it comes as a surprise that fundamental strategies of chromosome organization vary considerably from each other. Nonetheless, further prove will be needed to distinguish static replisomes as proposed for *B. subtilis* and *P. aeruginosa* (**Figure 3.1B**) (Lemon and Grossman, 1998; Vallet-Gely and Boccard, 2013) from active replisomes tracking along template DNA, while being pulled along with the growing pole in *C. glutamicum*. Apart from replisome dynamics, the detection of multiple replication events is further in line with high *oriC* and *terC* numbers per cell with up to eight *ori*Cs (**Figure 2.4B**). Here, *oriC* and *terC* domains may stay associated during part of a generation period, yet chromosome copies are not strictly prealigned (**Figure 2.3**, **Figure 2.5**, **Figure 2.9**), similar to *Deinococcus radiodurans* cells of comparably high DNA contents (Passot et al., 2015). Conclusively, our data evince unique features of chromosome organization in *C. glutamicum* that may in large part result from high chromosome numbers per cell, and moreover, point to the importance of expanding the pool of model organisms to perceive bacterial genome maintenance in its full diversity.

3.2. Cell cycle characteristics and implications for environmental adaptability

Bacterial life under varying environmental conditions requires a fine control of the cell cycle (Wang and Levin, 2009; Westfall and Levin, 2018). Here, dynamics in chromosome replication, segregation and cell growth need to compensate for changes in nutritional availability and to cope with environmental stresses, like temperature shifts, accumulation of metabolic products and drought. Our study reveals a unique combination of cell cycle features in *C. glutamicum* that permits conclusions on growth adaptability and lifestyle.

Our data reveal growth rate-dependent cell cycle parameters in *C. glutamicum*, where generation times roughly halve from 130 minutes in minimal medium supplemented with glucose to 63 minutes in complex medium. To achieve this cell cycle adaptation, our data indicate a trend of shortening C-periods by speeding up replisome velocities by roughly one fifth, of overlapping replication periods, of omitting B-periods and shortening D-periods (**Figure 2.14**) in *C. glutamicum* cells. These observations are in line with cell cycle studies of fast-growing bacteria. Here, shortening of non-replicative cell cycle stages are common phenomena upon increased nutrient availability and accordingly, even C-periods have been shown to vary amongst highly different growth rates (Michelsen et al., 2003; Rasmussen et al., 2007; Sharpe et al., 1998). Likewise, the capability of multi-forked replication had so far only been attributed to very fast-growing *E. coli*, *B. subtilis* and *V. cholerae* with doubling times down to 20 minutes (Cooper and Helmstetter, 1968; Stokke et al., 2011; Yoshikawa et al., 1964). However, high *oriC*/*terC* ratios and the detection of multiple replication forks per cell evidence overlapping replication cycles also in the model *C. glutamicum* (**Figure 2.9**, **Figure 2.11**). Our data are further supported by a recent study on the closely related *M. smegmatis* (Trojanowski et al., 2017) confirming that actinobacterial cell cycle control generally allows for multifork replication. While replication was reported to be asymmetric in *M. smegmatis* with only one of two *oriC*s being re-initiated (Trojanowski et al., 2017), in *C. glutamicum* a new round of replication is usually initiated at both polar *oriC*s (**Figure 2.4B**, **Figure 2.12C**). Furthermore, we show that uneven *oriC* numbers observed microscopically rather derive from variable *oriC*-cohesion times (**Figure 2.9F**). Since bacterial cell division and chromosome organization are interconnected processes, it is not surprising that irregular chromosome segregation is reflected by slightly asymmetric cell growth and septum placement in *C. glutamicum* and related actinobacteria (Aldridge et al., 2012; Donovan et al., 2013; Schubert et al., 2017).

Furthermore, *C. glutamicum* replisome velocities of 340 bases per second appear to be moderate (**Table 2**) compared to the most extreme replisome speeds known amongst bacteria with 50 and 1000 bases per second in *M. tuberculosis* and *E. coli*, respectively (Cooper and Helmstetter, 1968; Hiriyanna and Ramakrishnan, 1986). Notably, highly different DNA synthesis rates between the related species *M. tuberculosis* and *C. glutamicum* are likely not a matter of DNA polymerase activity per se, since these enzymes share a high level of homology (Timinskas et al., 2014). Instead, DNA synthesis rates may be linked to the bacterial metabolism, for example differences in nucleotide availability between *M. smegmatis* and *M. tuberculosis* were speculated to be rate-determining factors (Trojanowski et al., 2015).

Apart from well-known bacterial cell cycle features, recent studies further suggest that multiploidy may be a common prokaryotic characteristic, however, genome copy numbers in most bacterial species remained poorly explored to date (Soppa, 2014). Accordingly, the high DNA content with two up to twelve *oriC*s in *C. glutamicum* could not be explained by overlapping replication cycles alone (**Figure 2.12**). Even though the presence of multiple chromosomes per cell has been suggested before (Neumeyer et al., 2013), only the combination of flow cytometry and marker frequency analysis unambiguously supports the diploidy of *C. glutamicum* cells (**Figure 2.11**, **Figure 2.12**). Although it has been shown that ploidy levels change depending on growth phase and growth rate in certain bacteria (Maldonado et al., 1994; Postgate et al., 1984), we did not find growth conditions that support monoploid cell cycle stages in *C. glutamicum*. Even at very slow growth rates ($\mu = 0.15\ h^{-1}$) *C. glutamicum* usually harbors at least two chromosome copies per cell (**Figure 2.6**, **Figure 2.13E**). This strict diploidy in *C. glutamicum* postpones division of replicating sister chromosomes into separate cells by one generation. As a consequence, *oriC*-cohesion times can be highly variable, where nucleoid separation does not depend on a strict temporal coordination with the cell cycle (**Figure 2.9F**). By contrast, *oriC*-cohesion intervals are much more confined in mono- or meroploid *E. coli* and *C. crescentus* (Bates and Kleckner, 2005; Jensen, 2006; Nielsen et al., 2006).

Surprisingly, the presence of at least two chromosomes per cell is not conserved amongst closely related actinobacteria (Santi and McKinney, 2015; Trojanowski et al., 2015). Apart from that, studies of proteobacteria suggest that bacterial ploidy levels do not appear to correlate with species-specific features including growth rate or temperature, genome size and symbiotic or parasitic life styles (Pecoraro et al., 2011). Future research will need to address the evolutionary advantage(s) of diploidy and how ploidy is regulated in *C. glutamicum*. One might speculate that multiple chromosomes may be an environmental adaptation of the soil bacterium, where desiccation commonly effects DNA damage (Potts, 1994). Desiccation-induced DNA damage is known to become exacerbated in recombination-defective bacterial strains (Asada et al., 1979; Mattimore and Battista, 1996), while polyploidy was suggested to support DNA repair in bacteria and archaea (Hansen, 1978; Zerulla et al., 2014). Therefore, strict diploidy of *C. glutamicum* may increase the chance for DNA repair based on homologous recombination. In line with this hypothesis survival rates of Corynebacteria are comparably high upon long-term desiccation stresses (Gilichinsky et al., 1992; Miyamoto-Shinohara et al., 2008). Most strikingly, microbial analyses of long-term preserved ecosystems revealed a predominance of Corynebacteria in older permafrost sediments (Gilichinsky et al., 1992). Alternatively, multiplied chromosomes may serve

as storage polymers in *C. glutamicum*, as suggested for the polyploid archaeon *Haloferax volcanii* (Zerulla et al., 2014). Such an adaptation may contribute to the pronounced resistance of soil bacteria including Corynebacteria to starvation stress (Boylen and Mulks, 1978).

In summary, the combination of overlapping replication cycles and diploidy in *C. glutamicum* indicates a so far undescribed cell cycle regulation. Our data suggest adaptability to variable growth conditions and substantial advantages under very challenging environmental conditions, further adding to our understanding of growth behavior, genome structure and manipulation of the medically and economically relevant genus *Corynebacterium*.

3.3. ParB-*parS* complexes predefine multiscale chromosome structuring

Chromosome folding and segregation is mainly mediated directly or indirectly by ParB-*parS* complexes, key players of bacterial nucleoid organization. Currently, information on chromosome organization in other than the standard model species is lacking. This study gives a comprehensive picture on chromosome folding in *C. glutamicum* and characterizes the underlying structure of ParB-*parS*-nucleoprotein complexes.

We report a genomic cluster of ten *parS* sites in *C. glutamicum* that are located close to *oriC* and exhibit a very strict sequence identity, hinting to cluster generation by *parS*-duplication events. ParB spreading in a genomic range of around 32 Kb along a single *parS* site (**Figure 2.18B**) is consistent with ParB-enrichment signals in other bacteria (Breier and Grossman, 2007; Lagage et al., 2016; Tran et al., 2018). In addition, we show that one *parS* site is indeed sufficient for reliable chromosome segregation in *C. glutamicum*, similar to *B. subtilis* and *P. aeruginosa* (Lagage et al., 2016; Sullivan et al., 2009). Nonetheless, the more severe phenotypes of ParB modifications in presence of only one *parS* site (CBK025, CBK048, **Table S1**) allows to speculate that multiple *parS* repeats add an advantageous robustness against disturbances to DNA segregation processes. Therefore, it takes no wonder that also many other bacteria evolved arrays of *parS* sequences (Livny et al., 2007). Notably, additional ParB-enrichment signals at highly transcribed genes are ambiguous results that are generally considered to be physiologically irrelevant (Minnen et al., 2016; Nolivos et al., 2016; Teytelman et al., 2013). Such signals likely derive from formaldehyde actively reacting with single-stranded DNA during ChIP-seq experiments (McGhee and Von Hippel, 1977).

This study further revealed that ParB spreading along the *parS* cluster is interrupted between *parS*1-4, *parS*5-8 and *parS*9-10, which could be the result of roadblocks such as site-specific nucleoid-associated proteins shown before in other organisms (Debaugny et al., 2018; Murray et al., 2006). Therefore, the structure of ParB-*parS* clusters was analyzed in more detail by 2D PALM, revealing distinct ParB-dense regions within a cluster (**Figure 2.25**, **Figure 2.26**). Since these sub-clusters correlate to the number of ParB spreading-zones, our data confirm that the structure of ParB-nucleoprotein complexes is indeed affected by local changes in ParB-DNA interactions. In line with a recent study on ParB complex formation in *V. cholerae*, sub-clusters derive from independent nucleation and caging events that merge into one ParB-macro-complex per *oriC* in *C. glutamicum* (Debaugny et al., 2018). **Figure 3.2A** provides a model of the *C. glutamicum* ParB-*parS* complex structure based on our findings.

Different to *P. aeruginosa*, *C. glutamicum* tolerates *parS* insertions at *terC* (**Figure 2.22**) (Lagage et al., 2016). This comparably high flexibility in DNA segregation might derive from its genetic basis, making *C. glutamicum* an ideal model for studies on genomic *parS* localization: *oriC*-cohesion times can be highly variable and hence, are not strictly coordinated with cell cycle timing (**Figure 2.9F**). However, ectopic *parS* sites inserted at varying distances from the original cluster lead to severe chromosome segregation defects in *C. glutamicum* (**Figure 3.2B**). Accordingly, the main prerequisite for reliable chromosome partitioning is not a strict timing with the cell cycle, but the positioning of its starting point being coordinated with the direction of other processes like transcription or replication events. Surprisingly, also the anchoring process of ParB-*parS* complexes at cell poles is non-functional in *C. glutamicum*, suggesting that chromosomes do not reorient within cells according to their ectopic *parS* sites (**Figure 3.2B**). This observation is in stark contrast to *V. cholerae* and *C. crescentus* studies that demonstrate polar association of shifted *parS* sites (**Figure 3.2B**) (David et al., 2014; Toro et al., 2008; Umbarger et al., 2011) by specific landmark proteins (Bowman et al., 2008; Ebersbach et al., 2008; Yamaichi et al., 2012). Whether DivIVA-ParABS anchorage systems as described for *C. glutamicum* are influenced by additional, yet unknown factors linked to the chromosomal *oriC* region remains to be shown (Donovan et al., 2012). Besides this, even a *parS* site in 90 Kb *oriC*-distance (CBK036) impaired DNA segregation in *C. glutamicum*, while ectopic *parS* sites in 400 to more than 600 Kb distances to *oriC* are functional in other bacteria (Lagage et al., 2016; Toro et al., 2008). Therefore, provided that the competence zone for functional *parS* sites exceeds the native *parS* cluster range in *C. glutamicum* (**Figure 2.15A**), it would be considerably smaller than in other species (Lagage et al., 2016).

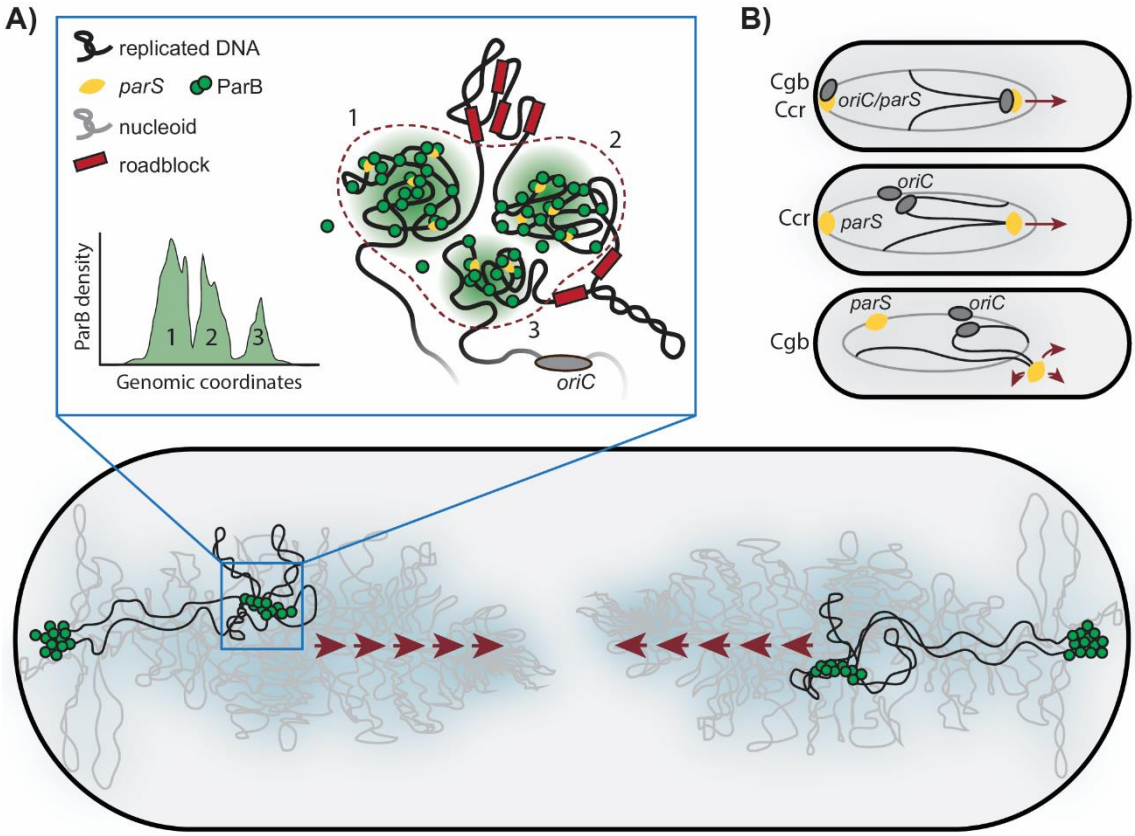

Figure 3.2 ParB/*parS*-mediated *oriC* structuring and separation along nucleoid-scaffolds.

(**A**) Top: Model of ParB-*parS* complex folding in *C. glutamicum*. Complexes consist of several ParB-dense regions (sub-clusters) formed by three nucleation zones that comprise several *parS* sites. Below: Directed chromosome segregation in a diploid *C. glutamicum* cell. Sister ParB-*parS* complexes track along nucleoid-bound ParA from cell poles towards midcell positions (red arrows). (**B**) Genomic positioning of *parS* impacts on reliable chromosome segregation in *C. glutamicum*. Shifting *parS* sites from *oriC*-proximal regions (top) to distant genomic loci reorients the chromosome in *C. crescentus* accordingly (Ccr, middle) but impairs polar *parS*-tethering and directed DNA segregation (red arrows) in *C. glutamicum* (Cgb, below).

Apart from structuring of *oriC*-complexes, 3C analyses demonstrate that *parS* sites are major determinants of global chromosome folding in *C. glutamicum*, supporting previous studies of other models (Le et al., 2013; Marbouty et al., 2015; Tran et al., 2017; Wang et al., 2015). The *C. glutamicum* chromosome adopts distinct short-range contacts and, in line with a longitudinal chromosome arrangement, replichores are cohered emanating from *parS* sites as shown in *B. subtilis* (**Figure 2.16**) (Marbouty et al., 2015; Wang et al., 2015). Our study clearly shows that ParB proteins are recruited at *parS* sites and in turn load SMC that is responsible for the alignment of

the two chromosomal arms (discussed below). Different to *C. crescentus*, chromosomal arms of *C. glutamicum* interact along their entire length like shown in *B. subtilis* and these interaction ranges are comparably more confined to corresponding opposite regions than in *C. crescentus* (Marbouty et al., 2015; Tran et al., 2017; Wang et al., 2015). Our data further suggest the existence of a *parS*-mediated folding pattern of the *oriC* domain that contrasts to other chromosomal regions. Here, broad chromosomal interactions are mediated in a 250 Kb range surrounding the *parS* cluster with contacts being confined by ParB, and in part by SMC (**Figure 2.20**). However, a hairpin structure as reported for *B. subtilis* (Marbouty et al., 2015) is absent in the *C. glutamicum oriC* region. Moreover, chromosomal interaction ranges tend to decrease from *parS* sites towards *terC* regions resembling the *B. subtilis* chromosome conformation, while the *E. coli* chromosome harbors distinct contact patterns with two loosely structured segments and a highly confined *terC* region (Lioy et al., 2018; Marbouty et al., 2015).

Further, we describe ParB/*parS*-dependent DNA segregation signals showing that the longitudinal chromosome arrangement allows for ParAB-driven *oriC*-segregation trailing along the nucleoid (**Figure 2.16**, **Figure 2.19**) as visualized in **Figure 3.2A**. A study on chromosome conformation in *C. crescentus* did not address comparably very weak signals, which may not have been distinguished from background in these analyses (Tran et al., 2017). ParB-*parS* segregation signals are likely enhanced in *C. glutamicum* contact maps due to a continuous succession of C-periods. We hypothesize that bacteria with polarly positioned *oriC*s and an *ori-ter* chromosomal organization, like in *C. glutamicum* and *C. crescentus*, rely on the ParABS system for *oriC*-segregation using the nucleoid-scaffold as a track. By contrast, the ParABS system cannot be efficiently used by organisms with central *oriC*s and replisomes. Here, *B. subtilis* ParABS is an exception, since severe *parAB* (*spo0J*/*soj*) phenotypes only occur during sporulation, where chromosomes organize in a longitudinal fashion (Ireton et al., 1994). Accordingly, segregation signals are present, but do not span the whole chromosomal length in *B. subtilis*, where a transversal chromosome arrangement only provides a track for initial *oriC*-segregation (Wang et al., 2015). Further, those *oriC*-contacts depend not only on ParB, but also on the SMC/ScpAB complex, underlining the deviating impacts of the condensin complexes on chromosome segregation between *C. glutamicum* and *B. subtilis* (Wang et al., 2015). Altogether, we reveal a combination of known chromosome folding mechanisms of models *B. subtilis*, *E. coli* and *C. crescentus* in *C. glutamicum*, further adding new aspects to segregation-specific chromosomal contacts in bacteria.

3.4. Functional divergence of *C. glutamicum* condensins

Condensins are two widely conserved enzyme machineries, which have been implicated in bacterial chromosome folding and segregation processes. Up to now, it was assumed that prokaryotes either harbor the SMC/ScpAB or the MukBEF complex (Cobbe and Heck, 2004) and accordingly, functional characterization of bacterial condensins was mainly restricted to species that exclusively harbor one type of condensin complex (Gruber, 2018; Nolivos and Sherratt, 2014). However, recent studies point to coexistences of several condensins in diverse bacterial species (Petrushenko et al., 2011). Likewise, our model bacterium *C. glutamicum* contains SMC/ScpAB and the poorly characterized Muk-like MksBEFG complexes. We hypothesized that also *C. glutamicum* condensins SMC/ScpAB and MksBEFG both function in chromosome organization, as it was described for the *P. aeruginosa* SMC/ScpAB and MksBEF complexes (Petrushenko et al., 2011). To our surprise, *C. glutamicum* condensins do not have redundant functions in chromosome organization. Functional implications of our findings on both bacterial condensin complexes are discussed in the following.

3.4.1. Assistance of SMC in ParABS-mediated chromosome organization

The functional interplay of ParABS and SMC/ScpAB in chromosome folding and segregation had been described in bacteria that do not contain a second condensin complex (Le et al., 2013; Lioy et al., 2018; Marbouty et al., 2015; Tran et al., 2017; Wang et al., 2015). However, also in *C. glutamicum* exclusively SMC/ScpAB appears to be recruited to the chromosome, where we identified ParB-*parS* complexes as specific loading points (**Figure 2.33**) similar to other model bacteria (Gruber and Errington, 2009; Minnen et al., 2011; Sullivan et al., 2009). Contact maps of *smc* mutant strains prove that SMC is the major player of chromosomal replichore cohesion in *C. glutamicum* (**Figure 2.32**), supporting the model of bacterial DNA organization by both ParABS and SMC/ScpAB (**Figure 3.3A)** (Bürmann and Gruber, 2015). Therefore, the function of SMC in chromosome folding is conserved in all organisms tested so far, including *C. glutamicum.*

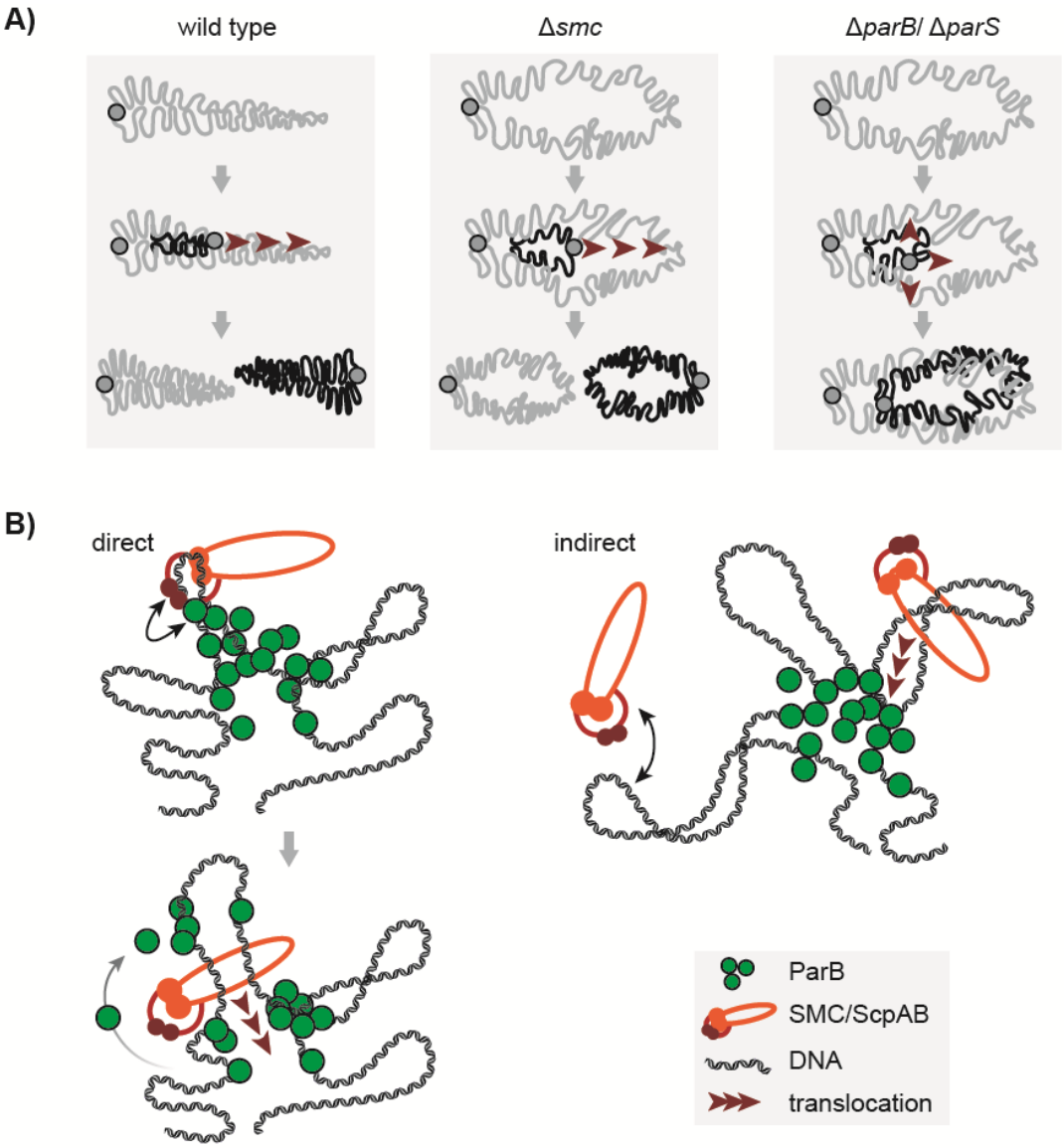

Figure 3.3: ParB-SMC/ScpAB cooperation in chromosome organization of *C. glutamicum*.

(**A**) Cartoon showing replichore cohesion and *oriC*-segregation-phenotypes in wild type and *smc* or *parB*/*parS* mutants. Chromosome and replicating sister DNA are illustrated by grey and black lines including *oriC* regions (grey circle); red arrows indicate direction of DNA segregation. (**B**) Models for chromosomal SMC/ScpAB-entrapment at *oriC*-proximal ParB-*parS* cluster. SMC/ScpAB is either recruited by direct interactions with ParB or indirectly by distinct ParB-*parS*-mediated DNA-structuring.

The bow-shaped structure in the contact map of a *smc* mutant strain with an ectopic *parS* site reflects an asymmetric progression of SMC complexes along chromosomal arms (**Figure 2.23**), which has been described before in *B. subtilis* and *C. crescentus* (Tran et al., 2017; Wang et al., 2017; Wang et al., 2015). Notably, in any study so far replichores could not be cohered by SMC past *terC* regions. Our results confirm that the interaction of chromosomal arms is incomplete.

Here, transcription of highly expressed genes that is to large parts co-oriented with replication may interfere with the relocation of SMC/ScpAB to *parS*-distant regions (Tran et al., 2017; Wang et al., 2017). Besides this, prominent condensin-roadblocks adjacent to the native *parS* sites shown here for *C. glutamicum* have been described before in *B. subtilis* (Minnen et al., 2016), suggesting that such structural features may be common amongst bacterial chromosomes and do not highly impair SMC relocation.

Moreover, bacterial two-hybrid analyses revealed a so far undescribed self-interaction between ScpA subunits of *C. glutamicum* condensin (**Figure 2.28**). Therefore, SMC/ScpAB might be able to assemble dimeric structures, like shown for the *E. coli* MukBEF complex (Badrinarayanan et al., 2012; Woo et al., 2009). These data support the previously suggested handcuffing model that is based on the observation of asymmetric arm cohesion emanating from ectopic *parS* sites. (Wang et al., 2017). According to this hypothesis, two SMC/ScpAB complexes would be physically coupled and could bypass roadblocks by individual release and rebinding events from DNA on their way towards *terC* (Wang et al., 2017). Further experimental prove will aid to our understanding of how SMC-movement is accomplished along entire bacterial chromosomes (Gruber, 2018).

Besides this, interactions between ParB and SMC/ScpAB have been suggested (Gruber and Errington, 2009; Marbouty et al., 2015; Minnen et al., 2011; Tran et al., 2017; Wang et al., 2015), however, it is so far unclear whether ParB acts as direct SMC loader similar to eukaryotic SMC complexes as illustrated in **Figure 3.3B** (Chao et al., 2017; Ciosk et al., 2000). Here, we describe a new phenotype for a ParB point mutation in the N-terminal protein-domain in *C. glutamicum*, which likely leads to weakened ParB-ParB dimer interaction as indicated by decreased and less defined ChIP-enrichment signals at *parS* sites (**Figure 2.40A**). Since this mutation further induces enhanced SMC/ScpAB-retention at *parS* sites, $ParB^{R175A}$ might block SMC-release from its loading site, for example by locking the ATP-bound state of SMC (Minnen et al., 2016). Building on a direct interaction, weak interaction signals of ParB with ScpB were detected in bacterial two-hybrid analyses (**Figure 2.28A**). Alternatively, SMC/ScpAB could load at chromosomal sites of distinct DNA topology mediated by ParB-*parS* complexes (**Figure 3.3B**). Consequently, structurally altered DNA at loading sites could result in an indirect SMC-entrapment in higher-order $ParB^{R175A}$-nucleocomplexes. Unfortunately, 3C data could not help to choose between one of those two models but in either case, the $ParB^{R175A}$ phenotype of *C. glutamicum* underlines the crosstalk between SMC/ScpAB and ParB in bacterial nucleoid organization. Microscopic analysis further suggests a correlation of SMC-mCherry foci with *oriC* organization, since chromosomal

SMC-loading requires ParB and *parS* (**Figure 2.36A**) as shown before in *B. subtilis* (Sullivan et al., 2009). Therefore, SMC foci likely reflect transient SMC-enrichment at ParB nucleoprotein complexes.

However, studies in *C. glutamicum* consolidate the idea that SMC-mediated replichore-interactions are only essential for origin segregation in bacteria that partition their chromosomes without ParABS (**Figure 3.3A**) (Nolivos and Sherratt, 2014), yet the high conservation of SMC/ScpAB amongst bacteria hints to an essential function (Cobbe and Heck, 2004). The mild *smc*-phenotype in combination with a ParB-eYFP modification (**Table S1**) strongly suggests a supportive role for SMC/ScpAB in the process of nucleoid separation. Other enzymatic machineries like DNA translocases SpoIIIE or SftA in *B. subtilis* and FtsK in *E. coli*, which clear DNA from the division plane, are essential in absence of condensins (Britton and Grossman, 1999; Kaimer et al., 2009; Yu et al., 1998). Therefore, similar protein-interrelations might counterbalance a loss of SMC in *C. glutamicum*, while SMC could in turn act as an advantageous backup system in DNA segregation. With regard to SMC-co-immunoprecipitation of non-nucleoid-associated proteins (**Table 3**), alternative roles for condensins in processes other than chromosome segregation should also be taken into consideration.

3.4.2. Role of MksB in maintenance of foreign plasmids

All bacterial and eukaryotic condensins have so far been implicated in the structural organization of chromosomes and DNA repair (reviewed in Hassler et al., 2018; Nolivos and Sherratt, 2014). Surprisingly, our data provide clear evidence that the class of MksBEFG proteins do not interact with the chromosome (**Figure 2.41**, **Figure 2.42**). Therefore, contrary to current opinion, chromosome maintenance is not a conserved feature amongst condensins.

Instead, we demonstrate a role for MksBEFG complexes in plasmid-related defense, as suggested recently by testing the impact of heterologous *mksBEFG*-overexpression on the uptake of one high copy number plasmid (Doron et al., 2018). However, the role of MksBEFG was never examined in native hosts. By contrast, we show that native Mks complexes in *C. glutamicum* appear to exclusively reduce the copy numbers of low-copy number plasmids per cell (**Figure 2.44**). The plasmid-dependent selectivity raises the question of how MksBEFG complexes discriminate between certain plasmids. In general, plasmids have been shown to adapt to their native host species. For instance, a plasmid isolate from waste water indicates the occurrence of natural recombination events between different plasmid backbones (Schlüter et al., 2003). Evolutionary

experiments further revealed a species-dependent stability of that plasmid and proposed adaptations to new bacterial hosts by compensatory mutations in the host and the plasmid during the process of slow plasmid loss (De Gelder et al., 2007). In line with the hypothesis of plasmid-host adaptation, high copy number plasmids used in this study derive from cryptic *C. glutamicum* plasmids (Cremer et al., 1990; Eikmanns et al., 1991), while replicons of both low copy number plasmids originate from a plasmid isolated from the closely related *C. diphteriae* (Kirchner and Tauch, 2003; Reinscheid et al., 1994). Similarly, in the study of Doron et al. (2018) the transformation efficiency of *B. subtilis* with a native expression vector was tested in presence of MksBEFG systems of related species of the genus *Bacillus*. Therefore, plasmid recognition by MksBEFG is likely based on plasmid-specific characteristics, like the structural organization of the replication origin or replication-associated proteins. For example, there is prove for mutations in plasmid-encoded replication initiator proteins increasing plasmid stability in the coevolved host or even increasing the overall host range (Maestro et al., 2003; Sota et al., 2010). Plasmid recognition by MksBEFG may as well be based on a distinct DNA topology, for instance plasmid supercoiling in *B. subtilis* seems reduced compared to other Gram-positive bacteria (Novick et al., 1986). Since MksBEFG lacks interaction with the chromosome, it is further appealing to speculate that the complex at the same time distinguishes self from foreign circular DNA. To this end, there are indications that related eukaryotic SMC5/6 associates with chromosomal DNA based on characteristic helical tensions that are dependent on the size of circular DNA (Kegel et al., 2011). Alternatively, MksBEFG could be excluded from bacterial chromosomes by an unknown nucleoid-associated protein analogous to the MukB-displacement from *terC* regions by MatP in *E. coli* (Nolivos et al., 2016).

Moreover, we show a direct interaction of MksG with the MksBEF complex via the MksF subunit for the first time (**Figure 2.28**). Notably, MksG subunits were proposed to be essential for the plasmid-related function of MksBEFG (Doron et al., 2018). This prediction is in line with experimental data, revealing a functional divergence of *P. aeruginosa* MksBEF aiding in chromosome segregation (Petrushenko et al., 2011) and *C. glutamicum* MksBEFG complexes functioning in plasmid maintenance shown here. Interestingly, in *Corynebacterineae* the *mks* operon is only present in 35 % of known species where MksG often does not exist, therefore, Mks complexes as well as their effect on DNA do not seem to be conserved even amongst related species. Since MksG has a predicted topoisomerase domain (Doron et al., 2018; Petrushenko et al., 2011), the MksBEFG mode of action could be related to alteration of DNA-supercoiling, similar to *E. coli* MukBEF complexes. Here, an interaction between the *E. coli* MukB complex with

topoisomerase IV subunit ParC had been shown to stimulate the activity and to promote *oriC*-recruitment of topoisomerase IV, thereby facilitating stabilization of overall negative supercoiling and decatenation of replicating sister *oriC*s (Hayama and Marians, 2010; Li et al., 2010; Petrushenko et al., 2006; Zawadzki et al., 2015). Implications of MukBEF on plasmid topology *in vivo* were also reported (Weitao et al., 2000). Based on the assumption of MksBEFG likewise mediating alterations in plasmid supercoiling, the reduction of plasmid copy numbers per cell can be explained by topology-based interfere with replication initiation, its progression or the transcription of plasmid-encoded replication proteins illustrated in **Figure 3.4** (Nesvera et al., 1997; Yang et al., 1979). Most strikingly, the activity of a plasmid replication initiator has been shown to depend on a distinct DNA twist (Pastrana et al., 2016). Alternatively, non-specific DNA binding of MksBEFG could result in steric hindrance of similar replication-related processes (**Figure 3.4**). Apart from that, the Mks system might interfere with plasmid segregation by coherence of sister DNA strands, analogous to trapping of sister chromatids by the eukaryotic cohesin complex (**Figure 3.4**) (reviewed in Nasmyth and Haering, 2009).

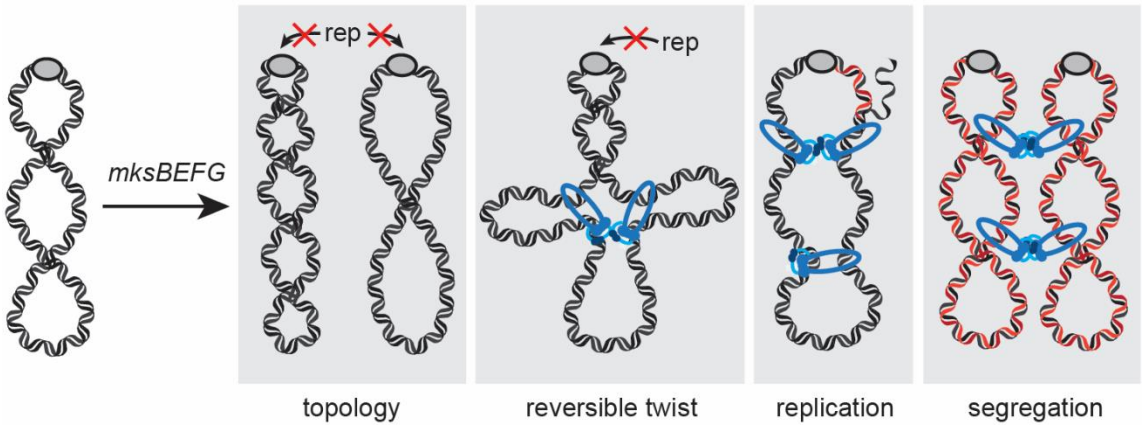

Figure 3.4: Models for MksBEFG-mediated reduction of plasmid copy numbers.

In the first two scenarios replication initiation (rep) is inhibited by changes in overall plasmid topology by the topoisomerase activity of MksG or by reversible alterations of DNA-twist by translocating MksBEFG complexes. In the third model plasmid replication or transcriptional processes are stalled due to steric hindrance by MksBEFG complexes, whereas model four implies a MksBEFG-mediated cohesion of sister plasmids leading to diminished segregation. Shown are plasmids (black lines) with origins of replication (grey circles), newly replicated DNA (red lines) and MksBEFG complexes (blue, open circles).

Further, the direct interaction of a Mks complex with a polar scaffold protein like the *C. glutamicum* DivIVA has not been described before (**Figure 2.28A**, **Figure 2.41B**), supporting the notion that MksBEFG condensins function differently from chromosome organizing complexes in a spatially confined way. In addition to interference with DNA topology, potential plasmid tethering to cell poles could equally result in plasmid defense by preventing DNA-transfer to daughter generations. Polar plasmid localization pattern had been described before for the *E. coli* ColE1 plasmid (Yao et al., 2007).

In any case, since plasmids are inevitable for genomic engineering and are of medical relevance as vehicles of antibiotic resistance, it is of immense importance to identify the Mks-mode of action and the Mks-targeted feature that specifies host range and plasmid copy numbers. Further, *mks* deletion strains are promising candidates to increase plasmid transformation efficiencies and to expand the genetic engineering toolbox with otherwise non-replicating plasmids of unrelated bacterial species. In particular, *mks* deletion strains of the economically important *C. glutamicum* could find biotechnological applications in areas of amino acid and vitamin production.

Interestingly, the Mks system was identified in a bioinformatics approach as a potential phage defense system due to its genomic co-occurrence with known systems like restriction modification systems and CRISPR/Cas in so called defense-islands (Doron et al., 2018), Therefore, further studies need to show whether MksB exclusively targets plasmids or whether it is an universal system to defend foreign DNA including bacteriophages. Accordingly, the closest eukaryotic relative to MksB, the Rad50 complex, is involved in innate immune defense combating viral DNA through several pathways. Here, binding of Rad50 complexes to phage DNA interferes with viral replication by activation of a checkpoint kinase that mediates local DNA damage response (Shah and O'Shea, 2015), by formation of catenanes via non-homologous end joining (Boyer et al., 1999; Stracker et al., 2002) or by inducing the production of interferons and interleukins (Kondo et al., 2013; Roth et al., 2014). In an even more striking analogy to the impact of MksBEFG on plasmids, the SMC5/6 complex was recently proposed to interfere with transcription of episomal virus genes by specific binding to circular DNA of hepatitis B virus (Decorsiere et al., 2016). Therefore, functions in defense against foreign DNA likely date back to an ancient origin shared by pro- and eukaryotic SMC-like proteins. However notably, our data reveal that MksBEFG is the only known condensin amongst pro- and eukaryotes that exclusively acts on non-chromosomal DNA.

3.5. Collaborative action of ParABS in chromosome orientation and segregation

ParABS systems are crucial for reliably segregating sister chromosomes in the course of bacterial DNA replication by a conserved diffusion-ratchet mechanism. The group of actinobacteria further shares fundamental principles of ParABS-mediated *oriC*-localization and -tethering to cell poles (Trojanowski et al., 2018). Here we have demonstrated how *C. glutamicum* ParA contributes to DNA segregation and *oriC*-association with cell poles, pointing to new aspects in localization interdependencies of the ParABS segregation system in actinobacteria.

Upon replication initiation in the diploid *C. glutamicum* one out of each replicated *oriC* pair segregates from cell poles toward the midcell position along nucleoid-associated ParA, while the other sister remains tethered to polar DivIVA (**Figure 2.3**, **Figure 2.4**) (Donovan et al., 2012). To this end, ParB-*parS* complexes establish separate dynamic ParA gradients within each cell half (**Figure 2.45**, **Figure 2.46**), while a fraction of ParA is retained at polar ParB-*oriC* complexes (**Figure 2.45**) (Donovan et al., 2010). By contrast, monoploid bacteria like *C. crescentus* or *V. cholerae* that segregate chromosomes to opposite cell poles establish single gradients across the full cell length (Fogel and Waldor, 2006; Ptacin et al., 2010). Further, deletion of ParA completely abolishes the directed ParB segregation yielding in more than 20 % of anucleate cells (**Figure 2.2**, **Figure 2.3**, **Table S1**) (Donovan et al., 2010), underlining the importance of ParABS for chromosome segregation in *C. glutamicum*. However, we also show a complete loss of polar *oriC*-tethering in absence of ParA (**Figure 2.2**, **Figure 2.47**) (Donovan et al., 2010), thus polar interactions of ParB with DivIVA described before (Donovan et al., 2012) appear to be strengthened by ParA (**Figure 2.45**). Here, a possible impact of ParA on *oriC*-cohesion remains to be shown. Hypothesizing a direct ParA-DivIVA interaction in *C. glutamicum* is supported by studies of closely related actinobacteria *M. smegmatis* and *S. coelicolor* that localize their *oriC* domains by ParA interactions with the DivIVA homologue Wag31 or indirectly using a protein adapter (Ditkowski et al., 2013; Ginda et al., 2013). Moreover, polar ParA-anchoring also appears to be a common chromosome organizing strategy amongst various bacterial phyla (Harms et al., 2013; Schofield et al., 2010; Yamaichi et al., 2012). Besides this, ParA-eYFP localizations in *parS* and *parB* deletion strains reveal that the polar ParA foci are in turn actively stabilized by ParB even at low local concentrations, since absence of ParB but not of *parS* inhibits ParA-association with the cell poles (**Figure 2.47**). These data point to an interdependent ParAB recruitment to cell poles, strongly suggesting DivIVA to be the common target of *C. glutamicum* partitioning

proteins. Notably, in actinobacteria other than *C. glutamicum* only polar ParA interactions were so far attributed to *oriC*-anchoring (Ginda et al., 2013; Jakimowicz et al., 2007b). Nonetheless, a possibly collaborate interaction of ParA and ParB with a polar landmark structure like in *C. glutamicum* has also been reported in *M. xanthus*, where ParAB interact with cytoskeletal bactofilin elements (Harms et al., 2013; Lin et al., 2017). Alternatively, the polar localization of ParA in *C. glutamicum* could be passively effected by ParB-mediated ParA-depletion from the nucleoid. This hypothesis is further supported by ParAB studies in other bacterial models lacking polar ParAB tethering factors (Marston and Errington, 1999; Ptacin et al., 2010). Here, ParA similarly localizes to nucleoid edges in presence of (dispersed) ParB and associates with the nucleoid in absence of ParB. In either way, a passive recruitment of *C. glutamicum* ParA towards septa is in line with time-lapse microscopy data indicating ParB pushing ParA ahead of itself (**Figure 2.46**). Therefore, ParA assembles rather late in the *C. glutamicum* cell cycle, where it may form two foci binding at either side of the closing septum. By contrast, ParA foci in the related *M. smegmatis* localize ParB-independently at cell poles and septa prior to ParB-*oriC*-segregation towards respective regions (Ginda et al., 2013). Deviant mechanisms in ParABS-mediated *oriC*-segregation may further explain why ParB-*oriC* complexes of *M. smegmatis* localize in greater distance to cell poles (Ginda et al., 2013) than in *C. glutamicum* (**Figure 2.4A**). Interestingly, a recent study evidences only mild DNA segregation defects upon impairment of ParA-DivIVA interactions in *M. smegmatis* (Pioro et al., 2019). This observation suggests the initial *oriC*-separation along nucleoid-associated ParA gradients to be the key factor for efficient chromosome segregation rather than subsequent *oriC*-tethering at cell poles. Instead, evidence exists for a role of cell pole-associated ParA and replisomes in apical growth of actinobacteria (Kois-Ostrowska et al., 2016; Pioro et al., 2019; Wolánski et al., 2011). Future research may elucidate the biological role of polar origin-tethering in *C. glutamicum* and the underlying mechanism of Par-DivIVA interactions, however it can be hypothesized that polar and septal ParAB-*oriC* localizations might interconnect processes involved in growth, cytokinesis and chromosome organization.

3.6. PldP links DNA organization with cell division in an indirect way

Division site selection is relatively flexible in *C. glutamicum* and related actinobacteria, where division septum-placement may slightly deviate from midcell positions (Donovan et al., 2013; Santi et al., 2013). Here, the chromosome has been shown to act as spatial determinant for septum placement, since *parABS*-phenotypes in chromosome partitioning are further associated with aberrant cell lengths (**Table S1**, **Figure 2.1**, **Figure 2.17**, **Figure 2.45**) (Donovan et al., 2013). The huge impact of DNA segregation on cell division may, in part, explain why *C. glutamicum* and related actinobacteria lack common Min systems that mediate precise Z-ring positioning at midcell and accessory nucleoid occlusion systems (Donovan and Bramkamp, 2014). Therefore, it is appealing to speculate that bacteria like *C. glutamicum*, in which these protein machineries are absent, needed to evolve alternative regulators dedicated to placing their Z-rings. Examples of alternative regulators that use the chromosome as topological factor for division site selection include the ParA family member MipZ in *C. crescentus* (Thanbichler and Shapiro, 2006). In *C. glutamicum*, the ParA-like ATPase PldP has been shown to influence division site selection by a yet unknown mechanisms (Donovan et al., 2010). Data presented here provide important indications for the function of PldP in cell division and its dependence on chromosome organization.

Apparent PldP-mislocalizations upon chromosome segregation defects (**Figure 2.49E**, **Figure 3.5A**) demonstrate that PldP indeed uses the nucleoid as landmark for spatial localization within cells, as expected for DNA-binding orphan ParAs of other species (Dubarry et al., 2019; Roberts et al., 2012). **Figure 3.5A** summarizes subcellular PldP and ParAB localizations in dependence of distinct *par* deletions. In particular, PldP mislocalization is most pronounced in absence of ParB and *parS* sites (**Figure 2.49E**, **Figure 3.5A**), supporting the hypothesis that ParB is the partner protein of PldP that triggers its ATP hydrolysis to position PldP within the cell. Here, *C. glutamicum* ParB would interact with two ParA-like ATPases similar to ParB of *C. crescentus* and *Rhodobacter sphaeroides*, which likewise localize ParA and its orphan paralog MipZ (Dubarry et al., 2019; Thanbichler and Shapiro, 2006). Bacterial-two hybrid analysis indicated PldP-ParB interactions in *C. glutamicum* (**Figure 2.45D**) (Donovan et al., 2010), however, we could not confirm this interaction via PldP-immunoprecipitation assays, assuming that potential PldP interaction with ParB might be transient (**Figure 2.51**). It remains to be tested whether the ATPase activity of PldP may be triggered by ParB, similar to ParA-like ATPases MinD of *E. coli* and Soj of *B. subtilis* in presence of their corresponding partner proteins MinE and Spo0J (Hu and Lutkenhaus, 2001; Leonard et al., 2005). In addition to the interaction of PldP with ParB, co-

immunoprecipitations confirm a PldP-ParA interaction, even though PldP localization is only weakly affected upon *parA* deletion (**Figure 2.49E**, **Figure 2.51**). Interestingly, also the two *R. sphaeroides* ATPases MipZ and ParA1 have been shown to interact, namely in a nucleotide-binding-dependent manner (Dubarry et al., 2019). In any case, it remains to be shown how chromosome partitioning ParAs impact on cellular positioning or the function of paralogous orphan ParAs. Since the cellular PldP localization at cell quarter positions resembles the one of the *R. sphaeroides* ParA-like ATPase PpfA (Roberts et al., 2012), the mechanism of PldP-like localization may be shared amongst some ParA family members.

Moreover, our data confirm that, contrary to ParA, *Corynebacterium*-specific PldP exclusively impacts on division site selection and not on chromosome partitioning (**Table S1**, **Figure 2.49A**, **D**) (Donovan et al., 2010). Consequently, PldP is hitchhiking the nucleoid to fulfill another function than ParA. Since PldP impacts on division septum placement (**Figure 2.49A**) (Donovan et al., 2010), it is appealing to speculate that PldP positions cell division proteins accordingly. Unlike ParA-like ATPases MinD of *E. coli* and MipZ of *C. crescentus* acting as negative regulators of FtsZ (**Figure 3.5B**) (Raskin and de Boer, 1999; Thanbichler and Shapiro, 2006), positive division site selectors of the ParA family, like *M. xanthus* PomZ and *S. coelicolor* SsgB, accumulate at midcell prior to and throughout Z-ring formation (**Figure 3.5B**) (Treuner-Lange et al., 2013; Willemse et al., 2011). However, despite cell cycle-dependent PldP localization in diffuse patches at sites of future cell division (**Figure 2.48**), PldP does not colocalize with FtsZ during septation and no interactions of PldP with division proteins could be evidenced (**Figure 2.50C**, **Figure 2.51**) (Donovan and Bramkamp, 2014) as illustrated in **Figure 3.5B**. Therefore, PldP is not a direct regulator of division septum placement in *C. glutamicum*.

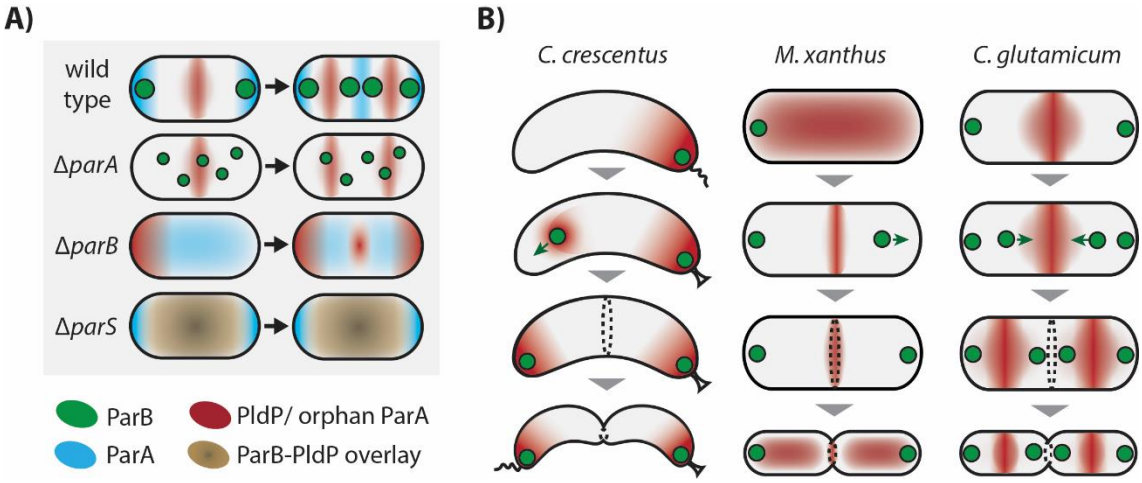

Figure 3.5: Cell cycle-dependent localization of ParA-like ATPases.

(**A**) PldP-dynamics are determined by the ParABS system. Cartoon illustrates the PldP-positioning in newborn and pre-divisional *C. glutamicum* cells relative to remaining Par proteins in dependence of *par* deletions. (**B**) Spatiotemporal localization of the orphan ParAs MipZ in *C. crescentus*, PomZ in *M. xanthus* and PldP in *C. glutamicum* in the course of a life cycle.

Instead, PldP is interacting with a large proteome fraction, thus PldP seems involved in a universal cellular function, like protein biosynthesis, folding, export or degradation. Remarkably many membrane-associated proteins were indentified, including components of the Sec- and Tat-pathways (**Table 5**). The large fraction of highly significant PldP-interactors harboring a peptide signal for the Sec-pathway (**Table 4**) further lends support for the notion that PldP could be involved in secretome regulation or localization. Secretory pathway machineries of different bacterial species appear to be differentially localized within cytoplasmic membranes (Brandon et al., 2003; Campo et al., 2004). Most strikingly, components of the *S. pneumoniae* Sec-pathway and an associated protease HtrA localize in equatorial rings and division septa, strongly resembling PldP localization in *C. glutamicum* (Tsui et al., 2011). Moreover, positioning and regulation of specialized secretion machineries by ParA/MinD family members had been described before (Atmakuri et al., 2007; Kusumoto et al., 2008; Perez-Cheeks et al., 2012).

Provided that the significantly enriched protein fraction in the control samples of PldP pulldown assays corresponds to their downregulation in the PldP-mCherry strain, the PldP fusion appears to be impaired in function. Notably, downregulation of the Sec-pathway in bacteria and yeast had been shown to impact on the expression levels of similar proteins, namely chaperones DnaK and GroE, proteases and ribosomal proteins (Bernstein and Hyndman, 2001; Hasona et al., 2007; Mutka and Walter, 2001). Furthermore, the signal recognition particle FtsY was significantly

enriched in pulldown controls, which transfers ribosome-nascent chain complexes to the secretion translocase (Angelini et al., 2005; Luirink et al., 1994). A link between PldP and FtsY is further supported by a study of the regulation of polar flagellum assembly in *Vibrio alginolyticus*, where the flagellum-promoting FtsY-homologue FlhF is negatively regulated by the ParA-like ATPase FlhG (Kusumoto et al., 2008). PldP may indirectly impact on division septum placement by regulating cell wall insertion of so far unknown factors that in turn determine Z-ring positioning, as it localizes to future sites of cell division before any other known protein.

Further, putative interaction partners of PldP involved in cell wall biogenesis, like the secreted Cmt1/2 and MurA-C (**Table 5**), suggest a function for PldP in cell elongation. Interestingly, the interference with apical cell growth using the drug ethambutol that targets arabinogalactan chains had been shown to interfere with daughter cell separation and resulted in cell width phenotypes (Schubert et al., 2017; Zhou et al., 2019). Similar effects had been described upon deletion of secreted peptidoglycan hydrolases (Tsuge et al., 2008; Zhou et al., 2019). Even though current data do not hint to such defects in *pldP* mutant cells (**Figure 2.49**), thorough quantifications of cell morphology and growth will be required.

Recent preliminary data further support significant PldP-interactions with the so far uncharacterized membrane protein Cg0359 and the threonine dehydratase IlvA (**Table 4**, AG Bramkamp, unpublished data). Synthetic phenotypes and localization interdependencies between PldP and Cg0359 or IlvA have been observed. In line with previous studies showing a connection between bacterial metabolism and cell morphology in *E. coli* (Westfall and Levin, 2018), PldP may alternatively act as a cell cycle regulator at a link between both processes. Further experimental confirmation and characterization of these protein interactions will be needed to understand their functional roles in *C. glutamicum*.

Conclusively, identification of the cellular PldP-function will help to understand the *Corynebacterium*-specific regulatory network of cell division and metabolism and may further be of interest for the industrial secretory protein production in *C. glutamicum* (Freudl, 2017).

3.7. Conclusions and outlook

Recent advances in our understanding of prokaryotic chromosome organization is built on a growing number of model species and major technical advances, gradually completing missing links between strikingly complex mechanisms of genome structure and dynamics. Here, we have identified unique spatiotemporal organization and segregation characteristics of chromosomal domains in *C. glutamicum* that underlie a distinct cell cycle strategy, comprising a combination of diploidy and overlapping replication cycles. Our findings further expand the general understanding of conserved functions and the mutual influence of ParB-*parS* and SMC/ScpAB protein machineries in bacterial chromosome organization. Moreover, these studies give clear evidence for an unexpected role of condensin MksBEFG outside of chromosomal structuring. Conclusively, we consolidate *C. glutamicum* in being a valuable model in the field of bacterial genome organization that awaits with important differences to classical model species based on diverse life style adaptations.

At the same time, findings of this study point the way towards future research goals: First, strict diploidy in *C. glutamicum* poses the question about its biological function. To this end, it will be essential to find conditions at which cell populations turn monoploid to test for advantages in DNA damage response or growth upon nutrient shortage. A second goal of studies on chromosome organization will be the development of genetic tools that allow for synchronized DNA cycling (Lee et al., 2002; Nair et al., 2009) in *C. glutamicum*. Temporal modulations of replication and segregation processes will add to our understanding of cell cycle regulation and growth. Furthermore, simultaneous labeling of additional loci on chromosomal replichores will allow for a comprehensive model of spatiotemporal domain organization in *C. glutamicum*. Here, future studies may benefit from plasmid-derived ParB/*parS* systems suitable for Gram-positive species (van Raaphorst et al., 2017). Moreover, having revealed interdependent ParABS localizations raises the question for the mechanistic basis of chromosome segregation in *C. glutamicum*. Future *in vitro* analyses may be complemented by reconstitution of a complete minimal synthetic partitioning system in *E. coli* (Donovan et al., 2012; Ptacin et al., 2010; Yamaichi and Niki, 2000). Besides this, it remains open why condensin SMC/ScpAB is highly conserved amongst bacterial species, although replichore cohesion appears to be widely redundant (Nolivos and Sherratt, 2014). Despite the current opinion about SMC/ScpAB and ParB-*parS* being self-sustained machineries, high-throughput transposon mutagenesis may identify additional synergistic factors involved in DNA segregation that collaborate with SMC (Mormann et al., 2006; Suzuki et al., 2006). A similar approach for PldP may aid future analyses

confirming interaction partners detected by co-immunoprecipitations. Finally, this study identified plasmids as novel targets for bacterial condensin. Functional characterization *in vitro* as well as *in vivo* studies on MksBEFG-mediated plasmid-localization and -topology will provide further insights in the MksBEFG system. Since MksBEFG is widespread amongst diverse bacteria, elucidating the underlying mechanism(s) of plasmid restriction is of general importance for bacterial cell biology, and hence is a major goal of future research in *C. glutamicum*.

4. Materials and Methods

4.1. Reagents

Experiments of this work were conducted using chemicals of companies Roth (Karlsruhe, Germany), AppliChem (Darmstadt, Germany), Merck (Darmstadt, Germany), Serva (Heidelberg, Germany), VWR (Radnor, PA, USA) and Sigma Aldrich Chemie (Steinheim, Germany). Products of molecular biological and biochemical procedures were further obtained from Roche (Rotkreuz, Switzerland), Macherey & Nagel (Düren, Germany), Genaxxon Bioscience (Ulm, Germany), Thermo Fisher Scientific (Waltham, MA, USA), Invitrogen (Carlsbad, CA, USA), GE Healthcare (Chicago, IL, USA), Illumina (San Diego, CA, USA) and New England Biolabs (Ipswich, MA, USA) with purity grades "per analysis", unless otherwise noted.

4.2. Oligonucleotides and plasmids

Oligonucleotides and plasmids used in this study are provided in **Table 4.1** and **Table 4.2**. Plasmid constructions are outlined in following chapters.

Table 4.1: Oligonucleotides used for strain construction and qPCR.

Restriction sites are indicated by an underline; primer modifications resulting in (point) mutations are highlighted in bold and green letters indicate *parS* sites.

Oligonucleotides **Strain construction**	**Sequence 5'–3'**	**Restric-** **tion site**
DivIVA-XbaI-F	CATTCTAGAGCCGTTGACTCCAGCTG	XbaI
DivIVA-BamHI-R	CATGGATCCCTCACCAGATGGCTTGTTGT	BamHI
ParB-XbaI-F	CATTCTAGAGGCTCAGAACAAGGGTT	XbaI

ParB-BamHI-R	CATGGATCCTTGGCCCTGGATCAAGGACA	BamHI
SMC-XbaI-F	CGCTCTAGAGATGTATTTGAAATCGTTGACG CTCAAGGGG	XbaI
SMC-KpnI-R	ATAGGTACCCGCCCCGCCACAGTTTCCA	KpnI
ScpA-XbaI-F	CGCTCTAGAGGTGCAGCTCGATAATTTT	XbaI
ScpA-XmaI-R	TATCCCGGGGCTCCCAGTCAC	XmaI
ScpB-XbaI-F	CGCTCTAGAGATGGAATCAATCTTGT	XbaI
ScpB-XmaI-R	ATACCCGGGGGAAGTCTTCAT	BamHI
MksB-XmaI-F	TAACCCGGGTAGTGACCAGCGAACAAGCTTT A	XmaI
MksB-KpnI-R	CGCGGTACCCATTTCTCGATCCTAGAGAAAC TGG	KpnI
MksE-XbaI-F	CTATCTAGAGATGAATGATCAGCTGTGG	XbaI
MksE-XmaI-R	ATACCCGGGGCTTCTGTTCC	XmaI
MksF-XbaI-F	ATATCTAGAGATGACCGTTGTATCGCA	XbaI
MksF-XmaI-R	ATACCCGGGGTTTATCCATCTC	XmaI
MksG-XbaI-F	ATATCTAGAGATGCCATTGTTTATCGACGAC	XbaI
MksG-XmaI-R	ATACCCGGGGCCCACGAATTACTTT	XmaI
SMC-seq-689bp-F	CTGGCTTTGAGATCGTGAAG	
SMC-seq-1589bp-F	AGGCGCTGGCTGGCGAGG	
MksB-seq-875bp-F	CACTGAAGAAGGCGCTGCCG	
MksB-seq-1595bp-F	GCGTGGTGACAACGGGGGAG	
pKNT25/pUT18-seq-F	GAGTTAGCTCACTCATTAGGCACC	
pKNT25-seq-R	GGCGTTTGCGTAACCAGCCTG	
pUT18-seq-R	TGATCACGCCGATATTCATGTC	
pUT18C-seq-F	ATGTACTGGAAACGGTGCCG	
pUT18C-seq-R	TAACTATGCGGCATCAGAGCAG	
pKT25-seq-F	ACATGTTCGCCATTATGCCGCATC	
pKT25-seq-R	CGAAAGGGGGATGTGCTGCAA	
pUT18C-mcs-HindIII-F	TATAAGCTTAGCCGCCAGCGAGG	HindIII
pKNT25-mcs-NheI-F	ATAGCTAGCGCCCAATACGCAAACC	NheI
pUT18-mcs-PvuII-F	ATACAGCTGGCACGACAGGTTTCC	PvuII
pKT25-mcs-HindIII-F	CGGAAGCTTTAATGCGGTAGTTTAT	HindIII

pUT18(C)/pK(N)T25-mcs-KpnI-R	TAAGGTACC**ATTACC**CGGGGATCCTCTAGA	KpnI
Δsmc-BamHI-up-F	CAGGGATCCAGCACACGCGTGTGAAAA	BamHI
Δsmc-up-R	**GGAATGAGTATGGAAGTTGG**AACGGGGTTAAAGTCTAG	
Δsmc-D-F	**CCAACTTCCATACTCCATCC**AACCTGCGCTGAGCACGG	
Δsmc-EcoRI-D-R	CAGGAATTCTGCGAAGAGCTTTTCGGT	EcoRI
Δsmc-seq-700up-F	GGTCACTGCAGGAACACT	
Δsmc-seq-700D-R	AGTTCTTGAACTCCGCCG	
ΔmksB-HindIII-up-F	CAGAAGCTTCAAGATGCGCTCAATGCT	HindIII
ΔmksB-PstI-up-R	ATACTGCAGTCACTTCTGTTCCTCTT	PstI
ΔmksB-PstI-D-F	ATACTGCAGATTCAGGGCAATT	PstI
ΔmksB-XbaI-D-R	CAGTCTAGAATTTGGTATGCACGCCTT	XbaI
ΔmksB-seq-700up-F	ATTACAGGATGGCAGTTCATCAG	
ΔmksB-seq-700D-R	CAGAATTACTTGCGGTTCTTGTAATTC	
ParB-HindIII-up-F	CATAAGCTTAGCTGAATCCTTTGGAAG	HindIII
ParB-SalI-up-R	CATGTCGACTTGGCCCTGGATCAAGGA	SalI
PAmCherry-SalI-F	CATGTCGACATGGTGAGCAAGGGCGAG	SalI
PAmCherry-XbaI-R	CATTCTAGACTTGTACAGCTCGTCCAT	XbaI
mCherry2-SalI-F	ATAGTCGACATGGTCAGCAAGG	SalI
mCherry2-XbaI-R	ATATCTAGAGGATCCTGAGCCG	XbaI
ParB-XbaI-D-F	CATTCTAGATAATTTTAAGTTTGGCGC	XbaI
ParB-BamHI-D-R	CATGGATCCCCTCCACATCAATCAGGC	BamHI
ParB-N-ter-SalI-F	CAGGTCGACATGGCTCAGAACAAGGGTTCC	SalI
ParB-seq-800D-R	CAGCTGCAGCCAACCCCGATGACCTGG	PstI
SMC-HindIII-up-F	CATAAGCTTAAGAAGTCGATGCG	HindIII
SMC-SphI-up-R	CATGCATGCCCCCGCCACAGTTT	SphI
mCherry-XbaI-F	CATTCTAGAATGGTGAGCAAGGGCGAG	XbaI
mCherry-BamHI-R	CATGGATCCTTACTTGTACAGCT	BamHI
SMC-BamHI-D-F	CATGGATCCTAAAACCTGCGCTG	BamHI
SMC-EcoRI-D-R	CATGAATTCTGCGAAGAGCTTTT	EcoRI
MksB-HindIII-up-F	CATAAGCTTAAGCCTTCGCCCGTTATG	HindIII

MksB-SphI-up-R	CATGCATGCTTTCTCGATCCTAGAGAA	SphI
mCherry-XbaI-R	GCGTCTAGATTACTTGTACAGCTCGTC	XbaI
MksB-BamHI-D-F	CATGGATCCTAACATGCCATTGTTTAT	BamHI
MksB-EcoRI-D-R	CATGAATTCATTTGGTATGCACGCCTT	EcoRI
ΔSMCload-HindIII-up-F	ATAAAGCTTGGGCTAACAAGGCTCTCG	HindIII
ΔSMCload-up-R	**GGAGCGGAGTATGGAAGTTGG**TTATTCAAAC ACCGTCTTGTTTTCA	
ΔSMCload-D-F	**CCAACTTCCATACTCCGCTCC**TAGGTAAGGA AGATGATTTTGGGG	
ΔSMCload-SalI-D-R	ATAGTCGACCTGCGAGCTCTCCTGA	SalI
cg0177-HindIII-up-F	ATAAAGCTTAATATCCACAACAGTCACAGTC	HindIII
cg0177-SalI-up-R	ATAGTCGACGAACGAGTATTTGTATTTCAAT	SalI
SMCload-SalI-F	ATAGTCGACATGACAACTTTCCACGAT	SalI
SMCload-XmaI-R	ATACCCGGGTGACGCAATACGTTATG	XmaI
cg0177-XmaI-D-F	ATACCCGGGGCTTTTAAGTTTTCTCG	XmaI
cg0177-EcoRI-D-R	ATAGAATTCGTACCCAGCGGGAATCA	EcoRI
cg0177-seq-700up-F	TGGTTGTCGTCATGAGCGTC	
cg0177-seq-700D-R	TGAAATTCATCCACGAACAC	
SMCload-SphI-up-R	TATGCATGCTTATTCAAACACCGTCTTGTTT	SphI
SMCloadr-SphI-F	CGTGCATGCGGAGCGGGGAAGATTGCA	SphI
SMCloadr-PstI-R	CGTCTGCAGAATCCATGCTGTAGATCGGG	PstI
SMCload-PstI-D-F	ATACTGCAGTAGGTAAGGAAGATGATTTTGG	PstI
parS1mut-HindIII-up-F	ATAAAGCTTGCGTTACTTTGGTGCTGATGC	HindIII
parS1mut-XmaI-up-R	ATA**C**C**C**G**G**G**A**C**A**C**C**TTGCGTGGCGATG	XmaI
parS1mut-XmaI-D-F	TAT**C**C**C**G**G**G**A**G**A**C**T**TTGCAAAAAATCATCGC C	XmaI
parS1mut-EcoRI-D-R	TATGAATTCGAAAATTTTCAGCAGCGCGCCG G	EcoRI
parS2mut-HindIII-up-F	ATAAAGCTTAGTTCGCTGAAGCTGGCG	HindIII
parS2mut-XmaI-up-R	TTT**C**C**C**G**G**G**A**T**T**C**G**TTGCCACATTTAAAG	XmaI
parS2mut-XmaI-D-F	TTT**C**C**C**G**G**G**A**T**A**C**T**TTGCCCTAAAGTACA	XmaI
parS2mut-EcoRI-D-R	ATAGAATTCCATCGTGGCTGAACCC	EcoRI
parS3mut-HindIII-up-F	ATAAAGCTTGCTTTAGCCAATGCCG	HindIII

parS3mut-XmaI-up-R	TTTCCCGGGATTCGTTTCGCGTGGGAAC	XmaI
parS3mut-XmaI-D-F	TTTCCCGGGATACTTCTGCTGATTTTTGTCT	XmaI
parS3mut-EcoRI-D-R	GCGGAATTCTGAGACTGACTTTCCTTCTG	EcoRI
parS4mut-HindIII-up-F	ATAAAGCTTCGATTATTGGTGTCGCCCT	HindIII
parS4mut-XmaI-up-R	ATACCCGGGATTCGTCGCCATTTTTTGT	XmaI
parS4mut-XmaI-D-F	ATACCCGGGATACTTCGCCATTTTTCTA	XmaI
parS4mut-EcoRI-D-R	ATAGAATTCTAAACGTACTGATATTTATGG	EcoRI
parS5mut-HindIII-up-F	ATAAAGCTTGGAGCTTGCGGAGCTTTT	HindIII
parS5mut-SalI-up-R	ATAGTCGACATTCGTTCTCCCTCTTTTCG	SalI
parS5mut-SalI-D-F	CGCGTCGACATACTTTCTCCCTCTTTAG	SalI
parS6mut-XmaI-up-R	ATACCCGGGATTCGTTGACCGAG	XmaI
parS6mut-XmaI-D-F	ATACCCGGGATACTTTGACCTTAAAGA	XmaI
parS6mut-EcoRI-D-R	ATAGAATTCTTCAGGAGCAGTTCCAGC	EcoRI
parS7mut-HindIII-up-F	TGTAAGCTTATGTGGCCCAGCATGAC	HindIII
parS7mut-XmaI-up-R	ATACCCGGGATTCGTTTCCCTCATTTGC	XmaI
parS7mut-XmaI-D-F	GTACCCGGGATACTTTGAAAGAAGTCAGA	XmaI
parS7mut-EcoRI-D-R	ATAGAATTCAAAGTGTTCGGGGCGAT	EcoRI
parS8mut-HindIII-up-F	ATAAAGCTTCTCTGCATCATTGAAAGCCAC	HindIII
parS8mut-XmaI-up-R	ATACCCGGGATTCGTTGGCATTCTTTGGAT	XmaI
parS8mut-XmaI-D-F	ATACCCGGGATACTTTGGCATTCTGGAGGGT TG	XmaI
parS8mut-EcoRI-D-R	GTCGAATTCCTGAAGGCAATCCCGTTCCGAA TG	EcoRI
parS9mut-HindIII-up-F	ATAAAGCTTGAAGTGTCCTACGAGCAGCTCG	HindIII
parS9mut-SalI-up-R	ATAGTCGACATTCGTTGAAAAACGCTCCAC	SalI
parS9mut-SalI-D-F	ATAGTCGACATACTTTGCAACAAAAATGGCG	SalI
parS10mut-XmaI-up-R	ATACCCGGGATTCGTTGAGGGTTCATC	XmaI
parS10mut-XmaI-D-F	ATACCCGGGATACTTTGAGGGTTTTACACCC	XmaI
parS10mut-EcoRI-D-R	ATAGAATTCGTGACTATCGGCGCGGAGTA	EcoRI
parS-cg0108-SalI-up-F	ATAGTCGACCGCCGCTTCACCATGA	SalI
parS-cg0108-up-R	TGTTTCACGTGAAACAGAATTCCGTGTAGCC GTGTCTGGG	

parS-cg0108-D-F	CGGAATTCTGTTTCACGTGAAACAAGTGCTA CAGTTCGACTTCACG	
parS-cg0108-XmaI-D-R	ATACCCGGGCGTAACAATCGTGGCGAAAG	XmaI
cg0108-seq-400up-F	GCGTCGTAAAGCAATTAAAGGC	
cg0108-seq-200D-R	CACAAATTGGCGCCTATATAGAT	
parS-cg0904-HindIII-up-F	ATAAAGCTTCGTATTCGTACTGCCGAGT	HindIII
parS-cg0904-up-R	TGTTTCACGTGAAACACGGACACGTCCATCA GCG	
parS-cg0904-D-F	TGTCCGTGTTTCACGTGAAACATTACTTTGG CTTTTCGCAGAAG	
parS-cg0904-NheI-D-R	ATAGCTAGCTCACATAACCCTTTCGTTAC	NheI
cg0904-seq-100up-F	TCCGGGTACCACTGTGG	
cg0904-seq-100D-R	TAACCACCTGAAGCGCTT	
parS-cg2563-HindIII-up-F	ATTAAGCTTCCGCGCTGACTGGTCTGCA	HindIII
parS-cg2563-up-R	TGTTTCACGTGAAACACGAAGACTCCCCGAA ACTCAC	
parS-cg2563-D-F	GAGTCTTCGTGTTTCACGTGAAACAGCTGCC TAGTTTGGTGTCCAAG	
parS-cg2563-NheI-D-R	ATAGCTAGCAAGTATTAACTCCCTCGGAAA	NheI
cg2563-seq-200up-F	CCTTCCGCTGTACTCGATCA	
cg2563-seq-300D-R	AGCATAGGCATAAGCGCAGT	
Δint-HindIII-up-F	ATAAAGCTTATTACCAGGAGCGCC	HindIII
parS-Δint-up-R	TGTTTCACGTGAAACACCGTTTGTTATGTGG ACCCTAC	
parS-Δint-D-F	ACGGTGTTTCACGTGAAACAAACGAAACAGT CTTGACCAGCATA	
Δint-NheI-D-R	ATAGCTAGCGGCGGCATCGTCAC	NheI
Δint-seq-700up-F	AGCAGATAAAGTTCCAATTGAATGG	
Δint-seq-700D-R	TTTTCCCAGAACCAGCACC	
ParB-N-ter-HindIII-F	GCCAAGCTTATGGCTCAGAACAAGGGTTCC	HindIII
ParB-R175A-R	ACGA**GC**CTCACCCATGAT**C**AGCT	
ParB-R175A-F	CATGGGTGAG**GC**TCGTTGGC	
ParB-C-ter-SalI-R	ATAGTCGACTTGGCCCTGGATCAAGGA	SalI
ParB-seq-800up-F	CAGGGTACCATTCATGGGCTTAAAGTTCTC	KpnI

E1084Q-HindIII-up-F	ATAAAGCTTTCGCAGAATTGCTGCG	HindIII
E1084Q-up-R	TC**T**AGA**G**CTGCTTCCACCT**G**ATCC	
E1084Q-D-F	**C**AGGTGGAAGCAGC**T**CT**A**GATGATG	
E1084Q-BamHI-D-R	ATAGGATCCATGAATGCGCTCGAGC	BamHI
DnaN-HindIII-up-F	CATAAGCTTGGTTGGCCGCGAAGGACT	HindIII
DnaN-SphI-up-R	CATGCATGCGCCTGGCAGGCGCACTGG	SphI
DnaN-XbaI-D-F	CATTCTAGATAAACACAAAAGTTTCAC	XbaI
DnaN-BamHI-D-R	CATGGATCCTCTGCTGGCTCGCCTTTG	BamHI
DnaN-N-ter-F	ATGGAGTCACAAAACGTGTCCTTC	
DnaN-BamHI-700D-R	CATGGATCCGGCGTGCCAACTGG	BamHI
Δint-PstI-up-R	ATACTGCAGCCGTTTGTTATGTG	PstI
Δint-EcoRI-D-F	CGCGAATTCAACGAAACAGTCTTGACC	EcoRI
cg0904-PstI-up-R	ATACTGCAGCGGACACGTCCATCAG	PstI
cg0904-EcoRI-D-F	ATAGAATTCTTACTTTGGCTTTTCGCAGA	EcoRI
LacI-SalI-F	ATAGTCGACAGGAGGAATTCACCAT	SalI
CFP-KpnI-R	ATAGGTACCTTACTTGTACAGCTCGTCC	KpnI
ParA-HindIII-up-F	CAGAAGCTTGTTTGGCGGATGCGTTGG	HindIII
ParA-SphI-up-R	ATAGCATGCTTTCGCAGGTTTTAGGCCG	SphI
mCherry-SphI-F	CATGCATGCGTGAGCAAGGGCGAGG	SphI
mCherry-SalI-R	CATGTCGACTTACTTGTACAGCTCGTC	SalI
ParA-SalI-D-F	ATAGTCGACTAGCAGTAAACTTCTTTGAA	SalI
ParA-XbaI-D-R	CAGTCTAGAACCAACTCGTCAAGTGCC	XbaI
ParA-N-ter-XbaI-F	CAGTCTAGATTAAGTTGAGTCGTTATA	XbaI
ParA-NheI-800D-R	CAGGCTAGCTACCGGACGGGAACGGCC	NheI
ΔparB-up-R	**GGAATGGAGTATGGAAGTTGG**CGCTCTTAG ACGCACCTT	
ΔparB-D-F	**CCAACTTCCATACTCCATTCC**TTTTAAGTTTG GCGCCAT	
ParB-XbaI-D-R	CAGTCTAGACCTCCACATCAATCAGGC	XbaI
ParA-HindIII-500up-F	CAGAAGCTTCTATCGCACGCCCAGATC	HindIII
PldP-SbfI-up-F	CATCCTGCAGGAGTGAGTGATGCAGGGAA	SbfI
PldP-XbaI-up-R	CATTCTAGAGTCGTTGACGCGGCTGATAA	XbaI

eYFP-XmaI-R	CATCCCGGGTTACTTGTACAGCTCGTCCA	XmaI
PldP-XmaI-D-F	CATCCCGGGTAGGTTGTTTTTCTA	XmaI
PldP-EcoRI-D-R	CATGAATTCCGCGGGAGCAGGCGA	EcoRI
PldP-EcoRI-600up-F	CAGGAATTCGCTCGCAGAAGTGTGGTTTTA	EcoRI
PldP-XbaI-800D-R	CAGTCTAGAACTGACACCGCAACTTGG	XbaI
ParB-NdeI-F	CAGCATATGGCTCAGAACAAGGGTTCC	NdeI
ParB-XhoI-R	CAGCTCGAGTTATTGGCCCTGGATCAA	XhoI
mCherry-SacI-F	CAGGAGCTCATGGTGAGCAAGGGCGAG	SacI
mCherry-EcoRI-R	CATGAATTCTTACTTGTACAGCTCGTC	EcoRI

Oligonucleotides qPCR	**Sequence 5'–3'**	**Genomic binding region**
Cg0002-165-F	TTTTGGGGAGTTGTGCACAG	*cg0002*
Cg0002-165-R	GGGTTGTGCAGGGATTTTGT	*cg0002*
Cg1702-159-F	TGAAGCTATCCTCAACGGCA	*cg1702*
Cg1702-159-R	TAACCAATCGCGATGCCTTG	*cg1702*
DivIVA-153-F	CTACAACGAAGACGAGGT	*Cg2361*
DivIVA-153-R	GCAGTTGAGGAACTAGCA	*Cg2361*
Cg0018-262-F	CCTGCTCAGAATGAAACC	*cg0018*
Cg0018-262-R	AGCTGCTACTACTTGGGC	*cg0018*
Bsu-oriC-F	GATCAATCGGGGAAAGTGTG	intergenic
Bsu-oriC-R	GTAGGGCCTGTGGATTTGTG	intergenic
Bsu-terC-F	TCCATATCCTCGCTCCTACG	intergenic
Bsu-terC-R	ATTCTGCTGATGTGCAATGG	intergenic
parS1-F	CAAGCTCATTCCAGCAGATG	*cg3362*
parS1-R	AACGAGGAATGCATTGGAGT	*cg3362*
parS10-F	CCGTTGAAGAACCAATGAGC	*cg3394*
parS10-R	CGAGAACCAAGGAAAGGCTA	*cg3394*
control1-F	TTGTTCGAGAGCTTGGGTTC	*cg2088 5‘*
control1-R	TCGGGTCACCTGGACTTAAC	*cg2088 5‘*
control2-F	TGATTCTGGAAGGGCTCCAT	*cg1046 3‘*
control2-R	AGCGATTCGTGACGAGAAGT	*cg1046 3‘*

SMCload-F	CGGTTCCGATGGAGTCACTT	*cg3349*
SMCload-R	ATTCCCGCAAAGGAACATGG	*cg3349*
pBHK18-F	CAGTGGGCTTACATGGCGATA	intergenic
pBHK18-R	AGGGCTTCCCAACCTTACCA	intergenic
pWK0-F	AATACGCAAACCGCCTCTCC	intergenic
pWK0-R	TAATTGCGTTGCGCTCACTG	intergenic
pJC1-F	CTTAACCGGCGCATGACTTC	intergenic
pJC1-R	TCTTGAGTCCAACCCGGAAA	intergenic
pEK0-F	TAATTGCGTTGCGCTCACTG	intergenic
pEK0-R	AATACGCAAACCGCCTCTCC	intergenic

Table 4.2: Plasmids utilized in this study.

Plasmid	Characteristics	Reference
pUT18	Cloning/expression vector, pUC19 derivative, T18 domain of CyaA, MCS 5' of T18, Amp^r	(Karimova et al., 2001)
pUT18C	Cloning/expression vector, pUC19 derivative, T18 domain of CyaA, MCS 3' of T18, Amp^r	(Karimova et al., 2001)
pKNT25	Cloning/expression vector, pSU40 derivative, T25 domain of CyaA, MCS 5' of T25, Kan^r	(Karimova et al., 2005)
pKT25	Cloning/expression vector, pSU40 derivative, T25 domain of CyaA, MCS 3' of T25, Kan^r	(Karimova et al., 2001)
pUT18C-zip	Control plasmid, T18 domain of CyaA fused to leucine zipper of GCN4, Amp^r	(Karimova et al., 2001)
pKT25-zip	Control plasmid, T25 domain of CyaA fused to leucine zipper of GCN4, Kan^r	(Karimova et al., 2001)
pUT18_mcs	pUT18 plasmid, insertion (TAATGG) between XmaI and KpnI restriction sites	This study
pUT18C_mcs	pUT18C plasmid, insertion (TAATGG) between XmaI and KpnI restriction sites	This study
pKNT25_mcs	pKNT25 plasmid, insertion (TAATGG) between XmaI and KpnI restriction sites	This study
pKT25_mcs	pKT25 plasmid, insertion (TAATGG) between XmaI and KpnI restriction sites	This study
pUT18-divIVA	pUT18 plasmid, *divIVA-cyaAT18* fusion	This study
pUT18C-divIVA	pUT18C plasmid, *cyaAT18-divIVA* fusion	This study
pKNT25-divIVA	pKNT25 plasmid, *divIVA-cyaAT25* fusion	This study
pKT25-divIVA	pKT25 plasmid, *cyaAT25-divIVA* fusion	This study

pUT18-parB	pUT18 plasmid, *parB-cyaAT18* fusion	This study
pUT18C-parB	pUT18C plasmid, *cyaAT18-parB* fusion	This study
pKNT25-parB	pKNT25 plasmid, *parB-cyaAT25* fusion	This study
pKT25-parB	pKT25 plasmid, *cyaAT25-parB* fusion	This study
pUT18-parBR175A	pUT18 plasmid, *parB*^{R175A}*-cyaAT18* fusion	This study
pUT18C-parBR175A	pUT18C plasmid, *cyaAT18-parB*^{R175A} fusion	This study
pKNT25-parBR175A	pKNT25 plasmid, *parB*^{R175A}*-cyaAT25* fusion	This study
pKT25-parBR175A	pKT25 plasmid, *cyaAT25-parB*^{R175A} fusion	This study
pUT18-smc	pUT18 plasmid, *smc-cyaAT18* fusion	This study
pUT18C-smc	pUT18C plasmid, *cyaAT18-smc* fusion	This study
pKNT25-smc	pKNT25 plasmid, *smc-cyaAT25* fusion	This study
pKT25-smc	pKT25 plasmid, *cyaAT25-smc* fusion	This study
pUT18-scpA	pUT18 plasmid, *scpA-cyaAT18* fusion	This study
pUT18C-scpA	pUT18C plasmid, *cyaAT18-scpA* fusion	This study
pKNT25-scpA	pKNT25 plasmid, *scpA-cyaAT25* fusion	This study
pKT25-scpA	pKT25 plasmid, *cyaAT25-scpA* fusion	This study
pUT18-scpB	pUT18 plasmid, *scpB-cyaAT18* fusion	This study
pUT18C-scpB	pUT18C plasmid, *cyaAT18-scpB* fusion	This study
pKNT25-scpB	pKNT25 plasmid, *scpB-cyaAT25* fusion	This study
pKT25-scpB	pKT25 plasmid, *cyaAT25-scpB* fusion	This study
pUT18-mksB	pUT18_mcs plasmid, *mksB-cyaAT18* fusion	This study
pUT18C-mksB	pUT18C_mcs plasmid, *cyaAT18-mksB* fusion	This study
pKNT25-mksB	pKNT25_mcs plasmid, *mksB-cyaAT25* fusion	This study
pKT25-mksB	pKT25_mcs plasmid, *cyaAT25-mksB* fusion	This study
pUT18-mksE	pUT18 plasmid, *mksE-cyaAT18* fusion	This study
pUT18C-mksE	pUT18C plasmid, *cyaAT18-mksE* fusion	This study
pKNT25-mksE	pKNT25 plasmid, *mksE-cyaAT25* fusion	This study
pKT25-mksE	pKT25 plasmid, *cyaAT25-mksE* fusion	This study
pUT18-mksF	pUT18 plasmid, *mksF-cyaAT18* fusion	This study
pUT18C-mksF	pUT18C plasmid, *cyaAT18-mksF* fusion	This study
pKNT25-mksF	pKNT25 plasmid, *mksF-cyaAT25* fusion	This study

pKT25-mksF	pKT25 plasmid, *cyaAT25-mksF* fusion	This study
pUT18-mksG	pUT18 plasmid, *mksG-cyaAT18* fusion	This study
pUT18C-mksG	pUT18C plasmid, *cyaAT18-mksG* fusion	This study
pKNT25-mksG	pKNT25 plasmid, *mksG-cyaAT25* fusion	This study
pKT25-mksG	pKT25 plasmid, *cyaAT25-mksG* fusion	This study
pK19mobsacB	Integration vector, *ori* pUC, Km^r, *mob sac*	(Schäfer et al., 1994)
pK19mobsacB-Δsmc	Integration vector, *ori* pUC, Km^r, *mob sac,* deletion of *smc*	This study
pK19mobsacB-ΔmksB	Integration vector, *ori* pUC, Km^r, *mob sac,* deletion of *mksB*	This study
pK19mobsacB-ΔparB	Integration vector, *ori* pUC, Km^r, *mob sac,* deletion of *parB*	(Donovan et al., 2010)
pK19mobsacB-parB-eYFP	Integration vector, *ori* pUC, Km^r, *mob sac, parB-eYFP*	This study
pK19mobsacB-parB-mCherry2	Integration vector, *ori* pUC, Km^r, *mob sac, parB-mCherry2*	This study
pK19mobsacB-parB-mNeonGreen	Integration vector, *ori* pUC, Km^r, *mob sac, parB-mNeonGreen*	This study
pK19mobsacB-parB-PAmCherry	Integration vector, *ori* pUC, Km^r, *mob sac, parB-PAmCherry2*	This study
pK19mobsacB-smc-mCherry	Integration vector, *ori* pUC, Km^r, *mob sac, smc-mCherry*	This study
pK19mobsacB-smc-PAmCherry	Integration vector, *ori* pUC, Km^r, *mob sac, smc-PAmCherry*	This study
pK19mobsacB-mksB-mCherry	Integration vector, *ori* pUC, Km^r, *mob sac, mksB-mCherry*	This study
pK19mobsacB-ΔSMCload	Integration vector, *ori* pUC, Km^r, *mob sac,* deletion of SMC binding site (1.1 Kb *hpaG* 3')	This study
pK19mobsacB-SMCload-cg0177	Integration vector, *ori* pUC, Km^r, *mob sac,* partial SMC binding site (1.1 Kb *hpaG* 3') *cg0177* 3'	This study
pK19mobsacB-SMCload-r	Integration vector, *ori* pUC, Km^r, *mob sac,* partial replacement of SMC binding site (1.1 Kb *hpaG* 3') by *B. subtilis* genomic region	This study
pK19mobsacB-parS1mut	Integration vector, *ori* pUC, Km^r, *mob sac,* point mutations in *parS1*	This study
pK19mobsacB-parS2mut	Integration vector, *ori* pUC, Km^r, *mob sac,* point mutations in *parS2*	This study
pK19mobsacB-parS3mut	Integration vector, *ori* pUC, Km^r, *mob sac,* point mutations in *parS3*	This study

pK19mobsacB-parS4mut	Integration vector, *ori* pUC, Km^r, *mob sac*, point mutations in *parS4*	This study
pK19mobsacB-parS5_6mut	Integration vector, *ori* pUC, Km^r, *mob sac*, point mutations in *parS5* and *parS6*	This study
pK19mobsacB-parS7mut	Integration vector, *ori* pUC, Km^r, *mob sac*, point mutations in *parS7*	This study
pK19mobsacB-parS8mut	Integration vector, *ori* pUC, Km^r, *mob sac*, point mutations in *parS8*	This study
pK19mobsacB-parS9_10mut	Integration vector, *ori* pUC, Km^r, *mob sac*, point mutations in *parS9* and *parS10*	This study
pK19mobsacB-parS-cg0108	Integration vector, *ori* pUC, Km^r, *mob sac*, *parS cg0108* 3'	This study
pK19mobsacB-parS-cg0904	Integration vector, *ori* pUC, Km^r, *mob sac*, *parS cg0904* 3'	This study
pK19mobsacB-parS-cg02563	Integration vector, *ori* pUC, Km^r, *mob sac*, *parS cg2563* 3'	This study
pK19mobsacB-parS-Δint	Integration vector, *ori* pUC, Km^r, *mob sac*, replacement of *cg1752* (*int*) by *parS*	This study
pK19mobsacB-parBR175A	Integration vector, *ori* pUC, Km^r, *mob sac*, *parB::parB*^{R175A}	This study
pK19mobsacB-smcE1084Q	Integration vector, *ori* pUC, Km^r, *mob sac*, *smc::smc*^{E1084Q}	This study
pK19mobsacB-dnaN-mCherry	Integration vector, *ori* pUC, Km^r, *mob sac*, *dnaN-mCherry*	This study
pLAU43	Km^R, Amp^R, pMB1 *ori*, *lacO*	(Lau et al., 2003)
pLAU53	araBp-lacI-eCFP, araBp-tetR-eYFP, pMB1 *ori*	(Lau et al., 2003)
pK19mobsacB-lacO-Δint	Integration vector, *ori* pUC, Km^r, *mob sac*, replacement of *cg1752* (*int*) by *lacO*	This study
pK19mobsacB-lacO-cg0904	Integration vector, *ori* pUC, Km^r, *mob sac*, *lacO cg0904* 3'	This study
pK19mobsacB-parA-eYFP	Integration vector, *ori* pUC, Km^r, *mob sac*, *parA-eYFP*	This study
pK19mobsacB-parA-mCherry	Integration vector, *ori* pUC, Km^r, *mob sac*, *parA-mCherry*	This study
pK19mobsacB-ΔparB_parA-eYFP	Integration vector, *ori* pUC, Km^r, *mob sac*, Δ*parB, designed for integration in parA::parA-eYFP background*	This study
pK19mobsacB-pldP-eYFP	Integration vector, *ori* pUC, Km^r, *mob sac*, *pldP-eYFP*	This study
pK19mobsacB-pldP-mCherry	Integration vector, *ori* pUC, Km^r, *mob sac*, *pldP-mCherry*	This study

pCLTON1PamtR	Modified pCLTON1 expression vector	Gerd Seibold
pCLTON1PamtR-*lacI-CFP*	pCLTON1PamtR, *lacI-CFP*	This study
pET-16b	*E. coli* protein expression vector, $p_{T7\text{-}lac}$, Amp^R, N-10xHis tag, pBR322	Novagen
pET-16b-ParB	pET-16b, *parB*	This study
pET-16b-ParBR175A	pET-16b, $parB^{R175A}$	This study
pEKEx2	*E. coli-C. glutamicum* shuttle expression vector, P_{tac}, $lacI_q$, Km^R, pBL1 $oriV_{C.g.}$, pUC18 $oriV_{E.c.}$	(Eikmanns et al., 1991)
pEKEx2-mCherry	pEKEx2, *mCherry*	This study
pBHK18	*E. coli-C. glutamicum* shuttle vector, Km^R, pNG2 $oriV_{C.g.}$, low copy number	(Kirchner and Tauch, 2003)
pWK0	*E. coli-C. glutamicum* shuttle vector, Km^R, pNG2 $oriV_{C.g.}$, low copy number	(Reinscheid et al., 1994)
pJC1	*E. coli-C. glutamicum* shuttle vector, Km^R, pCG1 $oriV_{C.g.}$	(Cremer et al., 1991)
pEK0	*E. coli-C. glutamicum* shuttle vector, Km^R, pBL1 $oriV_{C.g.}$	(Eikmanns et al., 1991)

4.3. Bacterial strains

Bacterial strains utilized in this work are listed in **Table 4.3**; strains constructed in the scope of this study have in parts been published before (Böhm et al., 2019; Böhm et al., 2017). Procedures of strain construction are explained in the subsequent chapter.

Table 4.3: Bacterial strains utilized in this study.

Strain	Characteristics	Reference
***E. coli* DH5α**	F^- ϕ80*lacZ*ΔM15 (*lacZYA-argF*)*U169 recA1 endA1 hsdR17*(r_K^- m_K^+) *supE44 phoA thi-1 gyrA96 relA1* λ^-	Invitrogen
***E. coli* BTH101**	F-, *cya*-99, *ara*D139, *gal*E15, *gal*K16, *rps*L1 (Str^r), *hsd*R2, *mcr*A1, *mcr*B1 strain	(Karimova et al., 1998)
***E. coli* BL21 pLysS**	F–, ompT, $hsdS_B$ (r_B–, m_B–), dcm, gal, λ(DE3), pLysS, Cm^r	Thermo Fisher Scientific
B. subtilis 168	*trpC2*	Laboratory collection

***C. glutamicum* RES 167**	Restriction-deficient mutant, otherwise considered wild type	(Tauch et al., 2002)
CDC001	RES167 derivative, Δ*parA*	(Donovan et al., 2010)
CDC002	RES167 derivative, *ΔpldP*	(Donovan et al., 2010)
CDC003	RES167 derivative, Δ*parB*	(Donovan et al., 2010)
CDC010	RES167 derivative, *divIVA::divIVA-mCherry*	(Donovan et al., 2012)
CDC018	RES167 derivative, *ftsZ::ftsZ-mCherry*	(Donovan, 2012)
CDC026	RES167 derivative, Δ*smc*	This study
CBK001	RES167 derivative, Δ*mksB*	This study
CBK002	RES167 derivative, Δ*parB*, Δ*smc*	This study
CBK003	RES167 derivative, Δ*parB*, Δ*mksB*	This study
CBK004	RES167 derivative, Δ*smc*, Δ*mksB*	This study
CBK005	RES167 derivative, Δ*parB*, Δ*smc*, Δ*mksB*	This study
CBK006	RES167 derivative, *parB::parB-mCherry2*	This study
CBK007	RES167 derivative, *parB::parB-eYFP*	This study
CBK008	RES167 derivative, *parB::parB-mNeonGreen*	This study
CBK009	RES167 derivative, *parB::parB-PAmCherry*	This study
CBK010	RES167 derivative, Δ*smc*, *parB::parB-eYFP*	This study
CBK011	RES167 derivative, Δ*smc*, Δ*mksB parB::parB-eYFP*	This study
CBK012	RES167 derivative, *smc::smc-mCherry*	This study
CBK013	RES167 derivative, *smc::smc-mCherry*, *parB::parB-mNeonGreen*	This study
CBK014	RES167 derivative, *smc::smc-mCherry* Δ*parB*	This study
CBK015	RES167 derivative, *mksB::mksB-mCherry*	This study
CBK016	RES167 derivative, *parS 3* mutated	This study
CBK017	RES167 derivative, *parS 2-3* mutated	This study
CBK018	RES167 derivative, *parS 2-4* mutated	This study
CBK019	RES167 derivative, *parS 2-6* mutated	This study
CBK020	RES167 derivative, *parS 2-7* mutated	This study
CBK021	RES167 derivative, *parS 2-8* mutated	This study

CBK022	RES167 derivative, *parS 2-9* mutated	This study
CBK023	RES167 derivative, *parS 2-10* mutated	This study
CBK024	RES167 derivative, *parS 1-10* mutated	This study
CBK025	RES167 derivative, *parB::parB-eYFP*, *parS 2-10* mutated	This study
CBK026	RES167 derivative, *parB::parB-eYFP*, *parS 1-10* mutated	This study
CBK027	RES167 derivative, *parB::parB-mCherry2*, *parS 2-10* mutated	This study
CBK028	RES167 derivative, *parB::parB-mCherry2*, *parS 1-10* mutated	This study
CBK029	RES167 derivative, *parB::parB-PAmCherry*, *parS 2-10* mutated	This study
CBK030	RES167 derivative, *parB::parB-mCherry2*, *parS 2-9* mutated	This study
CBK031	RES167 derivative, *parB::parB-PAmCherry*, *parS 2-9* mutated	This study
CBK032	RES167 derivative, *smc::smc-mCherry*, *parS 1-10* mutated	This study
CBK033	RES167 derivative, *smc::smc-mCherry*, partial *smc roadblock* (1.1 Kb) deleted	This study
CBK034	RES167 derivative, *smc::smc-mCherry*, partial *smc roadblock* deleted and reinserted into intergenic region 3' of *cg0177*	This study
CBK035	RES167 derivative, *smc::smc-mCherry*, partial *smc roadblock* (1.1 Kb) substituted by *B. subtilis* genomic locus of identical size	This study
CBK036	RES167 derivative, *parS 1-10* mutated, *parS* in intergenic region 3' of *cg0108*	This study
CBK037	RES167 derivative, *parS 1-10* mutated, *parS* in intergenic region 3' of *cg0904*	This study
CBK038	RES167 derivative, *parS 1-10* mutated, *parS* in intergenic region 3' of *cg2563*	This study
CBK039	RES167 derivative, *parS 1-10* mutated, *cg1752::parS*	This study
CBK040	RES167 derivative, *parB::parB-eYFP*, *parS 1-10* mutated, *parS* in intergenic region 3' of *cg0108*	This study
CBK041	RES167 derivative, *parB::parB-eYFP*, *parS 1-10* mutated, *parS* in intergenic region 3' of *cg0904*	This study
CBK042	RES167 derivative, *parB::parB-mCherry2*, *parS 1-10* mutated, *parS* in intergenic region 3' of *cg0904*	This study
CBK043	RES167 derivative, *parB::parB-eYFP*, *parS 1-10* mutated, *parS* in intergenic region 3' of *cg2563*	This study

CBK044	RES167 derivative, *parB::parB-eYFP*, *parS 1-10* mutated, *int (cg1752) ::parS*	This study
CBK045	RES167 derivative, *smc::smc-mCherry*, *parS 1-10* mutated, *parS* in intergenic region 3' of *cg0904*	This study
CBK046	RES167 derivative, *parS 1-10* mutated, *parS* in intergenic region 3' of *cg0904*, Δ*smc*	This study
CBK047	RES167 derivative, *parB::parB*^{R175A}*-mCherry2*	This study
CBK048	RES167 derivative, *parB::parB*^{R175A}*-mCherry2*, *parS 2-10* mutated	This study
CBK049	RES167 derivative, *parB::parB*^{R175A}, *smc::smc-mCherry*	This study
CBK050	RES167 derivative, *smc::smc*^{E1084Q}	This study
CBK051	RES167 derivative, *smc::smc*^{E1084Q}*-mCherry*	This study
CBK052	RES167 derivative, pEKEx2-mCherry	This study
CBK053	RES167 derivative, pBHK18	This study
CBK054	RES167 derivative, pWK0	This study
CBK055	RES167 derivative, pJC1	This study
CBK056	RES167 derivative, pEK0	This study
CBK057	RES167 derivative, Δ*mksB*, pBHK18	This study
CBK058	RES167 derivative, Δ*mksB*, pWK0	This study
CBK059	RES167 derivative, Δ*mksB*, pJC1	This study
CBK060	RES167 derivative, Δ*mksB*, pEK0	This study
CBK061	RES167 derivative, *divIVA::divIVA-mCherry*, *parB::parB-eYFP*	This study
CBK062	RES167 derivative, *dnaN::dnaN-mCherry*	This study
CBK063	RES167 derivative, *dnaN::dnaN-mCherry*, *parB::parB-eYFP*	This study
CBK064	RES167 derivative, *parB::parB-eYFP*, *int::lacO*	This study
CBK065	RES167 derivative, *parB-eYFP*, *int::lacO*, tet-inducible *lacI-CFP* expression	This study
CBK066	RES167 derivative, *lacO* in intergenic region 3' of *cg0904*	This study
CBK067	RES167 derivative, *lacO* in intergenic region 3' of *cg0904*, tet-inducible *lacI-CFP* expression	This study
CBK068	RES167 derivative, tet-inducible *lacI-CFP* expression	This study
CBK069	RES167 derivative, *parA::parA-eYFP*	This study
CBK070	RES167 derivative, *parA::parA-mCherry*	This study

CBK071	RES167 derivative, *parB::parB-eYFP, parA::parA-mCherry*	This study
CBK072	RES167 derivative, *ΔparA, parB::parB-eYFP*	This study
CBK073	RES167 derivative, *ΔparB, parA::parA-eYFP*	This study
CBK074	RES167 derivative, *parS 1-10* mutated, *parA::parA-eYFP*	This study
CBK075	RES167 derivative, *pldP::pldP-eYFP*	This study
CBK076	RES167 derivative, *pldP::pldP-mCherry*	This study
CBK077	RES167 derivative, *ΔparB, pldP::pldP-eYFP*	This study
CBK078	RES167 derivative, *ΔparA, pldP::pldP-eYFP*	This study
CBK079	RES167 derivative, *parS 1-10* mutated, *pldP::pldP-eYFP*	This study
CBK080	RES167 derivative, *pldP::pldP-eYFP*, *parA::parA-mCherry*	This study
CBK081	RES167 derivative, *ΔpldP, parB::parB-eYFP*	This study
CBK082	RES167 derivative, *ftsZ::ftsZ-mCherry*, *pldP::pldP-eYFP*	This study

4.4. Construction of bacterial plasmids and strains

Primers, plasmids and strains mentioned below are listed in **Table 4.1** - **Table 4.3**.

For protein-protein interaction screens genes of interest were amplified via PCR, digested with respective enzymes and ligated into bacterial two-hybrid vectors (Karimova et al., 1998). Chemically competent *E. coli* DH5α were utilized for plasmid cloning (Green and Rogers, 2013). Genes *divIVA* and *parB*/*parB*^{R175A} were amplified using primer pairs DivIVA-XbaI-F/DivIVA-BamHI-R and ParB-XbaI-F/ParB-BamHI-R from genomic DNA or pK19mobsacB-ParBR175A and resulting fragments were digested with XbaI/BamHI. For amplification of *scpA*, *scpB*, *mksE*, *mksF* and *mksG* primer pairs ScpA-XbaI-F/ScpA-XmaI-R, ScpB-XbaI-F/ScpB-XmaI-R, MksE-XbaI-F/MksE-XmaI-R, MksF-XbaI-F/MksF-XmaI-R and MksG-XbaI-F/MksG-XmaI-R were utilized, followed by restriction digests with XmaI/XbaI. Primer pairs SMC-XbaI-F/SMC-KpnI-R and MksB-XmaI-F/MksB-KpnI-R were used for PCR amplification of genes *smc* and *mksB*, which were subsequently digested with XbaI/KpnI or XmaI/KpnI. In order to increase the distance of XmaI and KpnI restriction sites a short sequence was inserted in between these sites by overhang PCRs using pUT18C-mcs-HindIII-F, pUT18-mcs-PvuII-F, pKNT25-mcs-NheI-F or

pKT25-mcs-HindIII-F in combination with pUT18(C)/pK(N)T25-mcs-KpnI-R for plasmids pUT18C, pUT18, pKT25 and pKNT25, respectively. Resulting fragments and corresponding vectors were digested with HindIII/KpnI, PvuII/KpnI or NheI/KpnI and subsequently ligated, resulting in plasmids pUT18_mcs, pUT18C_mcs, pKNT25_mcs and pKT25_mcs. All digested gene fragments mentioned above were ligated into pUT18, pUT18C, pKNT25 and pKT25 or pUT18_mcs, pUT18C_mcs, pKNT25_mcs and pKT25_mcs, respectively.

Derivatives of the suicide integration vector pK19mobsacB were used for clean allelic replacements in *C. glutamicum*, containing the modified genomic region of interest including its 500 bp up- and downstream homologous flanking sequences. Plasmid cloning was performed using *E. coli* DH5α.

In order to construct pK19mobsacB-Δsmc 500 bp upstream and downstream of *smc* were PCR-amplified using primer pairs Δsmc-BamHI-up-F/Δsmc-up-R and Δsmc-D-F/Δsmc-EcoRI-D-R, respectively. Both fragments served as templates in an overhang PCR, yielding a 1000 bp fragment, which was digested with BamHI and EcoRI and subsequently ligated into pK19mobsacB. pK19mobsacB-ΔSMCload was constructed accordingly, using primer pairs ΔSMCload-HindIII-up-F/ΔSMCload-up-R and ΔSMCload-D-F/ΔSMCload-SalI-D-R and HindIII in combination with SalI for restriction digest. For construction of pK19mobsacB-ΔmksB up- and downstream regions of *mksB* were PCR amplified using primers ΔmksB-HindIII-up-F/ΔmksB-PstI-up-R and ΔmksB-PstI-D-F/ΔmksB-XbaI-D-R. Resulting 500 bp fragments were digested with HindIII/PstI and PstI/XbaI and consecutively ligated into pK19mobsacB.

Fluorescent C-terminal fusions of ParB protein were obtained by utilizing plasmids pK19mobsacB-parB-mNeonGreen/-PAmCherry/-eYFP/mCherry2. To this end, 500 bp fragments upstream and downstream of ParB were PCR-amplified from the *C. glutamicum* genome using the primer pairs ParB-HindIII-up-F/ParB-SalI-up-R and ParB-XbaI-D-F/ParB-BamHI-D-R and digested with the respective restriction enzymes. Fluorophore sequences were amplified via PCR using primer pairs mCherry2-SalI-F/mCherry2-XbaI-R (mCherry2) or PAmCherry-SalI-F/PAmCherry-XbaI-R primers (mNeonGreen, eYFP, PAmCherry) and digested with SalI and XbaI. Finally, fragments were consecutively ligated into pK19mobsacB vectors.

For fluorescent versions of SMC and MksB proteins plasmids pK19mobsacB-smc-mCherry and pK19mobsacB-mksB-mCherry were constructed. At first, 500 bp regions up- and downstream of the 3' end of *smc* or *mksB* were amplified using primer pairs SMC-HindIII-up-F/SMC-SphI-up-

R and SMC-BamHI-D-F/SMC-EcoRI-D-R or MksB-HindIII-up-F/MksB-SphI-up-R and MksB-BamHI-D-F/MksB-EcoRI-D-R. Fluorophore sequences were amplified with primers mCherry-XbaI-F/mCherry-BamHI-R for SMC-mCherry fusion or with primers PAmCherry-SalI-F/mCherry-XbaI-R for the MksB-mCherry fusion construct. Up- and downstream fragments were digested via HindIII/SphI and BamHI/EcoRI, while enzymes SalI/BamHI or SalI/XbaI were utilized for restriction digest of fluorophore sequences fused to *smc* or *mksB*, respectively. Fragments were subsequently ligated into the pK19mobsacB plasmid, starting with the corresponding downstream region, followed by the fluorophore sequence and finally the upstream region.

In order to place part of a putative SMC binding site upstream of the *parS* cluster into an intergenic region 3' of *cg0177* (Fig. S7), genomic sequences 500 bp up-and downstream of the insertion site were amplified using primer pairs cg0177-HindIII-up-F/cg0177-SalI-up-R and cg0177-XmaI-D-F/cg0177-EcoRI-D-R; part of the genomic SMC binding site (1.1 Kb) was amplified using primers SMCload-SalI-F and SMCload-XmaI-R. Resulting fragments were digested with HindIII/SalI, SalI/XmaI and XmaI/EcoRI and consecutively ligated into pK19mobsacB, obtaining the plasmid pK19mobsacB-SMCload-cg0177.

Plasmid pK19mobsacB-SMCload-r was constructed for the partial replacement of the SMC binding site (1.1 Kb) with a *B. subtilis* genomic region of identical size. For amplification of up- and downstream 500 bp regions primer pairs ΔSMCload-HindIII-up-F/SMCload-SphI-up-R and SMCload-PstI-D-F/ΔSMCload-SalI-D-R were utilized, while the replacement sequence was amplified from *B. subtilis* genomic DNA via SMCload-SphI-F/SMCload-PstI-R. After digestion with enzymes HindIII/SphI, PstI/SalI or SphI/PstI fragments were successively ligated into pK19mobsacB.

Further, all *parS* sites were mutated comprising new XmaI or SalI restriction sites (see **Figure 2.17A**). For mutation of *parS1* primer pairs parS1mut-HindIII-up-F/parS1mut-XmaI-up-R and parS1mut-XmaI-D-F/parS1mut-EcoRI-D-R were utilized to mutate *parS1* and to amplify sequences 500 bp up- and downstream of *parS1*. Restriction digest was performed with both fragments using HindIII/XmaI or XmaI/EcoRI, respectively. Subsequent ligation into pK19mobsacB yielded plasmid pK19mobsacB-parS1mut. In order to mutate *parS2*, *parS3*, *parS4*, *parS7* and *parS8* plasmid construction was performed in the same way using primers parS2mut-HindIII-up-F/parS2mut-XmaI-up-R and parS2mut-XmaI-D-F/parS2mut-EcoRI-D-R, parS3mut-HindIII-up-F/parS3mut-XmaI-up-R and parS3mut-XmaI-D-F/parS3mut-EcoRI-D-R, parS4mut-HindIII-up-F/parS4mut-XmaI-up-R and parS4mut-XmaI-D-F/parS4mut-EcoRI-

D-R, parS7mut-HindIII-up-F/parS7mut-XmaI-up-R and parS7mut-XmaI-D-F/parS7mut-EcoRI-D-R or parS8mut-HindIII-up-F/parS8mut-XmaI-up-R and parS8mut-XmaI-D-F/parS8mut-EcoRI-D-R for amplification of fragments up- and downstream of the respective *parS* site. Matching fragments were each digested and ligated into pK19mobsacB, as exemplified for pK19mobsacB-parS1mut construction, resulting in plasmids pK19mobsacB-parS2mut, pK19mobsacB-parS3mut, pK19mobsacB-parS4mut, pK19mobsacB-parS7mut and pK19mobsacB-parS8mut.

Since *parS5* and *parS6* as well as *parS9* and *parS10* are localized in close proximity on the genome (< 100 bp distance), their deletions were accomplished using in each case one plasmid for both *parS* sites. For construction of pK19mobsacB-parS5_6mut genomic region upstream of *parS5*, downstream of *parS6* and in between both sides were PCR-amplified using parS5mut-HindIII-up-F/parS5mut-SalI-up-R, parS6mut-XmaI-D-F/parS6mut-EcoRI-D-R and parS5mut-SalI-D-F/parS6mut-XmaI-up-R and fragments were digested with HindIII/SalI, XmaI/EcoRI or SalI/XmaI, respectively and ligated into pK19mobsacB. Construction of pK19mobsacB-parS9_10mut was performed accordingly, using primer pairs parS9mut-HindIII-up-F/parS9mut-SalI-up-R, parS10mut-XmaI-D-F/parS10mut-EcoRI-D-R and parS9mut-SalI-D-F/parS10mut-XmaI-up-R for fragment amplification.

Insertion of *parS* 3' of *cg0108*, *cg0904* and *cg2563* were achieved via plasmids pK19mobsacB-parS-cg0108, pK19mobsacB-parS-cg0904 and pK19mobsacB-parS-cg02563. Primers containing *parS* sites were used to amplify regions 500 bp up- and downstream of the corresponding *parS* insertion site, namely parS-cg0108-SalI-up-F/parS-cg0108-up-R and parS-cg0108-D-F/parS-cg0108-XmaI-D-R, parS-cg0904-HindIII-up-F/parS-cg0904-up-R and parS-cg0904-D-F/parS-cg0904-NheI-D-R or parS-cg2563-HindIII-up-F/parS-cg2563-up-R and parS-cg2563-D-F/parS-cg2563-NheI-D-R, respectively. Each fragment pair served as template in an overhang PCR, yielding 1000 bp sequences with central *parS* sites. After restriction digest with SalI/XmaI or HindIII/NheI each fragment was ligated into pK19mobsacB. Plasmid pK19mobsacB-parS-Δint for *parS* insertion at *terC* was constructed in the same way, however by replacing an entire gene (*cg1752*). Regions 500 bp 3' and 5' of *cg1752* were amplified using Δint-HindIII-up-F/parS-Δint-up-R and parS-Δint-D-F/Δint-NheI-D-R.

For construction of pK19mobsacB-parBR175A primer pairs ParB-N-ter-HindIII-F/ParB-R175A-R and ParB-R175A-F/ParB-C-ter-SalI-R were used to amplify the N-and C-terminal parts of *parB* surrounding the coding region of $ParB^{R175}$. Primers introduce point mutations into this codon as well as into a neighboring SacI restriction site, resulting in fragments of 528 bp and 625 bp length.

Overhang PCR yielded a full *parB* sequence that was cut with HindIII/SalI and ligated into pK19mobsacB. pK19mobsacB-smcE1084Q was obtained in an analogous manner. Amplification of 500 bp genomic regions surrounding codon SMC^{E1084} were performed using primer pairs E1084Q-HindIII-up-F/E1084Q-up-R and E1084Q-D-F/E1084Q-BamHI-D-R, which further yield in an E1084Q mutation and an additional XbaI restriction site 3' of the codon sequence.

In order to construct pK19mobsacB-dnaN-mCherry, upstream and downstream homologous regions were amplified via primer pairs DnaN-HindIII-up-F/DnaN-SphI-up-R and DnaN-XbaI-D-F/DnaN-BamHI-D-R. The mCherry sequence was amplified using PAmCherry-SalI-F/mCherry-XbaI-R primer pairs. The resulting PCR fragments were digested with the respective restriction enzymes and consecutively ligated into pK19mobsacB vectors.

For terminus tracking a FROS system was constructed in strain *C. glutamicum parB::parB-eYFP*. To this end, the terminus proximal *int* gene (cg1752) was replaced by a *lacO* array (~120 operator copies) cut out of pLAU43 using XbaI and XmaI. Upstream and downstream homologous flanking sequences of *int* were PCR amplified using primer pairs Δint-HindIII-up-F/Δint-PstI-up-R and Δint-EcoRI-D-F/Δint-NheI-D-R and the resulting PCR fragments were digested with restriction enzymes as indicated in **Table 4.1**. All restricted fragments were subsequently ligated into pK19mobsacB plasmid, yielding pK19mobsacB-lacO-Δint. For labeling of the right chromosomal arm upstream of *cg0904* in *C. glutamicum*, pK19mobsacB-lacO-cg0904 was constructed. Here, the 500 bp *cg0904*-flanking regions were amplified using primer pairs parS-cg0904-HindIII-up-F/cg0904-PstI-up-R and cg0904-EcoRI-D-F/parS-cg0904-NheI-D-R, cut with respective enzymes and were ligated together with aforementioned *lacO* fragment into pK19mobsacB.

For pCLTON1PamtR-*lacI-CFP* construction the lacI-CFP sequence of pLAU53 was PCR-amplified using LacI-SalI-F/CFP-KpnI-R and digested with respective restriction enzymes. Subcloning was performed using pEKEx2 and after restriction digest with PstI and KpnI the fragment was ligated in pCLTON1PamtR. This plasmid was cloned into strains CBK064, CBK066 and *C. glutamicum* RES 167, obtaining CBK065, CBK067 and CBK068.

Plasmids pK19mobsacB-parA-eYFP/-mCherry served to construct C-terminal fluorescent ParA fusions. Here, 500 bp of the ParA C-terminal coding sequence, 500 bp of the downstream region as well as eYFP and mCherry sequences were PCR-amplified using primer pairs ParA-HindIII-up-F/ParA-SphI-up-R, ParA-SalI-D-F/ParA-XbaI-D-R and mCherry-SphI-F/mCherry-SalI-R. After restriction digest with corresponding enzymes, DNA-fragments were subsequently ligated

into pK19mobsacB. In order to generate a parB deletion in a *parA::parA-eYFP* background within the ParAB operon, pK19mobsacB-ΔparB_parA-eYFP was designed specifically for this purpose. To this end, the upstream and downstream regions of *parB* were PCR-amplified from *C. glutamicum parA::parA-eYFP* genomic DNA (mCherry-SphI-F/ΔparB-up-R, ΔparB-D-F/ParB-XbaI-D-R) and both resulting PCR-fragments were combined by overlap-PCR (mCherry-SphI-F/ParB-XbaI-D-R). Thereupon, restriction digest was performed using SphI and XbaI, followed by ligation into pK19mobsacB that was cut accordingly. The second *C. glutamicum* ParA-like ATPase PldP was likewise fluorescently tagged C-terminally. Constructions of pK19mobsacB-pldP-eYFP/-mCherry were performed analogous to pK19mobsacB-parA-eYFP/-mCherry, using primer pairs PldP-SbfI-up-F/PldP-XbaI-up-R, mCherry-XbaI-F/eYFP-XmaI-R (for mCherry or eYFP) and PldP-XmaI-D-F/PldP-EcoRI-D-R.

Histidine-tagged versions of ParB and ParB^{R175A} were generated by applying PCR (ParB-NdeI-F/ParB-XhoI-R) following a restriction digest (NdeI/XhoI) of the respective DNA fragment and ligation into pET-16b expression vector yielding pET-16b-ParB and pET-16b-ParBR175A.

Finally, for construction of the *E. coli -C. glutamicum* shuttle expression vector pEKEx2-mCherry the mCherry sequence was amplified via PCR using mCherry-SacI-F/mCherry-EcoRI-R, digested with corresponding restriction enzymes and ligated into the empty pEKEx2.

Vectors were transformed via electroporation into *C. glutamicum* cells (Schäfer et al., 1994). Genomic integration of pK19mobsacB plasmids were selected on kanamycin, while the second crossover event was confirmed by growth on 10 % sucrose. Screening of allelic replacements in *C. glutamicum* Δ*smc*, Δ*mksB* and Δ*parB* was performed by colony PCR using primer pairs Δsmc-seq-700up-F/Δsmc-seq-700D-R, ΔmksB-seq-700up-F/ΔmksB-seq-700D-R and ParB-seq-800up-F/ParB-seq-800D-R. In the specific case of Δ*parB*-verification in a *parA::parA-eYFP* background, oligonucleotides ParA-HindIII-500up-F/ParB-seq-800D-R were utilized. Fluorescent fusions of ParB, SMC, MksB, ParA and PldP were confirmed via primer pairs ParB-N-ter-SalI-F/ParB-seq-800D-R, SMC-seq-1589bp-F/Δsmc-seq-700D-R, MksB-seq-1595bp-F/ΔmksB-seq-700D-R, ParA-N-ter-XbaI-F/ParA-NheI-800D-R and PldP-EcoRI-600up-F/PldP-XbaI-800D-R, respectively. Insertions of the partial *smc loading site* in an intergenic region 3' of *cg0177* were screened using primer pairs cg0177-seq-700up-F/cg0177-seq-700D-R. In order to identify genomic *parS* mutations respective regions were amplified using upstream-forward and downstream-reverse primers as used for plasmid construction and digested with either XmaI or SalI. Sequencing of *parS* loci was performed for further verification. For verification of *parS* or *lacO* insertions 3' of *cg0108*, *cg0904* and *cg2563* or for replacement of *cg1752* by *parS* genomic loci

were amplified with primers cg0108-seq-400up-F/cg0108-seq-200D-R, cg0904-seq-100up-F/cg0904-seq-100D-R, cg2563-seq-200up-F/cg2563-seq-300D-R or Δint-seq-700up-F/Δint-seq-700D-R, respectively, followed by a control restriction digest using PmlI. To confirm the allelic replacements *dnaN::dnaN-mCherry*, primers DnaN-N-ter-F and DnaN-BamHI-700D-R were used and gene replacement *int::lacO* was confirmed by colony PCR using primer pairs Δint-seq-700up-F and Δint-seq-700D-R. Screening for $parB^{R175A}$ was performed by amplification of *parB* including 800 bp up- and downstream regions via primers ParB-seq-800up-F/ParB-seq-800D-R. A control digest was conducted with the resulting fragment using SacI. Integration of the point mutation smc^{E1084Q} was verified by amplification of the respective genomic region (E1084Q-HindIII-up-F/mCherry-EcoRI-R), followed by restriction digests using XbaI.

Assembly strategies of multiple consecutive allelic replacements are explained hereafter. *C. glutamicum* strains CBK002, CBK004 and CBK010 were obtained via transformation of pK19mobsacB-ΔparB, pK19mobsacB-ΔmksB or pK19mobsacB-parB-eYFP into strain CDC026 lacking *smc* and strain CBK003 (Δ*mksB* Δ*parB*) was constructed using the genetic background of CBK001 (Δ*mksB*). Further, CBK004 served as parent strain for construction of CBK005 and CBK011 harboring additional mutations Δ*parB* and *parB::parB-eYFP*, respectively. The dual-reporter strain CBK013, expressing ParB-mNeonGreen in combination with SMC-mCherry, was constructed via transformations of pK19mobsacB-smc-mCherry into CBK008; strain CBK014 derives from CBK012 transformed with pK19mobsacB-ΔparB. The complete loss of *parS* sites in strain CBK024 was accomplished via successive allelic replacements of *parS* by mutated sequences: the mutation of *parS3* (CBK016) followed the mutation of *parS2* (CBK017); thereupon *parS4* (CBK018) was mutated followed by *parS5* and *parS6* (CBK019). Next, *parS7* (CBK020) mutation, *parS8* mutation (CBK021), *parS9* mutation (CBK022), *parS10* mutation (CBK023) and *parS1* mutation (CBK024) were accomplished consecutively. CBK025, CBK027 and CBK029 derive from strain CBK023, which was transformed with pK19mobsacB plasmids coding for *parB-eYFP*, *parB-mCherry2*, *parB-PAmCherry*, respectively. Accordingly, stains CBK026, CBK28, CBK032, CBK074 and CBK079 are CBK024-derivatives harboring either endogenous *parB-eYFP*, *parB-mCherry2*, *smc-mCherry*, *parA-eYFP* or *pldP-eYFP*, while strains CBK030 and CBK031 obtained from CBK022 via transformation of pK19mobsacB-parB-mCherry2 or pK19mobsacB-parB-PAmCherry. CBK033 and CBK035 were generated by transformation of strain CBK012 expressing SMC-mCherry with plasmids pK19mobsacB-ΔSMCload or pK19mobsacB-SMCload-r; subsequent transformation of CBK033 with pK19mobsacB-SMCload-cg0177 yielded CBK034. In order to introduce *parS* sites at different regions within the *C. glutamicum* genome CBK024

served as parental strain: *parS* insertions at chromosomal 9.5°, 90°, 270° and 180° positions were achieved via transformation of either pK19mobsacB-parS-cg0108 (CBK036), pK19mobsacB-parS-cg0904 (CBK037), pK19mobsacB-parS-cg2563 (CBK038) or pK19mobsacB-parS-Δint (CBK039). Additional allelic replacements of *parB* or *smc* with fluorophore-coupled versions *parB-eYFP* or *parB-mCherry2* and *smc-mCherry* in above-named strains resulted in CBK040-CBK045. Secondly, *parS* insertion in CBK037 was combined with a *smc* deletion by transformation of pK19mobsacB-Δsmc yielding CBK046. Further, strains CBK047-CBK051, which express mutant $ParB^{R175A}$ or SMC^{E1084Q} proteins, derive from CBK006, CBK027 and CBK012 transformed with plasmid pK19mobsacB-parBR175A or pK19mobsacB-smcE1084Q, respectively. In order to label the *C. glutamicum terC* region via FROS, the *int::lacO*-modified strain CBK064 was further transformed with pCLTON1PamtR-*lacI-CFP* yielding CBK065. Strains CBK061 and CBK063 harboring ParB-eYFP in combination with either DnaN-mCherry or DivIVA-mCherry were obtained by transformation of CBK062 or CDC010 with pK19mobsacB-parB-eYFP. Further, CDC001 and CDC002 (Δ*parA* and Δ*pldP* backgrounds) were transformed with pK19mobsacB-parB-eYFP and/or pK19mobsacB-pldP-eYFP, yielding in strains CBK072, CBK078 and CBK081. CBK077 and CBK073 were obtained by transforming pK19mobsacB-ΔparB into CBK069 and CBK075 cells. Finally, CBK071 and CBK080 derive from pK19mobsacB-parA-mCherry-transformation into initial strains CBK007 and CBK075, while CBK082 was obtained by transformation of CDC018 with pK19mobsacB-pldP-eYFP, respectively.

4.5. Growth conditions and media

B. subtilis and *E. coli* cells were grown at 37° C in Lysogeny Broth (LB) medium supplemented with 25 and 50 µg/ml Kanamycin when appropriate. Growth experiments of *C. glutamicum* cells were performed using BHI complex medium (Oxoid™), BHI medium supplemented with 4 % glucose, minimal salt medium MMI (Nottebrock et al., 2003) supplemented with 4 % glucose or minimal salt medium CGXII (Keilhauer et al., 1993) supplemented with 120 mM acetate or 100 mM propionate as indicated in the text at 30° C. Cells were always preinoculated in BHI medium overnight; for growth in minimal media cells were first inoculated in BHI medium and rediluted in corresponding growth media overnight for pre-cultivation. Finally, cell cultures were adjusted to an OD_{600} of 0.5 for BHI and to an OD_{600} of 1 for growth in MMI or CGXII medium. 25 µg/ml Kanamycin was added where applicable. Extrachromosomal *lacI-cfp* or *mCherry* expression was induced using 0.15 µg/ml tetracycline or 0.5 mM isopropyl β-D-1-thiogalactopyranoside (IPTG)

at an OD_{600} between one and two. For replication run-outs exponentially growing *C. glutamicum* or *B. subtilis* cells were treated with 25 µg/ml or 200 µg/ml chloramphenicol for 4+ h. In order to compare mitomycin C-induced DNA damage repair between *C. glutamicum* mutant strains, cells were grown in BHI medium to an OD_{600} of 5. Subsequently, 10 µl of 10-fold serial dilutions were each plated on BHI- plates containing 0 - 400 ng/ml mitomycin C and incubated overnight at 30° C. To analyze UV-induced DNA damage, cells were plated on LB-agar plates following irradiation with UVB light using a UV-transilluminator (302 nm, 8 Watt, Bio Rad) for 0 – 30 sec prior to incubation at 30° C.

4.6. Molecular biological methods

4.6.1. DNA extraction from *E. coli* and *C. glutamicum* cells

Plasmid extractions from *E coli* or *C. glutamicum* cells were carried out using a NucleoSpin® Plasmid Kit (Macherey-Nagel) according to manufacturer's instruction. Protocol modifications were required for cell lysis of *C. glutamicum* cells. Here, cultures were grown in 10 ml BHI medium to exponential growth phases in presence of selection antibiotic, following incubation with 20 mg/ml lysozyme in P1 buffer overnight at 30° C prior to plasmid extraction.

Genomic DNA was isolated from *C. glutamicum* cells for qPCR analyses and usage in PCR reactions. Here, cells were washed in TE buffer (10 mM Tris-(hydroxymethyl)-aminomethan (Tris)-HCl pH 7.8, 1 mM ethylendiamin-tetraacetat (EDTA)) and incubated with 15 mg/ml lysozyme in TE buffer for 4 h at 37° C. Following overnight incubation at 37° C in lysis buffer (10 mM Tris-HCl pH 7.8, 270 mM NaCl, 1.6 mM EDTA, 1 % sodium dodecyl sulfate (SDS), 100 µg/ml proteinase K), one third liquid volume of saturated NaCl solution was added. After sedimentation of cell debris, ethanol precipitation was performed to purify and concentrate DNA from the supernatant.

4.6.2. DNA amplification

Polymerase chain reactions were carried out using Phusion® high fidelity polymerase (New England Biolabs) or ReproFast Polymerase (Genaxxon Bioscience) according to manufacturer's instruction. Purified genomic or plasmid DNA served as PCR templates. Overlap-PCRs were performed in order to generate sequence deletions or site-directed mutations, particularly in *parS*,

parB and *smc* coding regions, according to Link et al. (1997). With regards to the latter method, oligonucleotides were designed harboring respective point mutations at overlapping sequences and silent point mutations, which generate artificial restriction sites in order to pre-select positive colonies at later cloning stages.

4.6.3. Separation and purification of nucleic acids

Agarose gel electrophoresis was performed for separation of nucleic acids following PCR amplification or restriction digest. Here, 1 % agarose gels were run in TAE buffer (40 mM Tris-HCl pH 8, 1 mM EDTA, 20 mM acetic acid) at 100 V. When required, nucleic acids were subsequently extracted using a NucleoSpin® Gel Kit and PCR Clean-up Kit (Macherey-Nagel).

4.6.4. Quantification and sequencing of nucleic acids

Concentrations of nucleic acids were determined using a UV/VIS spectrophotometer (BioDrop μLite, Serva), while sequencing was undertaken by the inhouse sequencing service (Genomics service unit, Genetics, Faculty of Biology). To this end, approximately 50 ng of DNA fragments and 150 – 300 ng of plasmid DNA were submitted with sequencing primers in 10 mM Tris-HCl for sequencing reactions.

4.6.5. Enzymatic modification of nucleic acids

Restriction digest was performed according to manufacturer's instructions (New England Biolabs). In order to avoid re-ligation of plasmid DNA, alkaline phosphatase (Calf intestinal, New England Biolabs) was added to the reaction to dephosphorylate DNA-ends. Subsequently, ligation was performed using T4 DNA Ligase (New England Biolabs) on ice water, creating a temperature gradient overnight.

4.6.6. Chromosome Conformation Capture Libraries

Chromosome Conformation Capture (3C) libraries were generated as previously described by Val et al. (2016) with minor changes. Briefly, cells were grown in 200 ml of BHI medium at 30° C to an OD_{600} of 3 and rediluted to a final concentration of ~1 x 10^7 cells/ml. Cells were crosslinked using fresh formaldehyde for 30 min at room temperature (3 % final concentration; Sigma Aldrich Formalin 37 %) followed by 30 min at 4° C. Formaldehyde was quenched using a final

concentration of 0.25 M glycine for 20 min at room temperature. Cells were then collected by centrifugation, frozen in dry ice and stored at -80° C until use. Frozen pellets of ~10^9 cells were thawed on ice and suspended in a final volume of 1.1 ml 1 x TE buffer (10 mM Tris-HCl pH 8, 1 mM EDTA) and transfer in a VK01 Precellys Tube (beads beating). Fixed cells were disrupted using the following program on a precellys apparatus: 9 cycles x [20“ – 3500 rpm; 30“ – pause]. Lysate was transferred to a 1.5 ml tube, SDS 10 % was added to the mix to a final concentration of 0.5 % and the mix was incubated for 10 min at room temperature.

1 ml of lysate was then transferred in a 5 ml tube containing 4 ml of digestion mix (1 x NEB 3 buffer, 1 % Triton X-100, and 1000 U MluCI enzyme). DNA was digested for 3 h at 37° C under shaking. The insoluble fraction was then recovered through centrifugation (16,000 x g – 20 min) and the obtained pellet was resuspended in 1 ml of water and diluted in 15 ml of ligation reaction mix (1 x ligation buffer NEB without ATP, 1 mM ATP, 0.1 mg/ml BSA, 125 units of T4 DNA ligase 5 U/ml). Ligation was allowed to proceed for 4 h at 16° C, followed by incubation overnight at 65° C in presence of 250 mg/ml proteinase K, 0.5 % SDS and 5 mM EDTA. The next morning, DNA was precipitated using 1/10th volume of 3 M Na-Acetate (pH 5.2) and one volume of isopropanol. After one h at -80° C, DNA was pelleted, resuspended in 900 µl 1 x TE buffer and extracted with 900 µl phenol-chloroform (pH 8.0). DNA was again precipitated using 1/10th volume of 3 M Na-Acetate (pH 5.2) and 2.5 volume of cold ethanol. Finally, DNA was resuspended in 100 µL 1 x TE buffer supplemented with RNAse and incubated 30 min at 37° C. 3C libraries were then processed as described (Val et al., 2016) and paired end-sequenced on an Illumina NextSeq apparatus (2 x 35 bp). All the reads used in this study are available on the SRA database under the following accession number: PRJNA525583.

4.6.7. Contact map generation

Contact maps were generated as previously described (Lioy et al., 2018). Reads were aligned independently (forward and reverse) using Bowtie 2 in very sensitive mode and were assigned to a restriction fragment. Non-informative events (self-circularized DNA fragments, or uncut fragments) were discarded by taking into account the pair-reads relative directions and the distribution of the different configurations as described in Cournac et al. (2012). We then bin the genomes into regular units of 5 Kb to generate contact maps and normalized them using the sequential component normalization procedure (Cournac et al., 2012).

Ratio between contact maps was computed for each point of the map by dividing the amount of normalized contacts in one condition by the amount of normalized contacts in the other condition and by plotting the log2 of the ratio. The color code reflects a decrease or increase of contacts in one condition compared to the other (blue or red signal, respectively). No change is represented by a white signal.

4.6.8. Chromatin immunoprecipitation (ChIP)

In vivo ChIP experiments with *C. glutamicum* ParB, SMC or MksB proteins were conducted using strains with allelic replacements of respective proteins with mCherry-tagged versions. Exponentially growing cells were crosslinked in 1 % formaldehyde for 30 min at room temperature; for SMC- and MksB-mCherry ChIP experiments cells were treated with Crosslink Gold (Diagenode) for 30 min at room temperature and washed twice in phosphate-buffered saline (PBS; 137 mM NaCl, 10 mM Na_2HPO_4, 1.8 mM KH_2PO_4, 2.7 mM KCl, pH 7.4.) prior to formaldehyde crosslinking. Fixed cells were subsequently washed in PBS and suspended in protoplast buffer (50 mM Tris pH 7.4, 50 mM NaCl, 10 mM EDTA, 0.5 M sucrose, EDTA-free protease inhibitor cocktail) supplemented with 20 mg/ml of lysozyme for 2 h at 37° C. After washing in protoplast buffer pellets were resuspended in buffer L (50 mM HEPES-KOH pH 7.55, 40 mM NaCl, 1 mM EDTA, 1 % Triton X-100, 0.1 % deoxycholate, 0.1 mg/ml RNaseA; EDTA-free protease inhibitor cocktail) and DNA was sheared into fragments of around 800 bp length by sonication using an ultrasonic cell disruptor (Branson Ultrasonics Sonifier™; 20 % amplitude, pulse 0.5 sec on/off, 6 x 20 sec). following removal of cell debris (20000 g, 10 min, 4° C). Aliquots of cell extracts were stored for later use.

Dynabeads™ Protein G (Thermo Fisher Scientific) were bound to an α-mCherry antibody (polyclonal rabbit IgG, BioVision Inc.) in buffer L for 1.5 h at 4° C, washed in buffer L and subsequently incubated with cell extract for 2 h at 4° C. Thereafter, beads were washed in buffer L, in buffer L5 (50 mM HEPES-KOH pH 7.55, 500 mM NaCl, 1 mM EDTA, 1 % Triton X-100, 0.1 % deoxycholate), in buffer W (10 mM Tris-HCl pH 8, 250 mM LiCl, 0.5 % NP-40, 0.5 % deoxycholate, 1 mM EDTA), and TE buffer (10 mM Tris-HCl pH 8, 1 mM EDTA) consecutively and finally resuspended in TES buffer (10 mM Tris-HCl pH 8, 10 mM EDTA, 1 % SDS). Extract samples were also supplemented with TES buffer and SDS to a final concentration of 1 % SDS; crosslinks were reverted at 65° C overnight. Phenol-chloroform extraction yielded DNA pellets, which were further purified using a DNA purification kit (QIAquick®, Qiagen). qPCR was applied in order to confirm protein enrichment at specific chromosomal loci. Immunoprecipitation and

extract samples were diluted 1:10 and 1:100 in water, yielding concentrations of approximately 0.2 - 0.4 ng/µl.

4.6.9. ChIP-seq analyses

For sequencing analyses libraries of ChIP samples were prepared using Nextera XT or Nextera Flex library preparation kits (Illumina®), followed by sequencing utilizing an Illumina MiSeq system by the inhouse sequencing service (Genomics service unit, Genetics, Faculty of Biology). Reads were aligned to the *C. glutamicum* ATCC 13032 genome sequence (GeneBankID: BX927147.1), where RES167-specific genome deletions were manually cut using CLC Genomics Workbench. Data of extract and corresponding ChIP samples were each normalized based on read counts and the ratio of the number of reads per 0.5 Kb bin were determined via the Galaxy web platform (Afgan et al., 2016; Ramírez et al., 2016). ChIP data reported in this work can be accessed at SRA, accession number: PRJNA529385.

4.6.10. Real-time PCR

Genomic DNA was isolated from *C. glutamicum* or *B. subtilis* cells in exponential or stationary growth phases. DNA amplification was performed using a 2 x qPCR Mastermix (KAPA SYBR®FAST, Peqlab) according to manufacturer's instruction, where reaction volumes of 10 µl contained 200 nM oligonucleotides (**Table 4.1**) and 1.5 ng of DNA in case of marker frequency analyses or 4 µl of diluted DNA for ChIP validation as described in chapter **4.6.8**, respectively. Samples were measured in technical replicates via an iQ5 multicolor real-time PCR detection system (Bio-Rad) and CT-values were determined via the Bio Rad-IQ™5 software version 2.1. Primer efficiencies were estimated by calibration dilution curves and slope calculation (Rasmussen, 2001); data were analyzed via the $2^{-\Delta CT}$ method (Livak and Schmittgen, 2001) accounting for dilution factors and sample volumes used for DNA purification. qPCR data of ChIP samples were normalized according to the ParB-mCherry2 signal obtained at locus *parS1* in the wild type background, serving as reference in each experiment. For determination of *oriC*/*terC* ratios, DNA replication run-outs (see **4.5**) yielding *oriC*/*terC* ratios of 1 served as reference.

4.7. Microscopy

4.7.1. Fluorescence microscopy

Fluorescence microscopy was performed with exponentially grown cells mounted on agarose-coated slides (1 % agarose). Images were acquired on an Axio-Imager M1 fluorescence microscope (Carl Zeiss) with an EC Plan Neofluar 100 x/1.3 oil Ph3 objective and a 2.5 x optovar and a Hamamatsu ORCA-R2 camera. Fluorescence of protein fusions with eYFP and mCherry/mCherry2 or DNA stained via Hoechst 33342 (1 µg/ml, Thermo Scientific) were detected using filter sets 46 HE YFP (EX BP 500/25, BS FT 515, EM BP 535/30), 43 HE Cy 3 shift free (EX BP 550/25, BS FT 570, EM BP 605/70) and 49 DAPI shift free (EX G 365, BS FT 395, EM BP 445/50). Live cell imaging as well as detection of fluorescently labeled condensin subunits were carried out using a Delta Vision Elite microscope (GE Healthcare, Applied Precision) with a standard four color InsightSSI module, a 100 x/1.4 oil PSF U-Plan S-Apo objective, a CoolSNAP HQ2 CCD camera and the YFP (EX BP 513/17, EM BP 548/22) and mCherry (EX BP 575/25, EM BP 625/45) specific filter sets. In order to conduct time-lapse experiments exponentially grown cells were diluted to an OD_{600} of 0.01 in BHI and loaded in a microfluidic chamber (B04A CellASIC®, Onix); the environmental chamber was heated to 30° C and 0.75 psi were applied for nutrient supply throughout the experiment. Images were taken in 5 min intervals.

Computational analysis of still microscopy images was performed using the plug-in MicrobeJ (Ducret et al., 2016) and Morpholyzer for the image analysis platform Fiji, described before (Schindelin et al., 2012; Schubert et al., 2017). In short, the latter algorithm automatically detects cell outlines, extracting corresponding regions of interest from all image channels. Longitudinal center lines are determined for each cell, which account for curvatures. Subsequently, linear fluorescence profiles are extracted together with cell lengths for each cell. Data were further evaluated using the software R (Team, 2014) by sorting cells according to length, transferring cellular fluorescence profiles into color codes and finally aligning these profiles to channel-specific heat maps.

4.7.2. Photoactivated localization microscopy (PALM)

For sample preparation, *C. glutamicum* cells were harvested in exponential growth phases, washed twice in PBS and fixated in PBS + 3 % formaldehyde solution (36.5 - 38 % in H_2O + 10 - 15 % methanol, Sigma Aldrich) for 30 min at 30° C. Excess formaldehyde was subsequently quenched by adding 10 mM glycine, cells were sedimented at 5000 g for one min, resuspended in PBS containing 10 mM glycine and incubated for five min at room temperature. This quenching step was repeated three times; cells were finally diluted in buffer containing 50 mM Tris-HCl pH 7.4, 50 mM NaCl, 10 mM EDTA and 0.5 M sucrose.

Super-resolution imaging was performed on a Zeiss ELYRA P.1 microscope with laser lines HR diode 50 mW 405 nm and HR DPSS 200 mW 561 nm and an Andor EM-CCD iXon DU 897 camera. Cellular PAmCherry-tagged proteins were detected as described before using a long pass 570 nm filter (LP570) and an alpha Plan-Apochromat 100 x/1,46 Oil DIC M27 objective for imaging. Further, 100 nm TetraSpeck microspheres and the implemented drift correction tool served for drift correction; the Z-axis was stabilized via the "definite focus" system. PALM image calculation was performed applying the 2D x/y Gaussian fit (Zen2 software, Zeiss) using a peak mask size of 9 pixels, where one pixel corresponds to 100 nm and a peak intensity to noise ratio of 6. In order to exclude background and events resulting from the co-emission of co-localizing molecules, events were filtered for photon numbers between 70-350 and PSF width at 1/e maximum (70 - 170 nm) were applied. As a last step, events were grouped according to the following parameters: 3 on-frames with 0 off-frames allowed and a search radius of 30 nm.

When imaging strains containing ParB-PAmCherry, four imaging series were taken for each field of view, where each subsequent series was characterized by a specific 405 nm laser linear gradient intensity range (0.001 % to 0.01 %, 0.01 % to 0.1 %, 0.1 % to 1 % and 1 % to 10 %). Every other imaging parameter remained the same in between the time series. The frame count for each collection was 10000 frames and converted molecules were imaged using the 561 nm laser at 15 % (transfer mode) for 50 ms at a 200 - fold EMCCD gain. The workflow of protein cluster analysis is illustrated in **Figure 4.1**. The field of view in the bright field channel was corrected for illumination unevenness by dividing the field of view containing the cells of interest with an empty one (Process - Calculator Plus, Fiji) and enlarged 10 times (bicubic interpolation). The resulting image was thresholded (Image – Adjust - Threshold) with default parameters and converted to a binary mask. A Fiji macro was then run on the binary mask to close the mask holes present within cells and to enlarge the cells mask themselves. Cells that were in contact with each other were separated via water shading. The perimeter coordinates corresponding to masks representing cells

lying within the focus were extracted and used to exclude events originating from cells lying outside of the focal plane and the background. The clustering structures of events within a cell were identified via the OPTICS algorithm in R (Ankerst et al., 1999; Team, 2014).

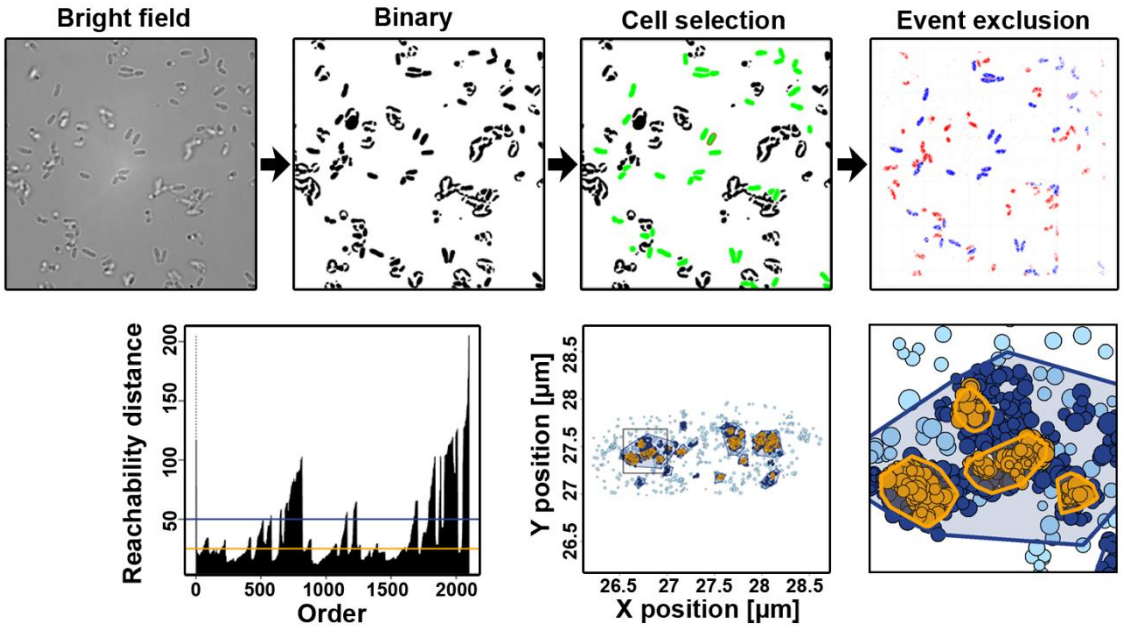

Figure 4.1: Workflow for ParB cluster analysis.

Top: Generation of binary masks from bright field image, cell selection and event exclusion. Below: Cluster-ordering in reachability plot (left) showing cluster-order of events within one cell and their reachability distances [nm]. Threshold lines for macro- (dark blue) and sub-clusters (yellow) are indicated. Events that are not part of clusters are displayed in light blue. Events within cell are assigned accordingly, see detail magnification (right).

Macro- and sub-clusters of ParB protein were identified by setting the following parameters within the OPTICS algorithm: minimum points = 32, epsilon = 3000. The threshold epsilon is 50 for the macro-clusters and 35 for the sub-clusters.

4.8. Protein biochemical methods

4.8.1. Preparation of *C. glutamicum* cell lysates

Exponentially growing cells (10 ml) were usually harvested at an OD_{600} of 3. All following steps were performed at 4° C. Cell pellets were washed once in 10 ml washing buffer (375 mM Tris-HCl pH 7.5 10 mM; NaCl 150 mM; EDTA 0.5 mM) and resuspended in 1.5 ml washing buffer supplemented with 1 mM PMSF. After cell disruption via FastPrep®-24 (MP Biomedicals) at 10 x 6.5 m/sec 30 sec cell debris was removed by centrifugation at 18000 g.

4.8.2. Polyacrylamide gel electrophoresis

Polyacrylamide gel electrophoresis was applied in order to separate proteins according to their size (Laemmli, 1970). Resolving (Tris-HCl pH 8.8, 12 % (v/v) acrylamide, 0.1 % (w/v) SDS, 0.05 % (w/v) ammonium persulfate, 0.05 % (w/v) tetramethylethylenediamine) and stacking gel (Tris-HCl pH 6.8, 4 % (v/v) acrylamide, 0.1 % (w/v) SDS, 0.05 % (w/v) ammonium persulfate, 0.13 % (w/v) tetramethylethylenediamine) were cast in Mini-PROTEAN® Systems (Bio-Rad). Cell lysates were supplemented with 4 x loading buffer (200 mM Tris-HCl pH 6.8, 50 % (w/v) glycerol, 10 % (w/v) SDS, 4 % ß-mercaptoethanol; 0.08 % (w/v) bromophenol blue) and run in electrophoresis cells (Mini-PROTEAN®, Bio-Rad) filled with running buffer (25 mM Tris; 0.192 M glycine; 3.5 mM SDS) at 150 V for 1 h. A pre-stained protein ladder (PageRuler™, Thermo Fisher Scientific) further served as size standard. Hereafter, Coomassie Brilliant Blue staining was performed in order to control sample application. SDS-gels were incubated for 1 h in staining solution (0.02 % Coomassie G-250, 25 % (v/v) methanol, 10 % (v/v) acetic acid) and subsequently destained using 10 % (v/v) acetic acid.

4.8.3. Western Blot and immunodetection

Proteins separated in SDS-gels were electro-transferred to PVDP-membranes, which were activated in methanol prior to use. To this end, Western Blots were performed in electrophoretic chambers (Bio-Rad), filled with transfer buffer (25 mM Tris-HCl pH 8.3, 0.2 M Glycine, 20 % (v/v) Methanol), at 300 mA for 3 h. Thereupon, non-specific binding sites were blocked for 1 h in 5 % skimmed milk powder in TBS-T (50 mM Tris-HCl pH 7.5, 150 mM NaCl, 0.1 % Tween 20). Subsequently, membranes were incubated in 1:2000 dilutions of anti-mCherry (polyclonal rabbit

IgG, BioVision Inc.) or anti-Histidine (monoclonal mouse IgG, GE Healthcare) primary antibodies in 5 % skimmed milk powder in TBS-T for 1 h, following three washing steps in TBS-T for 5 min each. Secondary antibodies anti-rabbit (polyclonal goat IgG, alkaline phosphatase conjugate, Sigma-Aldrich®) or anti-mouse (polyclonal goat IgG, horseradish peroxidase conjugate, Invitrogen™ Thermo Fisher Scientific) were applied in 1:10000 dilutions in 5 % skimmed milk powder in TBS-T for 1 h. After repeated washing in TBS-T, immunodetection was performed. Here, secondary antibodies were detected using either chromogenic alkaline phosphatase substrates 5-bromo-4-chloro-3-indolyl phosphate/nitro blue tetrazolium or luminol-/peroxide-based chemiluminescence reagents (Pierce™ ECL Western Blotting Substrate, Thermo Fisher Scientific) according to manufacturer's instruction and monitored via a ChemiDoc™ UV plate (Chemi Hi Sensitive protocol, Bio-Rad).

4.8.4. Protein identification via immunoprecipitation and mass spectrometry

For immunoprecipitation of interacting proteins strains CBK012, CBK015 and CBK052 were cultivated in BHI medium using culture flasks pretreated with 0.5 % sodium hypochlorite, harvested at exponential growth and lysed as described above. All following steps were performed at 4° C. Immunoprecipitation was performed with 25 µl magnetic RFP-Trap® agarose beads (Chromotek) incubated in 1 ml lysate for 1 h. Thereupon, beads were washed three times in washing buffer and again washed three times in 100 mM ammonium bicarbonate prior to storage at -20° C.

For proteomic analysis of interacting proteins, the magnetic beads were first washed with 50 µl of 100 mM TRIS, pH 7.6. Subsequently, 50 µl of 100 mM Tris-HCl pH 7.6 containing 4 M urea, 5 mM dithiothreitol for reduction of disulfide bond and 0.2 µg of LysC for predigestion of proteins were added to each sample. After incubation of 3 h, 100 µl of 100 mM Tris-HCl pH 7.6, 10 mM iodoacetamide was added for blocking of free cysteine side chains and samples were incubated in the dark for 5 min. Samples were diluted with 100 µl Tris-HCl pH 7.6 to reduce the urea concentration and 1 µg of trypsin was added to each sample. The samples were incubated for 14 h to complete protein digestion and subsequently trifluoroacetic acid was added to a final concentration of 0.5 % to acidify the samples. Peptide mixture were separated from the magnetic beads before the desalting step. The beads were washed 2 x with 75 µl of 0.1 % formic acid and the wash solvent was combined with the peptide mixtures. For sample desalting, 3 discs were stamped from C18 discs (Empore C18, 3M) and placed into a 200 µl pipette tip. Following binding of

peptides, stage tips were washed 2 x with 60 µl of 0.1 % formic acid and peptides were eluted with 40 % acetonitrile containing 30 % methanol and 0.1 % formic acid.

Samples were dried in a speedvac and resuspended in 10 µl of 0.1 % formic acid. Peptide mixtures were analyzed by liquid chromatography tandem mass spectrometry (LC-MS/MS) to identify and quantify proteins in all samples. First, peptides were separated by nano-reversed phase chromatography using a linear gradient from 2 to 35 % acetonitrile over 50 min in 0.1 % formic acid on an in house- packed chromatography column in a nano-electrospray emitter tip. Eluting peptides were directly infused into the mass spectrometer (QExactive, Thermo-Fisher) and detected in positive ionization mode. The operating cycle was programmed to detect peptides in the range from 300 to 1600 m/z and up to 10 precursors were selected for MS/MS analysis by CID fragmentation. Precursor ions required a charge state between + 2 and + 6 and a minimal signal intensity of 6 x 10 e^4. Protein mapping and quantitative analysis raw LC-MS/MS data were searched against a *C. glutamicum* database retrieved from Uniprot (page view 03/2017, 3093 protein entries) using a forward/reversed search by the Andromeda algorithm within the MaxQuant software suite. Peptides hits were searched with 17 ppm precursor mass deviation in the first search and 3 ppm for the main search. For MS/MS spectra, a mass accuracy of 25 ppm was set. As variable modifications, acetylation of the protein N-terminus, STY-phosphorylation, and methionine oxidation were selected. Carbamidomethylation of cysteine was the only fixed modification. Peptide match results were sorted by their probability score and filtered for 2 % reversed peptide hits and 5 % reversed protein hits.

To calculate protein enrichments and significance values, reversed protein hits and proteins with less than 3 quantitative values in any of the sample types (control, MksB IP, SMC IP, PldP IP) were filtered out. The iBAQ-values were log2 transformed and median normalized. In case of one missing value in the triplicate measurements the value was imputed using a closest neighbor method, for more missing data points a random value from a standard distribution downshifted by a factor of 1.8 from the sample distribution and width of 0.3 was selected. Samples were compared using a student's t-test which was false discovery rate-controlled by sample permutation. Proteomic data are available via ProteomeXchange with the project identifier PXD008916 (Deutsch et al., 2017).

4.8.5. Bacterial two-hybrid screening

Protein interactions obtained by mass spectrometry were confirmed via bacterial adenylate cyclase two-hybrid assays (Karimova et al., 1998). Interaction of two proteins of interest was assayed by fusing them with the adenylate cyclase subunits T25 and T18 using compatible vectors expressing those fragments (pKT25/pKNT25 and pUT18/pUT18C). Bacterial two-hybrid vectors were constructed as described before and two recombinant vectors each were co-transformed into *E. coli* BTH101 cells. Bacteria were subsequently plated on indicator medium LB/X-Gal (5-bromo-4-chloro-3-indolyl-β-D-galactopyranoside, 40 μg/ml) supplemented with IPTG (0.5 mM) and antibiotics kanamycin (50 μg/ml), carbenicillin (100 μg/ml) and streptomycin (100 μg /ml) and incubated at 30° C for 24 h. Interacting hybrid proteins were identified by blue-white screening and β-galactosidase assays in a 96 well plate-format as previously described (Mehla et al., 2017). Cotransformants harboring empty plasmids or pUT18C-zip/pKT25-zip plasmids served as positive and negative controls. Miller units of negative controls served as reference and were set to zero; Miller units of any other sample were normalized accordingly. All C- and N-terminal combinations of hybrid proteins were assayed and positive signals were confirmed through at least three replicates.

4.8.6. Protein purification

ParB protein production was performed in *E. coli* BL21 pLysS via the pET-16b vector-based system. Cells were grown in LB at 37° C; gene expression was induced adding 1 mM IPTG following growth for 12 h at 18° C. Subsequently, cells were suspended in washing buffer (50 mM Tris-HCl, pH 7.4; 100 mM NaCl; 5 mM; $MgCl_2$; 1 mM dithiothreitol) containing EDTA-free proteinase inhibitor (cOmplete™, Sigma) and DNAseI and lysed using a high-pressure cell homogenizer. Cell debris and membranes were removed by centrifugation at 4° C, 1700 g for 20 min and 150000 g for 45 min, respectively. Thereupon, batch purifications of Histidine-tagged protein were performed under native conditions using Ni-NTA agarose (Protino®, Macherey-Nagel) according to manufacturer's instruction. In brief, the equilibrated gel was incubated with clarified lysate for 60 min at 4° C under gentle agitation and washed twice in washing buffer containing 80 mM imidazole. Proteins were eluted in three steps using washing buffer with an imidazole concentration of 300 mM, concentrated via Amicon filter units (Merck) and further purified by applying size exclusion chromatography using an ÄKTApurifier system with a Superdex™ 200 gel filtration column (GE Healthcare Life Sciences).

4.8.7. Electrophoretic mobility shift assay

DNA-ParB binding was assayed using purified protein and double-stranded DNA fragments of approximately 1100 bp length with or without two *parS* sites generated by PCRs of a *C. glutamicum* genomic locus surrounding *parS9* and *parS10* using primer pairs parS9mut-HindIII-up-F/parS10mut-EcoRI-D-R. ParB concentrations of 0.05 to 25 µM were incubated with 100 ng DNA for 30 min at 30° C, following sample separation in native gels (3-12 % polyacrylamide, ServaGel™). DNA was stained using SYBR® Green I (Invitrogen).

4.9. Flow cytometry

Culture samples were fixed 1:9 (v/v) in 70 % ethanol and stored at 4° C until use. Cells were pelleted at 5000 rpm for 5 min and washed once in phosphate-buffered saline (PBS). The DNA staining procedure was adopted from a protocol described before (Hammes et al., 2008). Samples were preheated to 37° C and stained in SYBR® Green I (Invitrogen) with a final dilution of 1:10000 for 15 min and consequently diluted in PBS. Flow cytometry analysis was performed using a BD Accuri C6 (BD Biosciences) with a 488 nm blue laser. The measurements were conducted at a flow rate of 10 µl/min with an acquisition threshold set to 700 arbitrary units on FL1-H and a rate of events per second less than 5000. At least 200000 events per sample were collected. Data were analyzed by plotting samples as histograms versus the green channel (FL1-A, EM BP 533/30) at log scale. All experiments were performed in biological triplicates.

In order to calibrate the DNA measurements of different growth conditions *B. subtilis* cells were used as an internal standard. A replication run-out of *B. subtilis* cells grown in LB medium gave rise to cells with mainly 4 or 8 fully replicated chromosomes (Hill et al., 2012). Prior to ethanol fixation the cell wall was stained applying a click chemistry reaction (strain-promoted alkyne-azide cycloaddition). In short 5 mM 3-Azido-D-alanine (Baseclick GmbH), which incorporates into the cell wall, was added to the culture during the time of replication run-out. Cells were washed in PBS, incubated with 10 µM DBCO-PEG_4-5/6-Carboxyrhodamine 110 (Jena Bioscience) at 30° C for 20 min in the dark and subsequently washed three times in PBS + 0.1 % Tween 80. This standard was included with *C. glutamicum* cells during incubation with 1 µg/ml Hoechst 33342 DNA stain. Flow cytometry was performed with a FACSAria II (Becton Dickinson) using a 488 nm blue laser and a 355 nm UV laser and appropriate filter sets. 50000 events were collected per sample. Blots of DNA content versus the green channel were used to

identify *B. subtilis* subpopulations and *C. glutamicum* chromosome numbers were assessed in accordance with the standard in histograms versus DNA amount. For data analysis BD Accuri C6 software (BD Biosciences) or FlowJo software (Tree star, Inc.) were applied.

4.10. Analysis of the cell cycle

C- and D-periods were determined via equations relating to DNA amount per cell in exponential cultures (Bremer and Churchward, 1977; Hill et al., 2012), which were adapted to the *C. glutamicum* cell cycle model with double the number of chromosome equivalents at any time. Since only every second initiation is followed by a cell division the average *oriC*s per cell ($\bar{I}$) are defined as shown below. The term for the average *terC*s per cell ($\overline{T}$) was adjusted accordingly, where T_d is the doubling time:

$$\bar{I}=2\times2^{(C+D)/T_d}$$

$$\overline{T}=2\times2^{D/T_d}$$

Hence, the D-period was calculated as shown below; the average number of *oriC*s (I) per cell (N) was resolved by flow cytometry:

$$D=\frac{\ln\left(\frac{I}{2}/N\right)\times T_d}{\ln(2)}-C$$

The equation for determination of C periods does not change upon assumptions made above, where the *oriC* to *terC* ratio (I/T) was determined by marker frequency analysis:

$$C=\frac{\ln(I/T)\times T_d}{\ln(2)}$$

4.11. Statistical analyses

Nearest neighbor distance distributions, ANOVA, post hoc tests and t tests were performed using R (Team, 2014) or Perseus software (Tyanova et al., 2016); ANCOVA, correlation coefficients and linear regressions were calculated using Excel and Graph Pad Prism (GraphPad Software).

5. References

Adachi, S., Kohiyama, M., Onogi, T., and Hiraga, S. (2005). Localization of replication forks in wild-type and *mukB* mutant cells of *Escherichia coli*. Molecular Genetics and Genomics *274*, 264-271.

Afgan, E., Baker, D., van den Beek, M., Blankenberg, D., Bouvier, D., Čech, M., Chilton, J., Clements, D., Coraor, N., Eberhard, C., *et al.* (2016). The Galaxy platform for accessible, reproducible and collaborative biomedical analyses: 2016 update. Nucleic acids research *44*, W3-W10.

Aldridge, B.B., Fernandez-Suarez, M., Heller, D., Ambravaneswaran, V., Irimia, D., Toner, M., and Fortune, S.M. (2012). Asymmetry and aging of mycobacterial cells lead to variable growth and antibiotic susceptibility. Science *335*, 100-104.

Angelini, S., Deitermann, S., and Koch, H.-G. (2005). FtsY, the bacterial signal-recognition particle receptor, interacts functionally and physically with the SecYEG translocon. EMBO reports *6*, 476-481.

Ankerst, M., Breunig, M.M., Kriegel, H., and Sander, J. (1999). OPTICS: Ordering points to identify the clustering structure. In ACM SIGMOD international conference on Management of data (Philadelphia, Pennsylvania, USA, ACM Press), pp. 49-60.

Aragón, L. (2018). The Smc5/6 complex: new and old functions of the enigmatic long-distance relative. Annual review of genetics *52*, 89-107.

Arjes, Heidi A., Kriel, A., Sorto, Nohemy A., Shaw, Jared T., Wang, Jue D., and Levin, Petra A. (2014). Failsafe mechanisms couple division and DNA replication in bacteria. Current Biology *24*, 2149-2155.

Asada, S., Takano, M., and Shibasaki, I. (1979). Deoxyribonucleic acid strand breaks during drying of *Escherichia coli* on a hydorohobic filter membrane. Applied and environmental microbiology *37*, 266-273.

Atmakuri, K., Cascales, E., Burton, O.T., Banta, L.M., and Christie, P.J. (2007). *Agrobacterium* ParA/MinD-like VirC1 spatially coordinates early conjugative DNA transfer reactions. The EMBO journal *26*, 2540-2551.

Aussel, L., Barre, F.-X., Aroyo, M., Stasiak, A., Stasiak, A.Z., and Sherratt, D. (2002). FtsK is a DNA motor protein that activates chromosome dimer resolution by switching the catalytic state of the XerC and XerD recombinases. Cell *108*, 195-205.

Badrinarayanan, A., Le, T.B., and Laub, M.T. (2015). Bacterial chromosome organization and segregation. Annual review of cell and developmental biology *31*, 171-199.

Badrinarayanan, A., Reyes-Lamothe, R., Uphoff, S., Leake, M.C., and Sherratt, D.J. (2012). In vivo architecture and action of bacterial structural maintenance of chromosome proteins. Science (New York, N.Y.) *338*, 528-531.

Barutcu, A.R., Fritz, A.J., Zaidi, S.K., van Wijnen, A.J., Lian, J.B., Stein, J.L., Nickerson, J.A., Imbalzano, A.N., and Stein, G.S. (2016). C-ing the genome: a compendium of chromosome conformation capture methods to study higher-order chromatin organization. Journal of cellular physiology *231*, 31-35.

Bates, D., and Kleckner, N. (2005). Chromosome and replisome dynamics in *E. coli*: loss of sister cohesion triggers global chromosome movement and mediates chromosome segregation. Cell *121*, 899-911.

Beattie, T.R., and Reyes-Lamothe, R. (2015). A Replisome's journey through the bacterial chromosome. Frontiers in microbiology *6*, 562.

Berlatzky, I.A., Rouvinski, A., and Ben-Yehuda, S. (2008). Spatial organization of a replicating bacterial chromosome. Proceedings of the National Academy of Sciences *105*, 14136-14140.

Bernstein, H.D., and Hyndman, J.B. (2001). Physiological basis for conservation of the signal recognition particle targeting pathway in *Escherichia coli*. Journal of bacteriology *183*, 2187-2197.

Bigot, S., Saleh, O.A., Lesterlin, C., Pages, C., El Karoui, M., Dennis, C., Grigoriev, M., Allemand, J.F., Barre, F.X., and Cornet, F. (2005). KOPS: DNA motifs that control *E. coli* chromosome segregation by orienting the FtsK translocase. The EMBO journal *24*, 3770-3780.

Blakely, G., May, G., McCulloch, R., Arciszewska, L.K., Burke, M., Lovett, S.T., and Sherratt, D.J. (1993). Two related recombinases are required for site-specific recombination at *dif* and *cer* in *E. coli* K12. Cell *75*, 351-361.

Böhm, K., Giacomelli, G., Schmidt, A., Imhof, A., Koszul, R., Marbouty, M., and Bramkamp, M. (2019). Chromosome organization by a conserved condensin-ParB system in the actinobacterium *Corynebacterium glutamicum*. bioRxiv, 649749.

Böhm, K., Meyer, F., Rhomberg, A., Kalinowski, J., Donovan, C., and Bramkamp, M. (2017). Novel chromosome organization pattern in *Actinomycetales*—overlapping replication cycles combined with diploidy. mBio *8*, e00511-00517.

Bouthier de la Tour, C., Toueille, M., Jolivet, E., Nguyen, H.H., Servant, P., Vannier, F., and Sommer, S. (2009). The *Deinococcus radiodurans* SMC protein is dispensable for cell viability yet plays a role in DNA folding. Extremophiles : life under extreme conditions *13*, 827-837.

Bowman, G.R., Comolli, L.R., Zhu, J., Eckart, M., Koenig, M., Downing, K.H., Moerner, W.E., Earnest, T., and Shapiro, L. (2008). A polymeric protein anchors the chromosomal origin/ParB complex at a bacterial cell pole. Cell *134*, 945-955.

Boyer, J., Rohleder, K., and Ketner, G. (1999). Adenovirus E4 34k and E4 11k inhibit double strand break repair and are physically associated with the cellular DNA-dependent protein kinase. Virology *263*, 307-312.

Boylen, C.W., and Mulks, M.H. (1978). The survival of coryneform bacteria during periods of prolonged nutrient starvation. Microbiology *105*, 323-334.

Bramkamp, M., Emmins, R., Weston, L., Donovan, C., Daniel, R.A., and Errington, J. (2008). A novel component of the division-site selection system of *Bacillus subtilis* and a new mode of action for the division inhibitor MinCD. Molecular microbiology *70*, 1556-1569.

Brandon, L.D., Goehring, N., Janakiraman, A., Yan, A.W., Wu, T., Beckwith, J., and Goldberg, M.B. (2003). IcsA, a polarly localized autotransporter with an atypical signal peptide, uses the Sec apparatus for secretion, although the Sec apparatus is circumferentially distributed. Molecular microbiology *50*, 45-60.

Breier, A.M., and Grossman, A.D. (2007). Whole-genome analysis of the chromosome partitioning and sporulation protein Spo0J (ParB) reveals spreading and origin-distal sites on the *Bacillus subtilis* chromosome. Molecular microbiology *64*, 703-718.

Bremer, H., and Churchward, G. (1977). An examination of the Cooper-Helmstetter theory of DNA replication in bacteria and its underlying assumptions. Journal of theoretical biology *69*, 645-654.

Britton, R.A., and Grossman, A.D. (1999). Synthetic lethal phenotypes caused by mutations affecting chromosome partitioning in *Bacillus subtilis*. Journal of bacteriology *181*, 5860-5864.

Britton, R.A., Lin, D.C., and Grossman, A.D. (1998). Characterization of a prokaryotic SMC protein involved in chromosome partitioning. Genes & development *12*, 1254-1259.

Broedersz, C.P., Wang, X., Meir, Y., Loparo, J.J., Rudner, D.Z., and Wingreen, N.S. (2014). Condensation and localization of the partitioning protein ParB on the bacterial chromosome. Proceedings of the National Academy of Sciences of the United States of America *111*, 8809-8814.

Bürmann, F., and Gruber, S. (2015). SMC condensin: promoting cohesion of replicon arms. Nat Struct Mol Biol *22*, 653-655.

Bürmann, F., Shin, H.-C., Basquin, J., Soh, Y.-M., Giménez-Oya, V., Kim, Y.-G., Oh, B.-H., and Gruber, S. (2013). An asymmetric SMC–kleisin bridge in prokaryotic condensin. Nature Structural &Amp; Molecular Biology *20*, 371.

Campo, N., Tjalsma, H., Buist, G., Stepniak, D., Meijer, M., Veenhuis, M., Westermann, M., Müller, J.P., Bron, S., Kok, J., *et al.* (2004). Subcellular sites for bacterial protein export. Molecular microbiology *53*, 1583-1599.

Chao, W.C.H., Murayama, Y., Muñoz, S., Jones, A.W., Wade, B.O., Purkiss, A.G., Hu, X.-W., Borg, A., Snijders, A.P., Uhlmann, F., *et al.* (2017). Structure of the cohesin loader Scc2. Nature communications *8*, 13952.

Charaka, V.K., and Misra, H.S. (2012). Functional characterization of the role of the chromosome I partitioning system in genome segregation in *Deinococcus radiodurans*. Journal of bacteriology *194*, 5739-5748.

Chen, B.-W., Lin, M.-H., Chu, C.-H., Hsu, C.-E., and Sun, Y.-J. (2015). Insights into ParB spreading from the complex structure of Spo0J and *parS*. Proceedings of the National Academy of Sciences *112*, 6613-6618.

Chen, I.A., Chu, K., Palaniappan, K., Pillay, M., Ratner, A., Huang, J., Huntemann, M., Varghese, N., White, J.R., Seshadri, R., *et al.* (2019). IMG/M v.5.0: an integrated data management and comparative analysis system for microbial genomes and microbiomes. Nucleic acids research *47*, D666-d677.

Ciosk, R., Shirayama, M., Shevchenko, A., Tanaka, T., Toth, A., Shevchenko, A., and Nasmyth, K. (2000). Cohesin's binding to chromosomes depends on a separate complex consisting of Scc2 and Scc4 proteins. Molecular cell *5*, 243-254.

Cobbe, N., and Heck, M.M. (2004). The evolution of SMC proteins: phylogenetic analysis and structural implications. Molecular biology and evolution *21*, 332-347.

Connelly, J.C., Kirkham, L.A., and Leach, D.R. (1998). The SbcCD nuclease of *Escherichia coli* is a structural maintenance of chromosomes (SMC) family protein that cleaves hairpin DNA. Proceedings of the National Academy of Sciences of the United States of America *95*, 7969-7974.

Cooper, S., and Helmstetter, C.E. (1968). Chromosome replication and the division cycle of *Escherichia coli* B/r. Journal of molecular biology *31*, 519-540.

Cournac, A., Marie-Nelly, H., Marbouty, M., Koszul, R., and Mozziconacci, J. (2012). Normalization of a chromosomal contact map. BMC Genomics *13*, 436.

Cremer, J., Eggeling, L., and Sahm, H. (1990). Cloning the *dapA dapB* cluster of the lysine-secreting bacterium *Corynebacterium glutamicum*. Molecular and General Genetics MGG *220*, 478-480.

Cremer, J., Eggeling, L., and Sahm, H. (1991). Control of the lysine biosynthesis sequence in *Corynebacterium glutamicum* as analyzed by overexpression of the individual corresponding genes. Applied and environmental microbiology *57*, 1746-1752.

Cromie, G.A., and Leach, D.R.F. (2001). Recombinational repair of chromosomal DNA double-strand breaks generated by a restriction endonuclease. Molecular microbiology *41*, 873-883.

Cui, Y., Petrushenko, Z.M., and Rybenkov, V.V. (2008). MukB acts as a macromolecular clamp in DNA condensation. Nature Structural &Amp; Molecular Biology *15*, 411.

David, A., Demarre, G., Muresan, L., Paly, E., Barre, F.X., and Possoz, C. (2014). The two Cis-acting sites, *parS*1 and *oriC*1, contribute to the longitudinal organisation of *Vibrio cholerae* chromosome I. PLoS genetics *10*, e1004448.

De Gelder, L., Ponciano, J.M., Joyce, P., and Top, E.M. (2007). Stability of a promiscuous plasmid in different hosts: no guarantee for a long-term relationship. Microbiology *153*, 452-463.

Debaugny, R.E., Sanchez, A., Rech, J., Labourdette, D., Dorignac, J., Geniet, F., Palmeri, J., Parmeggiani, A., Boudsocq, F., Anton Leberre, V., *et al.* (2018). A conserved mechanism drives partition complex assembly on bacterial chromosomes and plasmids. Molecular Systems Biology *14*.

Decorsiere, A., Mueller, H., van Breugel, P.C., Abdul, F., Gerossier, L., Beran, R.K., Livingston, C.M., Niu, C., Fletcher, S.P., Hantz, O., *et al.* (2016). Hepatitis B virus X protein identifies the Smc5/6 complex as a host restriction factor. Nature *531*, 386-389.

Demarre, G., Galli, E., Muresan, L., Paly, E., David, A., Possoz, C., and Barre, F.-X. (2014). Differential management of the replication terminus regions of the two *Vibrio cholerae* chromosomes during cell division. PLoS genetics *10*, e1004557.

Deutsch, E.W., Csordas, A., Sun, Z., Jarnuczak, A., Perez-Riverol, Y., Ternent, T., Campbell, D.S., Bernal-Llinares, M., Okuda, S., Kawano, S., *et al.* (2017). The ProteomeXchange consortium in 2017: supporting the cultural change in proteomics public data deposition. Nucleic acids research *45*, D1100-d1106.

Diebold-Durand, M.L., Lee, H., Ruiz Avila, L.B., Noh, H., Shin, H.C., Im, H., Bock, F.P., Burmann, F., Durand, A., Basfeld, A., *et al.* (2017). Structure of full-length SMC and rearrangements required for chromosome organization. Molecular cell *67*, 334-347.e335.

Dingwall, A., and Shapiro, L. (1989). Rate, origin, and bidirectionality of *Caulobacter* chromosome replication as determined by pulsed-field gel electrophoresis. Proceedings of the National Academy of Sciences of the United States of America *86*, 119-123.

Ditkowski, B., Holmes, N., Rydzak, J., Donczew, M., Bezulska, M., Ginda, K., Kędzierski, P., Zakrzewska-Czerwińska, J., Kelemen, G.H., and Jakimowicz, D. (2013). Dynamic interplay of ParA with the polarity protein, Scy, coordinates the growth with chromosome segregation in *Streptomyces coelicolor*. Open Biology *3*, 130006.

Dixon, J.R., Selvaraj, S., Yue, F., Kim, A., Li, Y., Shen, Y., Hu, M., Liu, J.S., and Ren, B. (2012). Topological domains in mammalian genomes identified by analysis of chromatin interactions. Nature *485*, 376.

Donovan, C. (2012). Cytoskeleton proteins involved in chromosome segregation and cell division in *Corynebacterium glutamicum*. In Faculty of Mathematics and Natural Sciences, Institute for Biochemistry (Köln, Universität zu Köln).

Donovan, C., and Bramkamp, M. (2014). Cell division in *Corynebacterineae*. Frontiers in microbiology *5*, 132.

Donovan, C., Schauss, A., Krämer, R., and Bramkamp, M. (2013). Chromosome segregation impacts on cell growth and division site selection in *Corynebacterium glutamicum*. PloS one *8*, e55078.

Donovan, C., Schwaiger, A., Krämer, R., and Bramkamp, M. (2010). Subcellular localization and characterization of the ParAB system from *Corynebacterium glutamicum*. Journal of bacteriology *192*, 3441-3451.

Donovan, C., Sieger, B., Krämer, R., and Bramkamp, M. (2012). A synthetic *Escherichia coli* system identifies a conserved origin tethering factor in Actinobacteria. Molecular microbiology *84*, 105-116.

Doron, S., Melamed, S., Ofir, G., Leavitt, A., Lopatina, A., Keren, M., Amitai, G., and Sorek, R. (2018). Systematic discovery of antiphage defense systems in the microbial pangenome. Science *359*.

Dubarry, N., Willis, C.R., Ball, G., Lesterlin, C., and Armitage, J.P. (2019). *In vivo* imaging of the segregation of the 2 chromosomes and the cell division proteins of *Rhodobacter sphaeroides* reveals an unexpected role for MipZ. mBio *10*, e02515-02518.

Ducret, A., Quardokus, E.M., and Brun, Y.V. (2016). MicrobeJ, a tool for high throughput bacterial cell detection and quantitative analysis. Nature Microbiology *1*, 16077.

Ebersbach, G., Briegel, A., Jensen, G.J., and Jacobs-Wagner, C. (2008). A self-associating protein critical for chromosome attachment, division, and polar organization in *Caulobacter*. Cell *134*, 956-968.

Edwards, D.H., Thomaides, H.B., and Errington, J. (2000). Promiscuous targeting of *Bacillus subtilis* cell division protein DivIVA to division sites in *Escherichia coli* and fission yeast. The EMBO journal *19*, 2719-2727.

Eggeling, L., and Reyes, O. (2005). Experiments. In Handbook of *Corynebacterium glutamicum* (CRC Press).

Eikmanns, B.J., Kleinertz, E., Liebl, W., and Sahm, H. (1991). A family of *Corynebacterium glutamicum*/*Escherichia coli* shuttle vectors for cloning, controlled gene expression, and promoter probing. Gene *102*, 93-98.

Emanuelsson, O., Brunak, S., von Heijne, G., and Nielsen, H. (2007). Locating proteins in the cell using TargetP, SignalP and related tools. Nature Protocols *2*, 953.

Fennell-Fezzie, R., Gradia, S.D., Akey, D., and Berger, J.M. (2005). The MukF subunit of *Escherichia coli* condensin: architecture and functional relationship to kleisins. The EMBO journal *24*, 1921-1930.

Fisher, G.L.M., Pastrana, C.L., Higman, V.A., Koh, A., Taylor, J.A., Butterer, A., Craggs, T., Sobott, F., Murray, H., Crump, M.P., *et al.* (2017). The structural basis for dynamic DNA binding and bridging interactions which condense the bacterial centromere. eLife *6*, e28086.

Fisher, J.K., Bourniquel, A., Witz, G., Weiner, B., Prentiss, M., and Kleckner, N. (2013). Four-dimensional imaging of *E. coli* nucleoid organization and dynamics in living cells. Cell *153*, 882-895.

Fogel, M.A., and Waldor, M.K. (2005). Distinct segregation dynamics of the two *Vibrio cholerae* chromosomes. Molecular microbiology *55*, 125-136.

Fogel, M.A., and Waldor, M.K. (2006). A dynamic, mitotic-like mechanism for bacterial chromosome segregation. Genes & development *20*, 3269-3282.

Fossum, S., Crooke, E., and Skarstad, K. (2007). Organization of sister origins and replisomes during multifork DNA replication in *Escherichia coli*. The EMBO journal *26*, 4514-4522.

Frage, B., Döhlemann, J., Robledo, M., Lucena, D., Sobetzko, P., Graumann, P.L., and Becker, A. (2016). Spatiotemporal choreography of chromosome and megaplasmids in the *Sinorhizobium meliloti* cell cycle. Molecular microbiology *100*, 808-823.

Freudl, R. (2017). Beyond amino acids: Use of the *Corynebacterium glutamicum* cell factory for the secretion of heterologous proteins. Journal of Biotechnology *258*, 101-109.

Funayama, T., Narumi, I., Kikuchi, M., Kitayama, S., Watanabe, H., and Yamamoto, K. (1999). Identification and disruption analysis of the *recN* gene in the extremely radioresistant bacterium *Deinococcus radiodurans*. Mutation Research/DNA Repair *435*, 151-161.

Ganji, M., Shaltiel, I.A., Bisht, S., Kim, E., Kalichava, A., Haering, C.H., and Dekker, C. (2018). Real-time imaging of DNA loop extrusion by condensin. Science.

Gilichinsky, D.A., Vorobyova, E.A., Erokhina, L.G., Fyordorov-Davydov, D.G., Chaikovskaya, N.R., and Fyordorov-Dayvdov, D.G. (1992). Long-term preservation of microbial ecosystems in permafrost. Advances in space research : the official journal of the Committee on Space Research *12*, 255-263.

Ginda, K., Bezulska, M., Ziolkiewicz, M., Dziadek, J., Zakrzewska-Czerwinska, J., and Jakimowicz, D. (2013). ParA of *Mycobacterium smegmatis* co-ordinates chromosome segregation with the cell cycle and interacts with the polar growth determinant DivIVA. Molecular microbiology *87*, 998-1012.

Gorbatyuk, B., and Marczynski, G.T. (2005). Regulated degradation of chromosome replication proteins DnaA and CtrA in *Caulobacter crescentus*. Molecular microbiology *55*, 1233-1245.

Graham, T.G.W., Wang, X., Song, D., Etson, C.M., van Oijen, A.M., Rudner, D.Z., and Loparo, J.J. (2014). ParB spreading requires DNA bridging. Genes & development *28*, 1228-1238.

Green, R., and Rogers, E.J. (2013). Transformation of chemically competent *E. coli*. Methods in enzymology *529*, 329-336.

Griese, M., Lange, C., and Soppa, J. (2011). Ploidy in cyanobacteria. FEMS microbiology letters *323*, 124-131.

Gruber, S. (2018). SMC complexes sweeping through the chromosome: going with the flow and against the tide. Current opinion in microbiology *42*, 96-103.

Gruber, S., and Errington, J. (2009). Recruitment of condensin to replication origin regions by ParB/SpoOJ promotes chromosome segregation in *B. subtilis*. Cell *137*, 685-696.

Gruber, S., Veening, J.-W., Bach, J., Blettinger, M., Bramkamp, M., and Errington, J. (2014). Interlinked sister chromosomes arise in the absence of condensin during fast replication in *B. subtilis*. Current Biology *24*, 293-298.

Güthlein, C., Wanner, R.M., Sander, P., Böttger, E.C., and Springer, B. (2008). A mycobacterial smc null mutant is proficient in DNA repair and long-term survival. Journal of bacteriology *190*, 452-456.

Hadizadeh Yazdi, N., Guet, C.C., Johnson, R.C., and Marko, J.F. (2012). Variation of the folding and dynamics of the *Escherichia coli* chromosome with growth conditions. Molecular microbiology *86*, 1318-1333.

Hammes, F., Berney, M., Wang, Y., Vital, M., Köster, O., and Egli, T. (2008). Flow-cytometric total bacterial cell counts as a descriptive microbiological parameter for drinking water treatment processes. Water research *42*, 269-277.

Hansen, M.T. (1978). Multiplicity of genome equivalents in the radiation-resistant bacterium *Micrococcus radiodurans*. Journal of bacteriology *134*, 71-75.

Harms, A., Treuner-Lange, A., Schumacher, D., and Søgaard-Andersen, L. (2013). Tracking of chromosome and replisome dynamics in *Myxococcus xanthus* reveals a novel chromosome arrangement. PLoS genetics *9*, e1003802.

Hasona, A., Zuobi-Hasona, K., Crowley, P.J., Abranches, J., Ruelf, M.A., Bleiweis, A.S., and Brady, L.J. (2007). Membrane composition changes and physiological adaptation by *Streptococcus mutans* signal recognition particle pathway mutants. Journal of bacteriology *189*, 1219-1230.

Hassler, M., Shaltiel, I.A., and Haering, C.H. (2018). Towards a unified model of SMC complex function. Current biology : CB *28*, R1266-r1281.

Hayama, R., and Marians, K.J. (2010). Physical and functional interaction between the condensin MukB and the decatenase topoisomerase IV in *Escherichia coli*. Proceedings of the National Academy of Sciences of the United States of America *107*, 18826-18831.

Hempel, A.M., Wang, S.-b., Letek, M., Gil, J.A., and Flärdh, K. (2008). Assemblies of DivIVA mark sites for hyphal branching and can establish new zones of cell wall growth in *Streptomyces coelicolor*. Journal of bacteriology *190*, 7579-7583.

Hester, C.M., and Lutkenhaus, J. (2007). Soj (ParA) DNA binding is mediated by conserved arginines and is essential for plasmid segregation. Proceedings of the National Academy of Sciences of the United States of America *104*, 20326-20331.

Hiasa, H., and Marians, K.J. (1996). Two distinct modes of strand unlinking during θ-Type DNA replication. Journal of Biological Chemistry *271*, 21529-21535.

Hill, N.S., Kadoya, R., Chattoraj, D.K., and Levin, P.A. (2012). Cell size and the initiation of DNA replication in bacteria. PLoS genetics *8*, e1002549.

Hirano, M., and Hirano, T. (2004). Positive and negative regulation of SMC–DNA interactions by ATP and accessory proteins. The EMBO journal *23*, 2664-2673.

Hirano, M., and Hirano, T. (2006). Opening closed arms: long-distance activation of SMC ATPase by hinge-DNA interactions. Molecular cell *21*, 175-186.

Hiriyanna, K.T., and Ramakrishnan, T. (1986). Deoxyribonucleic acid replication time in *Mycobacterium tuberculosis* H37 Rv. Archives of microbiology *144*, 105-109.

Hu, Z., and Lutkenhaus, J. (2001). Topological regulation of cell division in *E. coli*: Spatiotemporal oscillation of MinD requires stimulation of its ATPase by MinE and phospholipid. Molecular cell *7*, 1337-1343.

Hwang, L.C., Vecchiarelli, A.G., Han, Y.W., Mizuuchi, M., Harada, Y., Funnell, B.E., and Mizuuchi, K. (2013). ParA-mediated plasmid partition driven by protein pattern self-organization. The EMBO journal *32*, 1238-1249.

Iniesta, A.A. (2014). ParABS system in chromosome partitioning in the bacterium *Myxococcus xanthus*. PloS one *9*, e86897.

Ireton, K., Gunther, N.W., and Grossman, A.D. (1994). *spo0J* is required for normal chromosome segregation as well as the initiation of sporulation in *Bacillus subtilis*. Journal of bacteriology *176*, 5320-5329.

Jakimowicz, D., Brzostek, A., Rumijowska-Galewicz, A., Żydek, P., Dołzbłasz, A., Smulczyk-Krawczyszyn, A., Zimniak, T., Wojtasz, Ł., Zawilak-Pawlik, A., Kois, A., *et al.* (2007a). Characterization of the mycobacterial chromosome segregation protein ParB and identification of its target in *Mycobacterium smegmatis*. Microbiology *153*, 4050-4060.

Jakimowicz, D., Żydek, P., Kois, A., Zakrzewska-Czerwińska, J., and Chater, K.F. (2007b). Alignment of multiple chromosomes along helical ParA scaffolding in sporulating *Streptomyces* hyphae. Molecular microbiology *65*, 625-641.

Jensen, R.B. (2006). Coordination between chromosome replication, segregation, and cell division in *Caulobacter crescentus*. Journal of bacteriology *188*, 2244-2253.

Jensen, R.B., and Shapiro, L. (1999). The *Caulobacter crescentus smc* gene is required for cell cycle progression and chromosome segregation. Proceedings of the National Academy of Sciences of the United States of America *96*, 10661-10666.

Jensen, R.B., Wang, S.C., and Shapiro, L. (2001). A moving DNA replication factory in *Caulobacter crescentus*. The EMBO journal *20*, 4952-4963.

Jonas, K. (2014). To divide or not to divide: control of the bacterial cell cycle by environmental cues. Current opinion in microbiology *18*, 54-60.

Joshi, M.C., Bourniquel, A., Fisher, J., Ho, B.T., Magnan, D., Kleckner, N., and Bates, D. (2011). *Escherichia coli* sister chromosome separation includes an abrupt global transition with concomitant release of late-splitting intersister snaps. Proceedings of the National Academy of Sciences *108*, 2765-2770.

Jun, S., and Mulder, B. (2006). Entropy-driven spatial organization of highly confined polymers: Lessons for the bacterial chromosome. Proceedings of the National Academy of Sciences *103*, 12388-12393.

Jun, S., and Wright, A. (2010). Entropy as the driver of chromosome segregation. Nature reviews. Microbiology *8*, 600-607.

Kaimer, C., Gonzalez-Pastor, J.E., and Graumann, P.L. (2009). SpoIIIE and a novel type of DNA translocase, SftA, couple chromosome segregation with cell division in *Bacillus subtilis*. Molecular microbiology *74*, 810-825.

Kalitsis, P., Zhang, T., Marshall, K.M., Nielsen, C.F., and Hudson, D.F. (2017). Condensin, master organizer of the genome. Chromosome Research *25*, 61-76.

Kamada, K., Miyata, M., and Hirano, T. (2013). Molecular basis of SMC ATPase activation: role of internal structural changes of the regulatory subcomplex ScpAB. Structure *21*, 581-594.

Karimova, G., Dautin, N., and Ladant, D. (2005). Interaction network among *Escherichia coli* membrane proteins involved in cell division as revealed by bacterial two-hybrid analysis. Journal of bacteriology *187*, 2233.

Karimova, G., Pidoux, J., Ullmann, A., and Ladant, D. (1998). A bacterial two-hybrid system based on a reconstituted signal transduction pathway. Proceedings of the National Academy of Sciences of the United States of America *95*, 5752-5756.

Karimova, G., Ullmann, A., and Ladant, D. (2001). Protein-protein interaction between *Bacillus stearothermophilus* tyrosyl-tRNA synthetase subdomains revealed by a bacterial two-hybrid system. Journal of molecular microbiology and biotechnology *3*, 73-82.

Katayama, T., Ozaki, S., Keyamura, K., and Fujimitsu, K. (2010). Regulation of the replication cycle: conserved and diverse regulatory systems for DnaA and *oriC*. Nature reviews. Microbiology *8*, 163-170.

Kegel, A., Betts-Lindroos, H., Kanno, T., Jeppsson, K., Ström, L., Katou, Y., Itoh, T., Shirahige, K., and Sjögren, C. (2011). Chromosome length influences replication-induced topological stress. Nature *471*, 392.

Keilhauer, C., Eggeling, L., and Sahm, H. (1993). Isoleucine synthesis in *Corynebacterium glutamicum*: molecular analysis of the *ilvB-ilvN-ilvC* operon. Journal of bacteriology *175*, 5595-5603.

Kidane, D., Sanchez, H., Alonso, J.C., and Graumann, P.L. (2004). Visualization of DNA double-strand break repair in live bacteria reveals dynamic recruitment of *Bacillus subtilis* RecF, RecO and RecN proteins to distinct sites on the nucleoids. Molecular microbiology *52*, 1627-1639.

Kiekebusch, D., and Thanbichler, M. (2014). Plasmid segregation by a moving ATPase gradient. Proceedings of the National Academy of Sciences of the United States of America *111*, 4741-4742.

Kirchner, O., and Tauch, A. (2003). Tools for genetic engineering in the amino acid-producing bacterium *Corynebacterium glutamicum*. Journal of Biotechnology *104*, 287-299.

Kois-Ostrowska, A., Strzałka, A., Lipietta, N., Tilley, E., Zakrzewska-Czerwińska, J., Herron, P., and Jakimowicz, D. (2016). Unique function of the bacterial chromosome segregation machinery in apically growing *Streptomyces* - targeting the chromosome to new hyphal tubes and its anchorage at the tips. PLoS genetics *12*, e1006488.

Kondo, T., Kobayashi, J., Saitoh, T., Maruyama, K., Ishii, K.J., Barber, G.N., Komatsu, K., Akira, S., and Kawai, T. (2013). DNA damage sensor MRE11 recognizes cytosolic double-stranded DNA and induces type I interferon by regulating STING trafficking. Proceedings of the National Academy of Sciences of the United States of America *110*, 2969-2974.

Kusiak, M., Gapczyńska, A., Płochocka, D., Thomas, C.M., and Jagura-Burdzy, G. (2011). Binding and spreading of ParB on DNA determine its biological function in *Pseudomonas aeruginosa*. Journal of bacteriology *193*, 3342-3355.

Kusumoto, A., Shinohara, A., Terashima, H., Kojima, S., Yakushi, T., and Homma, M. (2008). Collaboration of FlhF and FlhG to regulate polar-flagella number and localization in *Vibrio alginolyticus*. Microbiology *154*, 1390-1399.

Laemmli, U.K. (1970). Cleavage of structural proteins during the assembly of the head of bacteriophage T4. Nature *227*, 680-685.

Lagage, V., Boccard, F., and Vallet-Gely, I. (2016). Regional control of chromosome segregation in *Pseudomonas aeruginosa*. PLoS genetics *12*, e1006428.

Lammens, A., Schele, A., and Hopfner, K.-P. (2004). Structural biochemistry of ATP-driven dimerization and DNA-stimulated activation of SMC ATPases. Current Biology *14*, 1778-1782.

Lau, I.F., Filipe, S.R., Søballe, B., Økstad, O.-A., Barre, F.-X., and Sherratt, D.J. (2003). Spatial and temporal organization of replicating *Escherichia coli* chromosomes. Molecular microbiology *49*, 731-743.

Le, T.B., Imakaev, M.V., Mirny, L.A., and Laub, M.T. (2013). High-resolution mapping of the spatial organization of a bacterial chromosome. Science *342*, 731-734.

Lee, L.-F., Yeh, S.-H., and Chen, C.W. (2002). Construction and synchronization of *dnaA* temperature-sensitive mutants of *Streptomyces*. Journal of bacteriology *184*, 1214-1218.

Leipe, D.D., Wolf, Y.I., Koonin, E.V., and Aravind, L. (2002). Classification and evolution of P-loop GTPases and related ATPases. Journal of molecular biology *317*, 41-72.

Lemon, K.P., and Grossman, A.D. (1998). Localization of bacterial DNA polymerase: evidence for a factory model of replication. Science *282*, 1516-1519.

Lemon, K.P., and Grossman, A.D. (2000). Movement of replicating DNA through a stationary replisome. Molecular cell *6*, 1321-1330.

Lenarcic, R., Halbedel, S., Visser, L., Shaw, M., Wu, L.J., Errington, J., Marenduzzo, D., and Hamoen, L.W. (2009). Localisation of DivIVA by targeting to negatively curved membranes. The EMBO journal *28*, 2272-2282.

Leonard, T.A., Butler, P.J., and Löwe, J. (2005). Bacterial chromosome segregation: structure and DNA binding of the Soj dimer – a conserved biological switch. The EMBO journal *24*, 270-282.

Leonard, T.A., Butler, P.J.G., and Löwe, J. (2004). Structural analysis of the chromosome segregation protein Spo0J from *Thermus thermophilus*. Molecular microbiology *53*, 419-432.

Letek, M., Ordonez, E., Vaquera, J., Margolin, W., Flardh, K., Mateos, L.M., and Gil, J.A. (2008). DivIVA is required for polar growth in the MreB-lacking rod-shaped actinomycete *Corynebacterium glutamicum*. Journal of bacteriology *190*, 3283-3292.

Lewis, R.A., Bignell, C.R., Zeng, W., Jones, A.C., and Thomas, C.M. (2002). Chromosome loss from par mutants of *Pseudomonas putida* depends on growth medium and phase of growth. Microbiology *148*, 537-548.

Li, Y., Stewart, N.K., Berger, A.J., Vos, S., Schoeffler, A.J., Berger, J.M., Chait, B.T., and Oakley, M.G. (2010). *Escherichia coli* condensin MukB stimulates topoisomerase IV activity by a direct physical interaction. Proceedings of the National Academy of Sciences of the United States of America *107*, 18832-18837.

Lim, H.C., Surovtsev, I.V., Beltran, B.G., Huang, F., Bewersdorf, J., and Jacobs-Wagner, C. (2014). Evidence for a DNA-relay mechanism in ParABS-mediated chromosome segregation. eLife *3*, e02758.

Lin, D.C., and Grossman, A.D. (1998). Identification and characterization of a bacterial chromosome partitioning site. Cell *92*, 675-685.

Lin, L., Osorio Valeriano, M., Harms, A., Søgaard-Andersen, L., and Thanbichler, M. (2017). Bactofilin-mediated organization of the ParABS chromosome segregation system in *Myxococcus xanthus*. Nature communications *8*, 1817.

Link, A.J., Phillips, D., and Church, G.M. (1997). Methods for generating precise deletions and insertions in the genome of wild-type *Escherichia coli*: application to open reading frame characterization. Journal of bacteriology *179*, 6228-6237.

Lioy, V.S., Cournac, A., Marbouty, M., Duigou, S., Mozziconacci, J., Espeli, O., Boccard, F., and Koszul, R. (2018). Multiscale structuring of the *E. coli* chromosome by nucleoid-associated and condensin proteins. Cell *172*, 771-783.e718.

Livak, K.J., and Schmittgen, T.D. (2001). Analysis of relative gene expression data using real-time quantitative PCR and the 2(-Delta Delta C(T)) Method. Methods *25*, 402-408.

Livny, J., Yamaichi, Y., and Waldor, M.K. (2007). Distribution of centromere-like *parS* sites in bacteria: insights from comparative genomics. Journal of bacteriology *189*, 8693-8703.

Lloyd, R.G., Picksley, S.M., and Prescott, C. (1983). Inducible expression of a gene specific to the RecF pathway for recombination in *Escherichia coli* K12. Molecular and General Genetics MGG *190*, 162-167.

Lu, M., Campbell, J.L., Boye, E., and Kleckner, N. (1994). SeqA: a negative modulator of replication initiation in *E. coli*. Cell *77*, 413-426.

Luirink, J., ten Hagen-Jongman, C.M., van der Weijden, C.C., Oudega, B., High, S., Dobberstein, B., and Kusters, R. (1994). An alternative protein targeting pathway in *Escherichia coli*: studies on the role of FtsY. The EMBO journal *13*, 2289-2296.

Lutkenhaus, J. (2012). The ParA/MinD family puts things in their place. Trends in microbiology *20*, 411-418.

Maestro, B., Sanz, J.M., Díaz-Orejas, R., and Fernández-Tresguerres, E. (2003). Modulation of pPS10 host range by plasmid-encoded RepA initiator protein. Journal of bacteriology *185*, 1367-1375.

Maldonado, R., Jimenez, J., and Casadesus, J. (1994). Changes of ploidy during the *Azotobacter vinelandii* growth cycle. Journal of bacteriology *176*, 3911-3919.

Marbouty, M., Le Gall, A., Cattoni, D.I., Cournac, A., Koh, A., Fiche, J.B., Mozziconacci, J., Murray, H., Koszul, R., and Nollmann, M. (2015). Condensin- and replication-mediated bacterial chromosome folding and origin condensation revealed by Hi-C and super-resolution imaging. Molecular cell *59*, 588-602.

Marczynski, G.T. (1999). Chromosome methylation and measurement of faithful, once and only once per cell cycle chromosome replication in *Caulobacter crescentus*. Journal of bacteriology *181*, 1984-1993.

Marston, A.L., and Errington, J. (1999). Dynamic movement of the ParA-like Soj protein of *B. subtilis* and its dual role in nucleoid organization and developmental regulation. Molecular cell *4*, 673-682.

Massey, T.H., Mercogliano, C.P., Yates, J., Sherratt, D.J., and Löwe, J. (2006). Double-stranded DNA translocation: structure and mechanism of hexameric FtsK. Molecular cell *23*, 457-469.

Mattimore, V., and Battista, J.R. (1996). Radioresistance of *Deinococcus radiodurans*: functions necessary to survive ionizing radiation are also necessary to survive prolonged desiccation. Journal of bacteriology *178*, 633-637.

McGhee, J.D., and Von Hippel, P.H. (1977). Formaldehyde as a probe of DNA structure. 3. Equilibrium denaturation of DNA and synthetic polynucleotides. Biochemistry *16*, 3267-3276.

McGrath, P.T., Iniesta, A.A., Ryan, K.R., Shapiro, L., and McAdams, H.H. (2006). A dynamically localized protease complex and a polar specificity factor control a cell cycle master regulator. Cell *124*, 535-547.

Mehla, J., Caufield, J.H., Sakhawalkar, N., and Uetz, P. (2017). A comparison of two-hybrid approaches for detecting protein-protein interactions. Methods in enzymology *586*, 333-358.

Melby, T.E., Ciampaglio, C.N., Briscoe, G., and Erickson, H.P. (1998). The symmetrical structure of structural maintenance of chromosomes (SMC) and MukB proteins: long, antiparallel coiled coils, folded at a flexible hinge. The Journal of cell biology *142*, 1595-1604.

Mendell, J.E., Clements, K.D., Choat, J.H., and Angert, E.R. (2008). Extreme polyploidy in a large bacterium. Proceedings of the National Academy of Sciences *105*, 6730-6734.

Mercier, R., Petit, M.A., Schbath, S., Robin, S., El Karoui, M., Boccard, F., and Espeli, O. (2008). The MatP/*matS* site-specific system organizes the terminus region of the *E. coli* chromosome into a macrodomain. Cell *135*, 475-485.

Michelsen, O., Teixeira de Mattos, M.J., Jensen, P.R., and Hansen, F.G. (2003). Precise determinations of C and D periods by flow cytometry in *Escherichia coli* K-12 and B/r. Microbiology *149*, 1001-1010.

Minnen, A., Attaiech, L., Thon, M., Gruber, S., and Veening, J.W. (2011). SMC is recruited to oriC by ParB and promotes chromosome segregation in *Streptococcus pneumoniae*. Molecular microbiology *81*, 676-688.

Minnen, A., Bürmann, F., Wilhelm, L., Anchimiuk, A., Diebold-Durand, M.-L., and Gruber, S. (2016). Control of Smc coiled coil architecture by the ATPase heads facilitates targeting to chromosomal ParB/*parS* and release onto flanking DNA. Cell Reports *14*, 2003-2016.

Miyamoto-Shinohara, Y., Sukenobe, J., Imaizumi, T., and Nakahara, T. (2008). Survival of freeze-dried bacteria. The Journal of general and applied microbiology *54*, 9-24.

Mohl, D.A., Easter, J., Jr., and Gober, J.W. (2001). The chromosome partitioning protein, ParB, is required for cytokinesis in *Caulobacter crescentus*. Molecular microbiology *42*, 741-755.

Mormann, S., Lomker, A., Ruckert, C., Gaigalat, L., Tauch, A., Puhler, A., and Kalinowski, J. (2006). Random mutagenesis in *Corynebacterium glutamicum* ATCC 13032 using an IS6100-based transposon vector identified the last unknown gene in the histidine biosynthesis pathway. BMC Genomics *7*, 205.

Murray, H., Ferreira, H., and Errington, J. (2006). The bacterial chromosome segregation protein Spo0J spreads along DNA from *parS* nucleation sites. Molecular microbiology *61*, 1352-1361.

Mutka, S.C., and Walter, P. (2001). Multifaceted physiological response allows yeast to adapt to the loss of the signal recognition particle-dependent protein-targeting pathway. Molecular biology of the cell *12*, 577-588.

Nagpal, P., Jafri, S., Reddy, M.A., and Das, H.K. (1989). Multiple chromosomes of *Azotobacter vinelandii*. Journal of bacteriology *171*, 3133-3138.

Nair, N., Dziedzic, R., Greendyke, R., Muniruzzaman, S., Rajagopalan, M., and Madiraju, M.V. (2009). Synchronous replication initiation in novel *Mycobacterium tuberculosis dnaA* cold-sensitive mutants. Molecular microbiology *71*, 291-304.

Nasmyth, K., and Haering, C.H. (2009). Cohesin: its roles and mechanisms. Annual review of genetics *43*, 525-558.

Nesvera, J., Patek, M., Hochmannova, J., Abrhamova, Z., Becvarova, V., Jelinkova, M., and Vohradsky, J. (1997). Plasmid pGA1 from *Corynebacterium glutamicum* codes for a gene product that positively influences plasmid copy number. Journal of bacteriology *179*, 1525-1532.

Neumeyer, A., Hübschmann, T., Müller, S., and Frunzke, J. (2013). Monitoring of population dynamics of *Corynebacterium glutamicum* by multiparameter flow cytometry. Microbial biotechnology *6*, 157-167.

Nguyen, L., Scherr, N., Gatfield, J., Walburger, A., Pieters, J., and Thompson, C.J. (2007). Antigen 84, an effector of pleiomorphism in *Mycobacterium smegmatis*. Journal of bacteriology *189*, 7896-7910.

Nielsen, H.J., Li, Y., Youngren, B., Hansen, F.G., and Austin, S. (2006). Progressive segregation of the *Escherichia coli* chromosome. Molecular microbiology *61*, 383-393.

Nievera, C., Torgue, J.J.C., Grimwade, J.E., and Leonard, A.C. (2006). SeqA blocking of DnaA-*oriC* interactions ensures staged assembly of the *E. coli* pre-RC. Molecular cell *24*, 581-592.

Niki, H., Imamura, R., Kitaoka, M., Yamanaka, K., Ogura, T., and Hiraga, S. (1992). *E.coli* MukB protein involved in chromosome partition forms a homodimer with a rod-and-hinge structure having DNA binding and ATP/GTP binding activities. The EMBO journal *11*, 5101-5109.

Niki, H., Jaffe, A., Imamura, R., Ogura, T., and Hiraga, S. (1991). The new gene *mukB* codes for a 177 kd protein with coiled-coil domains involved in chromosome partitioning of *E. coli*. The EMBO journal *10*, 183-193.

Nolivos, S., and Sherratt, D. (2014). The bacterial chromosome: architecture and action of bacterial SMC and SMC-like complexes. FEMS microbiology reviews *38*, 380-392.

Nolivos, S., Upton, A.L., Badrinarayanan, A., Müller, J., Zawadzka, K., Wiktor, J., Gill, A., Arciszewska, L., Nicolas, E., and Sherratt, D. (2016). MatP regulates the coordinated action of topoisomerase IV and MukBEF in chromosome segregation. Nature communications *7*, 10466-10466.

Nottebrock, D., Meyer, U., Krämer, R., and Morbach, S. (2003). Molecular and biochemical characterization of mechanosensitive channels in *Corynebacterium glutamicum*. FEMS microbiology letters *218*, 305-309.

Novick, R.P., Edelman, I., and Lofdahl, S. (1986). Small *Staphylococcus aureus* plasmids are transduced as linear multimers that are formed and resolved by replicative processes. Journal of molecular biology *192*, 209-220.

Palecek, J.J., and Gruber, S. (2015). Kite proteins: a superfamily of SMC/kleisin partners conserved across bacteria, archaea, and eukaryotes. Structure *23*, 2183-2190.

Passot, F.M., Nguyen, H.H., Dard-Dascot, C., Thermes, C., Servant, P., Espéli, O., and Sommer, S. (2015). Nucleoid organization in the radioresistant bacterium *Deinococcus radiodurans*. Molecular microbiology *97*, 759-774.

Pastrana, C.L., Carrasco, C., Akhtar, P., Leuba, S.H., Khan, S.A., and Moreno-Herrero, F. (2016). Force and twist dependence of RepC nicking activity on torsionally-constrained DNA molecules. Nucleic acids research *44*, 8885-8896.

Patrick, J.E., and Kearns, D.B. (2008). MinJ (YvjD) is a topological determinant of cell division in *Bacillus subtilis*. Molecular microbiology *70*, 1166-1179.

Pecoraro, V., Zerulla, K., Lange, C., and Soppa, J. (2011). Quantification of ploidy in proteobacteria revealed the existence of monoploid, (mero-)oligoploid and polyploid species. PloS one *6*, e16392.

Pellegrino, S., Radzimanowski, J., de Sanctis, D., Erba, Elisabetta B., McSweeney, S., and Timmins, J. (2012). Structural and functional characterization of an SMC-like protein RecN: new insights into double-strand break repair. Structure *20*, 2076-2089.

Perez-Cheeks, B.A., Planet, P.J., Sarkar, I.N., Clock, S.A., Xu, Q., and Figurski, D.H. (2012). The product of *tadZ*, a new member of the *parA*/*minD* superfamily, localizes to a pole in *Aggregatibacter actinomycetemcomitans*. Molecular microbiology *83*, 694-711.

Petrushenko, Z.M., Lai, C.-H., Rai, R., and Rybenkov, V.V. (2006). DNA Reshaping by MukB right-handed knotting, left-handed supercoiling. Journal of Biological Chemistry *281*, 4606-4615.

Petrushenko, Z.M., She, W., and Rybenkov, V.V. (2011). A new family of bacterial condensins. Molecular microbiology *81*, 881-896.

Pham, T.M., Tan, K.W., Sakumura, Y., Okumura, K., Maki, H., and Akiyama, M.T. (2013). A single-molecule approach to DNA replication in *Escherichia coli* cells demonstrated that DNA polymerase III is a major determinant of fork speed. Molecular microbiology *90*, 584-596.

Pioro, M., Malecki, T., Portas, M., Magierowska, I., Trojanowski, D., Sherratt, D., Zakrzewska-Czerwinska, J., Ginda, K., and Jakimowicz, D. (2019). Competition between DivIVA and the nucleoid for ParA binding promotes segrosome separation and modulates mycobacterial cell elongation. Molecular microbiology *111*, 204-220.

Postgate, J.R., Kent, H.M., Robson, R.L., and Chesshyre, J.A. (1984). The genomes of *Desulfovibrio gigas* and *D. vulgaris*. Journal of general microbiology *130*, 1597-1601.

Postow, L., Hardy, C.D., Arsuaga, J., and Cozzarelli, N.R. (2004). Topological domain structure of the *Escherichia coli* chromosome. Genes & development *18*, 1766-1779.

Potts, M. (1994). Desiccation tolerance of prokaryotes. Microbiological reviews *58*, 755-805.

Ptacin, J.L., Lee, S.F., Garner, E.C., Toro, E., Eckart, M., Comolli, L.R., Moerner, W.E., and Shapiro, L. (2010). A spindle-like apparatus guides bacterial chromosome segregation. Nat Cell Biol *12*, 791-798.

Quon, K.C., Yang, B., Domian, I.J., Shapiro, L., and Marczynski, G.T. (1998). Negative control of bacterial DNA replication by a cell cycle regulatory protein that binds at the chromosome origin. Proceedings of the National Academy of Sciences of the United States of America *95*, 120-125.

Ramamurthi, K.S., and Losick, R. (2009). Negative membrane curvature as a cue for subcellular localization of a bacterial protein. Proceedings of the National Academy of Sciences *106*, 13541-13545.

Ramírez, F., Ryan, D.P., Grüning, B., Bhardwaj, V., Kilpert, F., Richter, A.S., Heyne, S., Dündar, F., and Manke, T. (2016). deepTools2: a next generation web server for deep-sequencing data analysis. Nucleic acids research *44*, W160-W165.

Randich, A.M., and Brun, Y.V. (2015). Molecular mechanisms for the evolution of bacterial morphologies and growth modes. Frontiers in microbiology *6*, 580.

Raskin, D.M., and de Boer, P.A. (1999). Rapid pole-to-pole oscillation of a protein required for directing division to the middle of *Escherichia coli*. Proceedings of the National Academy of Sciences of the United States of America *96*, 4971-4976.

Rasmussen, R. (2001). Quantification on the LightCycler. In Rapid Cycle Real-Time PCR Methods and Applications, W.C. Meuer S, Nakagawara K (ed.), ed. (Heidelberg: Springer Berlin Heidelberg), pp. 21-34.

Rasmussen, T., Jensen, R.B., and Skovgaard, O. (2007). The two chromosomes of *Vibrio cholerae* are initiated at different time points in the cell cycle. The EMBO journal *26*, 3124-3131.

Reinscheid, D.J., Kronemeyer, W., Eggeling, L., Eikmanns, B.J., and Sahm, H. (1994). Stable expression of *hom-1-thrB* in *Corynebacterium glutamicum* and its effect on the carbon flux to threonine and related amino acids. Applied and environmental microbiology *60*, 126-132.

Reyes-Lamothe, R., Nicolas, E., and Sherratt, D.J. (2012). Chromosome replication and segregation in bacteria. Annual review of genetics *46*, 121-143.

Reyes-Lamothe, R., Possoz, C., Danilova, O., and Sherratt, D.J. (2008). Independent positioning and action of *Escherichia coli* replisomes in live cells. Cell *133*, 90-102.

Ringgaard, S., Schirner, K., Davis, B.M., and Waldor, M.K. (2011). A family of ParA-like ATPases promotes cell pole maturation by facilitating polar localization of chemotaxis proteins. Genes & development *25*, 1544-1555.

Roberts, M.A.J., Wadhams, G.H., Hadfield, K.A., Tickner, S., and Armitage, J.P. (2012). ParA-like protein uses nonspecific chromosomal DNA binding to partition protein complexes. Proceedings of the National Academy of Sciences of the United States of America *109*, 6698-6703.

Rodionov, O., Lobocka, M., and Yarmolinsky, M. (1999). Silencing of genes flanking the P1 plasmid centromere. Science *283*, 546-549.

Roth, S., Rottach, A., Lotz-Havla, A.S., Laux, V., Muschaweckh, A., Gersting, S.W., Muntau, A.C., Hopfner, K.-P., Jin, L., Vanness, K., *et al.* (2014). Rad50-CARD9 interactions link cytosolic DNA sensing to IL-1β production. Nature Immunology *15*, 538.

Sanchez, A., Cattoni, D.I., Walter, J.C., Rech, J., Parmeggiani, A., Nollmann, M., and Bouet, J.Y. (2015). Stochastic self-assembly of ParB proteins builds the bacterial DNA segregation apparatus. Cell systems *1*, 163-173.

Santi, I., Dhar, N., Bousbaine, D., Wakamoto, Y., and McKinney, J.D. (2013). Single-cell dynamics of the chromosome replication and cell division cycles in mycobacteria. Nature communications *4*, 2470.

Santi, I., and McKinney, J.D. (2015). Chromosome organization and replisome dynamics in *Mycobacterium smegmatis*. mBio *6*.

Sawitzke, J.A., and Austin, S. (2000). Suppression of chromosome segregation defects of *Escherichia coli muk* mutants by mutations in topoisomerase I. Proceedings of the National Academy of Sciences *97*, 1671-1676.

Schäfer, A., Tauch, A., Jäger, W., Kalinowski, J., Thierbach, G., and Pühler, A. (1994). Small mobilizable multi-purpose cloning vectors derived from the *Escherichia coli* plasmids pK18 and pK19: selection of defined deletions in the chromosome of *Corynebacterium glutamicum*. Gene *145*, 69-73.

Schindelin, J., Arganda-Carreras, I., Frise, E., Kaynig, V., Longair, M., Pietzsch, T., Preibisch, S., Rueden, C., Saalfeld, S., Schmid, B., *et al.* (2012). Fiji: an open-source platform for biological-image analysis. Nat Meth *9*, 676-682.

Schlüter, A., Heuer, H., Szczepanowski, R., Forney, L.J., Thomas, C.M., Pühler, A., and Top, E.M. (2003). The 64508 bp IncP-1β antibiotic multiresistance plasmid pB10 isolated from a waste-water treatment plant provides evidence for recombination between members of different branches of the IncP-1β group. Microbiology *149*, 3139-3153.

Schofield, W.B., Lim, H.C., and Jacobs-Wagner, C. (2010). Cell cycle coordination and regulation of bacterial chromosome segregation dynamics by polarly localized proteins. The EMBO journal *29*, 3068-3081.

Schubert, K., Sieger, B., Meyer, F., Giacomelli, G., Böhm, K., Rieblinger, A., Lindenthal, L., Sachs, N., Wanner, G., and Bramkamp, M. (2017). The antituberculosis drug ethambutol selectively blocks apical growth in CMN group bacteria. mBio *8*, e02213-02216.

Schumacher, M.A., and Funnell, B.E. (2005). Structures of ParB bound to DNA reveal mechanism of partition complex formation. Nature *438*, 516.

Schwartz, M.A., and Shapiro, L. (2011). An SMC ATPase mutant disrupts chromosome segregation in *Caulobacter*. Molecular microbiology *82*, 1359-1374.

Shah, G.A., and O'Shea, C.C. (2015). Viral and cellular genomes activate distinct DNA damage responses. Cell *162*, 987-1002.

Sharpe, M.E., Hauser, P.M., Sharpe, R.G., and Errington, J. (1998). *Bacillus subtilis* cell cycle as studied by fluorescence microscopy: constancy of cell length at initiation of DNA replication and evidence for active nucleoid partitioning. Journal of bacteriology *180*, 547-555.

Sieger, B., Schubert, K., Donovan, C., and Bramkamp, M. (2013). The lipid II flippase RodA determines morphology and growth in *Corynebacterium glutamicum*. Molecular microbiology *90*, 966-982.

Sinden, R.R., Carlson, J.O., and Pettijohn, D.E. (1980). Torsional tension in the DNA double helix measured with trimethylpsoralen in living *E. coli* cells: Analogous measurements in insect and human cells. Cell *21*, 773-783.

Soppa, J. (2014). Polyploidy in archaea and bacteria: about desiccation resistance, giant cell size, long-term survival, enforcement by a eukaryotic host and additional aspects. Journal of Molecular Microbiology and Biotechnology *24*, 409-419.

Sota, M., Yano, H., M Hughes, J., Daughdrill, G.W., Abdo, Z., Forney, L.J., and Top, E.M. (2010). Shifts in the host range of a promiscuous plasmid through parallel evolution of its replication initiation protein. The ISME journal *4*, 1568.

Stokke, C., Waldminghaus, T., and Skarstad, K. (2011). Replication patterns and organization of replication forks in *Vibrio cholerae*. Microbiology *157*, 695-708.

Stracker, T.H., Carson, C.T., and Weitzman, M.D. (2002). Adenovirus oncoproteins inactivate the Mre11–Rad50–NBS1 DNA repair complex. Nature *418*, 348-352.

Sullivan, N.L., Marquis, K.A., and Rudner, D.Z. (2009). Recruitment of SMC by ParB-*parS* organizes the origin region and promotes efficient chromosome segregation. Cell *137*, 697-707.

Suzuki, N., Okai, N., Nonaka, H., Tsuge, Y., Inui, M., and Yukawa, H. (2006). High-throughput transposon mutagenesis of *Corynebacterium glutamicum* and construction of a single-gene disruptant mutant library. Applied and environmental microbiology *72*, 3750-3755.

Tanner, N.A., Loparo, J.J., Hamdan, S.M., Jergic, S., Dixon, N.E., and van Oijen, A.M. (2009). Real-time single-molecule observation of rolling-circle DNA replication. Nucleic acids research *37*, e27.

Tauch, A., Kirchner, O., Löffler, B., Götker, S., Pühler, A., and Kalinowski, J. (2002). Efficient electrotransformation of corynebacterium diphtheriae with a mini-replicon derived from the *Corynebacterium glutamicum* plasmid pGA1. Current microbiology *45*, 362-367.

Team, R.C. (2014). R: A language and environment for statistical computing. R Foundation for Statistical Computing, Vienna, Austria. (URL: http://www.R-project.org/).

Terakawa, T., Bisht, S., Eeftens, J.M., Dekker, C., Haering, C.H., and Greene, E.C. (2017). The condensin complex is a mechanochemical motor that translocates along DNA. Science *358*, 672-676.

Teytelman, L., Thurtle, D.M., Rine, J., and van Oudenaarden, A. (2013). Highly expressed loci are vulnerable to misleading ChIP localization of multiple unrelated proteins. Proceedings of the National Academy of Sciences *110*, 18602-18607.

Thanbichler, M., and Shapiro, L. (2006). MipZ, a spatial regulator coordinating chromosome segregation with cell division in *Caulobacter*. Cell *126*, 147-162.

Timinskas, K., Balvočiūtė, M., Timinskas, A., and Venclovas, Č. (2014). Comprehensive analysis of DNA polymerase III α subunits and their homologs in bacterial genomes. Nucleic acids research *42*, 1393-1413.

Toro, E., Hong, S.H., McAdams, H.H., and Shapiro, L. (2008). *Caulobacter* requires a dedicated mechanism to initiate chromosome segregation. Proceedings of the National Academy of Sciences of the United States of America *105*, 15435-15440.

Tran, N.T., Laub, M.T., and Le, T.B.K. (2017). SMC progressively aligns chromosomal arms in *Caulobacter crescentus* but is antagonized by convergent transcription. Cell reports *20*, 2057-2071.

Tran, N.T., Stevenson, C.E., Som, N.F., Thanapipatsiri, A., Jalal, A.S.B., and Le, T.B.K. (2018). Permissive zones for the centromere-binding protein ParB on the *Caulobacter crescentus* chromosome. Nucleic acids research *46*, 1196-1209.

Treuner-Lange, A., Aguiluz, K., van der Does, C., Gómez-Santos, N., Harms, A., Schumacher, D., Lenz, P., Hoppert, M., Kahnt, J., Muñoz-Dorado, J., *et al.* (2013). PomZ, a ParA-like protein, regulates Z-ring formation and cell division in *Myxococcus xanthus*. Molecular microbiology *87*, 235-253.

Trojanowski, D., Ginda, K., Pióro, M., Hołówka, J., Skut, P., Jakimowicz, D., and Zakrzewska-Czerwińska, J. (2015). Choreography of the *Mycobacterium* replication machinery during the cell cycle. mBio *6*.

Trojanowski, D., Hołówka, J., Ginda, K., Jakimowicz, D., and Zakrzewska-Czerwińska, J. (2017). Multifork chromosome replication in slow-growing bacteria. Scientific reports *7*, 43836-43836.

Trojanowski, D., Hołówka, J., and Zakrzewska-Czerwińska, J. (2018). Where and when bacterial chromosome replication starts: A single cell perspective. Frontiers in microbiology *9*, 2819-2819.

Tsuge, Y., Ogino, H., Teramoto, H., Inui, M., and Yukawa, H. (2008). Deletion of cgR_1596 and cgR_2070, encoding NlpC/P60 proteins, causes a defect in cell separation in *Corynebacterium glutamicum* R. Journal of bacteriology *190*, 8204-8214.

Tsui, H.-C.T., Keen, S.K., Sham, L.-T., Wayne, K.J., and Winkler, M.E. (2011). Dynamic distribution of the SecA and SecY translocase subunits and septal localization of the HtrA surface chaperone/protease during *Streptococcus pneumoniae* D39 cell division. mBio *2*, e00202-00211.

Tyanova, S., Temu, T., Sinitcyn, P., Carlson, A., Hein, M.Y., Geiger, T., Mann, M., and Cox, J. (2016). The Perseus computational platform for comprehensive analysis of (prote)omics data. Nature Methods *13*, 731.

Umbarger, Mark A., Toro, E., Wright, Matthew A., Porreca, Gregory J., Baù, D., Hong, S.-H., Fero, Michael J., Zhu, Lihua J., Marti-Renom, Marc A., McAdams, Harley H., *et al.* (2011). The three-dimensional architecture of a bacterial genome and its alteration by genetic perturbation. Molecular cell *44*, 252-264.

Val, M.-E., Marbouty, M., de Lemos Martins, F., Kennedy, S.P., Kemble, H., Bland, M.J., Possoz, C., Koszul, R., Skovgaard, O., and Mazel, D. (2016). A checkpoint control orchestrates the replication of the two chromosomes of *Vibrio cholerae*. Science Advances *2*.

Vallet-Gely, I., and Boccard, F. (2013). Chromosomal organization and segregation in *Pseudomonas aeruginosa*. PLoS genetics *9*, e1003492.

van Raaphorst, R., Kjos, M., and Veening, J.-W. (2017). Chromosome segregation drives division site selection in *Streptococcus pneumoniae*. Proceedings of the National Academy of Sciences *114*, E5959-E5968.

Vazquez Nunez, R., Ruiz Avila, L.B., and Gruber, S. (2019). Transient DNA occupancy of the SMC interarm space in prokaryotic condensin. Molecular cell.

Vecchiarelli, A.G., Han, Y.-W., Tan, X., Mizuuchi, M., Ghirlando, R., Biertümpfel, C., Funnell, B.E., and Mizuuchi, K. (2010). ATP control of dynamic P1 ParA-DNA interactions: a key role for the nucleoid in plasmid partition. Molecular microbiology *78*, 78-91.

Vecchiarelli, A.G., Hwang, L.C., and Mizuuchi, K. (2013). Cell-free study of F plasmid partition provides evidence for cargo transport by a diffusion-ratchet mechanism. Proceedings of the National Academy of Sciences of the United States of America *110*, E1390-1397.

Viollier, P.H., Thanbichler, M., McGrath, P.T., West, L., Meewan, M., McAdams, H.H., and Shapiro, L. (2004). Rapid and sequential movement of individual chromosomal loci to specific subcellular locations during bacterial DNA replication. Proceedings of the National Academy of Sciences of the United States of America *101*, 9257-9262.

Volff, J.N., and Altenbuchner, J. (2000). A new beginning with new ends: linearisation of circular chromosomes during bacterial evolution. FEMS microbiology letters *186*, 143-150.

Wang, G., and Maier, R.J. (2008). Critical role of RecN in recombinational DNA repair and survival of *Helicobacter pylori*. Infection and Immunity *76*, 153-160.

Wang, J.D., and Levin, P.A. (2009). Metabolism, cell growth and the bacterial cell cycle. Nat Rev Micro *7*, 822-827.

Wang, X., Brandão, H.B., Le, T.B.K., Laub, M.T., and Rudner, D.Z. (2017). *Bacillus subtilis* SMC complexes juxtapose chromosome arms as they travel from origin to terminus. Science *355*, 524-527.

Wang, X., Le, T.B.K., Lajoie, B.R., Dekker, J., Laub, M.T., and Rudner, D.Z. (2015). Condensin promotes the juxtaposition of DNA flanking its loading site in *Bacillus subtilis*. Genes & development *29*, 1661-1675.

Wang, X., Liu, X., Possoz, C., and Sherratt, D.J. (2006). The two *Escherichia coli* chromosome arms locate to separate cell halves. Genes & development *20*, 1727-1731.

Wang, X., Montero Llopis, P., and Rudner, D.Z. (2014a). *Bacillus subtilis* chromosome organization oscillates between two distinct patterns. Proceedings of the National Academy of Sciences *111*, 12877-12882.

Wang, X., Tang, Olive W., Riley, Eammon P., and Rudner, David Z. (2014b). The SMC condensin complex is required for origin segregation in *Bacillus subtilis*. Current Biology *24*, 287-292.

Weitao, T., Nordström, K., and Dasgupta, S. (2000). *Escherichia coli* cell cycle control genes affect chromosome superhelicity. EMBO reports *1*, 494-499.

Westfall, C.S., and Levin, P.A. (2018). Comprehensive analysis of central carbon metabolism illuminates connections between nutrient availability, growth rate, and cell morphology in *Escherichia coli*. PLoS genetics *14*, e1007205.

Wilhelm, L., Bürmann, F., Minnen, A., Shin, H.C., Toseland, C.P., Oh, B.H., and Gruber, S. (2015). SMC condensin entraps chromosomal DNA by an ATP hydrolysis dependent loading mechanism in *Bacillus subtilis*. eLife *4*.

Willemse, J., Borst, J.W., de Waal, E., Bisseling, T., and van Wezel, G.P. (2011). Positive control of cell division: FtsZ is recruited by SsgB during sporulation of *Streptomyces*. Genes & development *25*, 89-99.

Willis, L., and Huang, K.C. (2017). Sizing up the bacterial cell cycle. Nature Reviews Microbiology *15*, 606.

Wolánski, M., Wali, R., Tilley, E., Jakimowicz, D., Zakrzewska-Czerwińska, J., and Herron, P. (2011). Replisome trafficking in growing vegetative hyphae of *Streptomyces coelicolor* A3(2). Journal of bacteriology *193*, 1273-1275.

Woo, J.S., Lim, J.H., Shin, H.C., Suh, M.K., Ku, B., Lee, K.H., Joo, K., Robinson, H., Lee, J., Park, S.Y., *et al.* (2009). Structural studies of a bacterial condensin complex reveal ATP-dependent disruption of intersubunit interactions. Cell *136*, 85-96.

Wu, L.J., and Errington, J. (2003). RacA and the Soj-Spo0J system combine to effect polar chromosome segregation in sporulating *Bacillus subtilis*. Molecular microbiology *49*, 1463-1475.

Yamaichi, Y., Bruckner, R., Ringgaard, S., Möll, A., Cameron, D.E., Briegel, A., Jensen, G.J., Davis, B.M., and Waldor, M.K. (2012). A multidomain hub anchors the chromosome segregation and chemotactic machinery to the bacterial pole. Genes & development *26*, 2348-2360.

Yamaichi, Y., and Niki, H. (2000). Active segregation by the *Bacillus subtilis* partitioning system in *Escherichia coli*. Proceedings of the National Academy of Sciences *97*, 14656-14661.

Yamanaka, K., Ogura, T., Niki, H., and Hiraga, S. (1996). Identification of two new genes, *mukE* and *mukF*, involved in chromosome partitioning in *Escherichia coli*. Molecular and General Genetics MGG *250*, 241-251.

Yang, H.L., Heller, K., Gellert, M., and Zubay, G. (1979). Differential sensitivity of gene expression in vitro to inhibitors of DNA gyrase. Proceedings of the National Academy of Sciences of the United States of America *76*, 3304-3308.

Yao, S., Helinski, D.R., and Toukdarian, A. (2007). Localization of the naturally occurring plasmid ColE1 at the cell pole. Journal of bacteriology *189*, 1946-1953.

Yoshikawa, H., O'Sullivan, A., and Sueoka, N. (1964). Sequential replication of the *Bacillus subtilis* chromosome, III. Regulation of initiation. Proceedings of the National Academy of Sciences of the United States of America *52*, 973-980.

Youssef, M.M., Al-Omair, M.A., and Picksley, S.M. (2014). Genetic characterization of *Escherichia coli* RecN protein as a member of SMC family of proteins. Arabian Journal of Chemistry *7*, 327-334.

Yu, X.-C., Weihe, E.K., and Margolin, W. (1998). Role of the C terminus of FtsK in *Escherichia coli* chromosome segregation. Journal of bacteriology *180*, 6424-6428.

Zawadzki, P., Stracy, M., Ginda, K., Zawadzka, K., Lesterlin, C., Kapanidis, Achillefs N., and Sherratt, David J. (2015). The localization and action of topoisomerase IV in *Escherichia coli* chromosome segregation is coordinated by the SMC complex, MukBEF. Cell Reports *13*, 2587-2596.

Zechiedrich, E.L., and Cozzarelli, N.R. (1995). Roles of topoisomerase IV and DNA gyrase in DNA unlinking during replication in *Escherichia coli*. Genes & development *9*, 2859-2869.

Zerulla, K., Chimileski, S., Näther, D., Gophna, U., Papke, R.T., and Soppa, J. (2014). DNA as a phosphate storage polymer and the alternative advantages of polyploidy for growth or survival. PloS one *9*, e94819.

Zhang, H., and Schumacher, M.A. (2017). Structures of partition protein ParA with nonspecific DNA and ParB effector reveal molecular insights into principles governing Walker-box DNA segregation. Genes & development *31*, 481-492.

Zhou, X., Rodriguez-Rivera, F.P., Lim, H.C., Bell, J.C., Bernhardt, T.G., Bertozzi, C.R., and Theriot, J.A. (2019). Sequential assembly of the septal cell envelope prior to V snapping in *Corynebacterium glutamicum*. Nature Chemical Biology *15*, 221-231.

Zusman, D., and Rosenberg, E. (1970). DNA cycle of *Myxococcus xanthus*. Journal of molecular biology *49*, 609-619.

6. Appendix

Table S1: Percentage of DNA-free cells of relevant *C. glutamicum* strains used in this study.

DNA segregation-phenotypes: none (blue), < 10 % (green) or > 20 % (red) of DNA-free cells, n > 1000.

Strain	Genotype	Anucleate cells [%]
RES 167 WT	WT	0
CDC003	Δ*parB*	26.14
CDC026	Δ*smc*	0.1
CBK001	Δ*mksB*	0
CBK002	Δ*parB* Δ*smc*	27.08
CBK003	Δ*parB* Δ*mksB*	24.95
CBK004	Δ*smc* Δ*mksB*	0
CBK005	Δ*parB* Δ*smc* Δ*mksB*	25.62
CBK006	*parB::parB-mCherry2*	0
CBK007	*parB::parB-eYFP*	0.1
CBK010	*Δsmc parB::parB-eYFP*	4.25
CBK011	*Δsmc ΔmksB parB::parB-eYFP*	3.98
CBK012	*smc::smc-mCherry*	0
CBK013	*smc::smc-mCherry parB::parB-mNeonGreen*	0
CBK014	*smc::smc-mCherry* Δ*parB*	24.18
CBK015	*mksB::mksB-mCherry*	0
CBK023	$parS_{2\text{-}10mut}$	0.19
CBK024	$parS_{1\text{-}10mut}$	29.27
CBK025	$parS_{2\text{-}10mut}$ *parB::parB-eYFP*	6.71
CBK026	$parS_{1\text{-}10mut}$ *parB::parB-eYFP*	28.5
CBK032	$parS_{1\text{-}10mut}$ *smc::smc-mCherry*	30.38
CBK034	*smc::smc-mCherry* Δ *SMC roadblock*	0
CBK035	*smc::smc-mCherry SMC roadblock replaced*	0
CBK040	$parS_{1\text{-}10mut}$ *parS 3' cg0108 parB::parB-eYFP*	25.33
CBK041	$parS_{1\text{-}10mut}$ *parS 3' cg0904 parB::parB-eYFP*	23.48

CBK043	*$parS_{1\text{-}10mut}$ parS 3‘ cg2563 parB::parB-eYFP*	24.28
CBK044	*$parS_{1\text{-}10mut}$ int::parS parB::parB-eYFP*	24.98
CBK045	*$parS_{1\text{-}10mut}$ parS 3‘ cg0904 smc::smc-mCherry*	25.07
CBK047	*parB::parB-^{R175A}mCherry2*	17.83
CBK048	*parB::parB-^{R175A}mCherry2 $parS_{2\text{-}10mut}$*	31.74
CBK049	*parB::parB-^{R175A} smc::smc-mCherry*	19.09
CBK051	*smc::smc^{E1084Q}-mCherry*	0
CBK062	*dnaN::dnaN-mCherry*	0
CBK069	*parA::parA-eYFP*	0
CBK072	*ΔparA parB::parB-eYFP*	24.06
CBK073	*ΔparB parA::parA-eYFP*	24.02
CBK074	*$parS_{1\text{-}10mut}$ parA::parA-eYFP*	24.80
CBK075	*pldP::pldP-eYFP*	0
CBK077	*ΔparB, pldP::pldP-eYFP*	22.92
CBK078	*ΔparA, pldP::pldP-eYFP*	17.37
CBK079	*$parS_{1\text{-}10mut}$ pldP::pldP-eYFP*	24.14
CBK080	*pldP::pldP-eYFP parA::parA-mCherry*	0
CBK081	*ΔpldP parB::parB-eYFP*	0
CBK082	*ftsZ::ftsZ-mCherry pldP::pldP-eYFP*	0.3

List of figures

List of tables

Acknowledgements

First of all, I want to thank Prof. Dr. Marc Bramkamp for giving me the chance to work in his lab and his support and guidance through this project. Taking your time for all the helpful discussions and sharing your scientific enthusiasm with me have brought me a lot forward to achieve my goals. You were a great supervisor throughout my doctoral studies. Thank you!

Moreover, I am very thankful to all thesis committee members for their time and interest in my topic. I want to especially thank Prof. Dr. Christof Osman, who agreed on being the second reviewer of my thesis.

I want to acknowledge my collaborators Giacomo Giacomelli, Fabian Meyer, Agata Rhomberg, Dr. Catriona Donovan, Dr. Martial Marbouty, Prof. Dr. Romain Koszul, Dr. Andreas Schmidt, Prof. Dr. Axel Imhof and Prof. Dr. Jörn Kalinowski, who contributed with their great data to the success of this study.

Many thanks to Dr. Andreas Brachmann for his help with the genome sequencing.

I am very grateful for the helpful advice and interest of my thesis advisory-committee members Prof. Dr. Stephan Gruber and Prof. Dr. Andreas Klingl in my project.

Moreover, I would like to acknowledge the coordinator of my graduate school "Life Science Munich" of the LMU Munich, Francisca Rosa Mende, who supported me in many ways in the past four years.

To all group members Giacomo, Helge, Gustavo, Fabian, Lijun, Abigail, Jessica, Nadine, Karin and to all former colleagues: Thank you for all the great times spent together. You made the work in the lab very enjoyable. I will miss that time and working with all of you.

And finally, a heartfelt thanks to my parents and friends for all their support that I could always count on. I want to especially thank Christian for being a constant in my life and for giving me great confidence during challenging times.

Curriculum vitae